

Institutsbereich Geophysik, Astrophysik und Meteorologie
Institut für Physik
Karl - Franzens - Universität Graz
Universitätsplatz 5, A-8010 Graz, Austria
<http://www.uni-graz.at/igam>

W i s s e n s c h a f t l i c h e r B e r i c h t No. 21

Joint Temperature, Humidity, Ozone, and Sea Surface Temperature Retrieval from Infrared Atmospheric Sounding Interferometer Data

by
Marc Schwärz

December 2004





Institutsbereich Geophysik, Astrophysik und Meteorologie
Institut für Physik
Karl-Franzens-Universität Graz
Atmospheric Remote Sensing and Climate System Research Group
ARSCliSys - on the art of understanding the climate system



Wissenschaftlicher Bericht No. 21

Institutsbereich Geophysik, Astrophysik und Meteorologie
Institut für Physik
Karl-Franzens-Universität Graz
Universitätsplatz 5, A-8010 Graz, Austria

**Joint Temperature, Humidity, Ozone, and Sea Surface
Temperature Retrieval from Infrared Atmospheric
Sounding Interferometer Data**

by
Marc Schwärz

Graz, December, 2004

This report contains the Ph. D. thesis of Dr. Marc Schwärz, which he worked out during the years 2001 – 2004 at the IGAM/UoG.

Acknowledgments

First I would like to thank my supervisor Prof. Dr. Gottfried Kirchengast for his distinguished overall support and a great number of fruitful scientific discussions. The work was financially supported by the START research award of G. Kirchengast funded by the Bundesministerium für Bildung, Wissenschaft und Kultur (BMBWK, Vienna, Austria) and managed under program No. Y130-N03 of the Fonds zur Förderung der wissenschaftlichen Forschung (FWF, Austria).

Thanks go to all members of the Institute for Geophysics, Astrophysics, and Meteorology (IGAM), Institute of Physics, University of Graz, Austria, for fruitful discussions on many topics of science and programming and for the good teamwork special thanks go to my colleagues of the ARSCliSys research group, especially to Dr. Ulrich Foelsche, Mag. Christian Retscher, DI Armin Löscher, Dr. Johannes Fritzer, and Dr. Andrea Steiner.

I would like to thank Dr. P. Schluessel (EUMETSAT, Darmstadt, Germany) for providing the forward model RTIASI (which is a property of EUMETSAT) and the IASI level 1c noise values. Thanks to the ECMWF for providing atmospheric analysis fields, which have been kindly pre-processed in an early state of my work by U. Foelsche. Further thanks go to Dr. E. Weisz (SSEC, Univ. of Wisconsin, Madison, WI, U.S.A.) for valuable discussions on retrieval methodology.

Most of all I would like to thank my partner Susi and my child Zora for being that patient with me throughout all the years (and especially during the last weeks). My sincere thanks are due to my parents, my sister, and my brother for their understanding and their mental and emotional support whenever it was needed. Last but not least, I wish to thank all my friends, who accompanied me during the last years.

Contents

Introduction	1
1 Radiative Transfer	5
1.1 Introduction	5
1.2 Basic Composition and Fluxes of the Atmosphere	5
1.3 The Radiative Transfer Equation	8
1.3.1 General Radiative Transfer Equation	9
1.3.2 The Total Field	13
1.3.3 Formal Solution for the Upward Intensity	16
1.3.4 Solving the Special Case of <i>No Scattering</i>	18
1.4 Absorption Spectra of Atmospheric Gases	19
1.4.1 Excitation Modes	20
1.4.2 Spectral Line Shape and Line Strength	20
1.4.3 Calculation of Transmittances	24
1.4.4 Absorption in the Infrared	26
1.5 The Boundary Layer	28
1.5.1 Boundary Properties of Planetary Media	28
1.5.2 Sea Surface Temperature	30
2 METOP and IASI	31
2.1 The METOP Satellite Series	31
2.1.1 METOP Overview	32
2.1.2 The METOP Orbit	32
2.1.3 The Instruments on board of METOP	33

2.2	The IASI Instrument	36
2.2.1	Design and Functional Chain	37
2.2.2	Objectives and Main Specifications	41
2.2.3	Measurement Principle	45
2.2.4	Data Products	50
3	Discrete Inverse Theory	53
3.1	The Forward Model	53
3.1.1	Theoretical Considerations on Forward Modeling	53
3.1.2	Range and Null-space of the Forward Model Operator	54
3.2	The Inverse Problem	55
3.2.1	Least Squares Solution	56
3.2.2	Truncated SVD	56
3.2.3	Optimal Estimation	57
3.2.4	Other Methods	58
3.3	The Optimal Estimation Principle	59
3.3.1	The Bayesian Approach	59
3.3.2	Optimal Linear Inversion with Gaussian Statistics	60
3.3.3	Optimal Non-Linear Inversion	66
4	The Model RTIASI	69
4.1	General Considerations on Modeling Atmospheric Radiances	69
4.2	Composition of RTIASI	71
4.2.1	Calculation of the Fast Transmittance Coefficients	71
4.2.2	Profile Dataset Used	72
4.2.3	Transmittances	73
4.2.4	Radiative Transfer Model	74
4.3	Tangent Linear, Adjoint, and Gradient Matrix Models	77

5	IASI Retrieval and Channel Selection	81
5.1	Retrieval Setup	81
5.1.1	Joint Retrieval Algorithm	81
5.1.2	<i>A Priori</i> and Measurement Error Covariance Matrices	83
5.1.3	Simulation of the Measurement Vector	88
5.1.4	Generation of <i>A Priori</i> Profiles	88
5.2	Channel Selection	90
5.2.1	Information Content Theory	92
5.2.2	Maximum Sensitivity Approach	95
6	Retrieval Results and Performance Analysis	101
6.1	Performance Analysis of the Joint Algorithm	113
6.1.1	Retrieval Results for a Full Orbit	113
6.1.2	Profile Retrieval Characterization Results	122
6.2	Comparison of Different Channel Selection Methods	140
6.3	Comparison of Retrieval Algorithms	145
6.3.1	Single Parameter Retrievals	145
6.3.2	Upper Troposphere Humidity Retrieval	152
6.3.3	Impact of Additional Ozone Retrieval in the Joint Algorithm . . .	154
	Summary and Conclusions	157
	Appendix A	161
A.1	Construction of the Simulated IASI Swath	161
A.1.1	Calculation of the Points on a Measurement Ray	161
A.1.2	Calculation of the Surface Height Including Orography	165
A.2	RTIASI Pressure Levels	166
A.3	IASI Level 1c Noise Values	167
A.4	Determination of the Number of Channels	168

Appendix B	171
B.1 Basic Radiation Laws	171
B.2 Conversion of Physical Parameters	173
B.3 Basic Statistical Properties	174
B.4 Atmospheric Constituents	176
B.5 Physical Constants	177
B.6 Parameters of Earth and Atmosphere	178
Appendix C	179
C.1 List of Acronyms	179
C.2 List of Units	181
References	183

Introduction

Earth observation via space-based remote sensing has a history dating back to the TIROS (Television Infrared Observation Satellite) Program of the early 1960's starting with the launch of TIROS-1 on April 1, 1960, which had an operational period of only 78 days. Since that time satellite-based meteorology was improved by, e. g., the first determinations of atmospheric humidity and temperature profiles carried out by the NIMBUS satellite series in the early 1970's which also started to perform ozone measurements. In the last two decades, further improvements have been made on the horizontal sampling and accuracy of retrievals particularly with instruments such as the High Resolution Infrared Sounder (HIRS), as well as on the vertical resolution of the data by the Atmospheric Infrared Sounder (AIRS) on-board of the AQUA Satellite. Today's global system of meteorological satellite observations include geosynchronous spacecrafts flying at an altitude of about 36000 km and polar-orbiting satellites in low earth orbits of about 800 km.

The Infrared Atmospheric Sounding Interferometer (IASI), which will be part of the core payload of the METOP series of polar orbiting operational meteorological satellites currently prepared for EUMETSAT (first satellite to be launched in 2005), will provide a further significant improvement of vertical resolution of temperature and humidity profiles compared to existing operational satellites via a very high spectral resolution. Furthermore it will deliver ozone profiles and surface skin temperature as well as cloud parameters and column amounts of nitrous oxide (N_2O), methane (CH_4), and carbon monoxide (CO).

IASI is a Michelson type Fourier transform interferometer, which samples a part of the infrared (IR) spectrum contiguously from 645 cm^{-1} to 2760 cm^{-1} ($15.5 \mu\text{m} - 3.6 \mu\text{m}$) with an unapodized spectral resolution of about 0.5 cm^{-1} . The acquisition of information about the surface and the atmosphere is based on detection, recording, and analysis of electromagnetic (EM) radiation emitted by the earth mainly in the infrared range of the EM spectrum. The characteristics of the modification of radiation when passing through the atmosphere depends on the amount and properties of the atmospheric constituents. Therefore the information about the state of the atmosphere stored in the detected radiation may be retrieved from the measured spectrum.

Temperature profiles are obtained from observations in the absorption bands of carbon dioxide (CO_2), which is a relatively abundant trace gas of known and uniform distribution. Other atmospheric constituents absorbing in the thermal IR are H_2O (water vapor and temperature sounding), ozone (O_3 – ozone profiling), N_2O , CH_4 , and CO (trace gas

column amounts). The atmospheric window regions, where attenuation is minimal, are used to obtain surface and cloud properties. With the opportunity of a very high spectral resolution at several wavelengths, the possibility of observing different layers can be established by taking into account that radiances measured in the center of an absorption band arise from the upper atmospheric layers, while measurements at the wings of a band will sense deeper into the atmosphere.

The physical relation between the radiance observed at the satellite and the current state of the atmosphere is described via the theory of radiative transfer, which exhibits the radiance measured at the top of the atmosphere (TOA) as a sum of an emission term from the surface and of weighted Planck intensities emitted from every atmospheric layer. The weighting functions are related to the transmittances which depend, on their part, on the absorption coefficient and the density of the relevant absorbing gas whereas the Planck intensities describe the spectral radiance emitted by a blackbody.

Since the IASI instrument measures infrared radiation in more than 8000 channels, efficient retrieval algorithms have to be developed to fully exploit the potential of the instrument. Such retrieval algorithms rely on two processes. The first is the construction of exact and efficient forward models which calculate the radiances measured at the TOA corresponding to a certain state of the atmosphere (in the current study this will be done by the fast transmittance model RTIASI [*Matricardi and Saunders (1999)*]). On the other hand we have to develop inversion algorithms, also termed inverse models, to estimate the state of the atmosphere from the measured radiances. To this end, a physical-statistical approach has been utilized, incorporating the underlying physics and modeling the uncertainties in the measurements as well as in the prior knowledge of the state. Preceding this inversion, we implemented a channel selection scheme to reduce the number of IASI channels used, for removing redundant information for performance and computational reasons.

One of the primary objectives of the IASI instrument, according to the IASI science plan [*Camy-Peyret and Eyre (1998)*], is the improvement of the vertical resolution of temperature and water vapor profiles to about 1 km in the middle and lower troposphere as well as improving the retrieval accuracy to within 1 K in temperature and $\sim 10\%$ in specific humidity. The scientific motivation of this is based on the key role of water vapor in the upper troposphere and its effects on the global climate since only small changes in humidity and its trends have serious implications on the amount of thermal energy escaping to space [*Schmetz et al. (1995)*, *Spencer and Braswell (1997)*]. Additionally, this level of performance will greatly assist numerical weather prediction (NWP) in delivering accurate and frequent temperature and humidity profiles for operational and research needs and it will supply more accurate quantifications of the climate variability, particularly contributing to our knowledge of the climate of the upper troposphere.

Chapter 1 of this study starts with an introduction on the radiative transfer including absorption analysis of gases as well as the description of surface properties. Chapter 2 contains an overview of the METOP satellite and a comprehensive description of the future instrument IASI on which the current work is focused. An overview on inversion schemes as well as a detailed description of the optimal estimation retrieval methodology

is provided in chapter 3 whereas in chapter 4 the fast radiative transfer model RTIASI is described. Chapter 5 starts the specific part of this report via introducing the setup of the joint algorithm and the implementation of the channel selection schemes. In chapter 6 we carefully investigate the potential of IASI to provide accurate profiles of temperature and humidity, and sea surface temperature measurements, as well as improvements in ozone profiling. We show and discuss several simulation experiments regarding theoretical retrieval accuracy and resolution, retrieval scheme characteristics, empirical error estimates and the comparison of different channel selection setups. Furthermore, we show the improvements of the joint algorithm introduced in chapter 5 compared to more specific retrieval setups. A summary and a collection of main conclusions closes this report. Appendices A to C gather some useful background and reference information.

Chapter 1

Radiative Transfer in the Earth-Atmosphere System

1.1 Introduction

The System Earth exchanges energy with space by means of radiative transfer (main part) and particle transport. The radiation which is modified by various physical processes (e. g. absorption, transmission, scattering, diffraction) while propagating through the atmosphere arranges the thermal equilibrium between earth and its environment. The quantitative description of the radiation field resulting from the interaction between massive particles and massless ones (photons) is known as the theory of radiative transfer.

The particle exchange including processes like particle capturing by the magnetic field, incoming cosmic radiation or particle loss through the magnetopause is negligible for our purpose.

1.2 Basic Composition and Fluxes of the Atmosphere

The bulk atmosphere of our planet mainly consists of molecular nitrogen, N_2 ($\sim 78\%$ by volume), molecular oxygen, O_2 ($\sim 21\%$ by volume), and the noble gas argon, Ar ($\sim 1\%$ by volume). Trace gases include water vapor (H_2O), carbon dioxide (CO_2), ozone (O_3) and others (for details see Table B.1). Although some of the atmospheric constituents are of small amount and vary highly in space and time, such as water vapor, aerosols, clouds, etc., they are extremely important for the radiative transfer.

The atmosphere can be categorized either by its thermal structure or by its physical-chemical mixing behavior. The classification by mixing behavior is based on homogeneous mixing of the atmospheric constituents up to 100 km (homosphere) caused by turbulent air motions (mostly large scale convections in the troposphere and small scale

eddies beyond that region) whereas above 100 km diffusion stratifies the constituents according to their molecular and atomic mass, respectively (see Figure 1.1). In this region, which is termed the heterosphere, the mean molecular mass decreases monotonically with height.

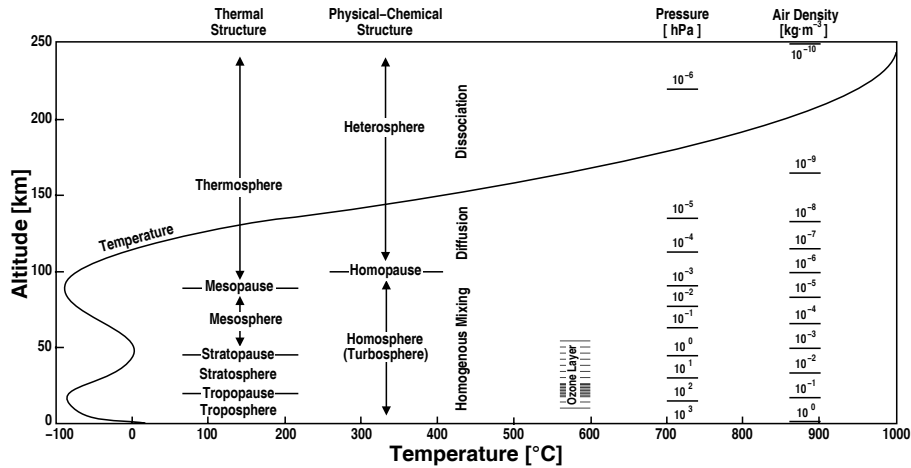


Figure 1.1: Vertical structure of the atmosphere with a typical temperature profile, pressure, and air density. Additionally the names of the atmospheric layers are depicted (source: [Reuter et al. (1997)] – adapted).

Categorization by the thermal structure leads to a separation of the atmosphere into 4 different layers: the troposphere, the stratosphere, the mesosphere, and the thermosphere (see Figure 1.1). Compared to the atmospheres of, e. g., Mars or Venus this is a rather sophisticated structure. The reasons are different heating effects in the various layers caused primarily by absorption of terrestrial radiation from the surface and by turbulent heat transfer but also by solar radiation (see section 1.4).

Temperature decreases with height at an average lapse rate of 6.5 °C per kilometer in the troposphere, which is dominated by convective motions. The stratosphere is dominated by radiative processes. Absorption of ultraviolet radiation by ozone results in a temperature increase in this layer. This can lead to a temperature value at the stratopause which may exceed 0 °C (273.15 K). Convective motion and radiative processes prevail in the mesosphere, where the temperature decreases again. In the thermosphere temperature increases once more due to the absorption of extreme ultraviolet radiation by O₂ and O (atomic oxygen).

Since sun and earth have different so called *blackbody temperatures* (a blackbody is a perfect emitter and complete absorber of radiation at all wavelengths) they emit electromagnetic radiation in different spectral ranges. The radiation from the sun consists roughly of 10% ultraviolet (0.01-0.4 μm), 45% visible (0.4-0.8 μm), and 45% infrared (IR) radiation (bulk in 0.8-4 μm) with a maximum at 0.48 μm (~6000K) and is referred to as shortwave (SW) radiation. The earth emits radiation in the IR in a range from about 3 to 100 μm with a peak intensity at about 10 μm which is termed longwave (LW) radiation.

The incident solar flux at the top of the atmosphere (TOA), $F_S = 1372 \text{ W m}^{-2}$, is distributed across the earth which leads to a global-mean SW flux incident on the TOA of $F_S/4 = 343 \text{ W m}^{-2}$, where the factor 4 represents the ratio of the surface area to the cross-sectional area of the intercepted beam of SW radiation. Since there is a non-uniformly distributed absorption of solar energy due to geometrical considerations, variations in optical properties, and variations in the cloud coverage, we have to introduce another quantity which is termed solar *insolation*. The solar *insolation* is defined as the SW flux at the TOA averaged over a period of time (e. g., one day) as a function of the solar zenith angle and of the length of the day.

Over long time scales the earth-atmosphere system is in thermal equilibrium – as a consequence of that the absorbed solar fluxes have to be balanced by thermal infrared fluxes emitted by the earth-atmosphere system. This balance and the energy fluxes between earth, atmosphere, and sun are illustrated in Figure 1.2.

The equilibrium in energy (globally and annually averaged) can be expressed by:

$$(1 - A)F_S\pi r^2 = 4\pi r^2\sigma T_E^4, \quad (1.1)$$

where A is the albedo of the earth which is the portion of incoming solar flux reflected back to space, σ is the Stefan-Boltzmann constant, and T_E is the blackbody temperature of the earth. The left hand side of Equation 1.1 represents the incident solar flux of cross sectional area πr^2 and the right hand side represents the flux emitted by a spherical ($4\pi r^2$) earth-atmosphere system based on the Stefan-Boltzmann law (for details, see e. g. [Salby (1996)]).

Inserting $F_S = 1372 \text{ W m}^{-2}$ and $A = 0.3$ in Equation 1.1 gives a surface temperature of the earth of about 255 K. However, the mean surface temperature of the earth is about 288 K. The discrepancy between these two values can be explained by the so called *greenhouse effect*, which is controlled by strong absorption of infrared radiation by atmospheric constituents like water vapor and clouds (H_2O), carbon dioxide (CO_2), ozone (O_3), methane (CH_4), nitrous oxide (N_2O), aerosols, and chlorofluorocarbons (CFC's).

The blackbody spectra of sun and earth are modified by various mechanisms caused by atmospheric constituents. SW radiation is attenuated primarily by reflection (clouds, aerosols), Rayleigh scattering (scattering by air molecules smaller than the wavelength) and by absorption. Wavelengths smaller than $0.1 \mu\text{m}$ are absorbed by N_2 , O_2 , and by atomic nitrogen (N) and oxygen (O) at altitudes above 100 km. Above $\sim 50 \text{ km}$ wavelengths shorter than $0.24 \mu\text{m}$ dissociate O_2 molecules into 2 O molecules. These oxygen atoms recombine with molecular oxygen to form ozone (O_3). Ozone absorbs radiation between 0.2 and $0.3 \mu\text{m}$ above $\sim 50 \text{ km}$ which in turn results in the dissociation of O_3 into molecular and atomic oxygen. Another ozone band can be found above $0.4 \mu\text{m}$. These absorption lines are the primary source of temperature increase in the stratosphere ($\sim 25 \text{ km}$). For a detailed view of the ozone cycles see, e. g., the fundamental papers of [Chapman (1930), Crutzen (1970)] or a summarizing description in [Seinfeld and Pandis (1998)].

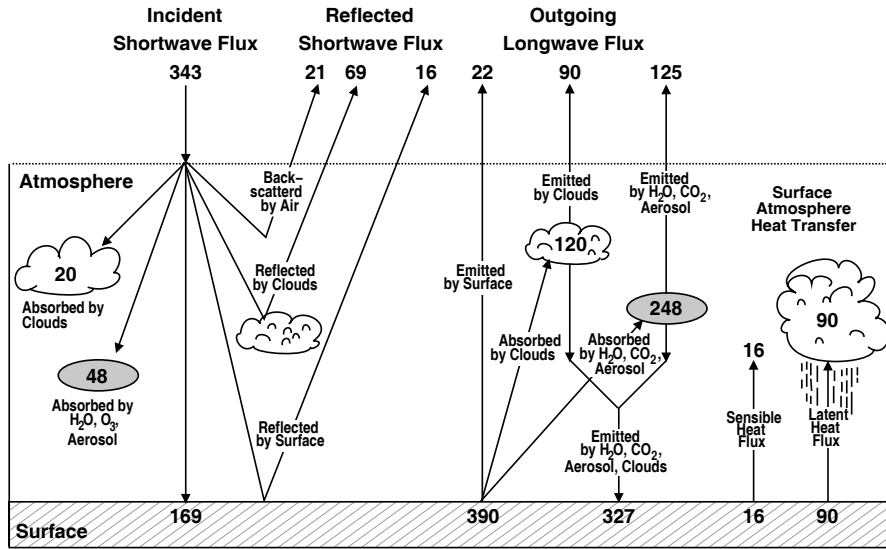


Figure 1.2: Global mean energy budget [$W m^{-2}$] (source: [Salby (1996)]).

Absorption by (H_2O) takes place in the near IR ($0.6-3.0 \mu m$) as well as in several narrow bands from about 0.9 to $2.1 \mu m$. For wavelengths extending from 0.76 to $100 \mu m$ most attenuation is by absorption, primarily caused by H_2O , CO_2 , and O_3 . Supplementary absorption bands in the IR arise from methane (CH_4), nitrous oxide (N_2O), and to a lesser extent carbon monoxide (CO), sulfur dioxide (SO_2), ammonia (NH_3), and CFC's. An interesting point is that except for O_3 virtually all the absorption occurs in the troposphere where the absolute concentration of any atmospheric constituent is large.

The term used for gases absorbing in the IR is *greenhouse gases* according to the effect that LW radiation is trapped in the lower atmosphere by repeated absorption and re-emission – the *greenhouse effect*. Only in the so called *atmospheric window* at wavelengths of $8-12 \mu m$ the absorption is weak enough for infrared radiation to pass freely through the atmosphere, except for some remaining continuum absorption, mainly by water vapor.

1.3 The Radiative Transfer Equation

A radiation field is modified by various physical processes as it propagates through the atmosphere. Emission depends on the composition and thermal structure, while absorption and scattering properties are defined by the dominant molecular opacity and cloud structure (see section 1.2). The way how the radiation field interacts with the atmosphere is described by the theory of radiative transfer. Various authors have dealt with this theory, e. g. [Kourganoff (1952), Goody (1964), Goody and Yung (1989)], and originally [Chandrasekhar (1950)], who approaches the subject from the point of view of mathematical physics. The description of this section is mostly based on [Hanel et al. (1992)].

1.3.1 General Radiative Transfer Equation

In this subsection we first will set up the needed geometry and then we will consider the microscopic processes to derive an Equation for the total radiation field.

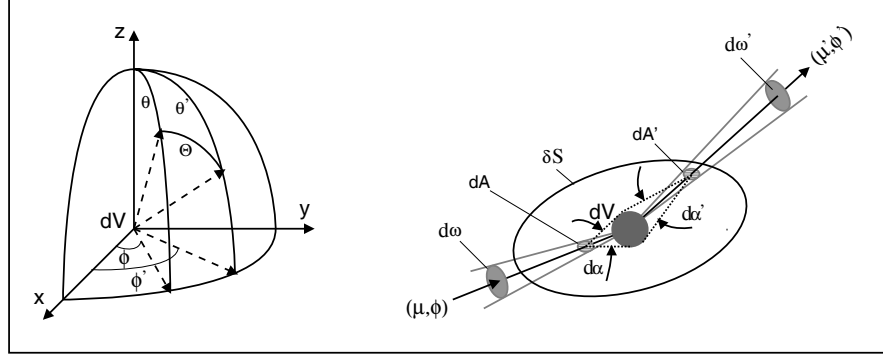


Figure 1.3: Scattering geometry. Radiation with incident direction (μ, ϕ) is scattered through the scattering angle Θ into the outgoing direction (μ', ϕ') (after: [Hanel et al. (1992)] – modified).

Suppose we have a volume element dV containing N_0 particles located at height z and angles $\mu = \cos \theta$ (θ , zenith angle: $0 \leq \theta \leq \pi$ with zero as the zenith) and ϕ (azimuthal angle: $0 \leq \phi < 2\pi$) above the surface (see Figure 1.3). We have also a specific intensity (or spectral radiance) I_ν defined as the rate at which radiant energy confined to a solid angle and unit wavenumber interval crosses unit surface area normal to the direction of incidence. Specifying the wavenumber by cm^{-1} the unit of the specific radiance is $[\text{W m}^{-2} \text{sr}^{-1} \text{cm}]$. Another needed parameter is the phase function for single scattering $p(\cos \Theta)$. It is defined by:

$$\frac{dE_\nu(z, \mu', \phi')}{E_\nu(z, \mu, \phi)} = p(\cos \Theta) \frac{d\omega'}{4\pi}, \quad (1.2)$$

where $E_\nu(z, \mu, \phi)$ represents the fraction of energy per unit time incident on dV having the direction (μ, ϕ) that is either absorbed or scattered in all directions and $dE_\nu(z, \mu', \phi')$ is the fraction of E_ν that is scattered into the direction (μ', ϕ') which is contained in the solid angle ω' . It describes the angular distribution of radiation scattered once through the angle Θ . Considering spherical trigonometry we find that the phase function is only a function of $(\mu', \phi'; \mu, \phi)$:

$$p(\cos \Theta) = p(\mu', \phi'; \mu, \phi), \quad (1.3)$$

and that it is symmetric in its solid angle directions:

$$p(\mu', \phi'; \mu, \phi) = p(\mu, \phi; \mu', \phi').$$

For the derivation of the radiative transfer Equation we are dealing with a monochromatic photonic field and a volume element dV restricted to dimensions considerably

smaller than the mean free path of an individual photon – i. e. only single interactions should be possible.

Let us construct now a convex closed surface, δS around dV such that the volume enclosed by δS is large compared to dV but small otherwise (see Figure 1.3). Let dA and dA' be elements of δS such that the direction from dA to dV is (μ, ϕ) and the direction from dV to dA' is (μ', ϕ') . Further let $d\omega$ and $d\omega'$, respectively, be the elements of solid angle containing dA and dA' as seen from dV and let $d\alpha$ and $d\alpha'$ be the solid angles containing dV as seen from dA and dA' , respectively. The considered photons have a wavenumber range $(\nu, \nu + d\nu)$ and have an extinction cross section in the range $(\chi, \chi + d\chi)$. In general the cross section χ depends on the wavenumber and, if the targets are not spherically symmetric, it depends on the direction as well.

If we now consider a beam of photons having the specifications defined above there are (mainly) four kinds of interaction they can undergo:

1. Scattering out of the beam.
2. Absorption.
3. Scattering into the beam.
4. Emission.

The first two kinds of processes are resulting in a loss in the radiation field whereas the last two processes are representing a gain. In the following we define losses and gains of the specific intensity by the symbols δ_- and δ_+ , respectively.

Scattering out of the beam

The amount of energy $\delta E_\nu(z, \mu, \phi)$ in the wavenumber range $(\nu, \nu + d\nu)$ crossing dV in a time dt , which has formerly been outside δS and has also crossed dA , is:

$$\delta E_\nu(z, \mu, \phi) = I_\nu(z, \mu, \phi) \mu_1 dA d\alpha d\nu dt \quad (1.4)$$

where μ_1 is the cosine of the angle between the direction (μ, ϕ) and $d\mathbf{A}$ (the roman bold notation points out the vector). A certain fraction of this energy is scattered in dV into the solid angle $d\omega'$. Considering the Equations 1.2 and 1.3 this fraction is:

$$\frac{d[\delta E_\nu(z, \mu', \phi')]}{\delta E_\nu(z, \mu, \phi)} = P(\chi) p_\chi(\mu', \phi'; \mu, \phi) \frac{d\omega'}{4\pi}, \quad (1.5)$$

where $P(\chi)$ is the probability that a photon incident on dV is extinguished (absorbed or scattered) by a particle of cross section χ and $p_\chi(\mu', \phi'; \mu, \phi)$ is the phase function depending on χ . It is normalized to the so called *albedo for single scattering*, $\tilde{\omega}_0$:

$$\tilde{\omega}_0(\chi) = \frac{1}{E_\nu(z, \mu, \phi)} \int dE_\nu(z, \mu', \phi') = \int_0^{4\pi} p(\mu', \phi'; \mu, \phi) \frac{d\omega'}{4\pi}, \quad (1.6)$$

which is defined as the ratio of radiant energy scattered in all directions to that extinguished (absorbed plus scattered). $P(\chi)$ is defined as the ratio of the total available effective extinction cross section of all particles in the cross section range $(\chi, \chi + d\chi)$ contained in dV to the geometrical cross section $d\sigma$ of dV as seen in the direction (μ, ϕ) which is given by:

$$P(\chi) = \frac{N(\chi)\chi d\chi dV}{d\sigma}, \quad (1.7)$$

where $N(\chi)$ is the number of particles per unit volume and unit cross section range centered at χ . Inserting Equation 1.7 and 1.4 in Equation 1.5 yields:

$$d[\delta E_\nu(z, \mu', \phi')] = \frac{N(\chi)\chi d\chi dV}{d\sigma} \times I_\nu(z, \mu, \phi)\mu_1 dA d\alpha d\nu dt p_\chi(\mu', \phi'; \mu, \phi) \frac{d\omega'}{4\pi}, \quad (1.8)$$

This means we obtain a loss of intensity (i. e. energy) $d[\delta_- I_{\nu,S}(z, \mu, \phi)]$ (the subscript S means scattering) from the direction (μ, ϕ) which in turn corresponds to the energy gain $[\delta E_\nu(z, \mu', \phi')]$ in the direction (μ', ϕ') . Comparing now Equation 1.4 (after differentiating it) with Equation 1.8 we obtain:

$$d[\delta_- I_{\nu,S}(z, \mu, \phi)] = \frac{N(\chi)\chi d\chi dV}{d\sigma} I_\nu(z, \mu, \phi) p_\chi(\mu', \phi'; \mu, \phi) \frac{d\omega'}{4\pi}. \quad (1.9)$$

Integrating Equation 1.9 gives the loss of the total intensity in the wavenumber range $(\nu, \nu + d\nu)$ and in the direction (μ, ϕ) by scattering in dV :

$$\delta_- I_{\nu,S}(z, \mu, \phi) = \frac{N_0 dV}{d\sigma} I_\nu(z, \mu, \phi) \int_0^\infty \int_0^{4\pi} D(\chi)\chi p_\chi(\mu', \phi'; \mu, \phi) \frac{d\omega'}{4\pi} d\chi, \quad (1.10)$$

where N_0 is the total number of particles per unit volume and $D(\chi)$ is the normalized distribution function of particle cross sections – i. e. $N(\chi) = N_0 D(\chi)$. Implicit in the χ integration is the averaging over orientation for particles with a lack in spherical symmetry.

Absorption

From the discussion above it follows, that the energy in the wavenumber range $(\nu, \nu + d\nu)$ crossing dA in a time dt , which is absorbed by particles in the cross section range $(\chi, \chi + d\chi)$, is:

$$d[\delta E_\nu(z, \mu, \phi)] = P_A(\chi) I_\nu(z, \mu, \phi)\mu_1 dA d\alpha d\nu dt, \quad (1.11)$$

where $P_A(\chi)$ is the probability of absorbing a photon in the treated wavenumber range:

$$P_A(\chi) = [1 - \tilde{\omega}_0(\chi)] P(\chi) = \frac{[1 - \tilde{\omega}_0(\chi)] N(\chi)\chi d\chi dV}{d\sigma}. \quad (1.12)$$

Thus, following the steps shown above, we obtain the total intensity in the wavenumber range $(\nu, \nu + d\nu)$ lost from the direction (μ, ϕ) by absorption in dV :

$$\delta_- I_{\nu,A}(z, \mu, \phi) = \frac{N_0 dV}{d\sigma} I_\nu(z, \mu, \phi) \int_0^\infty [1 - \tilde{\omega}_0(\chi)] D(\chi) \chi d\chi. \quad (1.13)$$

Scattering into the beam

If we want to obtain the gain to the radiation field by scattering photons into the direction of the beam (μ, ϕ) , we only have to reverse the initial and the final states. Doing this it can be shown that the gain of energy $d[\delta E_\nu(z, \mu, \phi)]$ in a time dt and in the direction (μ, ϕ) contained in the solid angle $d\omega$, which has resulted from a scattering in the cross section range $(\chi, \chi + d\chi)$ contained in dV , and which had the direction (μ', ϕ') and was contained in the solid angle $d\alpha'$ before the scattering event, is:

$$d[\delta E_\nu(z, \mu, \phi)] = \frac{N(\chi) \chi d\chi dV}{d\sigma'} \times I_\nu(z, \mu', \phi') \mu'_1 dA' d\alpha' d\nu dt p_\chi(\mu, \phi; \mu', \phi') \frac{d\omega}{4\pi}. \quad (1.14)$$

Here $d\sigma'$ is the geometrical cross section of dV as seen in the direction (μ', ϕ') , $d\alpha'$ is the solid angle spanned by $d\sigma'$ from the point of view of dA' , and μ'_1 is the cosine of the angle contained between the direction (μ', ϕ') and $d\mathbf{A}'$.

The gain in intensity at dV in the direction (μ, ϕ) has to be given by:

$$d[\delta E_\nu(z, \mu, \phi)] = d[\delta_+ I_S(z, \mu, \phi)] d\sigma d\omega d\nu dt, \quad (1.15)$$

since $d[\delta E_\nu(z, \mu, \phi)]$ is just the energy in a time dt that crosses normal to the surface element $d\sigma$ at dV and is contained in $d\omega$. The comparison of the Equations 1.14 and 1.15 yields:

$$d[\delta_+ I_{\nu,S}(z, \mu, \phi)] = \frac{N(\chi) \chi d\chi dV}{d\sigma} I_\nu(z, \mu', \phi') p_\chi(\mu, \phi; \mu', \phi') \frac{\mu'_1 dA' d\alpha'}{4\pi d\sigma'}. \quad (1.16)$$

Denoting the distance between dV and dA by r we can see from simple geometric considerations:

$$\mu'_1 dA' = r^2 d\omega', \quad d\sigma' = r^2 d\alpha'.$$

This leads us to a simplification of Equation 1.16:

$$d[\delta_+ I_{\nu,S}(z, \mu, \phi)] = \frac{N(\chi) \chi d\chi dV}{d\sigma} p_\chi(\mu, \phi; \mu', \phi') I_\nu(z, \mu', \phi') \frac{d\omega'}{4\pi}. \quad (1.17)$$

Integrating Equation 1.17 over all solid angles ω' and all particle cross sections χ yields the total contribution to the intensity in the direction (μ, ϕ) by scattering from dV :

$$\delta_+ I_{\nu,S}(z, \mu, \phi) = \frac{N_0 dV}{d\sigma} \int_0^\infty \int_0^{4\pi} D(\chi) \chi p_\chi(\mu, \phi; \mu', \phi') I_\nu(z, \mu', \phi') \frac{d\omega'}{4\pi} d\chi. \quad (1.18)$$

Emission

The last contribution to the radiation field we take into account is the thermal emission of photons from dV . Therefore we have to consider the surface δS of Figure 1.3 to be a perfectly insulating enclosure keeping the particles in dV at a constant temperature T . Since the radiation field in dV is in thermal equilibrium with its environment and is isotropic the amount of energy in the wavenumber range $(\nu, \nu + d\nu)$ emitted by particles in the cross section range $(\chi, \chi + d\chi)$ into the direction (μ, ϕ) contained in the solid angle $d\omega$, upon an instantaneous removal of the enclosure, is given by (c. f. Equations 1.11 and 1.12):

$$d[\delta E_\nu(z, \mu, \phi)] = B_\nu(T)N(\chi) [1 - \tilde{\omega}_0(\chi)] \chi d\chi dV d\omega d\nu dt, \quad (1.19)$$

where $B_\nu(T)$ is the Planck function. The term $[1 - \tilde{\omega}_0(\chi)] \chi$ is an emission cross section, identical to the absorption cross section, as required by the first law of thermodynamics and *Kirchhoff's law*, respectively. If now the total number of particles of all sizes and shapes per unit volume is N_0 , and the cross section distribution in dV is given by $D(\chi)$, like in the case of scattering and absorption, then the total contribution from all particles in dV in the direction (μ, ϕ) contained in the solid angle $d\omega$ is:

$$\delta_+ I_{\nu,E}(z, \mu, \phi) = \frac{N_0 dV}{d\sigma} B_\nu(T) \int_0^\infty [1 - \tilde{\omega}_0(\chi)] D(\chi) \chi d\chi. \quad (1.20)$$

If the enclosure is not set back, dV will be exposed to the local anisotropic radiation field of arbitrary energy density. How the emission intensity reacts on this is mainly a function of the importance of either the collision of molecules in gaseous or condensed state, respectively, or the interactions between these molecules and the radiation field, as a cause of molecular absorptions and emissions. If there is a dominance of interactions with the radiation field, the emission will consist (mainly) of spontaneous emissions of photons from excited molecules (isotropic), and induced emission through the perturbation due to the external field (anisotropic). Thus the radiation emitted from dV can not be isotropic unless the radiation field itself is strictly isotropic.

If the collisions between the molecules dominate we obtain thermal (isotropic) emission. This will occur in regions where the density of molecules is high enough to get many more inter-molecule collisions than collisions between photons and molecules (in general, e. g., inside liquid and solid matter). For molecules in the gas phase induced emission becomes important if N_0 is sufficiently small.

Equation 1.20 is acceptable upon a removal of the enclosure if collisions between molecules dominate, which is the case in practice for the atmosphere below about 80 km, i. e. for the region of interest in this study.

1.3.2 The Total Field

After considering all the microscopic processes changing the net intensity in the direction (μ, ϕ) due to the presence of the volume element dV we are now able to evaluate the total

field by adding all gains and losses from Equations 1.10, 1.13, 1.18, and 1.20:

$$\begin{aligned}
\delta I_\nu(z, \mu, \phi) &= -\delta_- I_{\nu,S}(z, \mu, \phi) - \delta_- I_{\nu,A}(z, \mu, \phi) + \delta_+ I_{\nu,S}(z, \mu, \phi) + \delta_+ I_{\nu,E}(z, \mu, \phi) \\
&= -\frac{N_0 dV}{d\sigma} I_\nu(z, \mu, \phi) \int_0^\infty \int_0^{4\pi} D(\chi) \chi p_\chi(\mu', \phi'; \mu, \phi) \frac{d\omega'}{4\pi} d\chi \\
&\quad - \frac{N_0 dV}{d\sigma} I_\nu(z, \mu, \phi) \int_0^\infty [1 - \tilde{\omega}_0(\chi)] D(\chi) \chi d\chi \\
&\quad + \frac{N_0 dV}{d\sigma} \int_0^\infty \int_0^{4\pi} D(\chi) \chi p_\chi(\mu, \phi; \mu', \phi') I_\nu(z, \mu', \phi') \frac{d\omega'}{4\pi} d\chi \\
&\quad + \frac{N_0 dV}{d\sigma} B_\nu(T) \int_0^\infty [1 - \tilde{\omega}_0(\chi)] D(\chi) \chi d\chi. \tag{1.21}
\end{aligned}$$

Of course Equation 1.21 can be simplified. First by defining a normalized effective phase function, $p_0(\mu, \phi; \mu', \phi')$, by:

$$p_0(\mu, \phi; \mu', \phi') \int_0^\infty \tilde{\omega}_0(\chi) D(\chi) \chi d\chi = \int_0^\infty D(\chi) \chi p_\chi(\mu, \phi; \mu', \phi') d\chi. \tag{1.22}$$

Multiplying both sides of Equation 1.22 by $d\omega'/(4\pi)$, integrating over all solid angles, and remembering the definition of the single scattering albedo (see Equation 1.6), we obtain:

$$\int_0^{4\pi} p_0(\mu, \phi; \mu', \phi') \frac{d\omega'}{4\pi} = 1. \tag{1.23}$$

Let us also define an effective extinction cross section χ_E and an effective single scattering albedo $\tilde{\omega}_0$ of dV :

$$\chi_E = \int_0^\infty D(\chi) \chi d\chi \tag{1.24}$$

and

$$\tilde{\omega}_0 \int_0^\infty D(\chi) \chi d\chi = \int_0^\infty \tilde{\omega}_0(\chi) D(\chi) \chi d\chi, \tag{1.25}$$

respectively, and a single scattering phase function $p(\mu, \phi; \mu', \phi')$ normalized to $\tilde{\omega}_0$ such that

$$p(\mu, \phi; \mu', \phi') = \tilde{\omega}_0 p_0(\mu, \phi; \mu', \phi'). \tag{1.26}$$

Introducing now the approximation of a plane-parallel atmosphere (infinitely extended in the x - and y -directions and variable in the z -direction only) which is valid locally for the earth, a volume element cylinder dV of height dz and base area $d\sigma_z$ is given by:

$$dV = d\sigma_z dz \tag{1.27}$$

Now we make the linear dimensions of $d\sigma_z$ arbitrarily much larger than dz , but still small enough that $d\sigma_z$ remains an element of the surface area. With that the sides of the cylinder can be neglected relative to $d\sigma_z$ in determining the effective cross section of dV as seen along a slant-path in the direction (μ, ϕ) . Thus the geometric cross section $d\sigma$ of dV is:

$$d\sigma = \mu d\sigma_z. \tag{1.28}$$

And after defining a normal optical depth τ_ν^* measured from the top of the atmosphere (TOA) inward, such that:

$$d\tau_\nu = -N_0\chi_E dz, \quad (1.30)$$

(thus $d\tau_\nu$ is the optical cross section for dV in z -direction) we can rewrite Equation 1.21 by splitting up the solid angle element $d\omega$ in its components ($d\omega = d\mu d\phi$), and letting the ratio $\delta I_\nu(z, \mu, \phi)/d\tau_\nu$ approach its limit as $d\tau_\nu \rightarrow 0$, to:

$$\begin{aligned} \mu \frac{dI(\tau_\nu, \mu, \phi)}{d\tau_\nu} &= I(\tau_\nu, \mu, \phi) \\ &\quad - \frac{1}{4\pi} \int_0^{2\pi} \int_{-1}^{+1} p(\mu, \phi; \mu', \phi') I(\tau_\nu, \mu', \phi') d\mu' d\phi' \\ &\quad - (1 - \tilde{\omega}_0) B_\nu(T). \end{aligned} \quad (1.31)$$

This is the radiative transfer Equation for an arbitrary, monochromatic field of radiation in a plane parallel atmosphere. In practice this field consists of a diffuse component that originates from thermal emission of the atmosphere and the planetary surface and a component (both diffuse and direct) that originates from the sun. The first component dominates in the middle and far infrared whereas the second one is the only contributor at visible wavelengths. Both components are important in the near infrared.

The Diffuse Field

In order to separate the diffuse field from the directly transmitted radiations we consider a collimated beam of radiation of flux πF_0 crossing a unit surface area normal to the beam. The magnitude of the flux in the downward direction crossing a unit area contained in a plane at the TOA, $\mu_0\pi F_0$ is:

$$\mu_0\pi F_0 = \int_0^{2\pi} \int_{-1}^{+1} \mu I(0, \mu, \phi) d\mu d\phi, \quad (1.32)$$

where μ_0 is the cosine of the zenith angle of the point source and $I(0, \mu, \phi)$ is the downward intensity of radiation in the direction (μ, ϕ) at $\tau_\nu = 0$. The only contribution from the point source is into the direction $(-\mu_0, \phi_0)$. So the intensity $I(0, \mu, \phi)$ should be of the form:

$$I(0, \mu, \phi) = C\delta_D(\mu + \mu_0)\delta_D(\phi - \phi_0) \quad (1.33)$$

*In the case of a non-scattering atmosphere the optical depth is also represented by:

$$d\tau_\nu = -k_\nu(z)\rho_a(z)dz = k_\nu(p)q(p)\frac{dp}{g}, \quad (1.29)$$

where k_ν is the absorption coefficient (mass absorption cross section), ρ_a is the density of absorbing gases, z is the height, $q = \rho_a/\rho$ is the gaseous mixing ratio, ρ is the air density, and g is the gravitational acceleration. The second representation is simply obtained by using the hydrostatic equation.

where the δ_D 's are Dirac δ -functions and C is a normalization factor which can be set to $C = \pi F_0$ by consulting Equation 1.32.

We now write the total intensity as a sum of an intensity arising from a diffuse radiation field $I_D(\tau_\nu, \mu, \phi)$ and an intensity directly transmitted from the point source to the level τ_ν , I_T . This latter intensity can be expressed by (c. f. Equation 1.33):

$$I_T(\tau_\nu, \mu, \phi) = \pi F_0 \delta_D(\mu + \mu_0) \delta_D(\phi - \phi_0) h(\tau_\nu), \quad (1.34)$$

where $h(\tau_\nu)$ can be determined by reducing Equation 1.31 for the special case $\mu = -\mu_0$ and $\phi = \phi_0$, which gives:

$$-\mu_0 \delta_D(\mu + \mu_0) \delta_D(\phi - \phi_0) \frac{dh(\tau_\nu)}{d\tau_\nu} = \delta_D(\mu + \mu_0) \delta_D(\phi - \phi_0) dh(\tau_\nu). \quad (1.35)$$

Solving it we obtain:

$$h(\tau_\nu) = e^{-\tau_\nu/\mu_0}, \quad (1.36)$$

which is often called *Beer's law of exponential attenuation*.

After dropping the subscript D Equation 1.31 for the *diffuse* radiation field becomes:

$$\begin{aligned} \mu \frac{dI(\tau_\nu, \mu, \phi)}{d\tau_\nu} &= I(\tau_\nu, \mu, \phi) \\ &\quad - \frac{1}{4\pi} \int_0^{2\pi} \int_{-1}^{+1} p(\mu, \phi; \mu', \phi') I(\tau_\nu, \mu', \phi') d\mu' d\phi' \\ &\quad - \frac{F_0}{4} e^{-\tau_\nu/\mu_0} p(\mu, \phi; -\mu_0, \phi_0) \\ &\quad - (1 - \tilde{\omega}_0) B_\nu(\tau_\nu), \end{aligned} \quad (1.37)$$

where $B_\nu(T)$ is replaced by $B_\nu(\tau_\nu)$ to point out that the temperature is a function of only optical depth while being situated in the approximation of plane parallel atmosphere.

1.3.3 Formal Solution for the Upward Intensity

Equation 1.37 is a first order linear integro-differential Equation which can be solved formally by finding an appropriate integration factor. We start by multiplying both sides of Equation 1.37 by $e^{-\tau_\nu/\mu}$, transferring the first term on the right side to the left, and gathering similar terms:

$$\begin{aligned} \mu \frac{d[e^{-\tau_\nu/\mu} I(\tau_\nu, \mu, \phi)]}{d\tau_\nu} &= -\frac{1}{4\pi} e^{-\tau_\nu/\mu} \int_0^{2\pi} \int_{-1}^{+1} p(\mu, \phi; \mu', \phi') I(\tau_\nu, \mu', \phi') d\mu' d\phi' \\ &\quad - \frac{F_0}{4} \exp \left[-\left(\frac{1}{\mu} + \frac{1}{\mu_0} \right) \tau_\nu \right] p(\mu, \phi; -\mu_0, \phi_0) \\ &\quad - (1 - \tilde{\omega}_0) e^{-\tau_\nu/\mu} B_\nu(\tau_\nu). \end{aligned} \quad (1.38)$$

By integrating between τ_ν and $\tau_{s,\nu}$, the optical depth at the surface (or lower boundary), and rearranging the different terms we obtain the upward intensity of τ_ν (multiplied by the integrating factor $e^{-\tau_\nu/\mu}$):

$$\begin{aligned}
I(\tau_\nu, \mu, \phi) e^{-\tau_\nu/\mu} &= I(\tau_{s,\nu}, \mu, \phi) e^{-\tau_{s,\nu}/\mu} \\
&+ \frac{1}{4\pi\mu} \int_{\tau_\nu}^{\tau_{s,\nu}} e^{-\tau'_\nu/\mu} \int_0^{2\pi} \int_{-1}^{+1} p(\mu, \phi; \mu', \phi') I(\tau'_\nu, \mu', \phi') d\mu' d\phi' d\tau'_\nu \\
&+ \frac{F_0}{4\mu} \int_{\tau_\nu}^{\tau_{s,\nu}} \exp \left[- \left(\frac{1}{\mu} + \frac{1}{\mu_0} \right) \tau'_\nu \right] p(\mu, \phi; -\mu_0, \phi_0) d\tau'_\nu \\
&+ \frac{1}{\mu} \int_{\tau_\nu}^{\tau_{s,\nu}} (1 - \tilde{\omega}_0) e^{-\tau'_\nu/\mu} B_\nu(\tau'_\nu) d\tau'_\nu. \tag{1.39}
\end{aligned}$$

This is only a formal solution since the unknown intensity itself is contained in it.

It is useful to separate the intensity arising from the surface (lower boundary) from the rest of the radiation field. The direct contribution to $I(\tau'_\nu, \mu', \phi')$ from the surface is the intensity $I(\tau_{s,\nu}, \mu', \phi')$ attenuated along the path length $(\tau_{s,\nu} - \tau'_\nu)/\mu'$ by the factor $\exp[(\tau_{s,\nu} - \tau'_\nu)/\mu']$. Thus Equation 1.39 can be written as follows:

$$\begin{aligned}
I(\tau_\nu, \mu, \phi) &= \\
(1) \quad &I(\tau_{s,\nu}, \mu, \phi) e^{-(\tau_{s,\nu} - \tau_\nu)/\mu} \\
(2) \quad &+ \frac{1}{4\pi\mu} \int_{\tau_\nu}^{\tau_{s,\nu}} \int_0^{2\pi} \int_0^1 e^{-(\tau'_\nu - \tau_\nu)/\mu} e^{-(\tau'_{s,\nu} - \tau_\nu)/\mu'} \\
&\quad \times p(\mu, \phi; \mu', \phi') I(\tau_{s,\nu}, \mu', \phi') d\mu' d\phi' d\tau'_\nu \\
(3) \quad &+ \frac{F_0}{4\pi} \int_{\tau_\nu}^{\tau_{s,\nu}} e^{-\tau'_\nu/\mu_0} e^{-(\tau'_\nu - \tau_\nu)/\mu} p(\mu, \phi; -\mu_0, \phi_0) d\tau'_\nu \\
(4) \quad &+ \frac{1}{\mu} \int_{\tau_\nu}^{\tau_{s,\nu}} (1 - \tilde{\omega}_0) e^{-(\tau'_\nu - \tau_\nu)/\mu} B_\nu(\tau'_\nu) d\tau'_\nu \\
(5) \quad &+ \frac{1}{4\pi\mu} \int_{\tau_\nu}^{\tau_{s,\nu}} \int_0^{2\pi} \int_{-1}^{+1} e^{-(\tau'_\nu - \tau_\nu)/\mu} \\
&\quad \times p(\mu, \phi; \mu', \phi') I(\tau'_\nu, \mu', \phi') d\mu' d\phi' d\tau'_\nu, \tag{1.40}
\end{aligned}$$

where the diffuse field $I(\tau'_\nu, \mu', \phi')$ is zero in the upward direction along the boundary ($\tau'_\nu = \tau_{s,\nu}$).

The different terms for the upward intensity in the direction (μ, ϕ) at a level τ_ν are representing:

- (1) the radiation originating directly from the lower boundary (generally the surface or a compact cloud deck) that is attenuated by the overlying atmosphere between the levels τ_ν and $\tau_{s,\nu}$,
- (2) the radiation originating from the lower boundary in the direction (μ', ϕ') that is scattered at τ'_ν into the direction (μ, ϕ) ,

- (3) the radiation from the sun that has penetrated to the level τ'_ν before undergoing a scattering process,
- (4) the radiation that is thermally emitted at the level τ'_ν , and
- (5) the radiation that has undergone one or more scattering processes before being scattered at τ'_ν into the direction (μ, ϕ) .

1.3.4 Solving the Special Case of *No Scattering*

The deduction of the formal solution is complicated and no analytic solution exists in the general case. But in many situations we can apply the approximation that scattering is negligible (at least in the thermal part of the spectrum in the absence of clouds where absorption and emission by atmospheric gases dominate and solar radiation can be neglected).

Hence, in a non-scattering atmosphere the RT Equation (see Equation 1.37) reduces to the form:

$$\mu \frac{dI(\tau_\nu, \mu, \phi)}{d\tau_\nu} = I(\tau_\nu, \mu, \phi) - B_\nu(\tau_\nu), \quad (1.41)$$

which is known as Schwarzschild's Equation. The upward intensity at the TOA then has the form:

$$I(0, \mu, \phi) = I(\tau_{s,\nu}, \mu, \phi) e^{-\tau_{s,\nu}/\mu} + \frac{1}{\mu} \int_0^{\tau_{s,\nu}} e^{-\tau'_\nu/\mu} B_\nu(\tau'_\nu) d\tau'_\nu. \quad (1.42)$$

For many applications it is useful to treat the atmosphere as being divided into thin layers. The top layer has an optical thickness $\tau_{1,\nu}$, the top two layers have a composite thickness of $\tau_{2,\nu}$, etc. The derivation of this concept will not be performed here but one can find a more detailed description of it in [Hanel *et al.* (1992)]. According to this the emitted intensity of the i -th layer can be described by:

$$I_E(\tau_{i-1,\nu}, \mu) = B_\nu(\tau_{i,\nu}) [1 - e^{-(\tau_{i,\nu} - \tau_{i-1,\nu})/\mu}], \quad (1.43)$$

where the azimuth-independent nature of the solution is indicated by deleting ϕ from the notation. Within the layer the Planck function can be considered as constant. It readily follows by repeated application of Equation 1.43 that the outgoing intensity at the TOA composed of $n - 1$ layers is:

$$I(0, \mu) = \sum_{i=1}^n e^{-\tau_{i-1,\nu}/\mu} B_\nu(\tau_{i,\nu}) [1 - e^{-(\tau_{i,\nu} - \tau_{i-1,\nu})/\mu}], \quad (1.44)$$

where $\tau_{0,\nu} = 0$, $B_\nu(\tau_{i,\nu})$ is a mean value of the Planck function between $\tau_{i,\nu}$ and $\tau_{i-1,\nu}$, and the n -th layer is the surface itself. Therefore $\tau_{n-1,\nu} = \tau_{s,\nu}$, $\tau_{n,\nu} = \infty$ and $B_\nu(\tau_{n,\nu})$ is the Planck intensity of the surface.

If we consider overhead viewing (i. e. $\mu = 1$) further, then we may write instead of Equation 1.42:

$$I(0) = I(\tau_{s,\nu})e^{-\tau_{s,\nu}} + \int_0^{\tau_{s,\nu}} e^{-\tau'_\nu} B_\nu(\tau'_\nu) d\tau'_\nu. \quad (1.45)$$

And after introducing the monochromatic transmittance (or transmission function) $T(\tau_\nu)$:

$$T(\tau_\nu) = e^{-\tau_\nu} \quad (1.46)$$

the upward part of the radiative transfer Equation for a monochromatic radiation field in a plane parallel atmosphere without scattering can be expressed by:

$$I = I(\tau_{s,\nu})T(\tau_{s,\nu}) + \int_{\tau_{s,\nu}}^0 B_\nu(\tau'_\nu) \frac{dT(\tau'_\nu)}{d\tau'_\nu} d\tau'_\nu. \quad (1.47)$$

where $T(\tau_{s,\nu})$ represents the surface transmittance to the TOA and $T(\tau_\nu)$ the atmospheric transmittance from the optical depth τ_ν to the TOA. If we consider the earth's surface as a blackbody it would be convenient to substitute $I(\tau_{s,\nu})$ by $B(\tau_{s,\nu})$, but to be strict, the infrared radiation from the surface is slightly less than that of a blackbody. Therefore an emissivity coefficient ϵ with values between 0.90 and 0.95 should be introduced, such that $I(\tau_{s,\nu}) = \epsilon_{s,\nu} B(\tau_{s,\nu})$.

Using height coordinates, Equation 1.47 can be rewritten to:

$$I = B_\nu(0)T_\nu(0) + \int_0^\infty B_\nu(T(z)) \frac{dT_\nu(z)}{dz} dz. \quad (1.48)$$

and using pressure coordinates we get:

$$I = B_\nu(p_s)T_\nu(p_s) + \int_{p_s}^0 B_\nu(T(p)) \frac{dT_\nu(p)}{dp} dp, \quad (1.49)$$

where p_s represents the surface pressure.

1.4 Absorption Spectra of Atmospheric Gases

The interaction of photons with massive particles is a very sophisticated topic which can be described analytically only for simple cases (e. g. hydrogen atom). For more complicated particles we have to use numerical methods or we must introduce approximations.

There are various forms of interactions like the photoelectric effect, the Compton effect, pair generation-annihilation, electronic excitation, vibrational and rotational modes, etc.

The quantitative description of quantum mechanical processes, which is sufficiently exact for our purpose is the *Schrödinger Equation*. Simply speaking, it describes the states of the particles by wave functions $\Psi(\mathbf{x}, t)$ and it expresses the different forms of

the energy (e. g. kinetic energy, potential energy, vibration energy, rotational energy, etc.) in an operator form:

$$\begin{aligned}
 E &\rightarrow \hat{E} = i\hbar \frac{\partial}{\partial t} \\
 p &\rightarrow \hat{p} = -i\hbar \nabla \\
 E_{kin} &\rightarrow \hat{E}_{kin} = -\frac{\hbar^2}{2m} \Delta \\
 \dots &\rightarrow \dots = \dots
 \end{aligned}
 \tag{1.50}$$

Hence, the Schrödinger Equation of a particle moving in a potential $V(\mathbf{x}, t)$ can be written as:

$$i \hbar \frac{\partial \Psi(\mathbf{x}, t)}{\partial t} = \left(-\frac{\hbar^2}{2m} \Delta + V(\mathbf{x}, t) \right) \Psi(\mathbf{x}, t)
 \tag{1.51}$$

Of course for more-atomic molecules we have to introduce also terms for vibration and rotation modes, which make the thing a bit more complicated. In solving these problems, we obtain discrete energy levels which are specified by the so called *quantum numbers* of the states between which the molecules can change.

For a more detailed view into the principles of quantum mechanics see e. g. [Messiah (1991), Messiah (1990)].

1.4.1 Excitation Modes

Infrared radiation can excite vibrational and rotational modes only, for everything else the energy of these photons is too low. The vibrational energy states are characterized by the vibrational quantum numbers $\Delta\nu = 0, \pm 1, \pm 2, \dots$ (not to be confused with the wavenumber). For each vibrational mode there exists rotational levels characterized by the rotational quantum number J with $\Delta J = \pm 1$ for diatomic molecules and $\Delta J = 0, \pm 1$ for polyatomic molecules. The vibrational transitions are coupled with these rotational transitions. In Figure 1.4 a classical interpretation of some vibration and rotation modes is illustrated.

In the atmosphere most molecules are in the ground vibrational state implying that observed transitions are so called *fundamental transitions*. In the present context fundamental refers to transitions from the ground state to the first excited state and vice versa ($\Delta\nu = \pm 1$). Pure rotational transitions ($\Delta\nu = 0$) occur in the far-infrared and microwave regions.

1.4.2 Spectral Line Shape and Line Strength

The transitions between the different energy levels (absorption or emission) are not truly discrete. Actual lines occupy a finite band of wavelength and their shape depends on

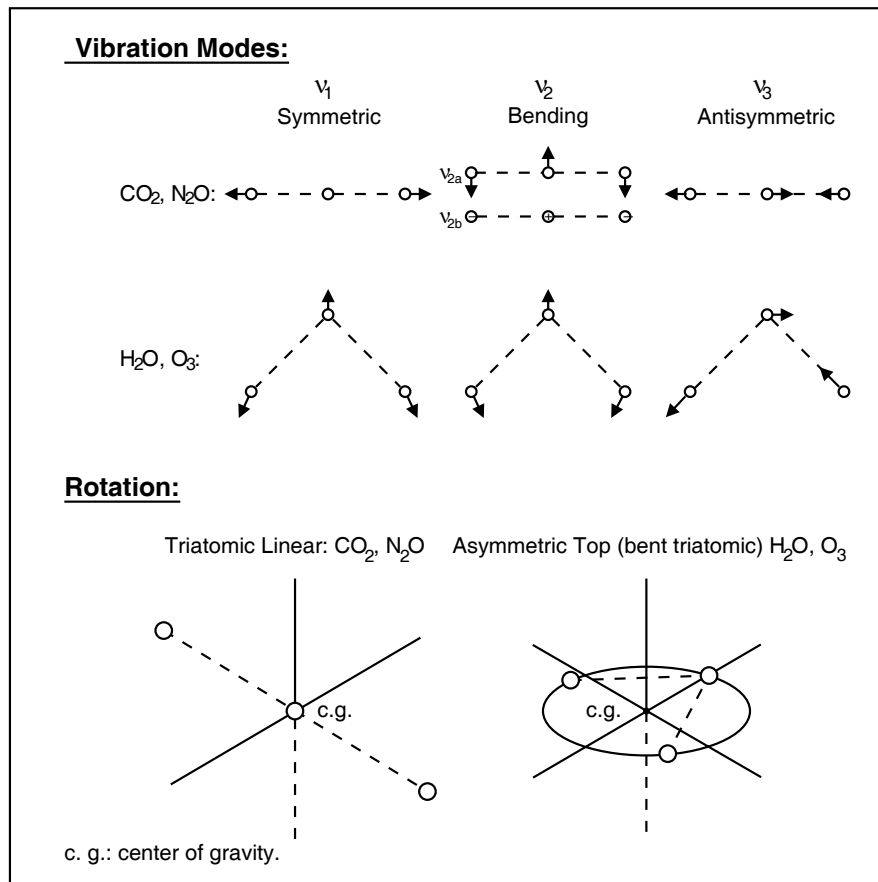


Figure 1.4: Vibration modes of tri-atomic atmospheric molecules and rotation axes for linear and asymmetric top molecules (after [Liou (2002)]).

the atmospheric conditions under which the absorption and emission takes place. Typically the broadening of spectral lines is caused by the damping of oscillator vibrations due to the loss of energy in emission (normal broadening), the perturbations resulting from reciprocal collisions between the absorbing molecules and between the absorbing and non-absorbing molecules (collisional or pressure broadening), and the *Doppler Effect* induced by the difference in the thermal velocities of the atoms and molecules (Doppler broadening). In general the natural broadening is negligible as compared to that caused by collisions and the Doppler effect.

The absorption of energy portions can be expressed by an absorption coefficient (mass absorption cross section) k_ν (at wavenumber ν) defined by:

$$k_\nu = S f(\nu - \nu_0), \quad (1.52)$$

where ν_0 is the line center, S is the line strength (normalization factor of the absorption coefficient) given by:

$$S = \int_0^\infty k_\nu d\nu, \quad (1.53)$$

and $f(\nu - \nu_0)$ is the shape function which describes the spectral width of an absorbing line. It is customary for the atmosphere to distinguish three different types of the spectral line shape, namely the Lorentz profile, the Doppler profile, and the Voigt (hybrid) profile.

Lorentz Profile

In the lower atmosphere the perturbations, resulting from reciprocal collisions between the absorbing molecules and between the absorbing and non-absorbing molecules, prevails the effect of line broadening by the *Doppler Effect*. Therefore, this type of broadening is also referred to as pressure or collisional broadening. It is essential for the IR bands of CO₂ and H₂O at altitudes below 30 km. The spectral width of this type of broadening can be described by the *Lorentz Profile* (Lorentz line shape – see Figure 1.5):

$$f_L(\nu - \nu_0) = \frac{\alpha_L}{\pi(\nu - \nu_0)^2 + \alpha_L^2}, \quad (1.54)$$

where α_L is the half width at half power (HWP) given to a good approximation by:

$$\alpha_L(p, T) = \alpha_0 \frac{p}{p_0} \left(\frac{T_0}{T} \right)^n, \quad (1.55)$$

where α_0 is the HWP at standard pressure, $p_0 = 1013$ hPa and standard temperature $T_0 = 273$ K. The exponent n ranges from $\frac{1}{2}$ to 1 depending on the type of molecules ($n = \frac{1}{2}$ is known as the classical value). Under the reference conditions, α_0 ranges from about 0.01 to 0.1 cm⁻¹ for most of the radiatively active gases in earth's atmosphere and depends on the spectral line. For the CO₂ molecule, it is fairly constant with a value of about 0.07cm⁻¹ (see [Liou (2002)]).

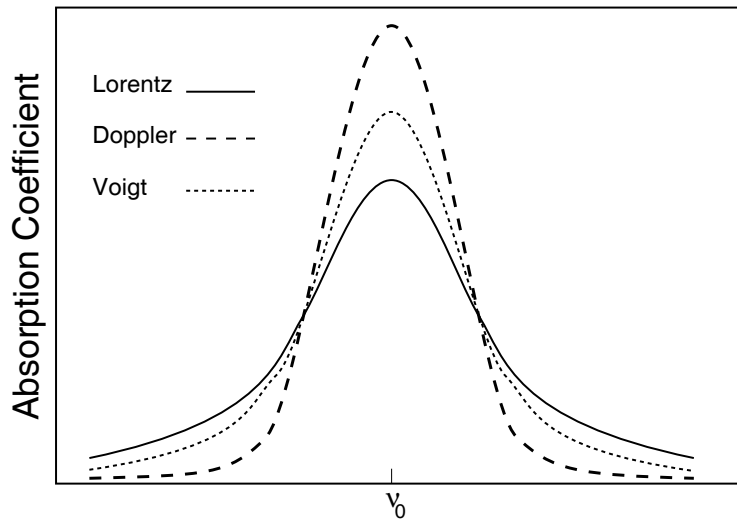


Figure 1.5: Lorentz, Doppler, and Voigt Line shape [Salby (1996)].

Doppler Profile

In atmospheric regions, where the pressure becomes small and the temperature-generated thermal velocities of the molecules become significant (above about 40 km) the so-called Doppler broadening prevails which results from the thermal random molecular motion. If the molecule has a velocity component (v) in the line of sight and if $v \ll c$ (c : speed of light) the associated frequency shift is:

$$\nu = \nu_0 \left(1 \pm \frac{v}{c}\right). \quad (1.56)$$

Let the probability that the velocity component lies between v and $v + dv$ be $p(v)dv$. If the translational states are in thermodynamic equilibrium, $p(v)dv$ is given by the Maxwell-Boltzmann distribution:

$$p(v)dv = \left(\frac{m}{2\pi kT}\right)^{\frac{1}{2}} \exp\left[-\frac{mv^2}{2kT}\right] dv, \quad (1.57)$$

where m denotes the mass of the molecule, k is the Boltzmann constant, and T is the absolute temperature. Based on this, the Doppler Profile (Doppler line shape – see Figure 1.5) can be written as:

$$f_D(\nu - \nu_0) = \frac{1}{\alpha_D \sqrt{\pi}} \exp\left[-\left(\frac{\nu - \nu_0}{\alpha_D}\right)^2\right], \quad (1.58)$$

where

$$\alpha_D = \nu_0 \left(\frac{2kT}{mc^2}\right)^{\frac{1}{2}} \quad (1.59)$$

is a measure of the Doppler width of the line. The half-width at half-maximum is $\alpha_D \sqrt{\ln 2}$. For the line of the rotational H₂O band at about 200 cm⁻¹ the Doppler half-width is 3.5×10^{-4} cm⁻¹ (see e. g., [Zuev (1974)]).

Voigt Profile

In altitude regions between about 20 to 50 km the effective line shapes are influenced by both collisional- and Doppler-broadening processes which have been expressed individually by $f_L(\nu - \nu_0)$ and $f_D(\nu - \nu_0)$, respectively. In fact, the Voigt line shape is a convolution of the Doppler and the Lorentz line shapes:

$$\begin{aligned} f_V(\nu - \nu_0) &= \int_{-\infty}^{\infty} f_L(\nu' - \nu_0) f_D(\nu' - \nu_0) d\nu' \\ &= \frac{1}{\pi^{3/2}} \frac{\alpha_L}{\alpha_D} \int_{-\infty}^{\infty} \frac{1}{(\nu' - \nu_0)^2 + \alpha_L^2} \exp\left[-\left(\frac{\nu - \nu'}{\alpha_D}\right)^2\right] d\nu'. \end{aligned} \quad (1.60)$$

The Voigt profile gives a line shape between the Lorentz and the Doppler line shape as illustrated in Figure 1.5.

Line Strength

The detailed form of the line strength (see Equation 1.53) is provided by quantum mechanics. For a single molecular transition from state j to state i we obtain:

$$S_{i,j} = \frac{n_j}{g_i n} \frac{2\pi\omega_{i,j} |R_{i,j}|^2}{3\hbar c} \left(1 - \exp \left[-\frac{\hbar\omega_{i,j}}{kT} \right] \right), \quad (1.61)$$

where n_j is the molecular concentration in the lower state, n is the total molecular concentration, g_i is the degeneracy factor or statistical weight, $\omega_{i,j}$ is the angular transition frequency, and \hbar , k , and c are the Planck and Boltzmann constant and the speed of light. The transition probability $|R_{i,j}|^2$ is given by:

$$R_{i,j} = \int \Psi_i^* \mathbf{M} \Psi_j dV, \quad (1.62)$$

where \mathbf{M} is the matrix of the dipole moment relative to the relevant time dependent Hamiltonian, dV is a volume element, and Ψ_i and Ψ_j are wave functions which are subjected to the orthogonality condition:

$$\int \Psi_i^* \Psi_j dV = 0, \quad (i \neq j). \quad (1.63)$$

At thermodynamic equilibrium the ratio n_j/n is defined by the Boltzmann factor in the form:

$$\frac{n_j}{n} = \frac{g_j e^{-E_j/kT}}{Q(T)}, \quad (1.64)$$

where $Q(T)$ is the total internal partition sum. Under atmospheric conditions $Q(T) \simeq 1$ holds true due to vibrations. For rotational transitions we may approximate the internal partition function by $Q(T) \simeq T$ for linear molecules, such as CO_2 , N_2O , or CO , and by $Q(T) \simeq T^{3/2}$ for non-linear molecules, such as H_2O , O_3 , and CH_4 , respectively.

1.4.3 Calculation of Transmittances

Evaluating the upwelling radiance according to Equation 1.47 requires accurate calculation of the spectral transmittances and therefore the absorption parameters for various gases are needed. They can be computed from fundamental quantum mechanical principles but they can also be derived by laboratory measurements for a limited number of spectral intervals. The absorption lines for many molecules such as H_2O , CO_2 , O_3 , N_2O , CH_4 , etc. have been intensively examined and the associated parameters including line position, line strength, line half-width, and lower energy state are documented and listed in databases such as the HIRTRAN (High Resolution Transmission) database [Rothman *et al.* (1996)].

Transmittance computation accounting for all absorption lines in a given spectral interval is referred to as line-by-line calculation. Therefore the monochromatic transmittance for given species including $j = 1, \dots, N$ lines is given by (c. f. Equation 1.46):

$$T_\nu = \prod_{j=1}^N T_{\nu j} = \exp \left[- \sum_{j=1}^N \tau_{\nu j} \right], \quad (1.65)$$

with the transmittance for the absorption line j (c. f. footnote on page 15):

$$T_{\nu j} = \exp \left[- \int_s k_{\nu j}(s) ds \right], \quad (1.66)$$

where s is the optical path for the absorbing gases and $k_{\nu j}$ is the absorption coefficient for the line j . According to Equation 1.52 the absorption coefficient can be expressed in terms of line strength and line shape in the form:

$$k_{\nu j}(p, T) = S_j(T) f_{\nu, j}(p, T). \quad (1.67)$$

The spectral intervals, the $k_{\nu j}$'s are calculated with, have to be smaller than the half-width in order to resolve individual lines. For e. g., CO₂ and O₃ absorbing in the upper stratosphere Doppler broadening is significant. The Doppler half-width of CO₂ in the 15 μm band and of O₃ in the 9.6 μm band is approximately 0.0005 - 0.0001 cm⁻¹. Since the spectral ranges of these two bands are about 400 cm⁻¹ more than half a million points have to be calculated to resolve the individual lines. In the troposphere, absorption is primarily accomplished by water vapor covering a range of about 15 000 cm⁻¹. With a Lorentz half-width of > 0.01 cm⁻¹ the required number of points to be computed lies at about one million. Based on numerical experiments, spectral resolutions of 0.001, 0.002 and 0.005 cm⁻¹ have been found to be adequate for H₂O, CO₂, and O₃, respectively [Liou (2002), Matricardi and Saunders (1999)].

In the IR radiative transfer calculation a further simplification of the transmittance computation can be made with the assumption that if the radiative parameters are defined in a spectral interval, $\Delta\nu$, which is small enough, the variations of the Planck function can be neglected. Hence, we may define the spectral transmittance as:

$$\begin{aligned} T_{\bar{\nu}} &= \int_{\Delta\nu} e^{-\tau} \frac{d\nu}{\Delta\nu} \\ &= \int_{\Delta\nu} \exp \left[- \int_s \sum_j k_{\nu j}(s) ds \right] \frac{d\nu}{\Delta\nu}. \end{aligned} \quad (1.68)$$

Discretizing the spectral interval with a spectral resolution $\Delta\nu_i$, where $i = 1, \dots, M$ runs over the whole spectral interval $\Delta\nu$, and assuming that the atmosphere consists of $n = 1, \dots, L$ layers, we finally obtain with the aid of equation 1.67:

$$T_{\bar{\nu}} = \sum_{i=1}^M \exp \left[- \sum_{n=1}^L \sum_{j=1}^N k_{ij}(p_n, T_n) \Delta s_n \right] \frac{\Delta\nu_i}{\Delta\nu}. \quad (1.69)$$

Note that adequate and reliable summations have to be performed to cover the absorption lines, the spectral interval, and the inhomogeneous path exactly.

We can conclude that these line-by-line calculations are computationally very expensive and may be impractical for many applications. Thus great effort is made to find simplified approaches to compute spectral transmittances (see e. g. chapter 4).

1.4.4 Absorption in the Infrared

In this subsection the principle absorbing gases of the thermal infrared are presented. The information given below is mostly based on [Liou (2002)].

Carbon Dioxide

The linearly symmetric CO₂ molecule has three vibrational modes illustrated schematically in Figure 1.4. The molecule occurs in the atmosphere in several isotopic states of which the most significant ones are C¹²O₂¹⁶, C¹³O₂¹⁶, and C¹⁶O¹⁶O¹⁸ with relative abundance of about 98.41%, 1.1% and 0.2% respectively.

The fundamental symmetrical "stretch" mode ν_1 can be found near 7.5 μm . This mode has no electric dipole moment and is therefore radiatively inactive. CO₂ does not have pure rotational transitions, since this is only possible for molecules with a permanent electric dipole moment. The 15 μm band represents the bending mode ν_2 , which is twofold degenerated and consists of the states ν_{2a} and ν_{2b} . The fundamental ν_2 transition is coupled with rotational transitions corresponding to $\Delta J = 0, \pm 1$. The fundamental ν_3 vibration-rotation band is responsible for high absorption at wavenumber 4.3 μm . In addition to the strong absorption bands at 4.3 μm and 15 μm , in which the primary absorptions are due to the fundamental ν_2 and ν_3 transitions, CO₂ has bands centered near 10.6, 9.4, 5.2, 4.8, 2.7, 2.0, 1.6, and 1.4 μm [Zuev (1974)]. The CO₂ molecule has of course several combinations (simultaneous transitions in two vibrational modes) and overtone bands (vibrational transitions between nonadjacent levels).

Water Vapor

In contrast to the CO₂ molecule, the H₂O molecule has an asymmetric configuration (bent triatomic). The most important isotopes are H₂O¹⁶, H₂O¹⁸, and HDO¹⁶, which are present in the atmosphere with 99.78, 0.2, and 0.0149 %, respectively. The molecule has three vibrational modes (see Figure 1.4) where the fundamental ν_2 band at 6.25 μm is the most important vibrational-rotational band of water vapor. The centers of the two other fundamental bands ν_1 and ν_3 are located close to one another at about 2.7 μm . Other vibrational-rotational bands of H₂O can be identified between 1.8 and 0.7 μm . The fine structure of the vibration-rotation spectrum of water vapor is very complex and consists of thousands of individual lines. The pure rotational absorption occurs in a band which ranges from ~ 0 to 1000 cm^{-1} (which corresponds to wavelengths from several centimeters to 10 μm) and is important in the generation of tropospheric cooling.

Ozone

The O₃ molecule has an asymmetric top configuration (like the H₂O – see Figure 1.4). Its most important isotopes are O₃¹⁶, O¹⁶O¹⁸O¹⁶, and O¹⁶O¹⁶O¹⁸. Electronic transitions occur in the ultraviolet region (Hartley and Huggins band) and in the visible (Chappuis band), see e. g. [Salby (1996)]. In the thermal infrared there are the ν_1 and ν_3 fundamental vibration modes, situated at 9.1 and 9.6 μm . These modes constitute the 9.6 μm band located in the so-called *atmospheric window* between 8-12 μm . This band contains a large number of fine-structure lines. The ν_2 fundamental band is centered at 14.27 μm . Overtone and combination frequencies of O₃ vibrations produce several bands between 2.7 and 5.7 μm , of which the 4.75 μm band is the most intensive one.

Methane

The CH₄ molecule exhibits a spherical top configuration. Since it has no permanent electric dipole moment (like the CO₂ molecule), methane has no pure rotational spectrum. The ν_1 band is fully symmetric and the ν_2 is twofold degenerate (see Figure 1.4). Both are inactive and have centers near 3.4 and 6.6 μm . The active ν_3 and ν_4 bands are threefold degenerate with line centers at 3.3 and 7.7 μm , respectively. In addition, methane possesses a rich spectrum of overtone and combination frequencies primarily located in the solar spectrum.

Nitrous Oxide

The N₂O molecule is a linear asymmetric molecule with an permanent electric dipole moment. Strong electronic bands are located in the far ultraviolet region. The three fundamental vibrational modes ν_1 , ν_2 , and ν_3 are active in the IR and have centers at 7.8, 17.0, and 4.6 μm , respectively. The ν_4 fundamental band overlaps the ν_4 fundamental band of CH₄. N₂O has many bands of overtones and combination frequencies. For instance, the region between 1.3 and 2.5 μm contains 18 bands.

Carbon Monoxide

The fundamental rotational band lies near 4.67 μm , while overtone and combination frequencies lie between 1.2 and 2.3 μm . The pure rotational spectrum can be found in the far IR and microwave region.

Chlorofluorocarbons

Methylchloride (CH₃Cl), carbon tetrachloride (CCl₄ or CFC-10), trichlorofluoromethane (CFCl₃ or CFC-11), methylchloroform (CH₃CCl₃), and dichlorodifluoromethane (CF₂Cl₂ or CFC-12) have several fundamental transitions primarily located in the *atmospheric*

window at 8-12 μm . These gases may significantly contribute to the greenhouse effect if their atmospheric abundance is increased.

1.5 The Boundary Layer

The radiation field of the atmosphere is affected by the presence of bounding surfaces, like a solid land material, a liquid (e. g. ocean), or an *effective surface*, such as a dense cloud deck. In this chapter the emissive and reflective properties of surfaces applicable to their longwave interactions are defined. IR surface properties are in general simpler than UV/visible properties, since reflection of IR radiation is usually unimportant. Furthermore, except at millimeter wavelengths, surfaces emit thermal radiation approximately isotropically.

Descriptions of surface interactions have historically been largely empirical, but in the past several decades, physically based models of surface reflection have gained in popularity with the need, e. g., to relate land reflectance to crop yield and ocean color to water fertility. The description below is mainly based on [Thomas and Stamnes (1999)].

1.5.1 Boundary Properties of Planetary Media

A radiation field can be effected by a surface by reflection of a portion of the incident radiation back into the medium, by absorption of a part of the incident radiation, by emission of thermal radiation, and by transmission of some of the incident radiation.

In the following a description of the processes related to the upwelling longwave field in terms of quantities that relate incoming and outgoing monochromatic intensities and fluxes is provided. Fortunately, the emittance of the surface in the IR depends only weakly upon its composition and structure.

Thermal Emission from the surface

Let $I_{E,\nu}^+(\mu, \phi)\mu d\omega$ be the emitted energy from a flat surface of temperature T_S within the solid angle $d\omega$ in the direction (μ, ϕ) (definition of the geometry see subsection 1.3.1 and Figure 1.3). The corresponding energy emitted by a black surface at the same temperature is $B_\nu(T_S)\mu d\omega$. The spectral *directional emittance* is defined as the ratio of the energy emitted by a surface of temperature T_S to the energy emitted by a blackbody at the same frequency and temperature:

$$\epsilon_\nu(\mu, \phi, T_S) \equiv \frac{I_{E,\nu}^+(\mu, \phi)\mu d\omega}{B_\nu(T_S)\mu d\omega} = \frac{I_{E,\nu}^+(\mu, \phi)}{B_\nu(T_S)}. \quad (1.70)$$

Generally, ϵ depends on the direction of the emission, the surface temperature, and the frequency of the radiation as well as on other properties of the surface (like refractive

index, etc.). The emittance is usually measured directly – in some cases it may be derived from first principles. Experimentally it is easier to measure the reflectance ρ and then deriving ϵ from the relationship $(1 - \rho)$. In the thermal infrared nearly all surfaces are efficient emitters, with ϵ 's generally exceeding 0.8. (For pure substances like water ice, the imaginary refractivity is needed to determine ϵ from theory.)

Absorption by the surface

Let $I_{\nu}^{-}(\mu', \phi')$ be the intensity incident on the surface in the direction (μ', ϕ') within a cone of solid angle $d\omega'$. A certain amount $I_{A,\nu}^{-}(\mu', \phi')\mu' d\omega'$ of the incident energy is lost by absorption. (The convention of using the negative sign in the notation of the intensity $I_{\nu}^{-}(\mu', \phi')$ emphasizes the downward direction of the beam.) The spectral *directional absorptance* is then defined as the ratio of absorbed energy to incident energy of the beam:

$$\alpha_{\nu}(-\mu, \phi, T_S) \equiv \frac{I_{A,\nu}^{-}(\mu', \phi')\mu' d\omega'}{I_{\nu}^{-}(\mu', \phi')\mu' d\omega'} = \frac{I_{A,\nu}^{-}(\mu', \phi')}{I_{\nu}^{-}(\mu', \phi')}. \quad (1.71)$$

Again the minus sign in the notation $(-\mu, \phi)$ emphasizes the downward direction of the incident intensity.

Kirchhoff's Law

Kirchhoff's Law relates the emissive and absorptive abilities of a body in thermodynamic equilibrium. In the following heuristic arguments will be applied to show how this law follows from very simple physical considerations.

Consider an opaque non-black surface within a hohlraum, which is exposed to the isotropic radiance $I_{\nu} = B_{\nu}(T)$. As a result of the isotropy of the radiation field, the upward radiation field emitted from the surface must also be uniform. But generally, not the whole of the radiation will be emitted because the surface material is not a blackbody (since the surface material is assumed to be opaque, only reflection and absorption have to be considered). The difference between the upward radiation and the smaller amount of emitted radiation has to be balanced by a reflected component $I_{R,\nu}^{+}$. For each direction of a radiation beam these two components must add to yield the Planck distribution:

$$I_{E,\nu}^{+}(\mu, \phi) + I_{R,\nu}^{+}(\mu, \phi) = B_{\nu}(T_S) \quad (1.72)$$

From the law of conservation of energy it follows, that the sum of the reflected and absorbed energy must be equal to the incident energy, which, in the hohlraum, is also the Planck function:

$$I_{A,\nu}^{-}(\mu, \phi) + I_{R,\nu}^{+}(\mu, \phi) = B_{\nu}(T_S) \quad (1.73)$$

Using now the Equations 1.70 - 1.73 we find *Kirchhoff's Law for an opaque surface*:

$$\alpha_{\nu}(-\mu, \phi, T_S) = \epsilon_{\nu}(\mu, \phi, T_S) \quad (1.74)$$

Kirchhoff's law describes the well-known connection between emission and absorption. The law is strictly valid only within an isothermal enclosure in thermodynamic equilibrium. However, in the form above it has much broader validity and for practical purposes may be considered to be an exact relationship for planetary surfaces.

1.5.2 Sea Surface Temperature

Due to the fact that very weak absorption appears in the region between 8-12 μm – the so called *atmospheric window* – we have a possibility to measure the surface temperature, especially the sea-surface temperature (SST).

An important aspect of SST measurements is the very high IR opacity of water. Unit optical depth occurs within an extremely small distance near the surface. This results in the fact that in the situation of a calm surface the so called *skin temperature* during daytime can be clearly different from that of the water just below the surface, the so called *surface bulk temperature*, due to the fact, that even a thin layer of water takes up a considerable amount of energy. A detailed discussion of the connection between surface skin temperature and surface bulk temperature can be found in [Emery *et al.* (2001)]. Due to its high opacity, the downward transport of IR radiation through the water is negligible. The energy of the surface is distributed mostly upwards by radiation and exchange of latent heat with the overlying atmosphere via evaporation and precipitation. The SST measured by infrared sensors always refers to this skin layer.

As a result of the high IR absorptance of the ocean and taking into account *Kirchhoff's law* the surface of the ocean has to be an efficient emitter of thermal radiation, too. The physically relevant quantity is the *net cooling rate*, that is the difference between the energy emitted and that received. It has been shown by measurements that an increasing ocean temperature is accompanied by a decreasing net cooling. This is a result of the strong dependence of the atmospheric radiation on the water vapor content of the atmosphere – an increasing SST causes an excess of the evaporation over the condensation which in turn results in a higher absolute humidity.

Chapter 2

The IASI Instrument on Board of the METOP-Series

In chapter 1 we tried to give an short theoretical survey of the interaction between earths surface and atmosphere with one another and with space via radiation.

In this chapter we will focus on the measurement of this radiation at the TOA. More precisely the Infrared Atmospheric Sounding Interferometer (IASI) will be introduced, which is developed by CNES (Centre National d'Etudes Spatial) for EUMETSAT (European Organisation for the Exploitation of Meteorological Satellites) as a core payload of the METOP satellite series developed by ESA (European Space Agency) to be operated by EUMETSAT. The description of this chapter is mainly based on various reports provided by CNES, ESA and EUMETSAT, such as the IASI Science Plan [*Camy-Peyret and Eyre (1998)*], as well as on the information obtained from web pages like <http://www.esa.int/export/esaME/index.html>, <http://www.eumetsat.de/>, and <http://smc.cnes.fr/IASI/>.

2.1 The METOP Satellite Series

METOP-1 will be Europe's first operational polar-orbiting weather satellite. It replaces one of two satellite services currently operated by the United States National Oceanic and Atmospheric Administration (NOAA). METOP will carry a set of instruments currently used by the NOAA satellites and a new generation of European instruments that offer improved remote sensing capabilities to both meteorologists and climatologists. The new instruments will increase the accuracy of temperature and humidity measurements, wind speed and wind direction measurements especially over the ocean, and profiles of ozone in the atmosphere. The present plan is to launch the three METOP satellites sequentially to maintain the service for at least 14 years, starting in late 2005.

2.1.1 METOP Overview

METOP is a 3-axis stabilized satellite with the lateral side oriented in the flight direction. The main instruments and the antennae for ground links are accommodated on the nadir side. Instruments requiring low temperature for infrared detection (e. g. IASI and HIRS) are mounted on a balcony at the longitudinal end of the satellite (anti-sun direction) for cold space views.

METOP is comprised of two major modules – the service module and the payload module. The design of the service module is largely derived from the SPOT 5/Envisat programs. It provides the main satellite support functions, such as command and control, communications with the ground, power, altitude and orbit control, and propulsion. It also interfaces with the launcher. The payload module is derived from Envisat. It accommodates the METOP instruments and associated payload support equipment (data management and communications, electrical distribution). A detailed listing of the specifications of the METOP satellite can be found in Table 2.1.

Satellite Extension		
Launch Configuration	length:	6.30 m
	envelope diameter:	3.45 m
In-Orbit Configuration	17.60 m × 6.70 m × 5.40 m	
Mass Budget		
Service Module	1450 kg	
Solar Array	268 kg	
Payload Module	1235 kg	
Fuel	316 kg	
Payload Instruments	975 kg	
Total	4244 kg	
Average Power Budget		
	Sunlight	Eclipse
Instruments	984 W	984 W
Payload Module	531 W	537 W
Service Module	489 W	489 W
Total	2004 W	2010 W

Table 2.1: Specifications of the METOP satellite (source: <http://www.esa.int>).

2.1.2 The METOP Orbit

The METOP orbit will be selected at an altitude of about 830 km. The satellite has an inclination of 98.7° to the equator to benefit from variations in the gravitational pull on the satellite due to the earth's shape, which causes the METOP orbit to rotate at approximately

1° per day. This precession eastwards matches the annual movement of the earth around the sun. Hence, from the point of view of METOP the satellite is in a constant position versus the sun, and the earth will pass beneath the satellite ground track at 9:30 in the morning of every day and all seasons. This type of orbit is called sun-synchronous orbit. NOAA will continue to operate its afternoon satellite service from a complementary orbit which follows a track at a local time of 14:30. Both together build the Initial Joint Polar System (IJPS).

In sun-synchronous orbit the ground track repeats precisely after a constant integer number of orbits and days. The presently planned orbit for METOP has a repeat cycle of 29 days and 412 orbits. The time to complete an orbit is about 101 minutes, which implies that METOP will make a little bit more than 14 revolutions per day. During each orbit the earth rotates approximately 25°, so that METOP will observe a different portion of the earth during each revolution (see Figure 2.1).

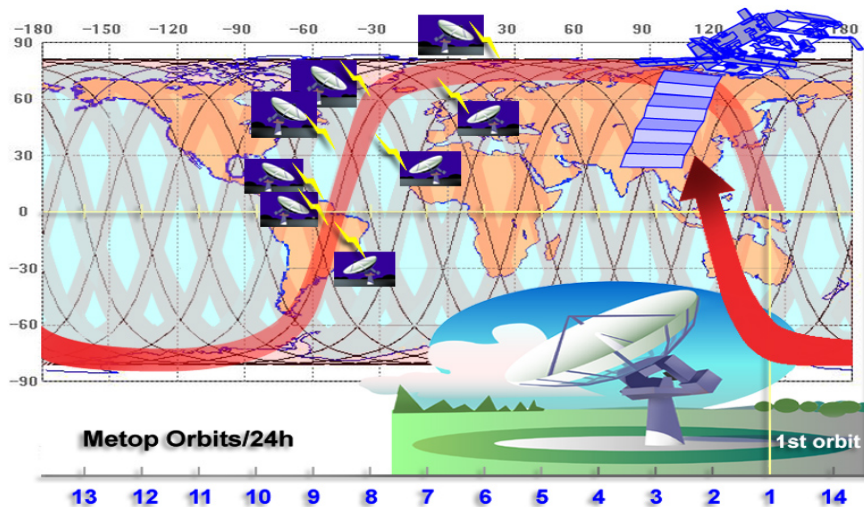


Figure 2.1: METOP will perform a little bit more than 14 revolutions per day (source: <http://www.esa.int/export/esaME/>).

2.1.3 The Instruments on board of METOP

Each METOP satellite will carry a payload of eight instruments for observing the planet, together with four additional ones performing communications and support services that have been provided by the European Space Agency (ESA), the European Organisation for the Exploitation of Meteorological Satellites (EUMETSAT), the American National Oceanic and Atmospheric Administration (NOAA), and the French Space Agency (CNES) (see Figure 2.2).

A core set of instruments for atmospheric sounding and earth imaging will be identical to those flown on the NOAA satellites. This core set includes the Advanced Very High

Resolution Radiometer (AVHRR) for imaging clouds and the surface of the earth. It will also include the High Resolution Infrared Radiation Sounder (HIRS), the Advanced Microwave Sounding Unit-A (AMSU-A), and the Microwave Humidity Sounder (MHS).

The additional METOP instruments – the Advanced Scatterometer (ASCAT), the Global Ozone Experiment-2 (GOME-2), the Global Navigation Satellite System Receiver for Atmospheric Sounding (GRAS), and of course the Infrared Atmospheric Sounding Interferometer (IASI) – will improve atmospheric soundings, as well as providing measurements of atmospheric ozone and near-surface winds over the ocean.

In the following a brief description of the different atmospheric instruments is given except to the IASI instrument which is addressed in detail in section 2.2.

AMSU-A1, AMSU-A2

The data from this instrument is used in conjunction with the HIRS instrument (and on board of the METOP satellites also with the IASI instrument) to calculate the global atmospheric temperature and humidity profiles from the earth's surface to the upper stratosphere (approximately 2 hPa or ~ 45 km) even under cloudy conditions. For its own the data is used to provide precipitation and surface measurements including snow cover, sea ice concentration, and soil moisture.

The AMSU-A1 measures in 15 microwave channels (from about 23 to 90 GHz) in a stepping mode with an instantaneous field of view (IFOV) at nadir of about 45 km, a swath width of about 2100 km and a scan separation of about 53 km. The number of pixels produced per scan is 30. AMSU-A2 has 5 microwave channels (90 to 184 GHz) which provides in total 20 microwave channels for the atmospheric sounding. AMSU-A2 scans across-track with an IFOV of 16 km and the same swath width as AMSU-A1.

ASCAT

This Instrument is the enhanced successor to the scatterometers flown on board of ESA's ERS-1 and ERS-2 satellites and measures wind speed and direction over the ocean. ASCAT is a C-band radar (4.2 to 5.75 GHz) with a center frequency at 5.25 GHz. The instrument, developed by ESA, will also monitor snow and ice cover over land and sea, but the primary product is the radar backscattering coefficient provided over a swath width of 2×500 km.

AVHRR

The AVHRR instrument is a six-channel imaging radiometer (one visible, two near-IR, three IR channels). The main objectives of the latest version, AVHRR/3 are global cloud imagery, mapping of surface temperature, sea-ice, snow-coverage, and vegetation. The instrument has an IFOV of 1.3 mrad providing a nominal spatial resolution of 1.1 km

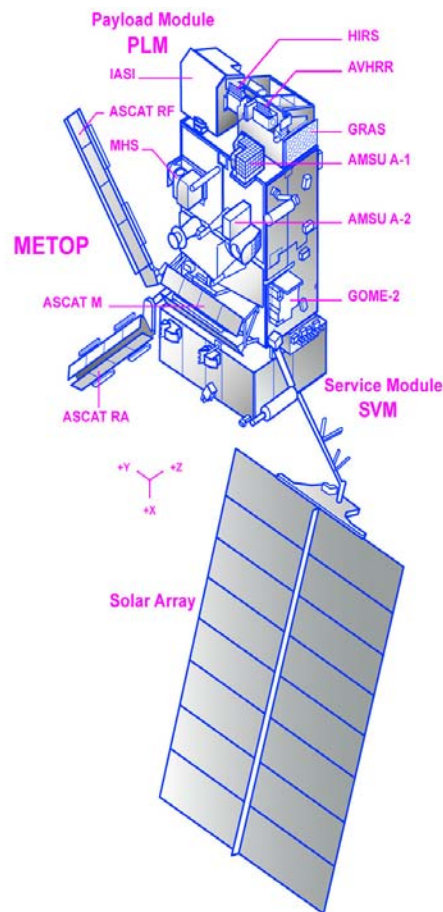


Figure 2.2: The METOP spacecraft configuration with its instruments (source: <http://www.esa.int/export/esaME/>).

at nadir. A continuously rotating elliptical scan mirror provides the cross-track scan, observing the earth from $\pm 55.4^\circ$ from nadir. The mirror scans at six revolutions per second to provide continuous coverage. Per scan about 2000 earth views (pixels) are provided.

GOME-2

The GOME-2 instrument is an across-track scanning nadir viewing spectrometer that observes solar radiation transmitted or backscattered from the earth's atmosphere or from its surface. The recorded spectra are used to derive a detailed picture of the atmospheric content to derive profiles of ozone and other trace gases like the nitrogen compounds NO, NO₂, or NO₃, the halogen compounds ClO and OClO as well as BrO, HCHO, and SO₂.

GRAS

GRAS is a GPS receiver that operates as an atmospheric-sounding instrument. It scans the atmosphere via the *occultation* principle. An occultation occurs whenever a GPS satellite rises or sets on the earth limbs as seen from a low earth orbiting (LEO) satellite. The GPS signal is refracted and slowed as it traverses the earth's atmospheric limb. This causes a phase delay that can be related to characteristic quantities like temperature or humidity via the refractivity field. A single GPS receiver will observe over 500 occultations per day, distributed uniformly about the globe with a vertical resolution of < 1 km.

HIRS

The HIRS/4 instrument is an infrared sounder measuring temperature profiles, moisture content, cloud height and surface albedo. HIRS/4 scans the earth's surface in 20 spectral bands – one visible channel, seven shortwave IR and 12 longwave IR channels. The IFOV for each channel is approximately 1.4° in the visible and shortwave IR channels and 1.3° in the longwave IR band. This provides a nominal spatial resolution of 20.3 km and 18.9 km at nadir, respectively.

Data from HIRS/4 is used in conjunction with data from the AMSU instruments to calculate vertical atmospheric temperature and pressure profiles from the earth's surface to an altitude of about 40 km.

MHS

MHS is an instrument designed to collect information on various aspects of the earth's atmosphere and surface, in particular atmospheric humidity and surface radiation (surface temperature). In addition it can be used to measure liquid water content in clouds and to estimate precipitation rates. The sounder is constructed as a five channel (between 89.0 and 190.3 GHz) self-calibrating, total power, microwave scanning radiometer. It scans the earth from left to right in a vertical plane. Each swath (swath width: ~ 2100 km) is made up of 90 contiguous individual pixels (scenes) sampled every 2.67 seconds. The scan is synchronized with the AMSU-A1 and AMSU-A2 instruments.

2.2 The IASI Instrument

In order to improve the vertical resolution and accuracy of the existing IR temperature sounders (namely the HIRS instruments on board of the NOAA satellites) in 1990 the French space agency, CNES, and the Italian space agency – Agenzia Spaziale Italiana (ASI) – initiated a joint study for an instrument based on a Michelson-type interferometer, IASI. After demonstrating the feasibility of the concept of the IASI instrument a further definition study was started in 1992, initially still with participation of CNES and ASI.

As a result of the discontinuation of ASI funded activities, CNES has carried on the definition study with additional support by EUMETSAT. Detailed design studies started in 1997, funded jointly by CNES and EUMETSAT with contributions from other European countries. After the completion of the feasibility and design activities, the development and manufacturing phase began in 1998 and is still in progress.

The following sections may be regarded as a summary of informations and various reports provided by CNES, ESA and EUMETSAT available at <http://smc.cnes.fr/IASI/>, such as the IASI Science Plan [*Camy-Peyret and Eyre (1998)*].

2.2.1 Design and Functional Chain

The Infrared Atmospheric Sounding Interferometer consists of a Fourier Transform Spectrometer based on a Michelson Interferometer, coupled to an integrated imaging system which allows characterization of cloudiness inside the spectrometer field of view. The scan duration of eight seconds and the horizontal spacing of the full Earth views are identical to those of the AMSU-A1 instrument. This facilitates synergistic use of the two instruments. The kilometric spatial resolution of the sampling of the imager of IASI enables a coregistration with the AVHRR/3 instrument, too.

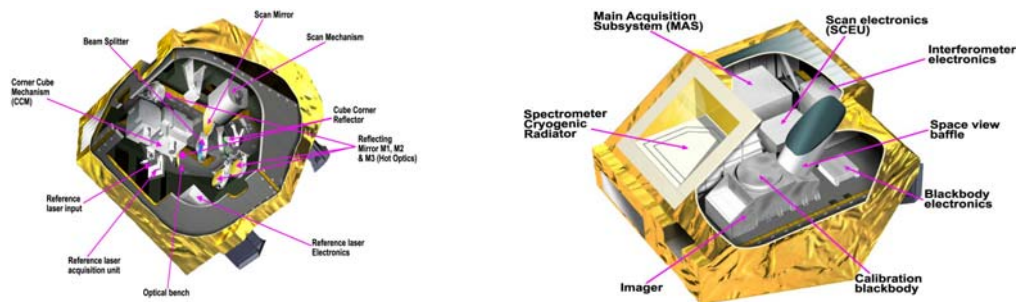


Figure 2.3: Schematically illustration of the components of IASI instrument (source: <http://www.esa.int/export/esaME/>).

The IASI sounder roughly can be separated into 3 modules – the optical subsystem, the analogue electronic chain, and the digital signal processing unit (see Figure 2.3). Furthermore the optical subsystem can be divided into a *scan mirror*, an *off-axis afocal telescope*, and a *Michelson interferometer* from where the recombined beam is mirrored into a so called *cold box*. This cold box subsystem itself includes a *spectral separation unit*, a *detection, amplification, and anti-aliasing filter* and at last the *analogue/digital (A/D) converter*. Additionally the IASI instrument has an integrated imager system. The path of the atmospheric radiation through the instrument is schematically described in Figure 2.4.

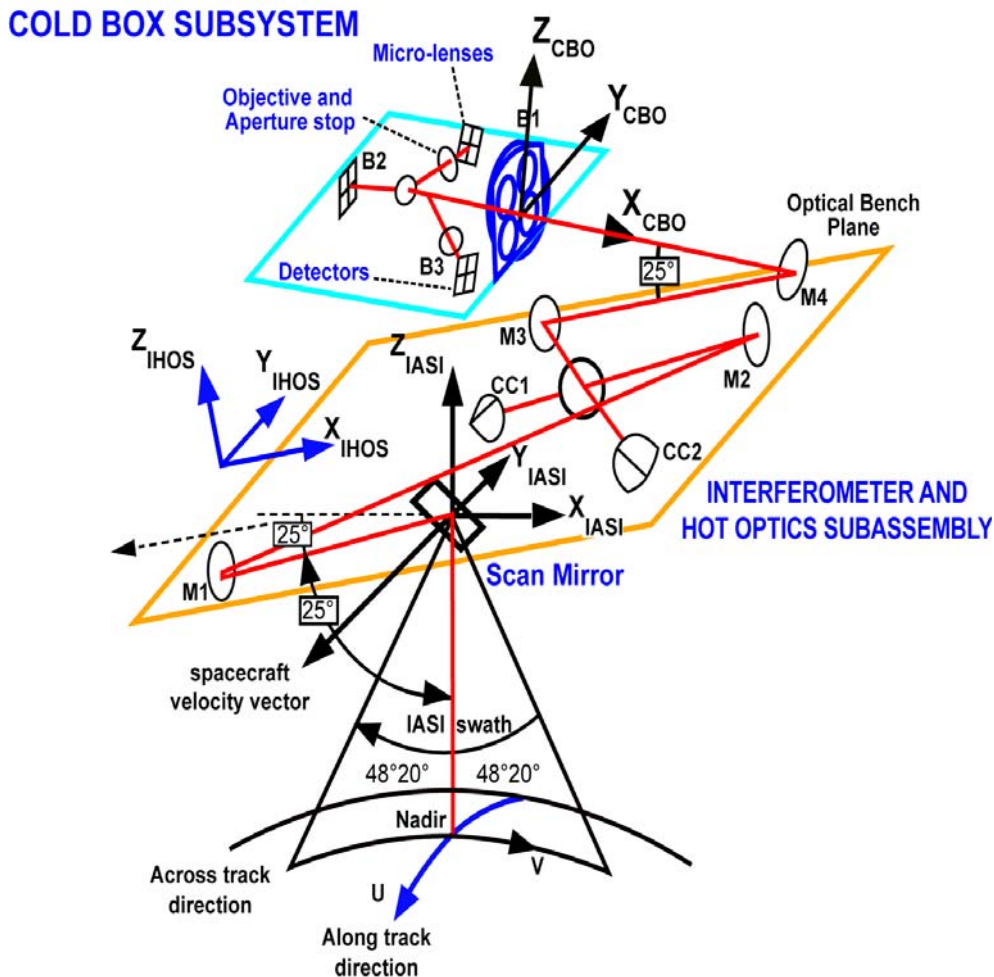


Figure 2.4: Optical path of the atmospheric radiation through the instrument (source: <http://www.esa.int/export/esaME/>).

The Scan Unit and the Telescope

The scan unit – a rotating mirror – is common to sounder and imager and provides scanning according to the geometric pattern depicted in Figure 2.5. IASI scans across-track in a *step and dwell* mode with a field of view of 48.3° to each side, which gives a swath-width of approximately ± 1026 km. The instrument performs 30 earth views (pixels) per scan, one every 216 ms (step time), with an IFOV size of $3.33^\circ \times 3.33^\circ$ (~ 48 km \times 48 km at nadir). The dwell time for each pixel is 150 ms. Each pixel consists of 4 sub-pixels with a diameter of 0.84° (12 km at nadir). They are analyzed simultaneously by 4 detectors, arranged in form of a 2×2 array (see Figure 2.4 – detectors). The total scan period including 30 earth views, calibration measurements, and returning to the starting position lasts 8 seconds.

The calibration is done by viewing a blackbody of known temperature (270 K – 300 K)

mounted inside the instrument, as well as viewing a cold blackbody (deep space scanning). This results in a scan separation step of about 53 km in platform-moving direction.

The off-axis afocal telescope has the purpose to transfer the aperture stop from the scanning mirror into the interferometer entrance mirror.

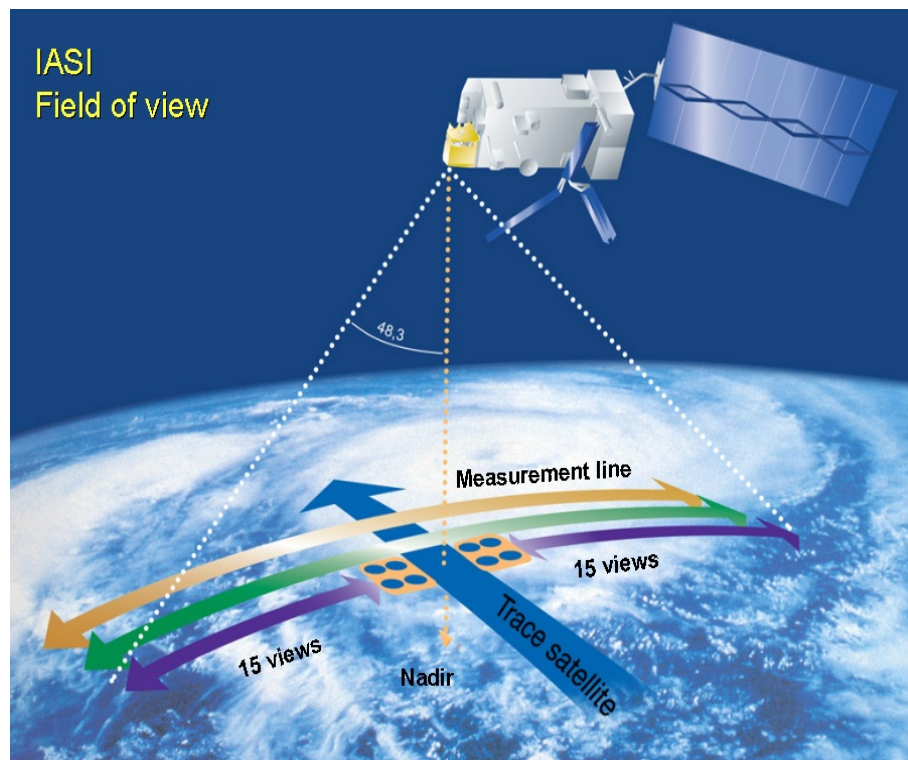


Figure 2.5: Scanning procedure and field of view of the IASI instrument (source: <http://smc.cnes.fr/IASI/>).

The Michelson Interferometer

The heart of IASI and the main part of the optical configuration shown in Figure 2.4, is the Michelson Interferometer. The incident radiation (mirror M2) is divided into two beams by the beamsplitter. One part of the radiation is reflected by a fixed mirror (CC2) (which in case of IASI is a corner cube (CC) reflector) which reflects the beam back to the beamsplitter. There it is reflected to the folder (mirror M3) and the focusing mirror (mirror M4). The other beam is reflected from the beamsplitter and goes to a movable corner cube reflector (CC1), which moves linearly by ± 1 cm corresponding to an optical path difference (OPD) of 2 cm. The reflected beam then transmits through the beamsplitter and finally reaches the folder and focusing mirror. The focusing mirror recombines the two beams at the detectors.

Spectral Separation

In order to secure the spectral performance during the separation and detection process a cooling of the *cold box* hosting these functions to below 100 K is required. This is achieved by a three-stage passive radiator which reduces the instrument background and thermo-electronic detector noise. The output of the interferometer – the relative amplitude versus optical path difference summed over all frequencies – is separated into three bands by two dichroic plates.

Detection, Amplification, and Anti-Aliasing Filter

For each pixel the detection is performed by three detectors, one for each of the three wavenumber bands. Band 1 and Band 2 use a photoconductive detector made of mercury cadmium tellurid (HgCdTe) and a photovoltaic detector made of the same semiconducting material, respectively. Band 3 uses a photovoltaic detector made of indium antimonide (InSb).

Further more, each band is pre-amplified to obtain three identical circuits, which are then amplified and subjected to a Butterworth anti-aliasing filter.

Analogue/ Digital converter

The crucial point of the A/D conversion is a constant time increment sampling at very precise and stably known increments of the OPD. Therefore an auxiliary monochromatic laser beam is used for measuring the OPD and triggering the sampling of the interferogram.

Inverse Fourier Transformation and Calibration

The digitized interferograms undergo an on-board processing for the detection and correction of spurious effects (basically non-linearities). Then an inverse Fourier transform is performed to obtain a digital spectrum. Afterwards the spectra are calibrated with the two calibration targets – cold space and internal black body (see Figure 2.6). This on-board processing reduces the data rate from 45 Megabits per second to 1.5 Megabits per second and is then downlinked from the satellite to the ground segment to form the Level 0 data.

The Imager System

The built-in imager system included in the IASI instrument consists of imager optics, detectors, amplifiers and the A/D converter. Its function is to prepare an accurate collocation between IASI and the METOP companion instrument AVHRR and it has also some stand-alone means for cloud analysis. The field-of-view of the imager, which is covered by a

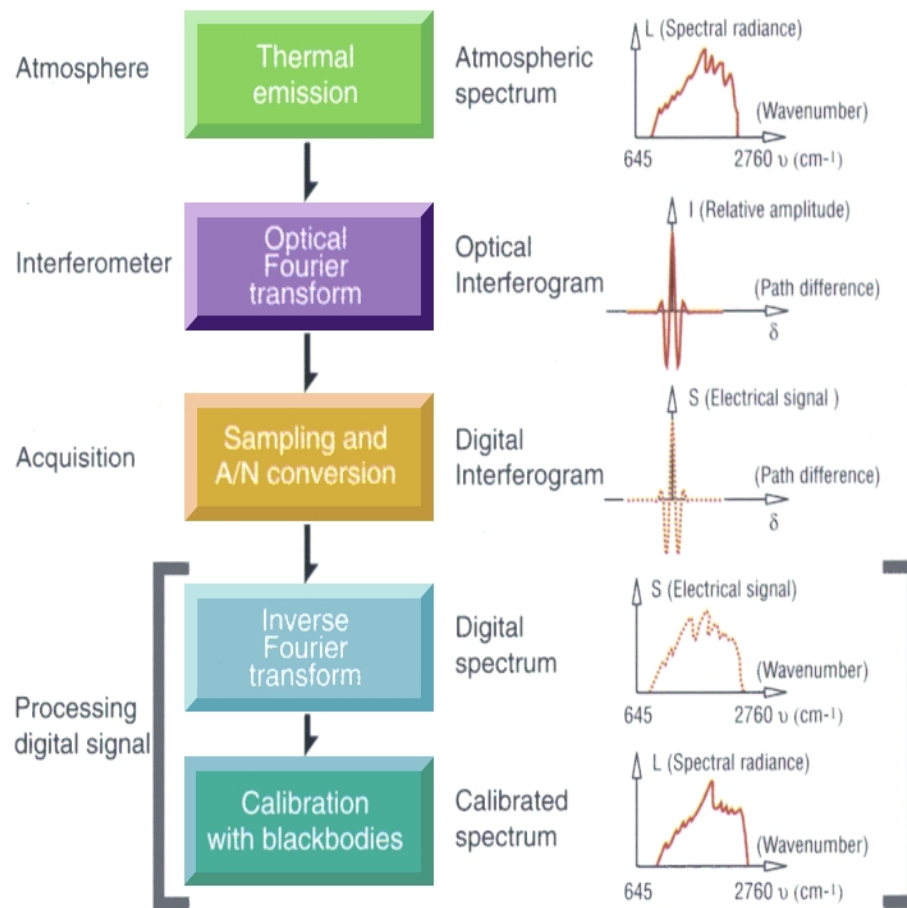


Figure 2.6: Processing chain of the IASI instrument (source: <http://smc.cnes.fr/IASI/>).

raster of 128×128 imager pixels (compressed to 64×64 for downlinking) coincides with that of the IASI sounding unit. The positioning error of the imager pixels with respect to the IASI sounding unit is less than 0.05° .

2.2.2 Objectives and Main Specifications

The main specifications and characteristics of IASI can be found in Table 2.2.

Objectives

The mission objectives assigned to IASI and its companion meteorological instruments include:

- *Operational Meteorology:* This comprises activities concerning operational meteorology coordinated by the World Weather Watch (WWW) of the World Meteorolog-

Parameter	Characteristics	
Scan Type	Step and dwell	
Scan Rate	8 s	
IFOV	3.33°	
IFOV Size at Nadir	48 km	
Pixel/View	4	
Views/Scan	30	
Swath	±48.3°	±1026 km
Spectral Range	645 to 2760 cm ⁻¹	15.5 to 3.62 μm
Spectral Resolution	0.35 to 0.5 cm ⁻¹	
Radiometric Resolution	0.25 to 0.5 K	
Lifetime	5 years	
Power	200 W	
Mass	210 kg	
Size	1.2 m × 1.1 m × 1.1 m	
Data Rate	1.5 Mbits s ⁻¹	

Table 2.2: Main Specifications of the IASI Instrument (sources: <http://www.esa.int> and <http://smc.cnes.fr/IASI/>).

ical Organization (WMO) like forecasting beyond 12 hours and operational Numerical Weather Prediction (NWP) based on assimilation techniques and computing facilities. The high spectral resolution of IASI conjugated with the performance of the remaining METOP instruments will bring NWP in a position to provide temperature and humidity profiles with improved accuracy and vertical resolution which will result in a major increase in quality.

- *Climate Monitoring and Global Change:* To understand global changes of the climate systematic observations of parameters such as sources and sinks of greenhouse gases, clouds (which influence the radiative transfer), ocean and land surface temperatures, and the hydrological cycles are needed.
- *Atmospheric Chemistry:* The increasing concentration of different trace gases will effect the climate and the chemical equilibrium. Since IASI and its companion Instruments will observe atmospheric constituents such as O₃, CH₄, N₂O, CO, and SO₂, valuable information about chemical processes and their impact on atmospheric composition and climate processes can be obtained.

Since the IASI data will have potential for use in various operational and research applications an intensive and effective research and development is required to obtain a successful interpretation and application of it. For this purpose CNES and EUMETSAT have established the IASI Sounding Science Working Group (ISSWG), following the release of a first Announcement of Opportunity (AO) for the scientific preparation of the IASI mission in 1995. Current scientific activities involve:

- radiative transfer modeling to compare simulated radiances with IASI radiances,
- simulation of IASI instrument processes, as well as on-board and on-ground data ingest processes,
- development of data pre-processing methods including combination of IASI data with data from other instruments on board of METOP,
- development of data inversion algorithms to retrieve temperature, humidity, ozone, other minor constituents and many other geophysical variables,
- monitoring, quality control, and validation processes of IASI data and products, and
- preparatory studies of appropriate interface development between IASI data and applications.

The primary objective of IASI is the retrieval of atmospheric profiles of temperature and humidity with improved resolution and accuracy as compared to current (e. g. HIRS) infrared instruments. The most important targets are:

- *temperature profiles* with an average accuracy of 1 K and a vertical resolution of 1 km (at least in the troposphere) and
- *humidity profiles* with an accuracy of 10% and 1 to 2 km vertical resolution.

Further products that can be retrieved from IASI measurements are *ozone profiles* (in particular column content), cloud parameters (like cloud cover, cloud top temperature, and liquid water amount), column amounts of N₂O, CH₄, and CO, and *sea- and land-surface skin temperatures*.

Spectral Specifications

The IASI sounder provides spectra of high radiometric quality in a wavenumber range from 645 cm⁻¹ to 2760 cm⁻¹ (corresponding wavelength range is 15.5 μm to 3.62 μm) with a constant sampling interval of 0.25 cm⁻¹. This nominal spectral sampling was determined by the line-spacing in the CO₂ absorption bands. The final choice of 0.25 cm⁻¹ was found adequate to provide sufficient spectral resolution for all defined objectives.

The spectrum measured by the instrument equals the ideal spectrum convolved by an appropriate instrument function, termed as the Instrument Spectral Response Function (ISRF). The spectral resolution, $\delta\nu$, is then defined as the full width at half maximum (FWHM) of the ISRF and is 0.35 cm⁻¹. Apodization refers to the removal of false side-lobes of the instrumental spectrum, introduced by the finite optical path displacement in the interferometer. The resolution slightly degrades due to apodization, leading to a resolution of about 0.5 cm⁻¹ for the apodized spectrum. A further relevant instrumental

	range [cm^{-1}]	range [μm]	$\delta\nu$ [cm^{-1}]	ϵ	retrieved parameter
Band 1	645 – 1210	15.50 – 8.26	≤ 0.35	≤ 0.046	temperature, O_3 , cloud properties
Band 2	1210 – 2000	8.26 – 5.00	≤ 0.39	≤ 0.056	humidity, N_2O , CH_4 , SO_2
Band 3	2000 – 2760	5.00 – 3.62	≤ 0.50	≤ 0.092	temperature, CO , N_2O , CH_4 , surface and cloud properties

Table 2.3: IASI spectral bands, resolution $\delta\nu$, shape error index ϵ , and retrieval parameters.

parameter is the shape error index ϵ , which specifies the error of the knowledge of the ISRF (for details see subsection 2.2.3).

The full spectral range of the IASI instrument is subdivided into three bands. Table 2.3 gives the boundaries of the three bands, their unapodized resolution $\delta\nu$, the shape error index ϵ , and the parameters which may be retrieved in the particular band. As mentioned above, the apodized resolution will be slightly lower.

These three bands include, in particular, the large water vapor absorption band at $1250\text{-}2000\text{ cm}^{-1}$ ($8\text{-}5\ \mu\text{m}$, center at $6.3\ \mu\text{m}$) and two strong CO_2 bands, one near 645 cm^{-1} ($15.5\ \mu\text{m}$) and the other near 2325 cm^{-1} ($4.3\ \mu\text{m}$). Finite spectral signatures of interest are caused by O_3 , CH_4 , N_2O , CO , and SO_2 (see Table 2.4 for detail).

Spectral Range	Primary Application
650 - 770 cm^{-1}	Temperature sounding (CO_2 band)
770 - 980 cm^{-1}	Surface and cloud properties
1000 - 1070 cm^{-1}	O_3 sounding
1080 - 1150 cm^{-1}	Surface and cloud properties
1210 - 1650 cm^{-1}	Water vapor and temperature sounding (and N_2O , CH_4 , and SO_2)
2100 - 2150 cm^{-1}	CO column amount
2150 - 2250 cm^{-1}	temperature sounding and N_2O column amount
2350 - 2420 cm^{-1}	temperature sounding
2420 - 2700 cm^{-1}	Surface and cloud properties
2700 - 2760 cm^{-1}	CH_4 column amount

Table 2.4: IASI spectral range (source: <http://www.esa.int> and <http://smsc.cnes.fr/IASI/>).

Radiometric Specifications

IASI measures radiance from a blackbody within the temperature range 4 to 315 K. The radiometric noise for the instrument is specified in terms of *noise equivalent to temperature difference* ($\text{NE}\Delta\text{T}$) at a given reference temperature of 280 K. This value includes

all noise contributions such as noise induced by detectors, amplifiers, analogue/digital converter, digital data processing errors, errors due to field-of view motion, fluctuation of the wavelength, radiometric calibration errors, or the errors induced by an inaccurate knowledge of the ISRF. In Table A.5 in appendix A the radiometric noise for a reference temperature of 280 K is given for every 50 cm^{-1} .

IASI calibration relies on measurements of cold and hot reference targets once every scan line. The absolute calibration accuracy is better than 0.5 K at 280 K. The homogeneity of the calibration depends on parameters such as the spectral position, the orbital repeatability, the lifetime repeatability, and the geometry, each one introducing a nominal error less than 0.15 K.

The IASI imager, whose aim lies mainly in the detection of clouds, is a broadband radiometer with one infrared channel ranging from 3.7 to $4.0 \mu\text{m}$ and measures a blackbody radiance within 4 to 315 K, too. The $\text{NE}\Delta\text{T}$ will be less than 0.5 K at the reference temperature specified above. The calibration accuracy is better than 1 K at 280 K reference temperature.

2.2.3 Measurement Principle

As mentioned above, the concept of the IASI instrument is a Michelson type Fourier interferometer. Albert A. Michelson (1852 – 1931) constructed his two-beam interferometer more than a century ago primarily to set up the famous *Michelson and Morley experiment* which should measure the motion of the earth relative to the *ether*. The negative result of it caused a major revision of the classical space time concepts and motivated A. Einstein to propose his *Theory of special relativity*.

To gain spectral information, Michelson looked at the "visibility curve" while gradually increasing the path in one arm of his interferometer. Applying a Fourier Transform using a mechanical Fourier analyzer constructed by himself and Stratten (1898), he was able to generate crude spectra of simple cases (single narrow red cadmium line as well as the yellow sodium doublet). But it lasted more than half a century until the potential of the instrument was recognized as a powerful spectrometer.

The advantage of the Michelson interferometer arises basically from two concepts [Bell (1972)]. The first is termed the *étendue* or *throughput* advantage, expressed by P. Jacquinet and C. Dufour (1948, c. f. [Hanel et al. (1992)]), which states that the flux throughput and brightness can be considered constant in a lossless optical system from the source to the detector. The size of the throughput is proportional to the power and it was found that under comparable conditions much more power can be put through an interferometer than through the best grating spectrometer. This high *étendue* has been fully realized with space-based interferometers observing the planets from outer space, but it may not always be possible to obtain it in other applications (e. g., stellar or low resolution planetary spectroscopy from the ground).

The second major advantage is called the multiplex advantage first stated by Fellgett (1958, c. f. [Hanel et al. (1992)]): Within a given spectral range the instrument measures

all spectral intervals simultaneously, while on the other hand conventional grating spectrometers are receiving information only in a narrow band (determined by the exit slit) at a given time.

Measurement Setup

The functional principle of a Michelson type Fourier interferometer is illustrated in Figure 2.7. The essential part of the instrument is the beamsplitter (A) whose function is to divide the incoming radiation beam into two parts of – nearly – equal intensity. After the reflection of one part of the radiation by a stationary mirror (B) – corner cube reflectors in the case of IASI – and the other part by a movable mirror (C) the beams are recombined at the beamsplitter and sent towards the detector (D). The moving mirror can be shifted smoothly within a distance (arm displacement) of $\pm L$ (where $L=1$ cm in the case of IASI) to obtain an OPD denoted by δ (and therefore a phase difference) of $2L$ between the two beams at the detector. (A further phase shift is gained due to the difference between the internal and the external reflections at the beamsplitter [Born and Wolf (1999)].)

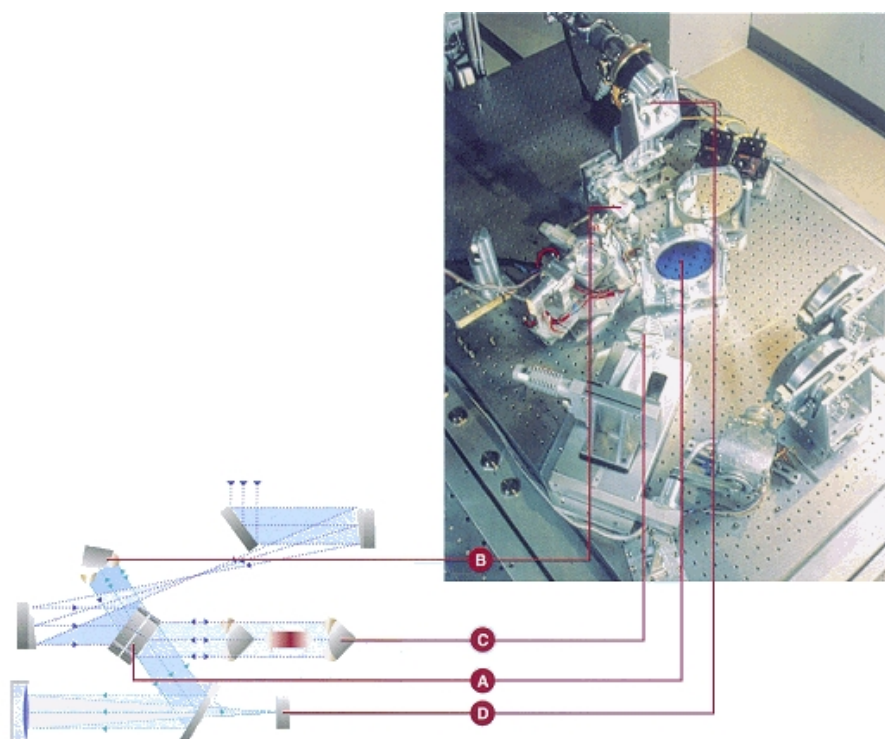


Figure 2.7: Picture of the laboratory breadboard of the IASI instrument and corresponding optical path diagram of a Michelson interferometer (source: <http://smc.cnes.fr/IASI/>).

If we suppose a collimated beam of monochromatic radiation striking the beamsplitter while the two mirrors are in the same distance to it (i. e. both arms have equal length) – this is called zero path difference (ZPD) $\delta = 0$ – in a non-absorbing beamsplitter the

phase difference between internal and external reflection is π . In this case both arms interfere destructively from the point of view of the detector. Shifting the movable mirror by a quarter of a wavelength (λ) results in a phase difference of $\lambda/2$ (or π) and therefore constructive interference at the detector. Hence the variation of the OPD produces a variation of the interferogram, which corresponds to the detection of the signal versus the OPD.

Each wavenumber produces its own characteristic flux pattern of the combined beams. In the case of a polychromatic source the interferogram is the sum of the fluxes of each wavelength.

Fourier Transform Analysis and Interferometry

The spectrum (radiance versus wavenumbers) is obtained by performing a Fourier Transform (FT) analysis of the (digitized) interferogram.

The FT $F(y)$ of a function $f(x)$ is mathematically defined as follows:

$$F(y) = \int_{-\infty}^{\infty} f(x) \exp [i2\pi yx] dx \equiv \text{FT} \{f(x)\}, \quad (2.1)$$

and the inverse Fourier Transform reads:

$$f(x) = \int_{-\infty}^{\infty} F(y) \exp [-i2\pi yx] dx \equiv \text{FT}^{-1} \{F(y)\}. \quad (2.2)$$

These two formulas constitute a pair used to transform a function from spatial or temporal domain into a wavenumber or frequency domain and vice versa. Following now the derivations of a standard Fourier transform book like [Bell (1972)] we finally obtain the inverse complex Fourier transform $B(\nu)$:

$$\boxed{B(\nu) = \int_{-\infty}^{\infty} \left[I_R(\delta) - \frac{1}{2}I_R(0) \right] \exp [-i2\pi\nu\delta] d\delta} \quad (2.3)$$

implying that $B(\nu)$, the intensity at wavenumber ν , is the Fourier transform of the interferogram (the flux versus the OPD, δ).

In case of IASI this means that $I_R(\delta)$ is measured by moving the corner cube between ± 1 cm, thus δ is explored within 2 cm. Then $I_R(0)$ is determined at the ZPD position, and $B(\nu)$ is calculated according to Equation 2.3. Usually $[I_R(\delta) - \frac{1}{2}I_R(0)]$ is referred to as interferogram, that is the oscillation of $I_R(\delta)$ about $\frac{1}{2}I_R(0)$.

Apodization and Instrument Spectral Response Function

The basic inverse Fourier transform integral, Equation 2.3 has infinite limits for the OPD, but in practice the interferogram can only be measured out to some δ . This produces

phenomena called *ringing* (or in case of the spectrum, sidelobes). The necessary modifications to correct these artifacts are termed *apodization*. Apodizing a function usually means multiplying the interferogram by an *apodization function*, which removes the false sidelobes introduced into the spectra by the finite OPD.

The spectrum calculated for finite OPD is called *instrumental spectrum*, $B_I(\nu)$:

$$B_I(\nu) = \int_{-L}^L \left[I_R(\delta) - \frac{1}{2}I_R(0) \right] \exp[-i2\pi\nu\delta] d\delta \quad (2.4)$$

where L is the maximal arm displacement. This FT would introduce sidelobes in the spectrum resulting from the finite δ . Let's now multiply the integrand by an apodization function $A(\delta)$:

$$B_I(\nu) = \int_{-L}^L \left[I_R(\delta) - \frac{1}{2}I_R(0) \right] A(\delta) \exp[-i2\pi\nu\delta] d\delta. \quad (2.5)$$

This states, that $\left[I_R(\delta) - \frac{1}{2}I_R(0) \right] A(\delta)$ is the FT of the instrumental spectrum $B_I(\nu)$. If chosen correctly, the spectrum resulting from Equation 2.5 will be closer to the ideal spectrum $B(\nu)$ than the unapodized spectrum (Equation 2.4) but with a lower spectral resolution.

Let us take the rectangular function – $\text{rect}(\delta)$ – for $A(\delta)$ as a reference case:

$$A(\delta) = \text{rect}(\delta) = \begin{cases} 1 & |\delta| \leq L \\ 0 & |\delta| > L \end{cases} \quad (2.6)$$

Therefore we can rewrite the instrumental spectrum:

$$B_I(\nu) = \int_{-\infty}^{\infty} \left[I_R(\delta) - \frac{1}{2}I_R(0) \right] \text{rect}(\delta) \exp[-i2\pi\nu\delta] d\delta. \quad (2.7)$$

Applying a FT on Equation 2.7 results in:

$$\text{FT} \{B_I(\nu)\} = \left[I_R(\delta) - \frac{1}{2}I_R(0) \right] \text{rect}(\delta). \quad (2.8)$$

Considering now equation 2.3 we can write the FT of the ideal spectrum as follows:

$$\text{FT} \{B(\nu)\} = \left[I_R(\delta) - \frac{1}{2}I_R(0) \right]. \quad (2.9)$$

In defining a function $F(\nu)$ to be the FT of the rectangular function $\text{rect}(\delta)$, we can write:

$$\text{FT} \{F(\nu)\} = \text{rect}(\delta). \quad (2.10)$$

Substituting Equations 2.9 and 2.10 into Equation 2.3 we obtain:

$$\text{FT} \{B_I(\nu)\} = \text{FT} \{B(\nu)\} \text{FT} \{F(\nu)\}. \quad (2.11)$$

With the convolution theorem which states that FT of the convolution of two functions is the product of the FT of two functions, we get:

$$\text{FT} \{B_I(\nu)\} = \text{FT} \{B(\nu) \otimes F(\nu)\}. \quad (2.12)$$

The FT of a rectangular function gives a sinc function (see Figure 2.8), defined as:

$$\text{sinc}(x) = \frac{\sin(x)}{x}.$$

Taking this into account, the FT of the rectangular apodizing function $A(\delta)$ specified in Equation 2.6 can be evaluated as:

$$F(\nu) = 2L \text{sinc}(2\pi\nu L) \quad (2.13)$$

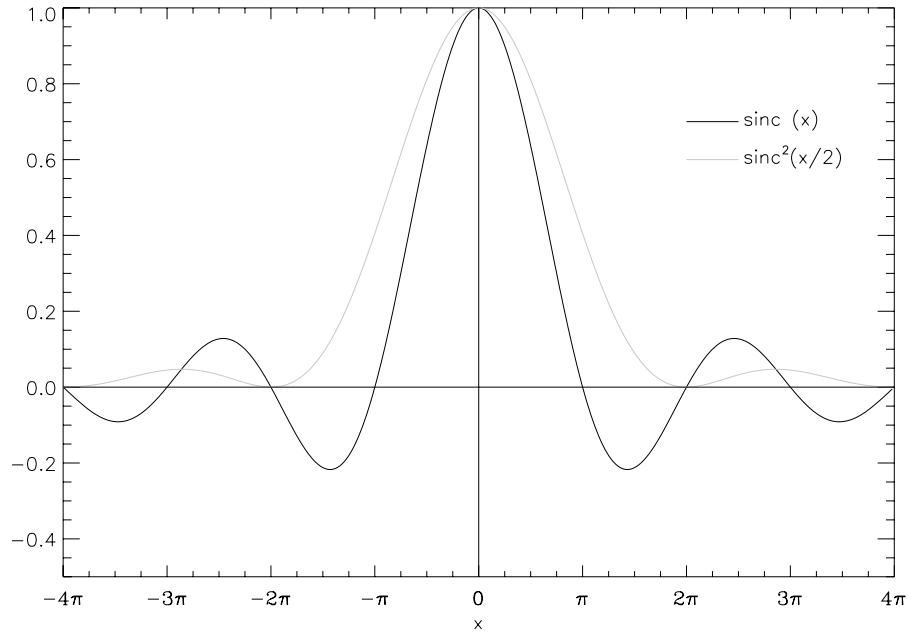


Figure 2.8: Black line: $\text{sinc}(x)$; gray line: $\text{sinc}^2(x/2)$.

In general $F(\nu)$ is representing the FT of the apodization function. It is termed the *instrumental spectral response function* (ISRF) or just *instrument function*. Hence, we can rewrite Equation 2.12 in the form:

$$B_I(\nu) = B(\nu) \otimes \text{ISRF}. \quad (2.14)$$

implying that the instrumental spectrum is the convolution of the ideal spectrum with the ISRF.

To show the impact of the apodization we assume a monochromatic source with wavenumber ν_0 . A radiation field of this kind can be represented as a positive Dirac-Delta function (distribution) $\frac{1}{2}\{\delta_D(\nu - \nu_0) + \delta_D(\nu + \nu_0)\}$, where the subscript D denotes the Dirac-Delta function to distinguish it from the OPD δ . The interferogram (i. e. the FT of the spectrum) is a cosine wave given by $\cos(2\pi\nu_0\delta)$. Therefore the instrumental spectrum of a monochromatic source is:

$$B_I(\nu_0) = 2L \operatorname{sinc}(2\pi\nu_0L), \quad (2.15)$$

which is indicated as the black line in Figure 2.8. The function shows quite significant (and deep) sidelobes. Introducing now a triangular apodization function $A(\delta) = 1 - |\delta|/L$ yields a spectrum – and in case of a monochromatic source also the ISRF – described by:

$$B(\nu_0) = L \operatorname{sinc}^2(\pi\nu_0L). \quad (2.16)$$

This function is shown as the gray line in Figure 2.8. It can be seen that on the one hand the apodization results in a decrease of the depth of the sidelobes whereas on the other hand the spectral resolution (defined as the FWHM of the ISRF) $\delta\nu$ increases in comparison to the rectangular apodization function. In Table 2.5 a few commonly used apodization function, their ISRF, and the FWHM's of the ISRF are summarized.

	Apodization Function	ISRF	FWHM
Uniform (rectangular)	1	$2L\operatorname{sinc}(2\pi\nu L)$	1.21π
Bartlett (triangular)	$1 - \frac{ \delta }{L}$	$L\operatorname{sinc}^2(\pi\nu L)$	1.77π
Cosine	$\cos\left(\frac{\pi\delta}{2L}\right)$	$\frac{4L \cos(2\pi\nu L)}{\pi(1-16L^2\nu^2)}$	1.64π
Gaussian	$\exp\frac{-\delta^2}{2\sigma^2}$	$2 \int_0^L \cos(2\pi\nu\delta) \exp\frac{-\delta^2}{2\sigma^2} d\delta$	$\sqrt{-8 \ln \frac{1}{2}} \sigma$
Hamming	$0.54 + 0.46 \cos\left(\frac{\pi\delta}{L}\right)$	$\frac{L(1.08-0.64L^2\nu^2)\operatorname{sinc}(2\pi\nu L)}{1-4L^2\nu^2}$	1.82π
Hanning	$\cos^2\left(\frac{\pi\delta}{2L}\right)$	$\frac{L\operatorname{sinc}(2\pi\nu L)}{\pi(1-4L^2\nu^2)}$	2.00π

Table 2.5: Selected apodization functions, their corresponding ISRF, and the FWHM of the ISRF (σ is the square root of the Gaussian variance).

The ISRF of the IASI instrument is a 0.5 cm^{-1} full width at half height (FWHH) Gaussian with a cardinal sinc function whose interferogram is a $\pm 2 \text{ cm}$ box function corresponding to the IASI $\pm 2 \text{ cm}$ OPD [Cayla (1996)].

2.2.4 Data Products

The data obtained from the IASI instrument will be classified into 4 levels – Level 0 to Level 3. All Products except the Level 0 data are processed on ground. The main purpose of the IASI Instrument will be to deliver temperature and water vapor profiles for NWP

at accuracies of 1 K or 10%, respectively, at a high vertical resolution. Additionally, cloud parameters, surface skin temperature, surface emissivity, and trace gases like ozone profiles, and column amounts of CO, CO₂, N₂O, and CH₄ will be gained. Another aim is the direct use of IASI radiances for NWP assimilation schemes.

To obtain the best analysis of the IASI measurements, the so called Level 2 processing combines IASI with concurrent measurements of AVHRR, AMSU-A, MHS, and ATOVS Level 2 Products. Of course a IASI stand alone processing is possible, too.

The following listing provides an overview on the special IASI data products (source: <http://smc.cnes.fr/IASI/>):

- **Level 0:** Raw IASI measurement data. After on-ground demultiplexing Level 0 data includes pre-calibrated spectra, the corresponding non calibrated images, calibration images, verification data and auxiliary data necessary for further processing.
- **Level 1a:** Non apodized calibrated spectra and corresponding images. This step of processing comprises data decoding, radiometric post-calibration, spectral calibration, IASI/AVHRR coregistration via IASI images, geolocation and dating.
- **Level 1b:** This data product is a Level 1a data re-sampled to the nominal interval.
- **Level 1c:** An apodized Level 1b data to obtain a nominal Instrument Spectral Response Function. This level includes also an analysis of the AVHRR radiances over the IASI pixels.
- **Level 2a:** Geophysical products derived from IASI in a stand-alone mode: profiles of temperature, humidity, and ozone, surface temperature, trace gas distribution, cloud parameters, etc. Level 2a data may exist as interim geophysical products during the commissioning and pre-operational IASI mission phases and as geophysical products after upgrading of the processing software at the end of the pre-operational phase. Some of them might be merged into a more limited number of geophysical product records depending on the processing architecture and needs of users.
- **Level 2b:** Geophysical products derived after co-processing of IASI data and those of the companion meteorological instruments. These products may be similar to Level 2a products but with higher accuracy and resolution and/or extracted over a wider range of cloudiness. Or they are additional geophysical products which can only be derived in a synergistic mode.
- **Level 3:** Gridded and time-averaged geophysical products derived from Level 2b products possibly in combination with information not obtained from EPS but from other sources (data from NWP forecasts etc.).

Chapter 3

Discrete Inverse Theory

The aim of inverse theory is to obtain useful information about the physical world as a result of drawing meaningful conclusions from observations. The term *inverse theory* should be seen in contrast to a *forward theory*, which is defined as the process of predicting the results of measurements on the basis of some general principles – the model – and a set of specific conditions – the parameters of the model – which are relevant to the problem dealt with [Menke (1984)]. As its name implies, inverse theory tries to solve the reverse problem: based on observations and a model it has the attempt to deduce estimates of the model parameters. It has to be pointed out that the inverse theory wants to provide information about the unknown numerical parameters that go into the model, and not to establish the model itself. Nevertheless it can often provide a useful method to test the correctness of a model.

In this chapter a short review of the aspects of inverse theory restricted to discrete linear and moderately non-linear problems (as they occur in the problems treated here) is given. For details see e. g. [Menke (1984), Rodgers (2000), Maybeck (1994), Maybeck (1982)].

3.1 The Forward Model

3.1.1 Theoretical Considerations on Forward Modeling

The state of a physical system, \mathbf{x} of dimension n (e. g. temperature profile, humidity profile, etc.), can be related to measurements, \mathbf{y} of dimension m , via a forward model (function), \mathbf{f} by:

$$\mathbf{y} = \mathbf{f}(\mathbf{x}) + \epsilon \quad (3.1)$$

where ϵ is defined as the measurement noise. The forward model is the theoretical representation of the physics of the treated system. It has to be pointed out that \mathbf{f} is only a model – a theoretical approximation – of the underlying physics, since the real processes may be too complex and in some aspects they may not be fully understood. The forward

model should be constructed in such a way that the detailed physics is prepared to an adequate accuracy [Maybeck (1994)].

Here a problem is worth mentioning. Since on the one hand our measurements are always discrete quantities whereas on the other hand the quantities to be retrieved are in most inverse problems continuous, most of the inverse problems are formally ill-posed or under-constrained in a theoretical sense. This problem can be solved by discretizing this continuous functions into a finite number of parameters. A further opportunity of the usage of a finite grid is that one can use vector-algebraic methods for solving the problems rather than the more general algebra of Hilbert spaces.

The forward model \mathbf{f} can be a linear or non-linear function of the state vector. Supposing that \mathbf{f} is governed by a nonlinear relation between \mathbf{x} and \mathbf{y} we are able to linearize the problem by expanding it in a Taylor series about an initial guess state \mathbf{x}_0 :

$$\mathbf{y} = \mathbf{f}(\mathbf{x}_0) + \left. \frac{\partial \mathbf{f}}{\partial \mathbf{x}} \right|_{\mathbf{x}=\mathbf{x}_0} (\mathbf{x} - \mathbf{x}_0) + O(\|\mathbf{x} - \mathbf{x}_0\|^2) + \boldsymbol{\epsilon} \quad (3.2)$$

The matrix of partial derivatives of the forward model with respect to \mathbf{x} evaluated at $\mathbf{x} = \mathbf{x}_0$ is denoted by \mathbf{K} and is called the *weighting function matrix* of dimension $m \times n$. (Derivatives of this type are known as Frechet derivatives. The term *weighting function matrix* is mostly used by the remote sounding community. Amongst other terms it may also be called the *Jacobian matrix*, the kernel (for this reason it is denoted by \mathbf{K}), and the tangent linear model.)

When ignoring higher order terms, which is appropriate for nearly linear or moderately non-linear problems, we can rewrite Equation 3.2 as:

$$\mathbf{y} - \mathbf{f}(\mathbf{x}_0) = \mathbf{K}(\mathbf{x} - \mathbf{x}_0) + \boldsymbol{\epsilon} \quad (3.3)$$

Within the framework of discrete inverse theory the forward and the inverse problem can be considered as an algebraic mapping between two vector spaces: the state space (of dimension n) and the measurement space (of dimension m). From this point of view performing a measurement is equivalent to a mapping from the state space into the measurement space (represented by the weighting function matrix \mathbf{K}), whereas the inverse problem is that of finding an appropriate inverse mapping from the measurement space back into the state space. Therefore each row of \mathbf{K} can be considered as a vector \mathbf{k}_i (weighting functions) in the state space.

3.1.2 Range and Null-space of the Forward Model Operator

At the beginning we want to consider a linear problem with an arbitrary number of dimensions in the absence of measurement errors:

$$\mathbf{y} = \mathbf{K}\mathbf{x} \quad (3.4)$$

The solution of this problem involves the determination if the problem has no solutions, one specific solution, or an infinite number of solutions. In particular, if there is no solution or no specific solution, it has to be investigated what and how much information can be extracted from a measurement \mathbf{y} about the state \mathbf{x} .

The m weighting functions \mathbf{k}_i span a subspace of the state space – called the *row space* or *range* – whose dimension is smaller or at most equal m , depending on the linear dependency of the \mathbf{k}_i 's to one another. The dimension of this subspace, the rank of the matrix \mathbf{K} , denoted by p , equals the linearly independent rows. If there are more measurements than parameters ($m > n$), the rank can not be greater than n , but can even be less. In this case the *range* does not comprise the whole state space. The *weighting function matrix* has also a *column space* of dimension p which is a subspace of the measurement space.

Suppose we have an orthogonal basis for the state space having p orthonormal base vectors forming the row space, and $n - p$ base vectors outside which are orthogonal to the row space. Hence only components of the state vector lying in the row space will contribute to the measurement, all other components will give a zero contribution, i. e. are unmeasurable. This $n - p$ dimensional space being orthogonal to the row space is called *null space* of \mathbf{K} .

These properties of the *weighting function matrix* can be utilized to determine the solvability of a problem. If a null space is existing, i. e., $p < n$, the problem is underdetermined. Hence the solution is not unique since there are components of the state space (parameters) which can not be determined by the measurement.

Let us consider for a moment only the components of the state vector in the range of \mathbf{K} . They are overdetermined if $m > p$, or well- or even-determined if $m = p$. Hence a problem can be simultaneously over-determined (in row space) and under-determined (if there is a null space). This condition is called *mixed determined*. Of course it is also possible that there are more measurements than unknowns ($m > n$), and nevertheless the problem is under-determined ($p < n$). A problem is well determined only if $m = n = p$.

In summary we can say that if a problem is well determined a unique solution can be found. If the problem is overdetermined in the row space and we suppose that there is no measurement error, the measurements are either linearly related in the same way as the \mathbf{k}_i 's or they are to some degree inconsistent, which is the normal situation if measurement errors are present.

3.2 The Inverse Problem

Supposing we have no measurement errors, the solution of the inverse problem to Equation 3.4 is to find an appropriate inverse mapping function from the measurement space into the state space, \mathbf{K}^{-g} , where g denotes the generalized inverse. Hence the inverse problem can be formulated as:

$$\mathbf{x}_{retr} = \mathbf{K}^{-g}\mathbf{y}, \quad (3.5)$$

where \mathbf{x}_{retr} is the retrieved state. If a unique solution exists (i. e. the problem is well-determined), the generalized inverse is simply the inverse of the *weighting function matrix*, \mathbf{K}^{-1} .

3.2.1 Least Squares Solution

In the case of an over determined problem (more measurements than unknowns ($m > n$), and the matrix \mathbf{K} being of full rank ($p = n$)), the solution is non-unique to the same degree as the system is inconsistent, but it is possible to define a best approximate answer determined by the principle of minimum misfits. Therefore one has to minimize the norm $\|\mathbf{K}\mathbf{x} - \mathbf{y}\|_n$, which becomes the well known least-squares solution, if the L_2^* norm is used. The generalized inverse is in this case given by:

$$\mathbf{K}^{-g} = (\mathbf{K}^T \mathbf{K})^{-1} \mathbf{K}^T, \quad (3.7)$$

yielding:

$$\mathbf{x}_{retr} = (\mathbf{K}^T \mathbf{K})^{-1} \mathbf{K}^T \mathbf{y}. \quad (3.8)$$

3.2.2 Truncated SVD

Let us next look at the case of a mixed-determined problem (i. e. simultaneously over- and under-determined). For this case the generalized inverse can be found by performing a special type of eigenvalue decomposition of the weighting function matrix, called the *singular value decomposition* (SVD) (see, e. g., [Press et al. (1992)]).

*The term norm is used to refer to some measure of length or size and is indicated by a set of double vertical bars: $\|\mathbf{A}\|$ is the norm of the vector \mathbf{A} . The most commonly used norms are those based on the sum of some power of the elements of the vector and are given the name L_n , where n is the power:

$$\begin{aligned} L_1 \text{norm:} \quad \|\mathbf{A}\|_1 &= \left[\sum_i |A_i|^1 \right] \\ L_2 \text{norm:} \quad \|\mathbf{A}\|_2 &= \left[\sum_i |A_i|^2 \right]^{1/2} \\ &\vdots \quad \dots \\ L_n \text{norm:} \quad \|\mathbf{A}\|_n &= \left[\sum_i |A_i|^n \right]^{1/n} \\ &\vdots \quad \dots \\ L_\infty \text{norm:} \quad \|\mathbf{A}\|_\infty &= \max_i |A_i|. \end{aligned} \quad (3.6)$$

The limiting case L_∞ gives only a weight to the largest element, which means it is equivalent to the selection of the vector element with the largest absolute value as the measure of length.

In SVD one starts from the assumption, that any $m \times n$ matrix with $m \geq n$ can be written as the product of a $m \times n$ column-orthonormal matrix \mathbf{U} , with a $n \times n$ diagonal matrix $\mathbf{\Lambda}$ which has positive or zero diagonal elements (the *singular values*, λ_i) times the transpose of a ($n \times n$) orthonormal matrix \mathbf{V} :

$$\mathbf{K} = \mathbf{U}\mathbf{\Lambda}\mathbf{V}^T, \quad (3.9)$$

where \mathbf{U} and \mathbf{V} have to satisfy the orthonormality requirement:

$$\mathbf{U}^T\mathbf{U} = \mathbf{V}^T\mathbf{V} = \mathbf{I} \quad (3.10)$$

with \mathbf{I} as the identity matrix. The singular values are equal to the square-roots of the eigenvalues of $\mathbf{K}^T\mathbf{K}$ (if $m \geq n$, or of $\mathbf{K}\mathbf{K}^T$, if $n \geq m$). If \mathbf{K} is of full rank, i. e. $p = \min(m, n)$, its singular values are all > 0 , which yields a generalized inverse of:

$$\mathbf{K}^{-g} = \mathbf{V}\mathbf{\Lambda}^{-1}\mathbf{U}^T, \quad (3.11)$$

where the diagonal elements of $\mathbf{\Lambda}^{-1}$ are simply the reciprocals of the singular values.

If \mathbf{K} is rank deficient, there are singular values which equal zero, introducing an infinity problem in $\mathbf{\Lambda}^{-1}$ ($1/\lambda_i = 1/0$), which is therefore undefined. In SVD this problem is solved by replacing those values of $1/\lambda_i$ which are infinite with $1/\lambda_i = 0$ establishing a truncated matrix $\mathbf{\Lambda}^{-g}$. Hence, the generalized inverse of the mixed determined problem of Equation 3.5 can be written as:

$$\mathbf{x}_{retr} = \mathbf{V}\mathbf{\Lambda}^{-g}\mathbf{U}^T\mathbf{y}. \quad (3.12)$$

Using SVD opens up the possibility of a clear diagnosis of the problem. Therefore a so called *condition number* of a matrix is defined as the ratio of the largest of the λ_i 's to the smallest λ_i . A problem is singular if its condition number is infinite, and it is *ill-conditioned* if its condition number is too large, i. e. the reciprocal approaches the machine's floating point precision (10^{-6} for single precision, or 10^{-12} for double precision; see [Press et al. (1992)]). Having an ill-posed problem it is thus appropriate to use a truncated SVD solution even for $\lambda_i \approx 0$ – typically if $\lambda_{max}/\lambda_{min} > \sim 10^3$ – since the very small singular values introduce an intolerably high error amplification in applying the inverse mapping to the measurement vector.

3.2.3 Optimal Estimation

In case of an ill-conditioned problem it is generally unavoidable to incorporate additional *a priori* information to get a meaningful result. A consistent theoretical framework to do this in a transparent and explicit manner is provided by the *Bayesian approach* leading to the *optimal estimation* algorithm:

$$\mathbf{x}_{retr} = \mathbf{x}_{ap} + \mathbf{S}_{retr}\mathbf{K}^T\mathbf{S}_\epsilon^{-1}(\mathbf{y} - \mathbf{K}\mathbf{x}_{ap}), \quad (3.13)$$

where \mathbf{x}_{ap} is the *a priori* state vector, \mathbf{S}_ϵ is the measurement error covariance Matrix, and \mathbf{S}_{retr} , the retrieval error covariance matrix is given by:

$$\mathbf{S}_{retr} = (\mathbf{K}^T \mathbf{S}_\epsilon^{-1} \mathbf{K} + \mathbf{S}_{ap}^{-1})^{-1}, \quad (3.14)$$

where \mathbf{S}_{ap} is the *a priori* error covariance matrix. As implied in the retrieval algorithm (with the presence of the measurement error covariance matrix) we are no longer dealing with a system without errors, but we are assuming measurement errors in this case. Hence, the forward modeling Equation 3.4, inverted by the optimal estimation algorithm expands into the form:

$$\mathbf{y} = \mathbf{K}\mathbf{x} + \epsilon, \quad (3.15)$$

where ϵ is the (random) error vector.

A detailed description of the Bayesian approach and a derivation of optimal estimation algorithms, mostly based on [Rodgers (2000)], is given in the section 3.3.

3.2.4 Other Methods

The methods described above are designed to solve linear problems, but for many cases this can not be assumed. The particular algorithm used to treat non-linear problems depends on the degree of non-linearity of the problem (a method to detect the degree of non-linearity is presented in [Rodgers (2000)]). A way to deal with e. g. moderately non-linear problems is the *iterative optimal estimation* algorithm – also called the *Gauss-Newton* scheme – which is described in section 3.3, too:

$$\mathbf{x}_{i+1} = \mathbf{x}_{ap} + \mathbf{S}_i \mathbf{K}_i^T \mathbf{S}_\epsilon^{-1} [(\mathbf{y} - \mathbf{y}_i) + \mathbf{K}_i(\mathbf{x}_i - \mathbf{x}_{ap})], \quad (3.16)$$

where the subscript i is the iteration index, and $\mathbf{y}_i = \mathbf{f}(\mathbf{x}_i)$, i. e. the forward model evaluated for the i -th iteration. The iterative retrieval error covariance Matrix \mathbf{S}_i can be written as:

$$\mathbf{S}_i = [\mathbf{S}_{ap}^{-1} + \mathbf{K}_i^T \mathbf{S}_\epsilon^{-1} \mathbf{K}_i]^{-1}. \quad (3.17)$$

Dependent on the quality of the used *a priori* profile, the first or the first two steps may need special aid with convergence due to linearization errors, which is often dealt with in extending the Gauss-Newton scheme to the Levenberg-Marquardt scheme [Rodgers (2000), Rieder and Kirchengast (1999)], which is a solution of second order to the non-linear least-square problem (see e. g. [Rodgers (2000), Press et al. (1992)]). Applying the Levenberg-Marquardt solution to the Gauss-Newton method yields:

$$\mathbf{x}_{i+1} = \mathbf{x}_i + (\mathbf{S}_{ap}^{-1} + \mathbf{K}_i^T \mathbf{S}_\epsilon^{-1} \mathbf{K}_i + \gamma_i \mathbf{D})^{-1} \{ \mathbf{K}_i^T \mathbf{S}_\epsilon^{-1} [\mathbf{y} - \mathbf{y}_i] - \mathbf{S}_{ap}^{-1} [\mathbf{x}_i - \mathbf{x}_{ap}] \}, \quad (3.18)$$

where γ_i is the step size and \mathbf{D} is a scaling matrix (e. g., $\mathbf{D} = \mathbf{S}_{ap}^{-1}$).

A more simple but often equivalently effective extension was introduced by [Liu *et al.* (2000)] termed the "D-rad" method. It is used in the current study and described in detail in chapter 5.

A comparatively new method which is used for the operational inversion of the IASI data is the *Neural Network* approach. An introduction to this scheme is, e. g., given by [Hastie *et al.* (2001)], whereas an application of neural network algorithm to the IASI data, preparing a joint temperature, humidity, and ozone profile retrieval is presented by [Aires *et al.* (2002)].

3.3 The Optimal Estimation Principle

3.3.1 The Bayesian Approach

Since we have to assume real measurements to be *noisy*, which means that they are subject to experimental errors, useful retrieval algorithms have to include such uncertainties. A very helpful and general way of dealing with noisy inverse problems is the *Bayesian* approach, where some prior knowledge (or expectation) of a special quantity is combined with new information. In particular, *Bayes' theorem* tells us, how an imperfect measurement (resulting from experimental errors), quantified by a *probability density function* (pdf) maps into the state space and is there combined with an also imperfect prior knowledge, which is quantified by a pdf, too.

A pdf is a scalar-valued function depending, in our case, on state and measurement vector, respectively. Let us start by defining:

- $P(\mathbf{x})$ as the prior pdf of the state \mathbf{x} . Hence, the quantity $P(\mathbf{x})d\mathbf{x}$ (with $d\mathbf{x}$ being a short form for: $dx_1 \cdot \dots \cdot dx_n$) is the probability, before performing the measurement that \mathbf{x} lies in the range $(\mathbf{x}, \mathbf{x} + d\mathbf{x})$. $P(\mathbf{x})$ is normalized to 1: $\int P(\mathbf{x})d\mathbf{x} = 1$.
- $P(\mathbf{y})$ as the prior pdf of the measurement with a similar meaning and normalization. $P(\mathbf{y})$ is therefore the pdf of the measurement *before it is made*.
- $P(\mathbf{x}, \mathbf{y})$ as the combined prior pdf of \mathbf{x} and \mathbf{y} , meaning that $P(\mathbf{x}, \mathbf{y})d\mathbf{x}d\mathbf{y}$ is the probability that \mathbf{x} lies in the interval $(\mathbf{x}, \mathbf{x} + d\mathbf{x})$ and \mathbf{y} lies in $(\mathbf{y}, \mathbf{y} + d\mathbf{y})$.
- $P(\mathbf{y}|\mathbf{x})$ as the conditional pdf of \mathbf{y} for a given \mathbf{x} , meaning that $P(\mathbf{y}|\mathbf{x})d\mathbf{y}$ is the probability that \mathbf{y} lies in the range $(\mathbf{y}, \mathbf{y} + d\mathbf{y})$ when \mathbf{x} has a given value.
- $P(\mathbf{x}|\mathbf{y})$ as the conditional pdf of \mathbf{x} for a given \mathbf{y} , meaning that $P(\mathbf{x}|\mathbf{y})d\mathbf{x}$ is the probability that \mathbf{x} lies in the range $(\mathbf{x}, \mathbf{x} + d\mathbf{x})$ when \mathbf{y} has a given value.

Evaluating this quantitatively, we can say that $P(\mathbf{x})$ is given by the integral of the

combined prior pdf, $P(\mathbf{x}, \mathbf{y})$, over all values of \mathbf{y} :

$$P(\mathbf{x}) = \int_{-\infty}^{\infty} P(\mathbf{x}, \mathbf{y}) d\mathbf{y}, \quad (3.19)$$

and $P(\mathbf{y})$ is found likewise. The conditional pdf, $P(\mathbf{x}|\mathbf{y})$, is proportional to the values of $P(\mathbf{x}, \mathbf{y})$ as a function of \mathbf{x} for a given value of \mathbf{y} . The proportionality constant is set in a way that $\int P(\mathbf{x}|\mathbf{y}) d\mathbf{x} = 1$:

$$P(\mathbf{x}|\mathbf{y}) = \frac{P(\mathbf{x}, \mathbf{y})}{\int P(\mathbf{x}, \mathbf{y}) d\mathbf{x}} = \frac{P(\mathbf{x}, \mathbf{y})}{P(\mathbf{y})} \quad (3.20)$$

Equivalent arguments can be used to show that $P(\mathbf{y}|\mathbf{x}) = P(\mathbf{x}, \mathbf{y})/P(\mathbf{x})$. By eliminating the combined prior pdf we obtain *Bayes' theorem* as the relationship between the two different conditional pdf's (see [Rodgers (2000)]):

$$\boxed{P(\mathbf{x}|\mathbf{y}) = \frac{P(\mathbf{y}|\mathbf{x})P(\mathbf{x})}{P(\mathbf{y})}} \quad (3.21)$$

$P(\mathbf{x}|\mathbf{y})$ is the posteriori pdf of the state for a given measurement. What we want to update with the measurements is the prior knowledge $P(\mathbf{x})$ of the state. To get $P(\mathbf{y}|\mathbf{x})$, which describes the knowledge of \mathbf{y} that would be obtained if the state were \mathbf{x} , we only need the forward model and the statistical description of the measurement error. The only remaining quantity is the denominator, $P(\mathbf{y})$, which formally can be obtained by integrating $P(\mathbf{x}, \mathbf{y})$ (i. e. $P(\mathbf{y}|\mathbf{x})P(\mathbf{x})$) over all \mathbf{x} . In practice, this is only a normalizing factor which is often not needed.

Bayes' theorem gives us a conceptual approach for solving the inverse problem:

- Before performing a measurement we have prior knowledge of the state expressed by a prior pdf.
- The process of measuring is expressed by a forward model which maps the state space into the measurement space.
- With Bayes' theorem we have a formalism to invert the mapping and calculate a posterior pdf by updating the prior pdf with a measurement pdf.

3.3.2 Optimal Linear Inversion with Gaussian Statistics

In this subsection we want to illustrate the Bayesian approach for a linear problem,

$$\mathbf{y} = \mathbf{K}\mathbf{x} + \boldsymbol{\epsilon}, \quad (3.22)$$

(definitions of the dimensions of the vectors and the matrix see subsection 3.1.1) with Gaussian (normal) distributed pdf's[†]:

$$P(\mathbf{x}) = \frac{1}{(2\pi)^{n/2} |\mathbf{S}_x|^{1/2}} \exp \left\{ -\frac{1}{2} (\mathbf{x} - \hat{\mathbf{x}})^T \mathbf{S}_x^{-1} (\mathbf{x} - \hat{\mathbf{x}}) \right\}, \quad (3.23)$$

where \mathbf{S}_x is of dimension $n \times n$ and has to be non-singular (the meaning of a singular \mathbf{S}_x is that there are components which are known exactly). The maximum probability value for \mathbf{x} equals the expected value, $E[\mathbf{x}] = \hat{\mathbf{x}}$, because the distribution is symmetric about $\mathbf{x} = \hat{\mathbf{x}}$. In general, \mathbf{S}_x is defined as:

$$\mathbf{S}_x = E \left[(\mathbf{x} - E[\mathbf{x}]) (\mathbf{x} - E[\mathbf{x}])^T \right] = E \left[(\mathbf{x} - \hat{\mathbf{x}}) (\mathbf{x} - \hat{\mathbf{x}})^T \right], \quad (3.24)$$

where E denotes the expectation value operator.

With the assumption of normal distributed (unbiased) errors:

$$E[\boldsymbol{\epsilon}] = 0, \quad (3.25)$$

the mean of the measurements can be evaluated to:

$$E[\mathbf{y}] = E[\mathbf{K}\mathbf{x} + \boldsymbol{\epsilon}] = \mathbf{K}\mathbf{x} + E[\boldsymbol{\epsilon}] = \mathbf{K}\mathbf{x}, \quad (3.26)$$

and thus, the covariance Matrix of the measurement reads:

$$E[(\mathbf{y} - \mathbf{K}\mathbf{x})(\mathbf{y} - \mathbf{K}\mathbf{x})^T] = E[\boldsymbol{\epsilon}\boldsymbol{\epsilon}^T] = \mathbf{S}_\epsilon. \quad (3.27)$$

The next step is to obtain the pdf of \mathbf{y} conditioned on \mathbf{x} (i. e. the description of the forward model):

$$P(\mathbf{y}|\mathbf{x}) = \frac{1}{(2\pi)^{m/2} |\mathbf{S}_\epsilon|^{1/2}} \exp \left\{ -\frac{1}{2} (\mathbf{y} - \mathbf{K}\mathbf{x})^T \mathbf{S}_\epsilon^{-1} (\mathbf{y} - \mathbf{K}\mathbf{x}) \right\}. \quad (3.28)$$

Finally, the statistical models for \mathbf{x} and \mathbf{y} – $P(\mathbf{x})$ and $P(\mathbf{y})$ – are required. Therefore, let \mathbf{x}_{ap} be an estimate of the normally distributed \mathbf{x} before the measurements were performed. *a priori* mean and *a priori* error covariance matrix are then defined as:

$$E[\mathbf{x}] = \mathbf{x}_{ap}, \quad (3.29)$$

$$E[(\mathbf{x} - \mathbf{x}_{ap})(\mathbf{x} - \mathbf{x}_{ap})^T] = \mathbf{S}_{ap}. \quad (3.30)$$

Thus the prior knowledge of \mathbf{x} is described by:

$$P(\mathbf{x}) = \frac{1}{(2\pi)^{n/2} |\mathbf{S}_{ap}|^{1/2}} \exp \left\{ -\frac{1}{2} (\mathbf{x} - \mathbf{x}_{ap})^T \mathbf{S}_{ap}^{-1} (\mathbf{x} - \mathbf{x}_{ap}) \right\}. \quad (3.31)$$

[†]For modeling pdf's the Gaussian distribution is commonly used since many processes are well described by it and because it is algebraically convenient.

We find by definition, that the error $\mathbf{x} - \mathbf{x}_{ap}$ committed by using \mathbf{x}_{ap} as an estimate of \mathbf{x} before the measurements are taken is unbiased, and that the covariance equals the state *a priori* error covariance matrix given in Equation 3.30. Furthermore, the quantity $\mathbf{K}\mathbf{x}_{ap}$ can be regarded as a measurement prediction before the measurements are taken:

$$E[\mathbf{y}] = E[\mathbf{K}\mathbf{x} + \boldsymbol{\epsilon}] = \mathbf{K}E[\mathbf{x}] + E[\boldsymbol{\epsilon}] = \mathbf{K}\mathbf{x}_{ap}. \quad (3.32)$$

The associated prior measurement error covariance matrix can be evaluated according to:

$$\begin{aligned} \mathbf{S}_{\epsilon,ap} &= E[(\mathbf{y} - \mathbf{K}\mathbf{x}_{ap})(\mathbf{y} - \mathbf{K}\mathbf{x}_{ap})^T] \\ &= E[(\mathbf{K}\mathbf{x} + \boldsymbol{\epsilon} - \mathbf{K}\mathbf{x}_{ap})(\mathbf{K}\mathbf{x} + \boldsymbol{\epsilon} - \mathbf{K}\mathbf{x}_{ap})^T] \\ &= \mathbf{K}^T E[(\mathbf{x} - \mathbf{x}_{ap})(\mathbf{x} - \mathbf{x}_{ap})^T] \mathbf{K} + E[\boldsymbol{\epsilon}\boldsymbol{\epsilon}^T] \\ &= \mathbf{K}^T \mathbf{S}_{ap} \mathbf{K} + \mathbf{S}_{\epsilon}, \end{aligned} \quad (3.33)$$

and therefore the pdf of the predicted measurements reads:

$$P(\mathbf{y}) = \frac{1}{(2\pi)^{m/2} |\mathbf{S}_{\epsilon,ap}|^{1/2}} \exp \left\{ -\frac{1}{2} (\mathbf{y} - \mathbf{K}\mathbf{x}_{ap})^T \mathbf{S}_{\epsilon,ap}^{-1} (\mathbf{y} - \mathbf{K}\mathbf{x}_{ap}) \right\} \quad (3.34)$$

Again the error $\mathbf{y} - \mathbf{K}\mathbf{x}_{ap}$ committed by the estimate $\mathbf{K}\mathbf{x}_{ap}$ of \mathbf{y} prior to the measurements is unbiased, and hence the error $\mathbf{y} - \mathbf{K}\mathbf{x}_{ap}$ and the measurement vector \mathbf{y} are sharing the same covariance, $\mathbf{S}_{\epsilon,ap}$ (c. f. Equation 3.33).

Substituting now the Equations 3.28, 3.31, and 3.34 for $P(\mathbf{y}|\mathbf{x})$, $P(\mathbf{x})$, and $P(\mathbf{y})$, respectively, into Bayes' theorem (Equation 3.21) we obtain the posterior pdf, which corresponds to the estimate of the state after the measurements have been taken:

$$P(\mathbf{x}|\mathbf{y}) = A \exp \left\{ -\frac{1}{2} \left[(\mathbf{y} - \mathbf{K}\mathbf{x})^T \mathbf{S}_{\epsilon}^{-1} (\mathbf{y} - \mathbf{K}\mathbf{x}) + (\mathbf{x} - \mathbf{x}_{ap})^T \mathbf{S}_{ap}^{-1} (\mathbf{x} - \mathbf{x}_{ap}) - (\mathbf{y} - \mathbf{K}\mathbf{x}_{ap})^T \mathbf{S}_{\epsilon,ap}^{-1} (\mathbf{y} - \mathbf{K}\mathbf{x}_{ap}) \right] \right\}, \quad (3.35)$$

with:

$$A = \frac{|\mathbf{S}_{\epsilon,ap}|^{1/2}}{(2\pi)^{n/2} |\mathbf{S}_{\epsilon}|^{1/2} |\mathbf{S}_{ap}|^{1/2}} = \frac{|\mathbf{K}^T \mathbf{S}_{ap} \mathbf{K} + \mathbf{S}_{\epsilon}|^{1/2}}{(2\pi)^{n/2} |\mathbf{S}_{\epsilon}|^{1/2} |\mathbf{S}_{ap}|^{1/2}}. \quad (3.36)$$

Since we are assuming Gaussian distributions, $P(\mathbf{x}|\mathbf{y})$ should also satisfy:

$$P(\mathbf{x}|\mathbf{y}) = \frac{1}{(2\pi)^{n/2} |\hat{\mathbf{S}}|^{1/2}} \exp \left\{ -\frac{1}{2} (\mathbf{x} - \hat{\mathbf{x}})^T \hat{\mathbf{S}}^{-1} (\mathbf{x} - \hat{\mathbf{x}}) \right\}, \quad (3.37)$$

where $P(\mathbf{x}|\mathbf{y})$ is completely specified by its mean, representing the optimal estimate, and by the associated estimation (or retrieval) error covariance matrix:

$$E[\mathbf{x}] = \hat{\mathbf{x}} \quad (3.38)$$

$$\hat{\mathbf{S}} = E[(\mathbf{x} - \hat{\mathbf{x}})(\mathbf{x} - \hat{\mathbf{x}})^T]. \quad (3.39)$$

Comparing the factor A from Equation 3.36 with the fraction preceding the exponential function in Equation 3.37 we obtain a representation for the retrieval error covariance matrix:

$$\begin{aligned}\hat{\mathbf{S}} &= \mathbf{S}_\epsilon \mathbf{S}_{ap} (\mathbf{K}^T \mathbf{S}_{ap} \mathbf{K} + \mathbf{S}_\epsilon)^{-1} \\ &= (\mathbf{K}^T \mathbf{S}_\epsilon^{-1} \mathbf{K} + \mathbf{S}_{ap}^{-1})^{-1}.\end{aligned}\quad (3.40)$$

It should be mentioned that another form of the retrieval error covariance matrix which will be used in subsection 5.2.1 reads as follows:

$$\hat{\mathbf{S}} = \mathbf{S}_{ap} - \mathbf{S}_{ap} \mathbf{K}^T (\mathbf{K}^T \mathbf{S}_{ap} \mathbf{K} + \mathbf{S}_\epsilon)^{-1} \mathbf{K} \mathbf{S}_{ap}.\quad (3.41)$$

On the other hand, the comparison of the two exponential terms of the Equations 3.35 and 3.37 and the usage of Equation 3.40 is resulting in:

$$\begin{aligned}\hat{\mathbf{x}} &= (\mathbf{K}^T \mathbf{S}_\epsilon^{-1} \mathbf{K} + \mathbf{S}_{ap}^{-1})^{-1} (\mathbf{K}^T \mathbf{S}_\epsilon^{-1} \mathbf{y} + \mathbf{S}_{ap}^{-1} \mathbf{x}_{ap}) \\ &= \mathbf{x}_{ap} + (\mathbf{K}^T \mathbf{S}_\epsilon^{-1} \mathbf{K} + \mathbf{S}_{ap}^{-1})^{-1} \mathbf{K}^T \mathbf{S}_\epsilon^{-1} (\mathbf{y} - \mathbf{K} \mathbf{x}_{ap}) \\ &= \mathbf{x}_{ap} + \hat{\mathbf{S}} \mathbf{K}^T \mathbf{S}_\epsilon^{-1} (\mathbf{y} - \mathbf{K} \mathbf{x}_{ap}),\end{aligned}\quad (3.42)$$

where we have used the identity $\mathbf{S}_{ap}^{-1} = \hat{\mathbf{S}}^{-1} - \mathbf{K}^T \mathbf{S}_\epsilon^{-1} \mathbf{K}$ (see Equation 3.40)[‡]. The difference $\mathbf{y} - \mathbf{K} \mathbf{x}_{ap}$ between the measurement and the estimate of the measurement is often termed *residual*.

Note that the Bayesian solution to the inverse problem is not $\hat{\mathbf{x}}$, but it is the Gaussian pdf $P(\mathbf{x}|\mathbf{y})$, of which $\hat{\mathbf{x}}$ is the expected state – even the most likely state since for a Gaussian distribution conditional mean and conditional mode are the same – and $\hat{\mathbf{S}}$ is the covariance. Note further, that $\hat{\mathbf{x}}$ is a linear function of the prior information and the measurements (what was expectable for a linear problem) and also the inverse covariance matrix $\hat{\mathbf{S}}^{-1}$ is a linear function of the inverse prior and measurement error covariances.

The quantity $\boldsymbol{\epsilon} = (\mathbf{x} - \hat{\mathbf{x}})$, the error committed in using $\hat{\mathbf{x}}$ as an estimate of the true state \mathbf{x} , is again normally distributed with zero mean:

$$E[\boldsymbol{\epsilon}] = E[\mathbf{x} - \hat{\mathbf{x}}] = E[\mathbf{x}] - \hat{\mathbf{x}} = \hat{\mathbf{x}} - \hat{\mathbf{x}} = 0,\quad (3.45)$$

[‡]The result given by Equations 3.40 and 3.42 can be obtained by various other methods. One of them is the minimization of a cost function in a Bayesian manner using the following cost function with an arbitrary positive semi-definite matrix \mathbf{S} :

$$J = \int_{-\infty}^{\infty} (\mathbf{x} - \hat{\mathbf{x}})^T \mathbf{S} (\mathbf{x} - \hat{\mathbf{x}}) P(\mathbf{x}|\mathbf{y}) d\mathbf{x},\quad (3.43)$$

which constitutes the expectation space of $(\mathbf{x} - \hat{\mathbf{x}})^T \mathbf{S} (\mathbf{x} - \hat{\mathbf{x}})$. Optimization of this cost function, i. e. $\partial J / \partial \mathbf{x} = 0$, yields:

$$\hat{\mathbf{x}} = \int_{-\infty}^{\infty} \mathbf{x} P(\mathbf{x}|\mathbf{y}) d\mathbf{x},\quad (3.44)$$

which is the expectation value or mean of \mathbf{x} . Evaluating Equation 3.44 we obtain the same result as Equation 3.42 [Gelb (1974)]. Since \mathbf{S} is arbitrary, the identity matrix can be chosen for it and we can rewrite J to the form $J = E[(\mathbf{x} - \hat{\mathbf{x}})(\mathbf{x} - \hat{\mathbf{x}})^T] = \text{trace}[\hat{\mathbf{S}}]$. Minimizing the trace of $\hat{\mathbf{S}}$ we find that the minimum variance estimate is just the conditional mean as described by Equation 3.42.

and its covariance equals the covariance of the state \mathbf{x} itself, i. e. the covariance $\hat{\mathbf{S}}$, given by the Equations 3.39 and 3.40.

If we do not consider any prior information, Equation 3.42 reduces to the standard weighted least-squares estimate:

$$\hat{\mathbf{x}} = (\mathbf{K}^T \mathbf{S}_\epsilon \mathbf{K})^{-1} \mathbf{K}^T \mathbf{S}_\epsilon^{-1} \mathbf{y}, \quad (3.46)$$

and to the form of Equation 3.8 of subsection 3.2.1 if the assumption of no errors was made (i. e. $\mathbf{S}_\epsilon = \mathbf{I}$).

In the literature two different forms of the estimate $\hat{\mathbf{x}}$ are specified depending on the size of the matrix being inverted. Equation 3.42 is known as the n -form ($\hat{\mathbf{S}}^{-1} = (\mathbf{K}^T \mathbf{S}_\epsilon^{-1} \mathbf{K} + \mathbf{S}_{ap}^{-1})$ is of the form $n \times n$ and has to be inverted). If we substitute for $\hat{\mathbf{S}}$ the form given by the first line of Equation 3.40, that is $\hat{\mathbf{S}} = \mathbf{S}_\epsilon \mathbf{S}_{ap} (\mathbf{K}^T \mathbf{S}_{ap} \mathbf{K} + \mathbf{S}_\epsilon)^{-1}$, into the last line of Equation 3.42, we obtain the m -form:

$$\hat{\mathbf{x}} = \mathbf{x}_{ap} + \mathbf{S}_{ap} \mathbf{K}^T (\mathbf{K} \mathbf{S}_{ap} \mathbf{K}^T + \mathbf{S}_\epsilon)^{-1} (\mathbf{y} - \mathbf{K} \mathbf{x}_{ap}). \quad (3.47)$$

where the $m \times m$ matrix $(\mathbf{K} \mathbf{S}_{ap} \mathbf{K}^T + \mathbf{S}_\epsilon)$ has to be inverted (therefore the term m -form).

Characterization Functions

Let us now investigate the above results in detail, and expand them further by deriving characterization functions. We start with looking at the partial derivatives of the inverse model (i. e. the retrieval) with respect to the measurements. The resulting matrix is termed the *gain matrix*, \mathbf{G} (or contribution matrix) and is of dimension $n \times m$:

$$\begin{aligned} \mathbf{G} &\equiv \frac{\partial \hat{\mathbf{x}}}{\partial \mathbf{y}} \\ &= (\mathbf{K}^T \mathbf{S}_\epsilon^{-1} \mathbf{K} + \mathbf{S}_{ap}^{-1})^{-1} \mathbf{K}^T \mathbf{S}_\epsilon^{-1} \\ &= \hat{\mathbf{S}} \mathbf{K}^T \mathbf{S}_\epsilon^{-1}. \end{aligned} \quad (3.48)$$

The columns of \mathbf{G} , termed *gain functions*, give us an understanding how each measurement contributes to the retrieved state. Note that the result of Equation 3.48 represents the n -form of the gain matrix, corresponding to the n -form of the state estimate (c. f. Equation 3.42). The m -form of \mathbf{G} is given by:

$$\mathbf{G} = \mathbf{S}_{ap} \mathbf{K}^T (\mathbf{K} \mathbf{S}_{ap} \mathbf{K}^T + \mathbf{S}_\epsilon)^{-1}. \quad (3.49)$$

Hence, we can rewrite both forms of the state estimate (Equations 3.42 and 3.47) into the following expression:

$$\begin{aligned} \hat{\mathbf{x}} &= \mathbf{x}_{ap} + \mathbf{G} (\mathbf{y} - \mathbf{K} \mathbf{x}_{ap}) \\ &= (\mathbf{I} - \mathbf{G} \mathbf{K}) \mathbf{x}_{ap} + \mathbf{G} \mathbf{y}. \end{aligned} \quad (3.50)$$

The first line indicates that the estimate is the sum of a weighted difference between the actual measurement \mathbf{y} and the prediction of the measurement $\mathbf{K}\mathbf{x}_{ap}$ on the one hand and the *a priori* state estimate \mathbf{x}_{ap} on the other hand. A further analysis of the gain matrix (Equation 3.48 and 3.49, respectively) yields that for very precise measurements (i. e. small \mathbf{S}_ϵ) the gain will be large and according to Equation 3.50 it can be concluded that the measured data contributes more to the estimated state than the prior information. If the reverse happens, i. e., if the uncertainty of \mathbf{x}_{ap} is small (i. e. small \mathbf{S}_{ap}), which reflects an accurate initial guess, while the measurements are uncertain, \mathbf{G} will be small, and therefore the retrieval will depend largely on its prior estimate whereas the influence of the measurements is less.

Other interesting characterization quantities are the partial derivatives of the estimated state with respect to the true state vector. The resulting matrix is called (amongst other terms) the *averaging kernel matrix*, the *model resolution matrix*, the *state resolution matrix*, or the *resolving kernel* (c. f. [Rodgers (2000)]). This $n \times n$ matrix can be evaluated to:

$$\mathbf{A} \equiv \frac{\partial \hat{\mathbf{x}}}{\partial \mathbf{x}} = \mathbf{G}\mathbf{K}, \quad (3.51)$$

with $\hat{\mathbf{x}}$ described by Equation 3.50 and $\mathbf{y} = \mathbf{K}\mathbf{x} + \epsilon$. Hence, Equation 3.50 can be reformulated to:

$$\begin{aligned} \hat{\mathbf{x}} &= (\mathbf{I} - \mathbf{A})\mathbf{x}_{ap} + \mathbf{A}\mathbf{x} + \mathbf{G}\epsilon \\ &= \mathbf{x}_{ap} + \mathbf{A}(\mathbf{x} - \mathbf{x}_{ap}) + \mathbf{G}\epsilon. \end{aligned} \quad (3.52)$$

Similar to the gain matrix the averaging kernel matrix can be evaluated in a n - and a m -form.

The rows of \mathbf{A} , called *averaging kernels*, are reflecting how an element of the true state is reproduced by the estimated state. Assuming an ideal inverse case, all elements of the estimated state originate entirely from the corresponding elements of the true state, i. e. \mathbf{A} would be an identity matrix. Real averaging kernels have of course a peak at the appropriate level of the state vector with a certain FWHM which is a measure of the spatial resolution of the observing system. Hence, the averaging kernels provide a simple characterization of the relationship between the retrieved and the true state.

Given the definitions of the gain function matrix and the averaging kernel matrix it is instructive to decompose the n -form of the retrieval error covariance matrix $\hat{\mathbf{S}}$ into two components of the form:

$$\hat{\mathbf{S}} = (\mathbf{A} - \mathbf{I}_n)\mathbf{S}_{ap}(\mathbf{A} - \mathbf{I}_n)^T + \mathbf{G}\mathbf{S}_\epsilon\mathbf{G}^T, \quad (3.53)$$

with \mathbf{I}_n as the identity matrix of dimension n . The first term on the right-hand-side is the so called smoothing error covariance matrix:

$$\mathbf{S}_s = (\mathbf{A} - \mathbf{I}_n)\mathbf{S}_{ap}(\mathbf{A} - \mathbf{I}_n)^T, \quad (3.54)$$

which expresses the contribution of the *a priori* error to $\hat{\mathbf{S}}$. The second one is the measurement-based covariance matrix:

$$\mathbf{S}_m = \mathbf{G}\mathbf{S}_\epsilon\mathbf{G}^T, \quad (3.55)$$

representing the contribution of the measurement errors.

The last characterization function which will be mentioned here is the signal-to-noise ratio (SNR) given by the SNR matrix defined by:

$$\tilde{\mathbf{K}} \equiv \mathbf{S}_\epsilon^{-\frac{1}{2}} \mathbf{K} \mathbf{S}_{ap}^{\frac{1}{2}}, \quad (3.56)$$

where the diagonal elements of $\tilde{\mathbf{K}}$ estimate the SNR profile associated with $\hat{\mathbf{x}}$ and its rows, the so-called SNR functions, indicate the relative influence of measurement and *a priori* uncertainties at different height levels, respectively. More thoroughly exploited, the number of singular values of $\tilde{\mathbf{K}}$ greater than about unity expresses the effective number of independent measurements made to be better than the measurement noise level.

3.3.3 Optimal Non-Linear Inversion

Since in general a linear inverse problem is one in which the cost function is quadratic in the state vector (see footnote on page 63), which leads to linear Equations when optimizing it, a non-linear problem consists not only of the issue of a non-linear forward model. Even a non-quadratic term resulting from some prior constraints would lead to a non-linear problem in the case of a linear forward model. A further reason for a non-linear problem would be a non-Gaussian pdf as prior information.

We are dealing here with a forward model \mathbf{f} , which is a non-linear mapping of the state space into the measurement space with an uncertainty described by the measurement error ϵ which in our case is assumed to be Gaussian:

$$\mathbf{y} = \mathbf{f}(\mathbf{x}) + \epsilon, \quad (3.57)$$

(see also section 3.1.1). Of course there can still be a null space resulting from the possibility of a non-unique mapping. However, since in contrast to the linear case the weighting function matrix \mathbf{K} depends on the state itself, the basis of the null space is not the same within the whole measurement space, but it is depending itself on the state.

If the inverse problem is no worse than moderately non-linear[§], and the measurement error is Gaussian as it is assumed here, the retrieval error will be Gaussian and we can

[§]An inverse problem can be classified according to its degree of linearity (see e. g. [Rodgers (2000)]):

- *Linear*: If the forward model is linear, i. e. $\mathbf{y} = \mathbf{K}\mathbf{x}$, and any prior information is Gaussian.
- *Nearly linear*: Non linear problems for which a linearization about some prior state is adequate to find a solution. Problems which are linear to the accuracy of the measurements, or to the required accuracy of the solution.
- *Moderately non-linear*: These are problems where the linearization is adequate for the error analysis but not for finding the solution.
- *Grossly non-linear*: The rest, which means problems which are non-linear even within the range of the errors. An extreme example for that would be any problem involving clouds such as the important question of sounding the troposphere in the nadir view with infrared instruments, e. g., IASI in cloudy situations. Situations which are regarded as grossly non-linear are skipped here, since we will consider only clear sky inversions of IASI measurements.

apply the error analysis of the linear case (i. e. using the same definition of the characterization functions).

The Bayesian solution for the non-linear problem can be derived straightforwardly from the linear case (Equations 3.22 to 3.35), with the modification that the forward model is now a general function of the state, the measurement error is once more Gaussian, and there is a prior estimate with Gaussian errors:

$$P(\mathbf{x}|\mathbf{y}) = A \exp \left\{ -\frac{1}{2} \left[(\mathbf{y} - \mathbf{f}(\mathbf{x}))^T \mathbf{S}_\epsilon^{-1} (\mathbf{y} - \mathbf{f}(\mathbf{x})) + (\mathbf{x} - \mathbf{x}_{ap})^T \mathbf{S}_{ap}^{-1} (\mathbf{x} - \mathbf{x}_{ap}) \right] \right\}, \quad (3.58)$$

with:

$$A = \frac{1}{(2\pi)^{n/2} |\mathbf{S}_\epsilon|^{1/2} |\mathbf{S}_{ap}|^{1/2}}. \quad (3.59)$$

Here the normalization factor $P(\mathbf{y})$ of Bayes' rule, Equation 3.21, has been omitted for convenience.

To find the state of maximum probability we use another method than given in subsection 3.3.2, namely the so called *maximum likelihood* method. It is based on the maximization of a likelihood function L , which is typically chosen to be the natural logarithm of the conditional probability of \mathbf{x} for a given \mathbf{y} , $P(\mathbf{x}|\mathbf{y})$, described by Equation 3.58:

$$\begin{aligned} L &= -2 \ln P(\mathbf{x}|\mathbf{y}) \\ &= \left[(\mathbf{y} - \mathbf{f}(\mathbf{x}))^T \mathbf{S}_\epsilon^{-1} (\mathbf{y} - \mathbf{f}(\mathbf{x})) + (\mathbf{x} - \mathbf{x}_{ap})^T \mathbf{S}_{ap}^{-1} (\mathbf{x} - \mathbf{x}_{ap}) \right] + \ln(A). \end{aligned} \quad (3.60)$$

To maximize it we have to set $\nabla_{\mathbf{x}} L(\mathbf{x})$ to zero:

$$\begin{aligned} \mathbf{g}(\mathbf{x}) &\equiv \nabla_{\mathbf{x}} L(\mathbf{x}) = \\ &= - \left[\nabla_{\mathbf{x}} \mathbf{f}(\mathbf{x}) \right]^T \mathbf{S}_\epsilon^{-1} (\mathbf{y} - \mathbf{f}(\mathbf{x})) + \mathbf{S}_{ap}^{-1} (\mathbf{x} - \mathbf{x}_{ap}) = \\ &= - \mathbf{K}^T \mathbf{S}_\epsilon^{-1} (\mathbf{y} - \mathbf{f}(\mathbf{x})) + \mathbf{S}_{ap}^{-1} (\mathbf{x} - \mathbf{x}_{ap}) \stackrel{!}{=} 0, \end{aligned} \quad (3.61)$$

where $\mathbf{K} = \nabla_{\mathbf{x}} \mathbf{f}(\mathbf{x})$. The difficulty involved in this Equation roots mainly in the non-linearity of the forward model. If it is not too non-linear a typical method to find the zeros of a function is Newtonian iterations [Rodgers (2000)]. For a general vector Equation, $\mathbf{g}(\mathbf{x}) = 0$, the iterative solution is analogous to Newton's method for the scalar case, and hence yields:

$$\mathbf{x}_{i+1} = \mathbf{x}_i - \left[\nabla_{\mathbf{x}} \mathbf{g}(\mathbf{x}_i) \right]^{-1} \mathbf{g}(\mathbf{x}_i) \quad (3.62)$$

Using the middle part of Equation 3.61 the derivative of $\mathbf{g}(\mathbf{x}_i)$ can be evaluated as:

$$\nabla_{\mathbf{x}} \mathbf{g}(\mathbf{x}) = - \left[\nabla_{\mathbf{x}} \mathbf{K}^T(\mathbf{x}) \right] \mathbf{S}_\epsilon^{-1} (\mathbf{y} - \mathbf{f}(\mathbf{x})) + \mathbf{K}^T \mathbf{S}_\epsilon^{-1} \mathbf{K} + \mathbf{S}_{ap}^{-1}. \quad (3.63)$$

This represents the *Hessian* of the maximum likelihood function, i. e., the matrix of second derivatives of L with respect to \mathbf{x} .

Looking at Equation 3.63 in detail it can be recognized that it involves the Jacobian \mathbf{K} (first derivative of the forward model \mathbf{f}) and $\nabla_{\mathbf{x}} \mathbf{K}^T$, the second derivative of \mathbf{f} (the Hessian of the forward model). The latter is a complicated object in the majority of cases. But a further investigation of the first term of equation 3.63 shows that it can be ignored in many situations, especially when the product of the noise (modeled by \mathbf{S}_ϵ) and the non-linearity (described by the residual, $[\mathbf{y} - \mathbf{f}(\mathbf{x})]$), is small, what is the case for moderately non-linear problems. Note that both, non-linearity and noise contribute to the size of this term.

Doing so (means, ignoring the term with the Hessian) and substituting the Equations 3.61 and 3.63 into the Newtonian iteration, 3.62, gives the *Gauss-Newton* method:

$$\mathbf{x}_{i+1} = \mathbf{x}_i + (\mathbf{K}_i^T \mathbf{S}_\epsilon^{-1} \mathbf{K}_i + \mathbf{S}_{ap}^{-1})^{-1} [\mathbf{K}_i^T \mathbf{S}_\epsilon^{-1} (\mathbf{y} - \mathbf{f}(\mathbf{x}_i)) - \mathbf{S}_{ap}^{-1} (\mathbf{x}_i - \mathbf{x}_{ap})], \quad (3.64)$$

which, after some rearrangements, results in:

$$\mathbf{x}_{i+1} = \mathbf{x}_{ap} + \mathbf{S}_i \mathbf{K}_i^T \mathbf{S}_\epsilon^{-1} [(\mathbf{y} - \mathbf{y}_i) - \mathbf{K}_i (\mathbf{x}_{ap} - \mathbf{x}_i)], \quad (3.65)$$

with:

$$\mathbf{y}_i = \mathbf{f}(\mathbf{x}_i) \quad \text{and:} \quad \mathbf{S}_i = (\mathbf{K}_i^T \mathbf{S}_\epsilon^{-1} \mathbf{K}_i + \mathbf{S}_{ap}^{-1})^{-1}. \quad (3.66)$$

It is convenient, but of course not necessary, to start the iteration with $\mathbf{x}_0 = \mathbf{x}_{ap}$.

So far we have found an algorithm which provides a state estimate \mathbf{x}_i for moderately non-linear problems by combining new measurement data \mathbf{y} with an initial state estimate \mathbf{x}_{ap} . The convergence criteria used to determine the number of iterations is introduced in subsection 5.1.1. These results combined with the characterization functions derived in the linear part, which are valid even for moderately non-linear problems, as mentioned above, are the basic equations used in the current study.

Chapter 4

The Fast Radiative Transfer Model RTIASI

4.1 General Considerations on Modeling Atmospheric Radiances

According to section 1.4 atmospheric constituents are absorbing and emitting electromagnetic radiation at the same specific wavelengths λ . The intensity of the radiation depends on the temperature T of the emitting gas according to the Planck function:

$$B_\lambda(T) = \frac{2hc^2}{\lambda^5(e^{hc/\lambda kT} - 1)}, \quad (4.1)$$

or in terms of the wavenumber ν ($\lambda\nu = 1$; $\lambda d\nu + \nu d\lambda = 0$):

$$B_\nu(T) = \frac{2hc^2\nu^3}{(e^{h\nu/kT} - 1)}. \quad (4.2)$$

The radiances I_ν , measured on-board of meteorological satellites, which are constituting the real solution of the radiative transfer equation at a specific wavenumber ν in pressure coordinates p (which is the used grid in the fast radiative transfer model RTIASI) is given by (c. f. Equation 1.49):

$$I_\nu = B_\nu(p_s)T_\nu(p_s) + \int_{p_s}^0 B_\nu(T(p))W_\nu(p)d(\ln p), \quad (4.3)$$

where p_s is the surface pressure*. $W_\nu(p)$ are the atmospheric weighting functions (to distinguish them from the weighting functions used in the inversion, which correspond to

*The measurement can also be specified in terms of the Brightness temperature T_B which is the black-body temperature corresponding to the radiance I_ν :

$$T_B \equiv B_\nu^{-1}(I_\nu) = \frac{h\nu}{k \ln(1 + \frac{2hc^2\nu^3}{I_\nu})}. \quad (4.4)$$

the rows of the matrix obtained by differentiating the forward model with respect to the state vector) in logarithmic scale of the pressure, given by:

$$W_\nu(p) = \frac{\partial T_\nu(p)}{\partial(\ln p)}, \quad (4.5)$$

where $T_\nu(p)$ is the transmittance from level p to the measuring instrument. Equation 4.3 ignores clouds and other absorbers. The term $B_\nu(p_s)T_\nu(p_s)$ constitutes the contribution from the surface. The term weighting functions can be explained by the fact that the radiance equals the Planck function "weighted" by $W_\nu(p)$. This may be understood in such a way that the total measured radiance contains contributions from a range of atmospheric pressure levels and $W_\nu(p)$ gives the relative contribution from each level.

Let us make a deeper look into the equations 4.3 and 4.5. It can be said that the atmospheric parameters are coupled to the measured radiances through the radiative transfer. Of course the information that can be extracted out of the measurements is limited by the complex nature of the transmission process as well as by factors concerning the measurement process including spectral range and resolution, observational geometry and instrumental noise. Nevertheless we can construct a method for the determination of atmospheric parameters: If, e. g., the mixing ratio (intrinsic in the transmittance) of an atmospheric constituent, say CO_2 is well known, temperature as the only unknown can be determined from the measured radiance. If on the other hand the temperature is known, we can obtain the total mass of the absorbing gas.

Performing further a set of measurements $i = 1, \dots, m$ at certain wavenumbers ν_i whose weighting functions cover the whole of the atmosphere sufficiently, profiles of the specific parameter can be derived. Therefore we may rewrite Equation 4.3 for a set of closely space wavenumbers (by ignoring the surface part):

$$I_{\nu_i} = \int_{p_s}^0 B_{\bar{\nu}}(T(p))W_{\nu_i}(p)d(\ln p), \quad (4.6)$$

where $\bar{\nu}$ is a representative wavenumber, implying that the Planck function does not vary much in small spectral intervals. The weighting function curve represents the part of the atmosphere where the upwelling radiance arises and the peak denotes the height of maximum contribution to it. Clearly, measurements near the center of an absorption band contain information from higher levels (according to the treated region of the weighting function) whereas when moving from the center to the wings of the band the contributions are from progressively lower levels. The overlap between the different weighting functions allows the definition of temperature profiles although the radiance data is finite.

The calculation of the radiances can be done by line-by-line transmittance models or by fast transmittance models. The latter have the ability to keep pace with the multitude of observations of the new generations of atmospheric sounders which measure thousands of spectral channels (such as IASI and the Advanced Infrared Sounder (AIRS)).

4.2 Composition of the Fast Radiative Transfer Model RTIASI

The fast transmittance model RTIASI has been developed (and is still being further developed) for studies and exploitation of IASI radiances before the actual launch of the METOP satellite as well as for the development of data assimilation and retrieval algorithms. The following description of the model is mostly based on [Eyre (1991), Matricardi and Saunders (1999), Matricardi (1999)] since the version used in this study is not the newest one. The improvements of the current release, RTIASI-4, are a new scheme for prediction of the water vapor continuum, a refinement of the vertical pressure grid, an inclusion of trace gases such as CO₂, N₂O, CO and CH₄ as profile variables, as well as the introduction of a solar term to evaluate the solar radiance reflected by a land or water surface in a non-scattering atmosphere. A detailed description of the new features and improvements of RTIASI-4 are given in [Matricardi (2003)]. We plan to upgrade to the newest version in the future.

The basic property of RTIASI is that it provides *fast transmittance coefficients* (FTC) which have been computed for a set of atmospheric profiles representing the range of variations in temperature and absorber amount found in the real atmosphere. The model calculates the diverse atmospheric profiles (temperature, humidity, and ozone) on 43 fixed pressure levels, from 0.1 hPa (which corresponds approximately to a height of 65 km) to surface (see Table A.4). In the version of RTIASI used in this work all gases (such as CO, CO₂, NO, N, O, CH, CFC11, CFC12) except water vapor and ozone are assumed to be constant regarding to time and space, and therefore they are called *fixed gases*. The FTC's are then used to calculate optical depths (and transmittances) for any desired input profile. Having them, radiances and brightness temperatures, respectively, are calculated via the solution of the radiative transfer equation.

4.2.1 Calculation of the Fast Transmittance Coefficients

The framework for the fast transmittance calculation used in RTIASI is based on algorithms which have been developed over several years for different spaceborne instruments by [McMillin and Fleming (1976), Fleming and McMillin (1977), McMillin et al. (1979), Susskind et al. (1983), Eyre and Woolf (1988), Eyre (1991), Rayer (1995)], and [Hannon et al. (1996)]. The method used for the calculation of the transmittances is a linear regression scheme applied to the optical depths. Note that it was not made on the level-to-space transmittances because using optical depths gave significantly more accurate results [Matricardi and Saunders (1999)].

The calculation of the optical depth τ for the layer from pressure level j to space along a path at scanning angle θ involves a polynomial, X , with terms that are functions of temperature, absorber amount, pressure, and viewing angle. The convolved optical

depth at wavenumber ν from level j to space can be written as:

$$\tau_{j,\nu} = \tau_{j-1,\nu} + \sum_{k=1}^M a_{j,\nu,k} X_{j,k}, \quad (4.7)$$

where the functions $X_{j,k}$ constitute the profile dependent predictors of the transmittance model, M is their number (10 for fixed gases and ozone and 14 for water vapor), and $a_{j,\nu,k}$ are the FTC's. To compute them, a set of atmospheric profiles (see subsection 4.2.2) is used to calculate for each profile and several viewing angle accurate line-by-line level-to-space transmittances for all levels defined by the atmospheric pressure level grid. After converting these level-to-space transmittances $T_{j-1,\nu}$ to optical depths $\tau_{j,\nu}$, the regression coefficients, $a_{j,\nu,k}$, are calculated via the linear regression scheme defined in Equation 4.7.

4.2.2 Profile Dataset Used

The FTC's are calculated for three different cases (temperature, humidity, and ozone) using two different sets of training data. For the fixed gases and for water vapor a set of 42 profiles has been selected from the TIGR (TOVS Initial Guess Retrieval) dataset (1761 profiles). For ozone 33 profiles selected from 383 NESDIS profiles (supplemented by a few extreme Antarctic profiles) have been used. These profiles containing temperature and absorber amount of the variable gases at the 43 standard pressure levels were found to cover most of the range of observed temperature, water vapor, and ozone behavior [Matricardi and Saunders (1999)].

The calculation of line-by-line transmittances, or optical depths, respectively, for these profiles and 6 different scanning angles, used as regression data for obtaining the FTC's, were performed with the GENLN2 line-by-line transmittance and radiance model. The basic inputs for the model are the atmospheric profiles which define the gas conditions of the gases that are spectroscopically active over the spectral interval relevant to the user, the spectral resolution, and an appropriate molecular spectral line data. These line parameters defined for each line at a certain wavenumber ν were obtained from the HIRTRAN molecular database [Rothman *et al.* (1996)]. It contains molecular data such as half-width, line position, line strength, and lower energy state for about one million spectral lines for 35 different molecules (the used version of RTIASI contains the data of the 1996 edition of the HIRTRAN database).

The model adjusts line strengths and half-widths to path, temperature, pressure (collisional broadening) and Doppler effects (Doppler broadening, see subsection 1.4.2). In addition to the line-by-line absorption, the important continuum absorption bands (e. g., water vapor continuum) have been considered in the calculation.

The line-by-line transmissions were computed over the IASI spectral range with a spectral resolution of 0.001 cm^{-1} , which was found sufficient for keeping the radiance spectra below the instrumental noise. This was done along the path from each pressure level to space for 6 scanning angles, namely for those for which the secant equals 1.0,

1.25, 1.5, 1.75, 2.0, and 2.25. Since IASI measures a spectrum whose natural resolution is much higher ("infinite resolution") than the instrument resolution, the radiances (and transmittances) have to be convolved by the ISRF of the IASI instrument (see subsection 2.2.3). RTIASI computes the radiances via the convolution of the transmittances rather than convolving the monochromatic radiances (polychromatic approximation). Since the error introduced by this approximation is lower than the radiometric noise it is acceptable for most purposes.

4.2.3 Transmittances

Given an RTIASI input profile which should contain temperature, water vapor volume mixing ratio, and ozone volume mixing ratio profiles as well as surface variables like emissivity, pressure, temperature, and skin temperature, the optical depths are estimated according to Equation 4.7 with predictor values calculated from the input and reference profile variables. These optical depths are then converted to transmittances.

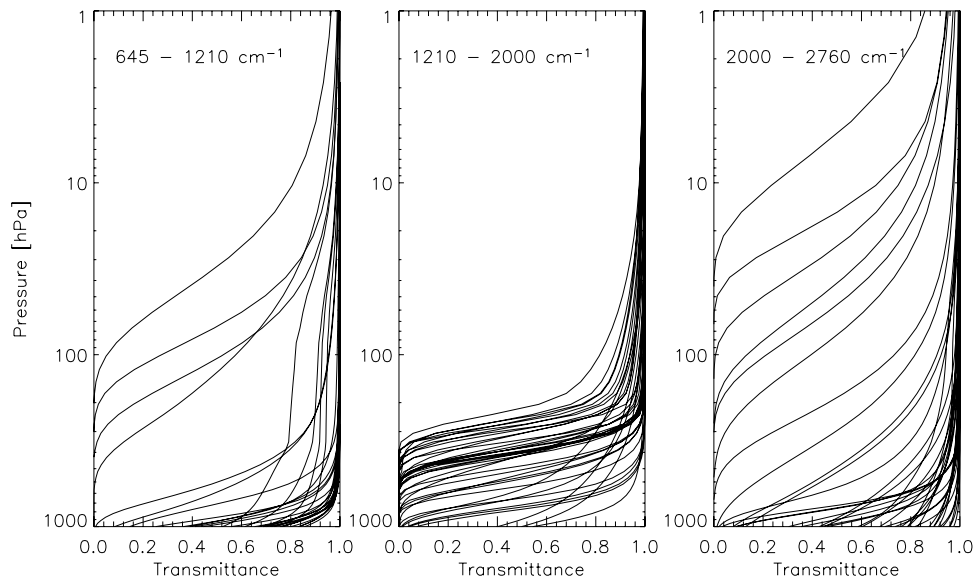


Figure 4.1: Total transmittances of every 50th IASI channel calculated by RTIASI. The input was a U. S. standard mid-latitude summer atmosphere (temperature, humidity, and ozone profiles), and the plots are divided into the three main spectral bands of the IASI instrument.

The total (convolved) transmittance for all gases is a product of the three individual one's:

$$T_{j,\nu} = T_{j,\nu}^F T_{j,\nu}^W T_{j,\nu}^O, \quad (4.8)$$

where the upper indices F , W , and O are standing for fixed gases, water vapor, and ozone, respectively. Although this equation is true for monochromatic transmittances, it has to be mentioned that for real non-monochromatic channels the convolution of all the

gases is different from the product given in Equation 4.8 but it can be considered to be a good approximation if the transmittance varies relative slowly with wavenumber (note that the IASI ISRF is narrow and is essentially symmetric about its centroid – for details see [Matricardi and Saunders (1999)]). Figure 4.1 shows a set of total transmittances divided into the three main IASI bands (see Table 2.3) calculated with a U. S. standard mid-latitude summer atmosphere (temperature, humidity, and ozone profiles) as input.

4.2.4 Radiative Transfer Model

RTIASI calculates IASI Level 1c radiances, which are the radiance product that will be distributed to the users (NWP centers, etc.). Figure 4.2 shows the radiances and the appropriate brightness temperatures calculated by RTIASI for a U. S. standard mid-latitude summer atmosphere.

The formulation of the radiative transfer equation used in RTIASI assumes a plane parallel atmosphere in local thermodynamic equilibrium with no scattering. Thus, the upwelling radiance at the TOA can be written as:

$$R(\nu, \theta) = (1 - N)R^{Clr}(\nu, \theta) + NR^{Cld}(\nu, \theta), \quad (4.9)$$

where $R^{Clr}(\nu, \theta)$ is the clear column radiance and $R^{Cld}(\nu, \theta)$ is the overcast ("cloudy") radiance at wavenumber ν and zenith angle θ , respectively, and N is the fractional cloud coverage which in this model is assumed to be in a single layer with unit cloud top emissivity.

If further the assumption of specular reflections at the earth's surface is made, the monochromatic clear-column radiance can be written as:

$$\begin{aligned} R^{Clr}(\nu, \theta) &= T_s(\nu, \theta)\epsilon_s(\nu, \theta)B(\nu, T_s) \\ &+ \int_{T_s}^1 B(\nu, T)dT' \\ &+ [1 - \epsilon_s(\nu, \theta)]T_s^2(\nu, \theta) \int_{T_s}^1 \frac{B(\nu, T)}{T'^2}dT', \end{aligned} \quad (4.10)$$

where $B(\nu, T)$ is the Planck function for a scene temperature T , T is the atmospheric transmittance, and $\epsilon_s(\nu, \theta)$ is the surface emissivity (the subscript s refers to the surface). The first term of Equation 4.10 is a contribution from the surface, whereas the second and third terms are contributions from the atmosphere. In detail it can be said that the second term refers to active emissions by the atmosphere (upward part) and the third term constitutes a downward emission which is reflected by the surface.

On the other hand the overcast radiance $R^{Cld}(\nu, \theta)$ is defined by:

$$R^{Cld}(\nu, \theta) = T_{Cld}(\nu, \theta)B(\nu, T_{Cld}) + \int_{T_{Cld}}^1 B(\nu, T)dT', \quad (4.11)$$

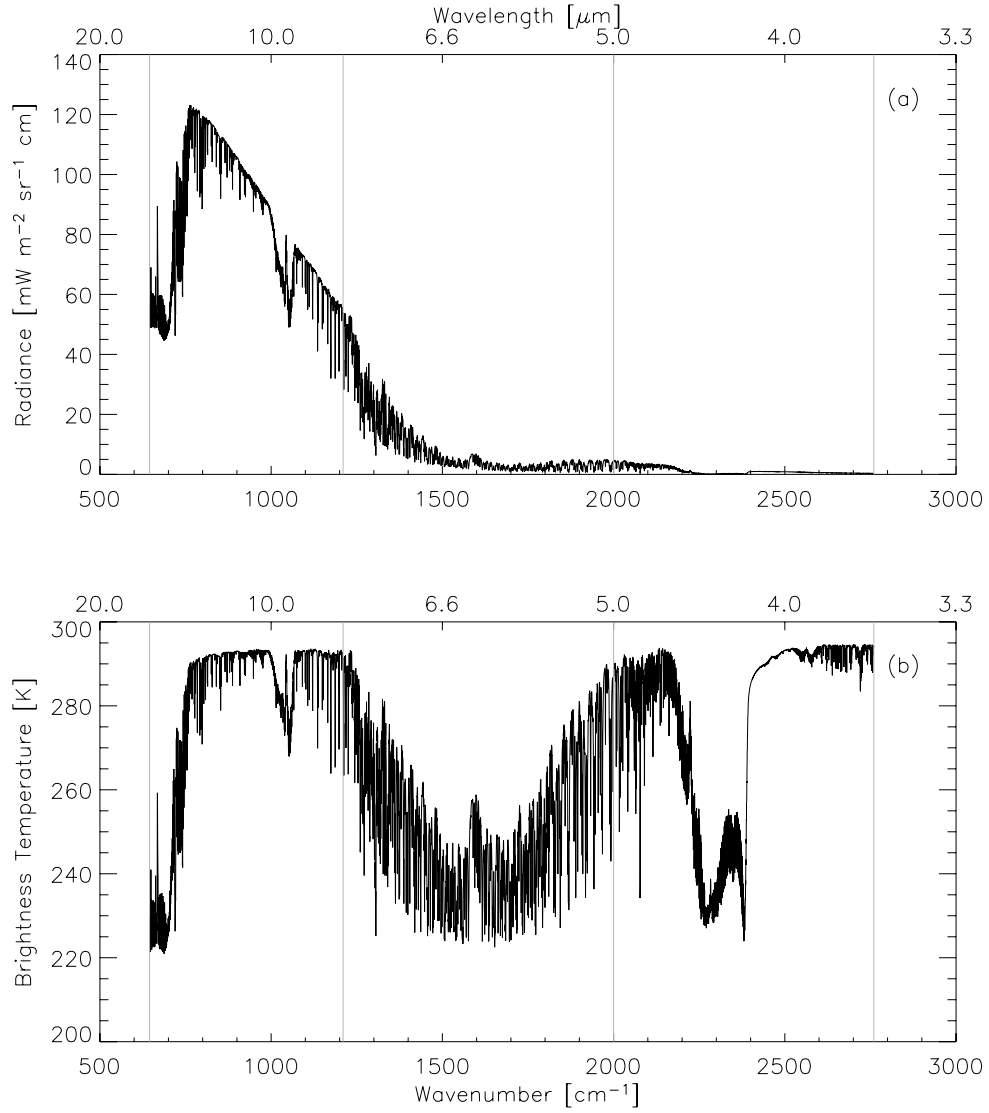


Figure 4.2: Radiances (a) and brightness temperatures (b) versus wavenumbers (and wavelengths, top axis) for a U. S. standard mid-latitude summer atmosphere calculated by RTIASI. The gray lines indicate the limits of the IASI main spectral bands.

where T_{Cl_d} is the cloud top to space transmittance, and T_{Cl_d} is the cloud top temperature.

To represent the outgoing radiances as viewed by IASI, the spectrum of monochromatic radiances introduced in Equation 4.9 has to be convolved with the appropriate ISRF:

$$\hat{R}(\bar{\nu}, \theta) = \int_{-\infty}^{\infty} R(\nu', \theta) f(\bar{\nu} - \nu') d\nu', \quad (4.12)$$

where the $\hat{\cdot}$ symbol over R denotes the convolution and $f(\bar{\nu} - \nu')$ is the normalized ISRF with $\bar{\nu}$ as the central wavenumber of the IASI channel. The ISRF of the IASI instrument

is a 0.5 cm^{-1} FWHH Gaussian with a cardinal sinc function, whose interferogram is a $\pm 2 \text{ cm}$ box function corresponding to the IASI $\pm 2 \text{ cm}$ OPD [Cayla (1996)] (see subsection 2.2.3 above for details).

The calculation of the radiances in RTIASI is performed with the assumption that the atmosphere is subdivided into a number of homogeneous layers of fixed pressure. Hence, we can rewrite Equation 4.9 in a discrete layer notation (for a single viewing angle to simplify the notation):

$$\begin{aligned} \hat{R}_{\bar{\nu}}^{Clr} &= T_{s,\bar{\nu}} \epsilon_{s,\bar{\nu}} B_{\bar{\nu}}(T_s) \\ &+ \sum_{j=1}^L \hat{R}_{j,\bar{\nu}}^u \\ &+ [1 - \epsilon_{s,\bar{\nu}}] \sum_{j=1}^L \hat{R}_{j,\bar{\nu}}^u \frac{T_{s,\bar{\nu}}^2}{T_{j,\bar{\nu}} T_{j-1,\bar{\nu}}} \\ &+ R'_{\bar{\nu}}, \end{aligned} \quad (4.13)$$

where L is the number of atmospheric layers (starting from space, layer 1, to the first layer above the surface, layer L), $T_{j,\bar{\nu}}$ is the convolved transmittance from a given pressure level p_j to space, $T_{s,\bar{\nu}}$ is the convolved transmittance from surface to space, and $\hat{R}_{j,\bar{\nu}}^u$, the upwelling radiance, is defined as:

$$\hat{R}_{j,\bar{\nu}}^u = B_{\bar{\nu}}(T_j) (T_{j-1,\bar{\nu}} - T_{j,\bar{\nu}}), \quad (4.14)$$

where T_j is defined here as the layer mean temperature obtained using the Curtis-Godson air density weighted mean value assuming that the temperature varies linearly between the layer boundaries (therefore it has to be taken into account that the path lengths are variational which means that the thickness of the layers is not constant; for details see e. g., [Liou (2002)]). The last term of Equation 4.13, $R'_{\bar{\nu}}$, is a small atmospheric contribution from the surface to the first layer above the surface. Note that for the derivation of Equation 4.13 the implicit assumption was made that the total transmittance of an atmospheric path is the product of the transmittances of the constituent sub-paths (see subsection 4.2.3).

The calculation of the sea-surface emissivities $\epsilon_{s,\bar{\nu}}$ are based on the model of [Masuda et al. (1988)] with an refractive index of pure water based on [Hale and Querry (1973)] which is adjusted [Friedman (1969)] to the sea water values and then interpolated to the wavenumber $\bar{\nu}$ to be given as an input with surface wind speed and the zenith angle θ to compute the rough sea-surface emissivity. Over land the emissivity is set to 0.97.

The TOA overcast radiance in discrete notation can be written as follows:

$$\hat{R}_{\bar{\nu}}^{Clid} = T_{Clid,\bar{\nu}} B_{\bar{\nu}}(T_{Clid}) + \hat{R}_{\bar{\nu}}'' + \sum_{j=1}^{L_{Clid}} \hat{R}_{j,\bar{\nu}}^u, \quad (4.15)$$

where L_{Ct} is the layer above the cloud (the subscript Ct denotes the cloud top). Note that the emissivity of the cloud top is assumed to be unity which is a tolerable assumption for optically thick water clouds in the IR.

The middle term in Equation 4.15, $\hat{R}_{\bar{p}}''$, is an interpolated value of the radiance below the cloud top and the level above the cloud top to include also the additional radiance from the last full layer to the cloud top. If the cloud top pressure p_c lies between standard pressure levels J and $J - 1$ the overcast radiance at p_c is obtained by:

$$\hat{R}_{\bar{p}}'' = (1 - f_{ct}) \hat{R}_{J,\bar{p}}^{Cld} + f_{ct} \hat{R}_{J-1,\bar{p}}^{Cld}, \quad (4.16)$$

where $\hat{R}_{J,\bar{p}}^{Cld}$ and $\hat{R}_{J-1,\bar{p}}^{Cld}$ are the TOA overcast radiances of level J and $J - 1$, respectively, and f_{ct} is given by:

$$f_{ct} = \frac{p_J - p_c}{p_J - p_{J-1}}. \quad (4.17)$$

4.3 Tangent Linear, Adjoint, and Gradient Matrix Models

The RTIASI package contains also programs for the computation of the tangent linear (TL) and the adjoint (AD) model as well as for the calculation of the gradient matrix, \mathbf{K} (partial derivatives of the brightness temperatures – note not radiances – with respect to the profile variables). In the following a short introduction to the TL and AD modeling is given which is mostly based on [*Matricardi (1999)*].

If we represent the radiative transfer scheme as an operator for transforming an atmospheric state vector, \mathbf{x} , into a measurement vector (radiances or brightness temperatures):

$$\mathbf{y} = \mathbf{F}(\mathbf{x}), \quad (4.18)$$

the tangent linear operation can be written in terms of the gradient of this equation:

$$\delta\mathbf{y} = \mathbf{K}(\mathbf{x})\delta\mathbf{x}, \quad (4.19)$$

where $\mathbf{K}(\mathbf{x})$ is the matrix of partial derivatives of $\mathbf{F}(\mathbf{x})$ with respect to \mathbf{x} . Hence, the adjoint of this operation can be described in terms of the transpose of $\mathbf{K}(\mathbf{x})$:

$$\text{grad}_{\mathbf{x}} = \text{grad}_{\mathbf{x}}\mathbf{y} \cdot \text{grad}_{\mathbf{y}} = \mathbf{K}^T(\mathbf{x}) \cdot \text{grad}_{\mathbf{y}}. \quad (4.20)$$

Therefore, in principle, both the tangent linear and the adjoint operations can be performed by computing the gradient matrix, $\mathbf{K}(\mathbf{x})$, and then evaluating the appropriate dot product. However, if the systems get too large it may not be feasible to calculate the full matrix and we have to perform the TL and AD operations without explicitly calculating the Jacobians. Therefore we may represent these operations in a general way:

$$\text{tangent linear:} \quad \delta\mathbf{y} = \text{TL}(\mathbf{x}, \delta\mathbf{x}) \quad (4.21)$$

$$\text{adjoint:} \quad \text{grad}_{\mathbf{x}} = \text{AD}(\mathbf{x}, \text{grad}_{\mathbf{y}}) \quad (4.22)$$

For the direct model described in section 4.2 the TL and AD model have been designed following the method described by [Thepaut and Moll (1990)], whereas the K-matrix calculation was developed modifying the AD model.

The outputs of the gradient matrix model are the exact partial derivatives, i. e. the increment in brightness temperature if one element is perturbed by 1 K or 1 ppmv. The resulting weighting functions corresponding to the same channels and input profile as in Figure 4.1 are shown in Figure 4.3.

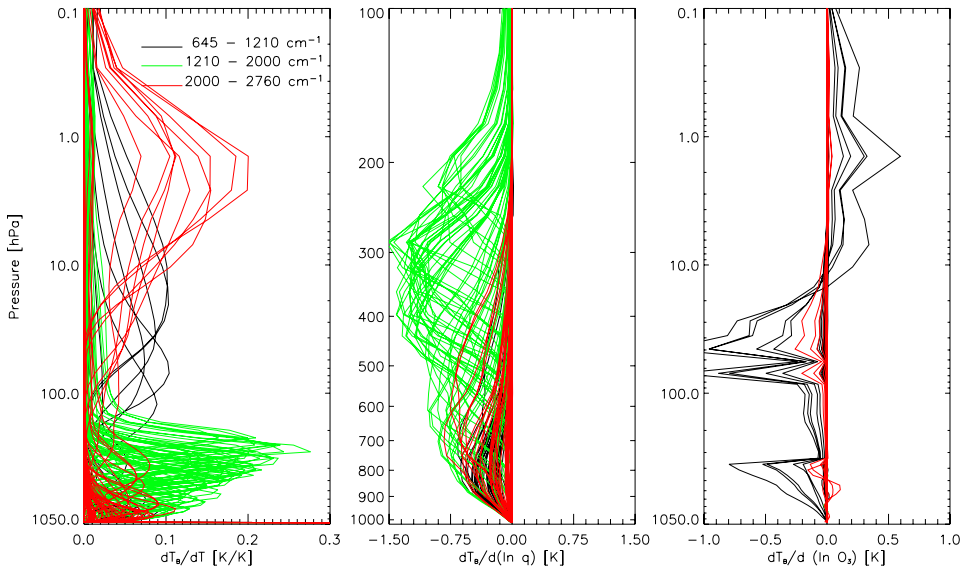


Figure 4.3: Weighting functions (rows of the gradient matrix, \mathbf{K}) of every 50th IASI channel calculated by RTIASI. The input was a U. S. standard mid-latitude summer atmosphere (temperature, humidity, and ozone profiles). The three panels show the weighting functions for temperature (left), humidity (middle), and ozone (right). The three different colors illustrate the three main IASI spectral bands (black: 645.0 – 1210 cm^{-1} , green: 1210 – 2000 cm^{-1} , red: 2000 – 2760 cm^{-1}). In case of the temperature panel it has to be pointed out, that the 2 m temperature is plotted at a pressure of 1017.0 hPa and the surface skin temperature at a pressure of 1020.0 hPa, respectively.

Inspecting Figure 4.3 in detail, we can recognize different things: An overview over all three panels (temperature, humidity, and ozone \mathbf{K} 's) shows differences in the absolute values of the peaks of the three different species, which can be associated with the different values temperature, humidity, and ozone sensitivities take in practice.

An explicit look at the temperature weighting functions exhibits the different regions where the \mathbf{K} 's have their peak as well as the different FWHM they are occurring with. As mentioned above, the weighting functions give the relative contribution from a given atmospheric layer to the spectral radiance at the TOA. The maximum contribution occurs at the layer of unit optical depth whereas the width of the Jacobians are determining the vertical resolution of the retrieval soundings. Therefore it can be said that for the main spectral bands one and three the vertical resolution is not very high (except in the

lowest tropospheric region) but they are responsible for the gain of the information in the stratospheric region. In addition they show the surface window regions (8-12 μm and $<4 \mu\text{m}$, see section 1.5) in a distinct way (the window channels of the first IASI spectral band are over-plotted by the channels of the third band) with peaks far beyond a value of 0.3 K/K. On the other hand we have a good vertical resolution for the second spectral band of IASI (mainly H_2O absorption) in the tropospheric region.

The middle panel shows only the >100 hPa of the atmosphere (i. e. mainly the troposphere) where the water vapor concentration is high. We see that most of the information can be expected in the upper troposphere, between 500 and 200 hPa, where the strong H_2O absorption band (centered at 6.3 μm , see subsection 1.4.4) is situated in the second IASI spectral band. A comparison with the temperature channels in the troposphere shows a strong correspondence in width and peaking behavior.

The relatively sparse occurrence (few visible stronger peaks) of the ozone weighting functions provide an indication that we have only very narrow absorption bands for ozone in the IASI spectral region. Additionally we can recognize that the main contributions are arising in the first and third IASI spectral band – the second band produces no noteworthy information since containing no relevant ozone band

In summary we can say at this point that improvements on the atmospheric state can be expected for the surface skin temperature (in a cloud free condition), as well as for temperature and humidity in the tropospheric region and for ozone mainly in the stratosphere (with some additional contributions in the troposphere). More difficulties can be expected for temperature in the stratosphere and especially the vertical resolution of the tropopause will provide difficulties. The following chapters 5 and 6 describe our retrieval algorithm and performance results in detail.

Chapter 5

IASI Retrieval and Channel Selection

The aim of this chapter is a detailed description of the setup of the inversion scheme we have implemented to retrieve atmospheric parameters from the IASI brightness temperatures (radiances) and how to generalize this to a joint retrieval algorithm. It is outlined how the measurement vectors are simulated to get quasi-realistic measurements (IASI level 1c data, see section 2.2.4) and how *a priori* profiles consistent with the *a priori* error covariance matrix are generated. Furthermore, the design of the measurement error covariance matrix and the *a priori* error covariance matrices (different ones for temperature, humidity, and ozone) is described.

A fundamental task for the retrieval of atmospheric parameters (e. g., temperature, humidity, ozone, and SST) with high resolution infrared sounders (like IASI or AIRS) is the reduction of the number of channels (i. e. number of elements of wavenumbers) used in the inversion scheme. This and two useful channel selection methods are described which are applied to pre-selected regions of the spectrum sensitive to the specific parameters.

5.1 Retrieval Setup

5.1.1 Joint Retrieval Algorithm

As a simple and instructive example which is used to illustrate the construction of the vectors and matrices needed for the joint retrieval we start with the assumption of a linear problem, c. f. Equation 3.22:

$$\mathbf{y} = \mathbf{K}\mathbf{x} + \boldsymbol{\epsilon}. \quad (5.1)$$

With \mathbf{y} depending only on one set of parameters, e. g., a temperature profile, \mathbf{x}_T (where T refers to temperature), equation 5.1 can be illustrated in the following way:

$$\begin{pmatrix} y_1 \\ \vdots \\ y_m \end{pmatrix} = \begin{pmatrix} (\mathbf{k}_{T,1} \) \\ \vdots \\ (\mathbf{k}_{T,m} \) \end{pmatrix} \begin{pmatrix} x_{T,1} \\ \vdots \\ x_{T,n} \end{pmatrix} + \begin{pmatrix} \epsilon_1 \\ \vdots \\ \epsilon_m \end{pmatrix}, \quad (5.2)$$

where:

$$\mathbf{k}_{T,i} = \left(\frac{\partial y_i}{\partial x_{T,1}} \quad \cdots \quad \frac{\partial y_i}{\partial x_{T,n}} \right), \quad (5.3)$$

are the so called *weighting functions* (c. f. section 3.1), which give the dependence of one measurement, y_i , on the atmospheric temperature profile, \mathbf{x}_T .

Generalizing this to the special case of a joint temperature, humidity, and ozone profile and surface temperature retrieval used in this work, the setup of the vectors and the Jacobian matrix can be written as follows:

$$\begin{pmatrix} y_1 \\ \vdots \\ y_m \end{pmatrix} = \begin{pmatrix} (\mathbf{k}_{T,1}, k_{SAT,1}, k_{SST,1}, \mathbf{k}_{H,1}, \mathbf{k}_{O,1}) \\ \cdots \quad \vdots \quad \cdots \\ (\mathbf{k}_{T,m}, k_{SAT,m}, k_{SST,m}, \mathbf{k}_{H,m}, \mathbf{k}_{O,m}) \end{pmatrix} \begin{pmatrix} \mathbf{x}_T \\ x_{SAT} \\ x_{SST} \\ \mathbf{x}_H \\ \mathbf{x}_O \end{pmatrix} + \begin{pmatrix} \epsilon_1 \\ \vdots \\ \epsilon_m \end{pmatrix}, \quad (5.4)$$

where the subscripts SAT , SST^* , H , and O are referring to surface air temperature (2 m temperature), surface skin temperature, humidity, and ozone, respectively. The calculation of the "sub"-weighting functions for the atmospheric parameters is performed in the same way as in the single parameter case (c. f. Equation 5.3).

Since here we are dealing with a problem which is assumed to be moderately non-linear, the used inversion method is an iterative optimal estimation algorithm (Gauss-Newton method, c. f. Equations 3.65 and 3.66 of subsection 3.3.3):

$$\mathbf{x}_{i+1} = \mathbf{x}_{ap} + \mathbf{S}_i \mathbf{K}_i^T \mathbf{S}_\epsilon^{-1} [(\mathbf{y} - \mathbf{y}_i) - \mathbf{K}_i (\mathbf{x}_{ap} - \mathbf{x}_i)], \quad (5.5)$$

with:

$$\mathbf{y}_i = \mathbf{f}(\mathbf{x}_i) \quad \text{and:} \quad \mathbf{S}_i = (\mathbf{K}_i^T \mathbf{S}_\epsilon^{-1} \mathbf{K}_i + \mathbf{S}_{ap}^{-1})^{-1}. \quad (5.6)$$

Hence, the only matrix left with a special setup in the joint representation is the *a priori* error covariance matrix, \mathbf{S}_{ap} . It is constructed as a block-diagonal matrix based on the assumption that there are no cross correlations between temperature, humidity (used in form of specific humidity), and ozone:

$$\mathbf{S}_{ap} = \begin{pmatrix} \begin{pmatrix} \mathbf{S}_{ap,T} \end{pmatrix} & \mathbf{0} & \mathbf{0} \\ \mathbf{0} & \begin{pmatrix} \mathbf{S}_{ap,H} \end{pmatrix} & \mathbf{0} \\ \mathbf{0} & \mathbf{0} & \begin{pmatrix} \mathbf{S}_{ap,O} \end{pmatrix} \end{pmatrix}. \quad (5.7)$$

*It has to be mentioned that the term SST is also used as a shortcut of the sea surface temperature in this work. This exhibits a slight inconsistency which can be neglected in this study since we are treating only surface temperatures of the ocean in this work and therefore the two terms refer to the same thing.

Note that the surface parameters, SAT and SST are implicitly included in the matrix $\mathbf{S}_{ap,T}$ to illustrate that correlations between the temperature profile, the surface air temperature, and the surface skin temperature are of course assumed. The values of the variances and covariances of the *a priori* error covariance matrices for the different atmospheric parameters, $\mathbf{S}_{ap,T}$, $\mathbf{S}_{ap,H}$, and $\mathbf{S}_{ap,O}$, are given in subsection 5.1.2.

For the measurement error covariance matrix, \mathbf{S}_ϵ , the same setup applies as for the *a priori* error covariance matrices (see subsection 5.1.2) except that the measurement error covariance matrix is modified in its diagonal according to [Liu *et al.* (2000)]:

$$\mathbf{S}_\epsilon(k, k) = \max \left[\frac{(\mathbf{y}(k) - \mathbf{y}_i(k))^2}{\alpha}, \sigma^2(k) \right], \quad (5.8)$$

where k is the channel index, i is the iteration index, σ is the measurement noise, i. e. the original diagonal element of \mathbf{S}_ϵ , and α is a control parameter which is set to 4 in this study, following [Weisz *et al.* (2003)]. This correction is implemented in the algorithm in the way that at each iteration step the difference between the actual measurements, i. e. the measurements obtained by forward modeling the state of the previous iteration, and the "true" measurements is compared with the measurement error, and then the larger value of the two quantities is taken to be the diagonal element of the measurement error covariance matrix.

This procedure, termed *D-rad method* [Liu *et al.* (2000)], aids convergence in the case of a "poor" *a priori* profile, since in this case the assumed measurement error grows and the retrieval algorithm, Equation 5.5, does not attach too much weight to the particular measurements. Usually, this process affects and helps the retrieval only in the very first iteration step, since the first factor of Equation 5.8 decreases very quickly. [Liu *et al.* (2000)] found the "D-rad" extended Gauss-Newton algorithm to perform equally well or better than the Levenberg-Marquardt algorithm in aiding convergence when a poor initial guess profile was given (c. f. [Lerner *et al.* (2002)]).

The convergence criterion for Equation 5.5 is given by (c. f. [Rodgers (2000)]):

$$\chi^2 \leq m, \quad (5.9)$$

where m is the number of used channels and the cost function χ^2 is obtained by:

$$\chi^2 = (\mathbf{y} - \mathbf{y}_i)^T \mathbf{S}_\epsilon^{-1} (\mathbf{y} - \mathbf{y}_i) + (\mathbf{x}_i - \mathbf{x}_{ap})^T \mathbf{S}_{ap}^{-1} (\mathbf{x}_i - \mathbf{x}_{ap}). \quad (5.10)$$

If this criterion is not met, the iteration loop is terminated either if $\chi_i^2 \geq \chi_{i-1}^2$ or the number of iterations, i , exceeds 6.

5.1.2 *A Priori* and Measurement Error Covariance Matrices

A Priori Error Covariance Matrices

In the performance study in chapter 6 we will use two different kinds of *a priori* profiles: On the one hand we use the 24 hour forecast field of a high resolution (T511-L60)

ECMWF (European Centre for Medium-Range Weather Forecasts) analysis field used as "true" atmosphere and on the other hand we construct *a priori* profiles consistent with the *a priori* error covariance matrices (c. f. subsection 5.1.4) since it is sometimes useful for simulation studies to accurately know the *a priori* error covariance matrices for an application. For these two types of *a priori* profiles we have different sets of *a priori* error covariance matrices.

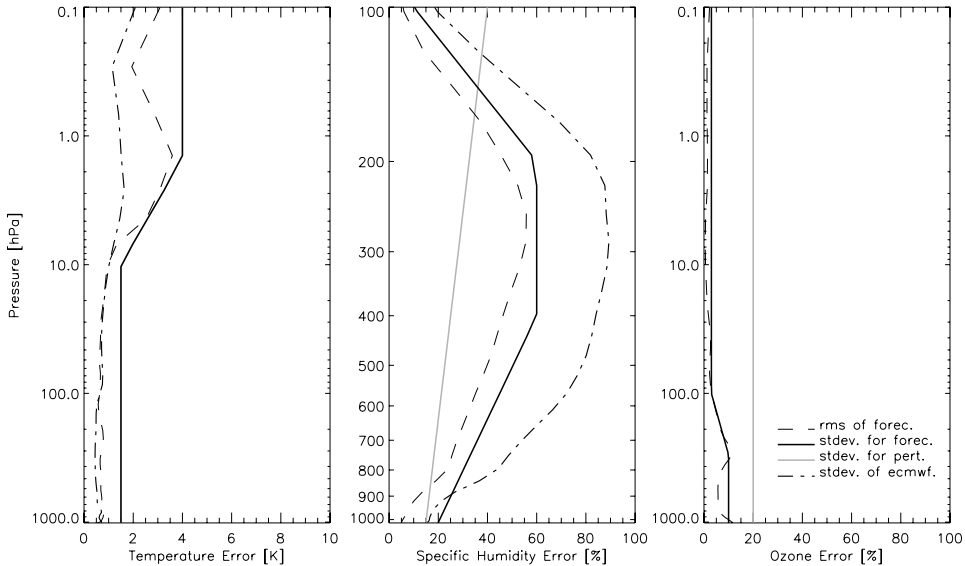


Figure 5.1: Used standard deviation values (solid lines) and rms values (dashed lines) for temperature (left), humidity (middle), and ozone (right). Additionally, the standard deviation values used by ECMWF for temperature and humidity are plotted as dashed-dotted lines. The two different colors imply the two different used *a priori* profiles. In the case of humidity the gray solid line implies the standard deviation values used for perturbing the humidity in the case of a temperature only retrieval (c. f. subsection 6.3.1).

The errors for the forecast field were obtained by calculating the root mean square (rms) profiles between the analysis and the forecast field (dashed lines in Figure 5.1) at the geographic locations where the fields are defined but interpolating the height grid to the RTIASI pressure level grid.

To minimize perturbation effects of the covariances on the retrieval the rms was afterwards approximated by straight lines, selecting conservative outer bounds to the estimated rms profiles. (see Figure 5.1). The values obtained by this approximation were then used as standard deviation values in the *a priori* error covariance matrices. The fixed values for the standard deviations are presented in detail in Table 5.1. The values according to the RTIASI pressure levels are obtained via interpolation.

For the second class of *a priori* profiles (those which are produced consistent with the *a priori* matrices, gray lines), the same values as in the case of the forecast field were taken for temperature and humidity (except for humidity in case of temperature-only retrieval, see caption of Figure 5.1). For ozone a fixed value of 20 % over the whole RTIASI

Forecast field as <i>a priori</i>					
Temperature					
Pressure [hPa]	0.10	1.50	10.00	1013.25	SST, SAT
Error [K]	4.00	4.00	1.50	1.50	1.50
Humidity					
Pressure [hPa]	100.00	200.00	400.00	1013.25	
Error [%]	10.00	60.00	60.00	20.00	
Ozone					
Pressure [hPa]	0.10	100.00	300.00	1013.25	
Error [%]	3.00	3.00	10.00	10.00	
<i>A priori</i> profiles consistent with the <i>a priori</i> error covariance matrix					
Temperature					
Pressure [hPa]	0.10	1.50	10.00	1013.25	SST, SAT
Error [K]	4.00	4.00	1.50	1.50	1.50
Humidity					
Pressure [hPa]	100.00	200.00	400.00	1013.25	
Error [%]	10.00	60.00	60.00	20.00	
Ozone					
Pressure [hPa]		0.10		1013.25	
Error [K]		20.00		20.00	

Table 5.1: Standard deviation values versus pressure values for temperature, humidity, and ozone for the two different kinds of *a priori* profile classes. The vertical transition between different uncertainty values was modeled linearly, see Figure 5.1.

pressure range was used to obtain appreciable errors since the daily variations which are obtained by the ECMWF model are quite small as one learns in investigating the rms values of ozone of the 24 h forecast field with respect to the corresponding analysis field. Figure 5.1 illustrates also this third class of standard deviation values and the exact values are given in Table 5.1. The errors of surface air temperature were always modeled the same way as the upper air temperatures, whereas the SST error was generally assumed 1.5 K in all simulations since forecast-minus-analysis differences from the ECMWF fields were clearly too small to be used for performance testing.

Since the RTIASI pressure levels define a quite dense grid, especially in the lower atmosphere correlations between the levels have to be taken into account. We assume non-diagonal elements of the different *a priori* error covariance matrices with correlation lengths $L = 6$ km for temperature, $L = 3$ km for humidity, and $L = 10$ km for ozone obeying an exponential drop-off according to:

$$S_{ij} = \sigma_i \sigma_j \exp \left[-\frac{|z_i - z_j|}{L} \right], \quad (5.11)$$

where $\sigma_i = \sqrt{S_{ii}}$ is the standard deviation at level i and $z_{i,j}$ denotes the height in kilometers at the particular pressure levels i and j , respectively. The height, z , was calculated for

this purpose by utilizing the hydrostatic equation $z = -H \log(p/p_0)$, with a scale height, $H = 7$ km and a surface pressure, $p_0 = 1013.25$ hPa. Figure 5.2 illustrates the covariance matrix for temperature with the squares of the values of the assumed uncertainty field (c. f. Table 5.1) as standard deviations.

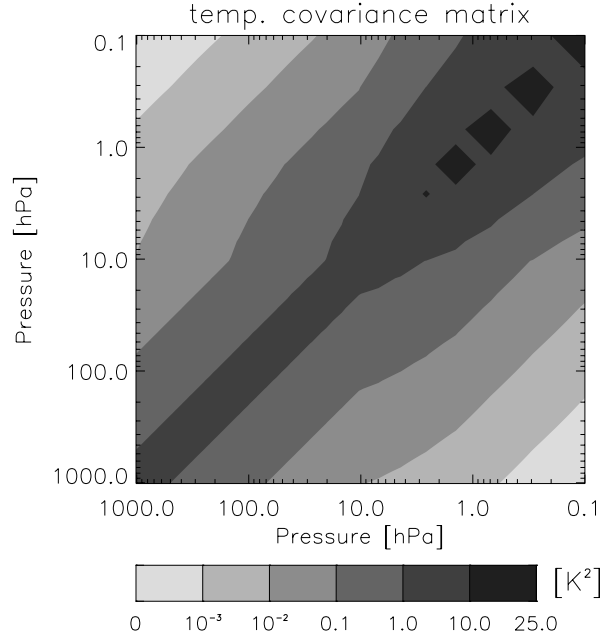


Figure 5.2: Illustration of the *a priori* temperature error covariance matrix with standard deviations and error correlation length as discussed above.

Measurement Error Covariance Matrices

In order to create an appropriate and consistent measurement error covariance matrix, \mathbf{S}_ϵ , we assume the squares of the IASI level 1c noise values (c. f. appendix A, Table A.5) to be the diagonal elements. Since these values are specified at a reference temperature, T_r , they have to be properly scaled, based on the Planck law, from this reference temperature to the actual brightness temperatures calculated by RTIASI (see Figure 5.3). The scaling factor which has to be multiplied with the noise values is obtained by (c. f. [Weisz (2001)]):

$$f = \frac{z_1}{z_2}, \quad (5.12)$$

with:

$$\begin{aligned} z_1 &= T_B^2 \exp\left[\frac{hc\nu}{kT_r}\right] \exp\left[\frac{hc\nu}{kT_B}\right]^2 \\ z_2 &= T_r^2 \exp\left[\frac{hc\nu}{kT_r}\right]^2 \exp\left[\frac{hc\nu}{kT_B}\right], \end{aligned} \quad (5.13)$$

where T_B is the actual brightness temperature, $T_r = 280$ K is the reference temperature of the IASI level 1c noise values, ν is the wavenumber, and h , c , and k are the Planck constant, the speed of light in vacuum, and the Boltzmann constant, respectively.

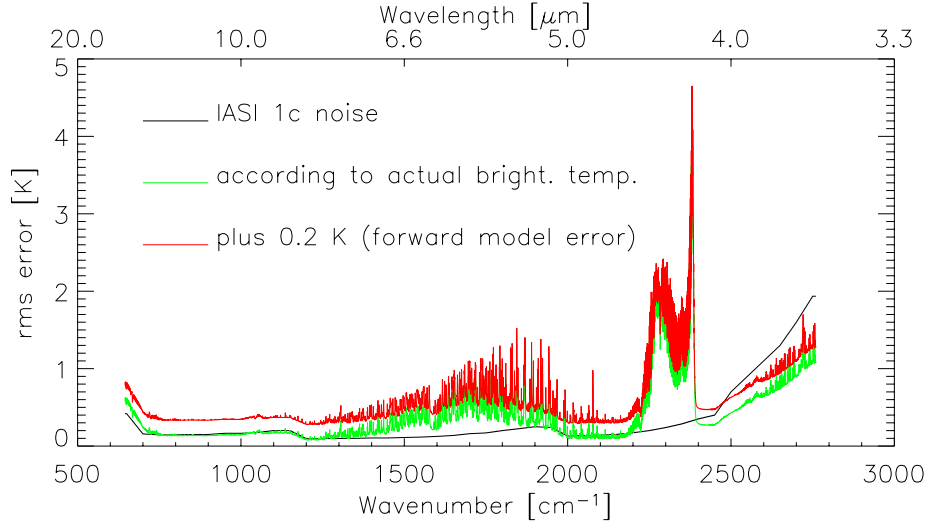


Figure 5.3: Interpolated IASI level 1c noise values, their modification according to the actual brightness temperature, and these values after adding the 0.2 K forward model error for a U. S. standard mid-latitude summer atmosphere.

Finally, the temperature modified level 1c noise values are superposed with an 0.2 K forward model error to roughly account for errors in the forward model [Collard (1998), Weisz (2001)]. The impact of the RTIASI forward model error on the IASI retrieval accuracy was studied by [Sherlock (2000)]. Figure 5.3 shows the interpolated IASI level 1c noise values, their modification according to the actual brightness temperature, and these values after adding the 0.2 K forward model error for a U. S. standard mid-latitude summer atmosphere.

Since RTIASI simulates radiances, which are apodized with a Gaussian function (c. f. subsection 2.2.3), an apodization of the random noise is required as well. This procedure leads to a correlation between neighboring channels, which also has to be accounted for in the measurement error covariance matrix. The generation of these non-diagonal elements of S_ϵ takes place according to:

$$S_{ij} = \frac{c_{ij}}{\sqrt{S_{ii}S_{jj}}}, \quad (5.14)$$

where correlation is assumed between the three nearest neighbor channels with values for c_{ij} of:

$$c_{ij} = \begin{cases} 0.71 & \text{first neighbor,} \\ 0.25 & \text{second neighbor,} \\ 0.04 & \text{third neighbor.} \end{cases} \quad (5.15)$$

This produces a covariance matrix with a rather steep descent from the main diagonal (c. f. [Weisz (2001)]).

5.1.3 Simulation of the Measurement Vector

The measurements used in the current simulation study are constructed as implied by Equation 3.57:

$$\mathbf{y} = \mathbf{f}(\mathbf{x}) + \boldsymbol{\epsilon}. \quad (5.16)$$

The fast radiative transfer model RTIASI, described in detail in chapter 4, acts as forward model, \mathbf{f} . It requires an input profile containing temperature values in K and water vapor and ozone mixing ratio values in ppmv at the 43 fixed pressure levels from surface (1013.25 hPa) to 0.1 hPa (c. f. appendix A, Table A.4). Additionally, surface parameters have to be specified. These parameters are sub-divided into parameters which are retrieved (the surface air and the surface skin temperature in K), parameters which have to be input as a priori values and then kept constant during the retrieval (the surface air humidity in ppmv and the surface pressure in hPa), and parameters with predefined default values which are never changing in space and time (the u- and v-component of the wind speed in m s^{-1} , the cloud top pressure, and the effective cloud coverage). With this vector as input, RTIASI calculates radiances and brightness temperatures, respectively, as well as the Jacobian Matrix \mathbf{K} .

To obtain quasi realistic measurements we have to add an additional noise term, $\boldsymbol{\epsilon}$ (c. f. Equation 5.16). The noise is modeled (c. f. [Weisz (2001)]) by first creating normally distributed random numbers with standard deviation values according to the IASI level 1c noise table (Table A.5) interpolated to the IASI wavenumbers (c. f. Figure 5.3). Since RTIASI calculates apodized radiances and brightness temperatures this noise is convoluted with the ISRF of the IASI instrument which is a 0.5 cm^{-1} full width at half height (FWHH) Gaussian with a cardinal sinc function (c. f. subsection 2.2.3). Additionally, the noise is properly scaled, based on the Planck law, from the reference temperature of the IASI level 1c noise values to the actual brightness temperatures calculated by RTIASI (c. f. subsection 5.1.2).

In Figure 5.4 an arbitrary realization of a random noise for the whole IASI spectrum calculated in the way described above is illustrated. Comparing this with Figure 5.3 we can identify two reasons for the occurrence of high noise values: The first is the scaling to the actual brightness temperature resulting in higher noise for lower brightness temperature and the second reason is the increasing values of the IASI level 1c noise values for wavenumbers $>2500 \text{ cm}^{-1}$.

5.1.4 Generation of A Priori Profiles

In this subsection we will discuss the construction of *a priori* profiles consistent with the *a priori* error covariance matrices (c. f. subsection 5.1.2). For this purpose we use the so called *error patterns* method [Rodgers (2000)].

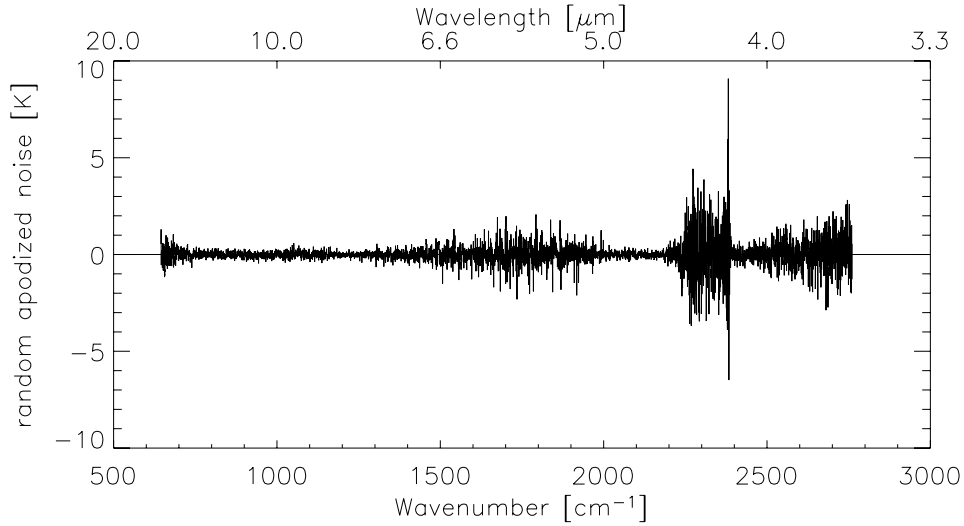


Figure 5.4: Random apodized noise values calculated for a U. S. standard mid-latitude summer atmosphere.

This method assumes that any covariance matrix, \mathbf{S} , can be decomposed as:

$$\mathbf{S} = \sum_i \lambda_i \mathbf{l}_i \mathbf{l}_i^T = \sum_i \mathbf{e}_i \mathbf{e}_i^T \quad \text{with:} \quad \mathbf{e}_i = \sqrt{\lambda_i} \mathbf{l}_i, \quad (5.17)$$

where \mathbf{l}_i are the eigenvectors and λ_i are the eigenvalues of the covariance matrix \mathbf{S} . The \mathbf{e}_i which are the eigenvectors scaled by the square-roots of the eigenvalues are called error patterns, in the sense that the error ϵ_x (where the subscript x implies that it is an error of the state vector, to distinguish it from the measurement error, ϵ) can be expressed as a sum of these error patterns, each multiplied by a random factor a_i :

$$\epsilon_x = \sum_i a_i \mathbf{e}_i, \quad (5.18)$$

where the a_i have to be normally distributed random deviates with unit variance. To illustrate this concept Figure 5.5 shows the ten most significant error patterns of the temperature error covariance matrix illustrated in Figure 5.2.

Hence, we have a simple way to construct *a priori* profiles consistent with \mathbf{S} : we only have to calculate a noise vector, ϵ_x , as described above and add it to the state vector \mathbf{x} of the "true" field.

It can be verified that the empirical covariance matrix:

$$\mathbf{S}_{emp} = E [\epsilon_x \epsilon_x^T] \quad (5.19)$$

of an ensemble of realizations ϵ_x can reconstruct the original error covariance matrix, \mathbf{S} (E is the expectation value operator). This is illustrated in Figure 5.6 for ensembles of 100 and 10 000 different random error vectors ϵ_x , respectively. The Figure points out that with an increasing number of ensemble members, the empirical matrix converges to the original one.

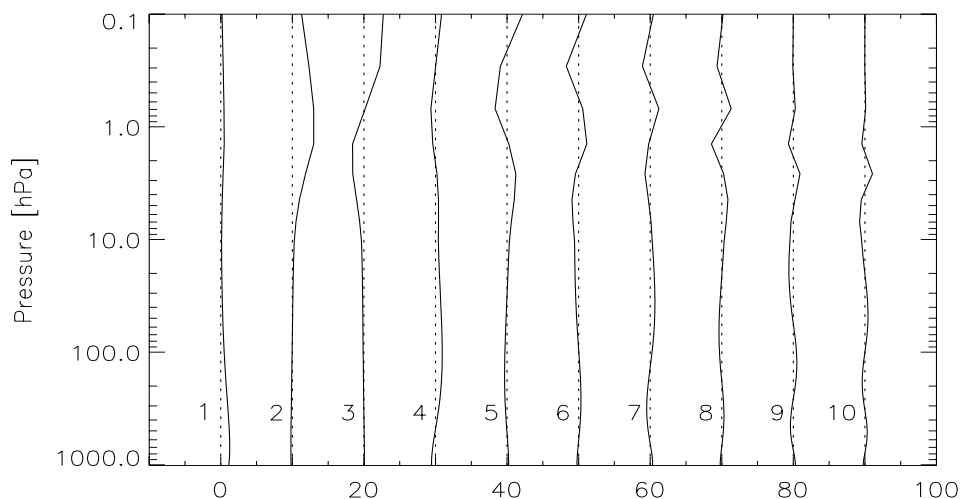


Figure 5.5: First ten scaled eigenvectors, i. e. error patterns, of the covariance matrix shown in Figure 5.2.

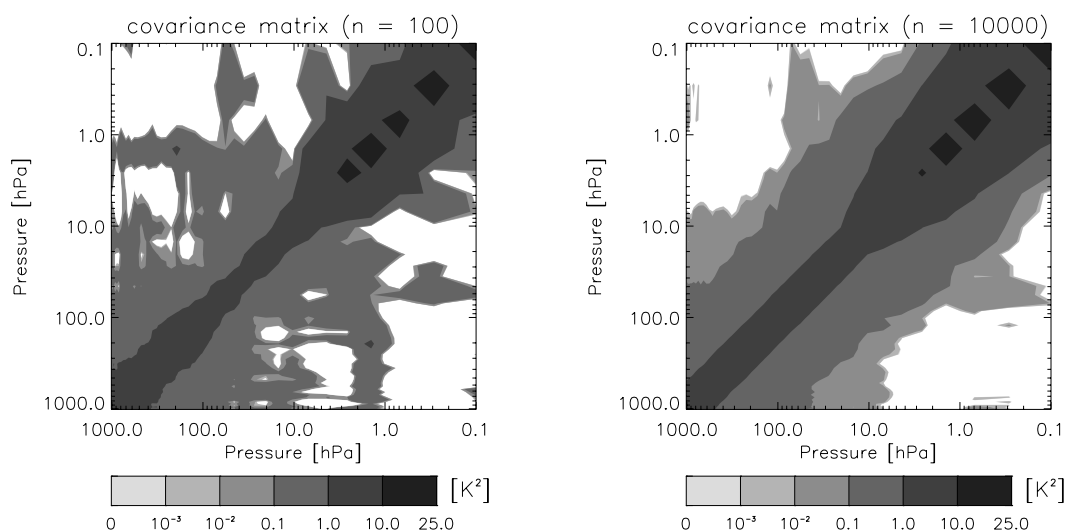


Figure 5.6: Empirical *a priori* temperature error covariance matrices using ensembles of 100 (left) and 10 000 (right) realizations. Legend, c. f. Figure 5.2.

5.2 Channel Selection

Since the full IASI spectra contain 8461 channels it is essential to reduce this number and remove redundant information for performance and computational reasons.

[*Press et al. (1992)*] point out that sets of linear equations can be routinely solved for a dimension of the matrices, N , as large as a few hundred with double precision (64 bits) representation if the equations are not close to singular (i. e. some of the equations are close to linearly dependent). Even larger sets, N , in the thousands can be solved if the

coefficients are sparse (that means most of them are zero).

In section 6.3 it will be shown that in the case of this study numerical instabilities are beginning to arise at a number of channels between 1000 and 2000, resulting from successive inversions of different matrices, which causes an accumulation of roundoff errors, etc.

Losses in performance occur particularly during the process of matrix inversion, which is a N^3 problem as well as in the gradient matrix modeling which depends also not linearly on the number of channels (the increase of the number of channels from about 300 to about 1800 causes a factor of about 12 increase in CPU time, c. f. Table 6.1. Note that this results also from numerical instabilities which cause an increase in iteration loops in the retrieval).

Hence, our task is to find an optimal subset of channels, which is sufficiently sensitive to the retrieved variables. For this purpose we follow the approach of [Lerner *et al.* (2002)] and [Weisz *et al.* (2003)]. We first perform a raw elimination of regions of the IASI spectrum (see Table 2.4) starting with those channels at wavenumbers larger than 2500 cm^{-1} . The reason for this is that these channels have larger measurement errors (above 0.7 K, c. f. Table A.5 and Figure 5.3) compared to the remaining spectrum as well as the increasing importance of solar contributions in this spectral range ($<4\mu\text{m}$) which is not taken into account in the used version of the forward model. Additionally, this region comprises CH_4 channels which are not of interest in the current study.

With the luxury of high spectral resolution we can also exclude those channels – $1220\text{--}1370\text{ cm}^{-1}$ (N_2O , CH_4 , and SO_2) and $2085\text{--}2220\text{ cm}^{-1}$ (CO and N_2O) – whose "foreign" gas emissions contribute significantly to the measured brightness temperatures (see Table 2.4). The associated trace gas constituents can be considered as uncertainties in the temperature and humidity profile retrieval since they are only modeled approximately in the used version of RTIASI[†].

At this point we have about 6200 channels (for the full joint retrieval) which is still far too much for most operational and climatological applications as well as from the point of view of numerical analysis and performance mentioned above. It is instructively shown in [Rodgers (1996)] that it is no advantage to utilize all pieces of information, since they are highly redundant for most purposes. Therefore we perform a further reduction of the number of channels by utilizing two different methods: the information content (IC) theory and the maximum sensitivity (MS) approach.

[†]In section 6.3 we perform some specific retrievals in order to compare them with the results of the joint retrieval. For those cases the spectral regions were further confined. For the temperature and humidity only retrieval, respectively, the channels ranging from $825\text{--}1100\text{ cm}^{-1}$ were excluded since there the "atmospheric window" as well as an ozone band is situated which are not needed in the case of temperature and humidity profiling. On the other hand, the "atmospheric window" channels, more precisely, those channels between 825 cm^{-1} and 975 cm^{-1} , were used to perform the SST-only retrieval.

5.2.1 Information Content Theory

”Information” is a very general term that has been used in several ways by different authors. The measure for information content we want to refer to here is based on the information theory which was developed by Shannon in the 1940’s [Shannon and Weaver (1976)]. Information as he described it depends on the *entropy* of probability density functions which is very closely related to the concept of entropy used in thermodynamics. Information content which is a scalar quantity is therefore useful for the optimization of observing systems as well as for their characterization and intercomparison. The summarized description below is guided by the more detailed description of [Rodgers (1996), Rodgers (2000)].

In thermodynamics entropy is defined as the natural logarithm (in information theory base 2 is often used) of the number of distinct internal states of a thermodynamic system consistent with the measured macro state (pressure, temperature, etc.). The information content is then the change in the logarithm of the number of distinct possible internal states of the system being measured, consistent with the change in knowledge of the system resulting from the measurement, i. e. in information theory one tries to find out to know how much information is contained in a possible outcome by knowing it. This means if an outcome x_i has a probability density $P(x_i)$, $-\log(P(x_i))$ defines the information gained by knowing the value of the outcome. Hence, if $P(x_i) = 1$, then the information is zero implying that we gain no information when knowing the certain state.

Let us now try to quantify this. The entropy is defined as:

$$S(P(x_i)) = -k \sum_i P(x_i) \ln P(x_i), \quad (5.20)$$

where $P(x_i)$ is the probability of the system being in state x_i . We see that the Gibbs definition of thermodynamic entropy and the Shannon definition for discrete information systems are the same, apart from the numerical factor k . In thermodynamics k is the Boltzmann constant and in information theory $k = 1$ and the logarithm is usually taken to base two. The entropy $S(P(x_i))$ represents the mean information provided per possible outcome x_i of a system x which implies that the entropy defines the information of an event as a whole.

Therefore the information content of a single state x gained by a single measurement y depends on the entropies of the pdf’s before and after the measurement:

$$H = S(P(x)) - S(P(x|y)), \quad (5.21)$$

where $P(x)$ is the pdf of x and $P(x|y)$ is the pdf of x conditioned on y (c. f. subsection 3.3.1). Hence, H measures the amount of information that x obtains from y , which means H determines the reduction in uncertainty in x by learning the value of y .

Generalizing this to n different states and m measurements we can describe the information content H gained by performing a measurement y as the change in entropy according to:

$$H = S(P(\mathbf{x})) - S(P(\mathbf{x}|y)), \quad (5.22)$$

where $P(\mathbf{x})$ and $P(\mathbf{x}|\mathbf{y})$ are once more the pdf's of the state \mathbf{x} and of \mathbf{x} conditioned on \mathbf{y} , respectively.

Since we are focusing on moderately non-linear problems we can assume Gaussian distributed pdf's. Additionally, we will use the logarithm taken to base two and we will set $k = 1$, as mentioned above, since we are focusing on information aspects. Therefore, the entropy for a normal distributed pdf with covariances \mathbf{S} is given by [Rodgers (1996), Rodgers (2000)]:

$$S(P) = \frac{1}{2} \log_2 |\mathbf{S}|. \quad (5.23)$$

Hence, the information content of a measurement for a prior covariance \mathbf{S}_1 and a posterior covariance \mathbf{S}_2 can be written as:

$$H = \frac{1}{2} \log_2 |\mathbf{S}_1| - \frac{1}{2} \log_2 |\mathbf{S}_2| = \frac{1}{2} \log_2 |\mathbf{S}_1 \mathbf{S}_2^{-1}| = -\frac{1}{2} \log_2 |\mathbf{S}_2 \mathbf{S}_1^{-1}|. \quad (5.24)$$

If we now select the channels sequentially by retaining the channel with highest H and removing it afterwards from the subsequent calculations we obtain:

$$H_i = \frac{1}{2} \log_2 \left| \hat{\mathbf{S}}_i^{-1} \hat{\mathbf{S}}_{i-1} \right|, \quad (5.25)$$

where the matrix $\hat{\mathbf{S}}_i$ is the posterior (retrieval) error covariance matrix given by (c. f. Equation 3.41):

$$\hat{\mathbf{S}}_i = \hat{\mathbf{S}}_{i-1} - \hat{\mathbf{S}}_{i-1} \mathbf{K}^T \left(\mathbf{K}^T \hat{\mathbf{S}}_{i-1} \mathbf{K} + \mathbf{S}_\epsilon \right)^{-1} \mathbf{K} \hat{\mathbf{S}}_{i-1}. \quad (5.26)$$

Utilizing a scaling of the Jacobian matrix \mathbf{K} (c. f. Equation 3.56) in the form:

$$\tilde{\mathbf{K}} = \mathbf{S}_\epsilon^{-\frac{1}{2}} \mathbf{K} \mathbf{S}_{ap}^{\frac{1}{2}}, \quad (5.27)$$

such that the measurement error covariance matrix becomes a unity matrix (with \mathbf{S}_ϵ and \mathbf{S}_{ap} defined in subsection 5.1.2 except that all non-diagonal elements of \mathbf{S}_ϵ are assumed to be zero), Equation 5.26 can be rewritten as follows:

$$\hat{\mathbf{S}}_i = \hat{\mathbf{S}}_{i-1} \left\{ \mathbf{I} - \frac{\tilde{\mathbf{k}}(\hat{\mathbf{S}}_{i-1} \tilde{\mathbf{k}})^T}{1 + (\hat{\mathbf{S}}_{i-1} \tilde{\mathbf{k}})^T \tilde{\mathbf{k}}} \right\} \quad (5.28)$$

where the $\tilde{\mathbf{k}}$ are the scaled weighting functions (scaled rows of the Jacobian matrix) and \mathbf{I} is the identity matrix.

The information content of a measurement using Gaussian distributed pdf's can be expressed by using the n -form of the retrieval error covariance matrix (c. f. Equation 3.40) which results in (using once more the scaled weighting functions, c. f. Equation 5.27):

$$H_i = \frac{1}{2} \log_2 \left(1 + \tilde{\mathbf{k}}^T \hat{\mathbf{S}}_{i-1} \tilde{\mathbf{k}} \right). \quad (5.29)$$

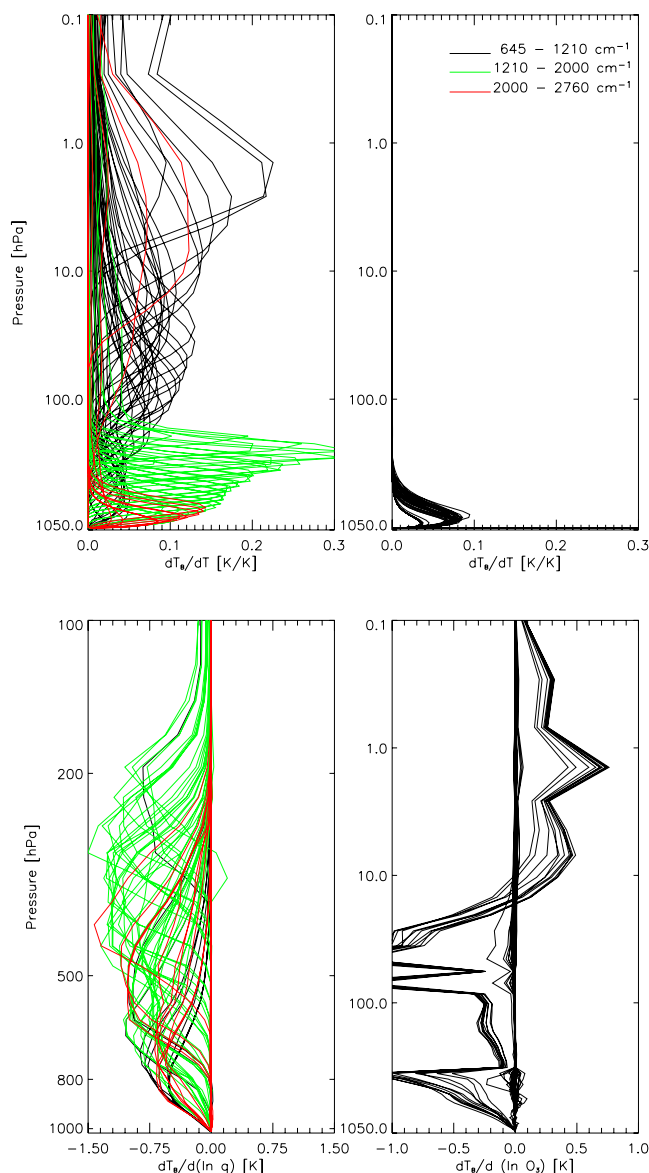


Figure 5.7: Selected channels via IC theory for temperature (top left), surface skin temperature (top right), humidity (bottom left), and ozone (bottom right). The three different colors illustrate the three main IASI spectral bands (black: $645.0 - 1210 \text{ cm}^{-1}$, green: $1210 - 2000 \text{ cm}^{-1}$, red: $2000 - 2760 \text{ cm}^{-1}$). In the case of the temperature panels the 2 m temperature is plotted at a pressure of 1017.0 hPa and the surface skin temperature at a pressure of 1020.0 hPa. The channels were selected for a U. S. standard mid-latitude summer atmosphere, the calculations were performed by RTIASI.

This selection method is implemented in the way that at first the total number of IASI channels is pre-sorted according to the pressure levels where the weighting functions of the channels are peaking. The information content is then calculated using Equation 5.29 for every available channel at each specific pressure level, starting with $S_0 = I$ (hav-

ing in mind that the $\tilde{\mathbf{k}}$'s are scaled). Now the channel with the highest H is retained and additionally removed from the subsequent calculations. After that \mathbf{S} is updated according to Equation 5.28. The number of selected channel per level is determined by taking 10% of the total number of peaking channels. Additionally, maximum and minimum threshold numbers of channels are defined. The detailed method which follows [Lerner *et al.* (2002)] is described in appendix A, section A.4.

Figure 5.7 shows the weighting functions for the selected channels for a U. S. standard mid-latitude summer atmosphere divided into the three main IASI spectral bands. The top left panel illustrates those weighting functions which were selected for the temperature profile retrieval, in the top right one can see the weighting functions of the selected surface channels, whereas the bottom left panel and the bottom right panel are showing the selected channels of humidity and ozone, respectively.

As indicated by the green color we can recognize a strong correspondence between the temperature and humidity weighting functions in the troposphere resulting from the strong H_2O absorption situated in the second IASI spectral band (c. f. section 4.3 and Figure 4.3). Additional temperature channels were selected in the strong CO_2 band centered at $15 \mu\text{m}$ (black lines) generally contributing to atmospheric regions higher than the tropopause as well as a few channels situated in the CO_2 band centered at $4.3 \mu\text{m}$ (red lines).

The reason that there are only channels from the first IASI spectral band selected for surface skin temperature and ozone is that the channels for these constituents are only selected in one or two small regions, respectively, located in the first IASI spectral band ($825 \text{ cm}^{-1} - 975 \text{ cm}^{-1}$: atmospheric window; $650 \text{ cm}^{-1} - 750 \text{ cm}^{-1}$ and $975 \text{ cm}^{-1} - 1100 \text{ cm}^{-1}$: ν_1 , ν_2 and ν_3 fundamental vibration modes of ozone, c. f. subsection 1.4.4).

5.2.2 Maximum Sensitivity Approach

As an alternative which is simpler and faster than using the selection method defined in subsection 5.2.1 an approach solely based on the weighting function matrix scaled by the measurement errors is introduced (c. f. [Weisz *et al.* (2003)]). The method tries to selectively choose those channels whose instrument noise is small or the measurement sensitivity to the treated atmospheric constituent (temperature, humidity, ozone, or sea surface temperature) is high. This is accomplished by maximizing the sensitivity-to-error ratio, a matrix denoted by:

$$\mathbf{H} = \mathbf{S}_\epsilon^{-\frac{1}{2}} \mathbf{K}, \quad (5.30)$$

where again the measurement error covariance matrix, \mathbf{S}_ϵ , is taken as a diagonal matrix by ignoring the inter-channel correlation for this purpose. The square-root of the inverse of \mathbf{S}_ϵ , more precisely, the inverse square-roots of its diagonal elements (the standard deviations, defined in subsection 5.1.2) are expressing the uncertainty of a measurement, i. e. \mathbf{S}_ϵ is a measure of the quality of the measurement.

Advancing further the approach of [Weisz *et al.* (2003)], the implementation of this channel selection algorithm starts once more with using the pre-information where the

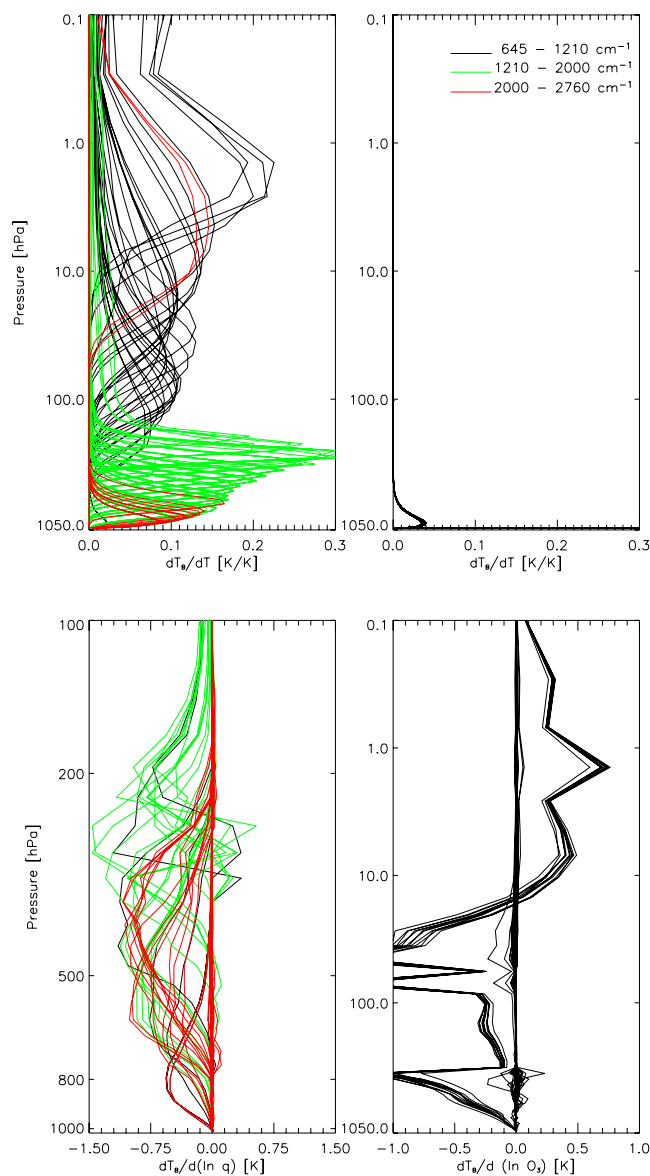


Figure 5.8: Selected channels via MS approach for temperature (top left), surface skin temperature (top right), humidity (bottom left), and ozone (bottom right). The three different colors illustrate the three main IASI spectral bands (black: $645.0 - 1210 \text{ cm}^{-1}$, green: $1210 - 2000 \text{ cm}^{-1}$, red: $2000 - 2760 \text{ cm}^{-1}$). In the case of the temperature panels the 2 m temperature is plotted at a pressure of 1017.0 hPa and the surface skin temperature at a pressure of 1020.0 hPa. The channels were selected for a U. S. standard mid-latitude summer atmosphere, the calculations were performed by RTIASI.

weighting functions of the channels are peaking (c. f. subsection 5.2.1). Then the sensitivity-to-error ratio matrix is calculated one time and a special number of channels is selected per level. The number of channels selected per level is determined in the same way as in information content theory (see appendix A, section A.4).

In Figure 5.8 the weighting functions for the selected channels for a U. S. standard mid-latitude summer atmosphere divided into the three main IASI spectral bands are illustrated. Like in Figure 5.7 the top left panel shows those weighting functions which were selected for the temperature profile retrieval, in the top right one can see the weighting functions of the selected surface channels, whereas the bottom left panel and the bottom right panel are showing the selected channels of humidity and ozone, respectively.

A comparison of these weighting functions with those selected via the IC theory (c. f. Figure 5.7) exhibits that the channels selected with the MS approach for the different constituents show a stronger correlation between one another (which means that they seem to be more linearly dependent) and that they are less evenly distributed, especially in the case of the humidity channels (in the case of ozone the weighting functions for both, IC theory and MS approach, have similar shapes). In terms of computational efficiency the IC-based selection and the MS-based selection have closely similar demands (see section 6.2 for further details).

* * *

As a summary, Figure 5.9 shows two different numbers of selected channels (310 and 909 for panels (a,c) and (b,d), respectively) for the two channel selection methods (IC theory and MS approach, panels (a,b) and (c,d), respectively). The yellow and green dashed lines are illustrating the specific spectral regions for the selection of surface skin temperature channels ($825\text{ cm}^{-1} - 975\text{ cm}^{-1}$) and ozone channels ($650\text{ cm}^{-1} - 750\text{ cm}^{-1}$ and $975\text{ cm}^{-1} - 1100\text{ cm}^{-1}$), respectively. The spectral regions for selecting the temperature and humidity channels is indicated by the light dashed black lines ($645\text{ cm}^{-1} - 825\text{ cm}^{-1}$, $1100\text{ cm}^{-1} - 1220\text{ cm}^{-1}$, $1370\text{ cm}^{-1} - 2085\text{ cm}^{-1}$, $2220\text{ cm}^{-1} - 2500\text{ cm}^{-1}$).

The two selection methods show a quite similar behavior for the ozone channels (indicated by the green crosses) whereas this is not the case for the surface channels (yellow plus signs). This can also be seen in comparing Figure 5.7 and Figure 5.8 where in the case of IC theory we have strong additional contributions from near surface channels (c. f. Figure 5.9 (a) and (b)).

A comparison of the two selection methods regarding the temperature profile channels exhibits similarities but also quite significant differences in the spectral region where they occur as well as in their distribution, especially in the case of selecting about 900 channels.

Inspecting panel (b) and panel (d) in detail we can see that in the case of the selection with the MS approach the channels are more accumulated in special spectral regions (near 700 cm^{-1} , between 1400 cm^{-1} and 1600 cm^{-1} , and around 2000 cm^{-1}). Additionally, the MS approach selects almost no channels at the ascending wing of the CO_2 band centered at 667 cm^{-1} which is done when using the IC theory. These differences are resulting in discrepancies especially in the temperature only retrieval which will be pointed out in a forthcoming paper [Weisz *et al.* (2004)].

Since the H_2O absorption covers the complete IASI spectral range (e. g. the ν_2 fundamental vibration mode ranging from 640 cm^{-1} to 2800 cm^{-1} and centered at 1600 cm^{-1} ,

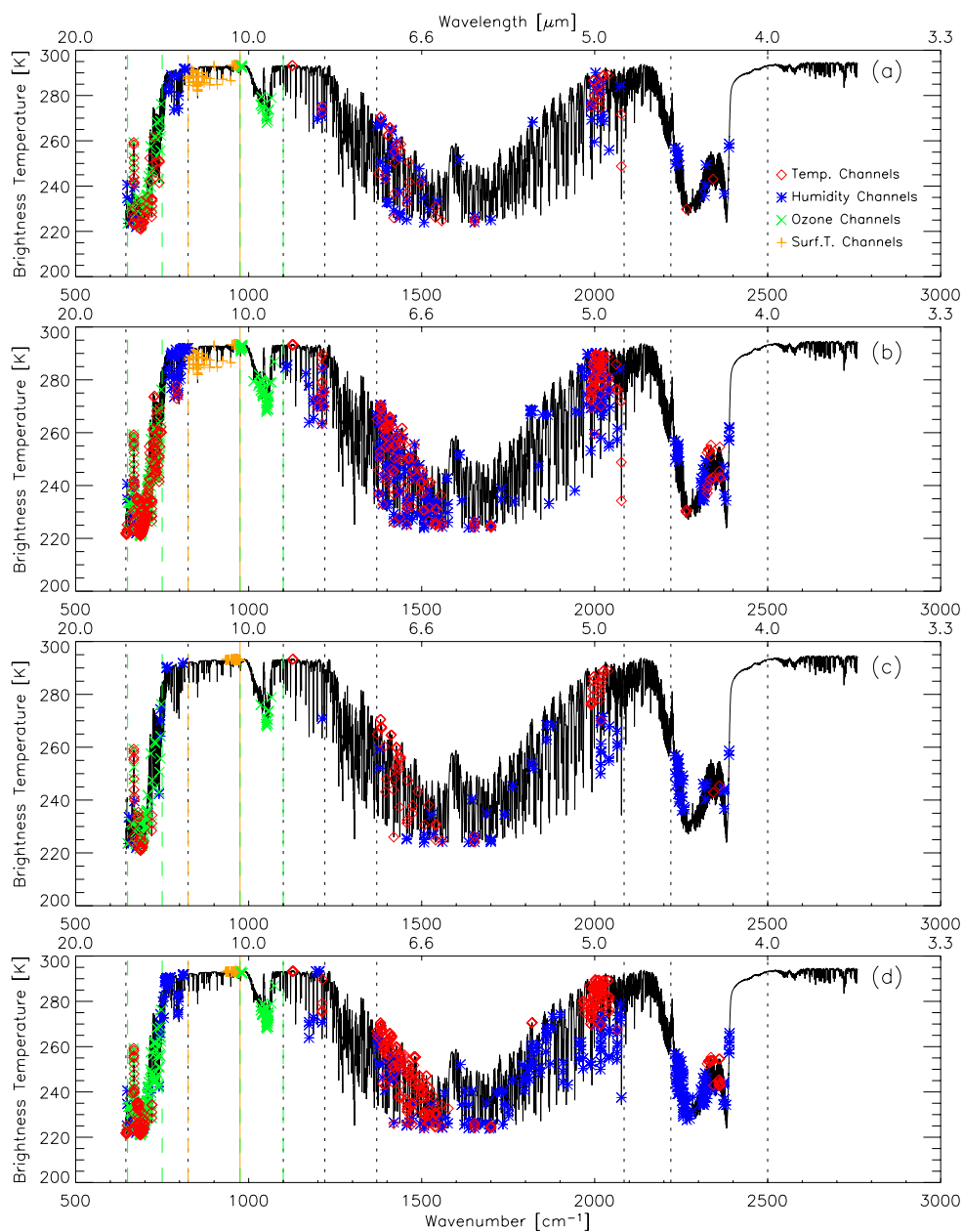


Figure 5.9: Selected channels for temperature, humidity, and ozone profiles as well as for surface skin temperature overplotted on the brightness temperature spectrum calculated with RTIASI for a U. S. standard mid-latitude summer atmosphere. The red diamonds indicate the temperature channels, the blue asterisks the humidity channels, the green crosses the ozone channels and the yellow plus signs the SST channels. Panel (a) and (b) were selected via IC theory whereas for panel (c) and (d) the MS approach was used. The final number of selected channels for the panels (a) and (c) (adding the channels for all constituents) was 310 whereas the summation of the channels for the panels (b) and (d) gave 909.

or the H_2O continuum ranging from $\sim 200 \text{ cm}^{-1}$ to 1200 cm^{-1} , c. f. subsection 1.4.4) there is no special spectral domain preferred for the selection of channels in the allowed

region. This behavior is illustrated well in all four panels of figure 5.9.

Nevertheless the two methods show differences in the region where the channels are selected. The IC theory exhibits an accumulation of chosen channels between 1400 cm^{-1} and 1600 cm^{-1} and around 2000 cm^{-1} (c. f. the accumulation of the temperature channels selected with the MS approach) whereas the MS method has clusters of chosen channels near 2300 cm^{-1} .

Concluding it can be said that an intelligent channel selection method is essential for a useful retrieval. Especially a clustering of channels which is too strong or ignoring crucial spectral regions by a selection method yields a degradation of the results. The impact of the two channel selection methods described here on the retrieval accuracy is discussed in section 6.2. For a temperature only retrieval this was shown in [Weisz (2001), Weisz *et al.* (2003)].

Chapter 6

Retrieval Results and Performance Analysis

In the previous chapters the theoretical background as well as some practical implementation setups were described. In chapter 3 the inversion scheme used in this study was derived, chapter 4 introduced the forward model used, and chapter 5 provided a description of the retrieval setup, including the definition of the covariance matrices as well as the channel selection schemes.

The task of this chapter is to show the performance of the developed algorithm. At the beginning it has to be mentioned that all retrievals in this chapter were performed with the assumption of clear sky all over the retrieval region. In section 6.1 the joint algorithm is compared for different *a priori* profile sets as well as for different sets used for the channels selection. In addition, we will specify the characteristics of the retrieval (e. g. vertical resolution, contribution of a special channel to the retrieved state, etc.) for some representative preselected profiles. Section 6.2 compares the different channel selection algorithms described in section 5.2 for three sets of numbers of selected channels. Finally, section 6.3 compares the results of the joint algorithm with the results of more specific retrieval setups.

The retrievals shown in this chapter were performed for a quasi-realistic orbit arc of METOP with a full swath of the IASI instrument. The swath was modeled by first calculating the ground points of a METOP sub-orbital track using a standard orbit software extracted from the Mission Analysis Planning System of the EGOPS software package [Kirchengast *et al.* (2002)] and then calculating the points along sounding rays defined by the RTIASI pressure level grid via the principles of spherical trigonometry. A detailed description of this procedure is given in the appendix A, section A.1.

The number of profiles for the full orbit resulting from this procedure is 22 800. Figure 6.1 shows the ground track of the simulation region – it is an orbit ranging from Africa over Antarctica, the Pacific Ocean and the Arctic region back to Africa via eastern Europe. The red points show the nadir points of the METOP satellite for every 8-*th* second whereas the green points illustrates the surface points of a selected profile region ranging

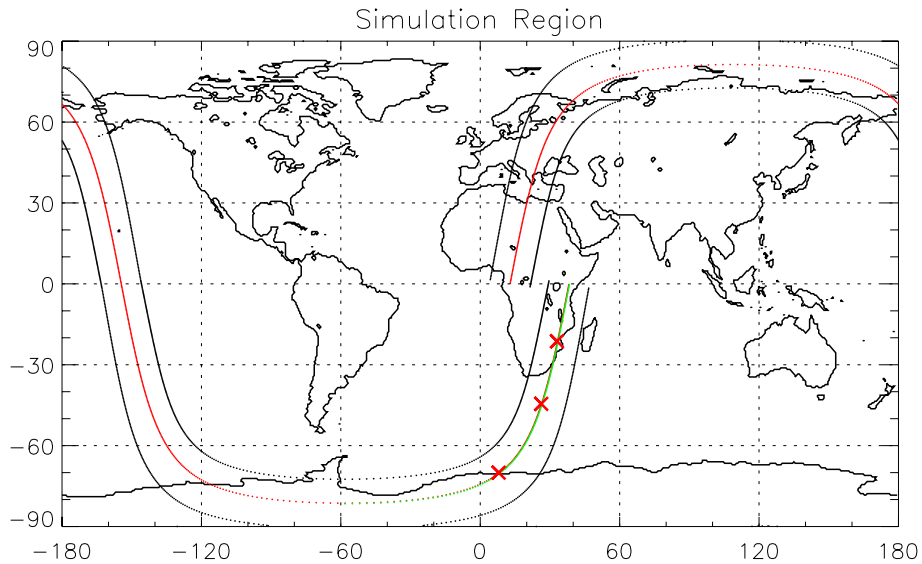


Figure 6.1: Ground track of the simulation region for this study. The red points indicate the nadir points of the METOP satellite for every 8-th second. The green points illustrate the surface points of a selected profile region ranging from Africa to Antarctica (191 profiles) for an obliquity angle of 1.5° . The three red crosses are the positions of the profiles for which the error characterization functions are discussed.

from Africa to Antarctica (191 profiles) for an obliquity angle of 1.5° (almost nadir looking) off the nadir direction. The profiles of this region are shown as exemplary results of the present end-to-end simulation study. The three red crosses indicate the positions of those profiles for which the error characterization functions are shown and discussed (subsection 6.1.2).

To obtain quasi-realistic atmospheric conditions a high resolution (T511L60) ECMWF analysis field from September 15, 2002, 12 UTC, was used to create the "true" profiles. The individual values of the profiles were obtained by interpolating the values of the analysis field to the points according the RTIASI pressure level grid which were calculated via the method described above. The example slices, the location of the "true" field for the 191 profiles whose ground points are illustrated as the green line in Figure 6.1 are shown in Figure 6.2, top, for the temperature profiles, and in Figure 6.3 for the humidity profiles (top) and the ozone profiles (bottom). Figure 6.2, bottom, shows the surface skin temperature (SST) for the whole swath.

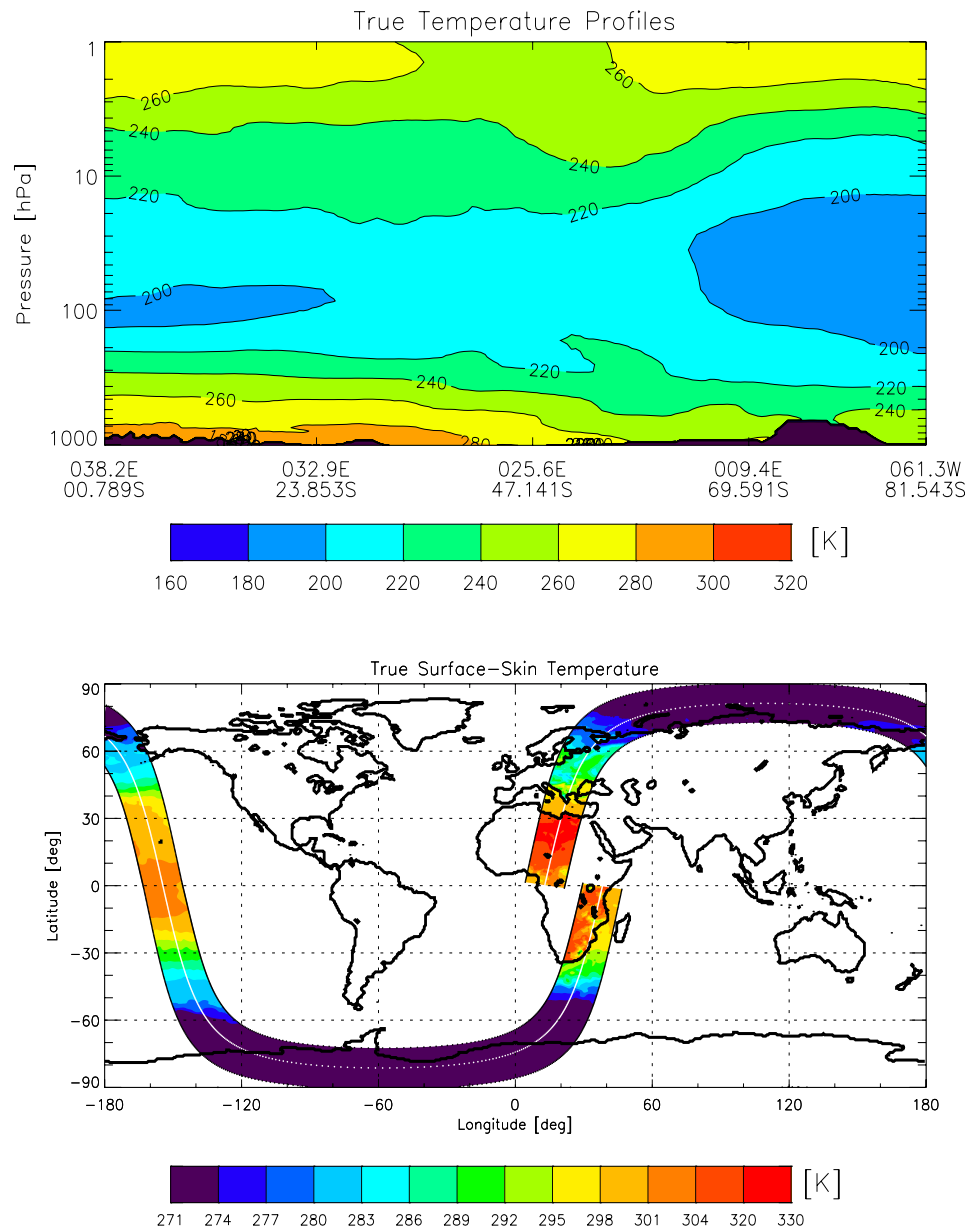


Figure 6.2: "True" temperature profile (top) and surface skin temperature field (bottom) obtained from a high resolution (T511L60) ECMWF analysis field from September 15, 2002, 12 UTC. The profiles are illustrated for the 191 profiles whose ground points are illustrated as the green line in Figure 6.1.

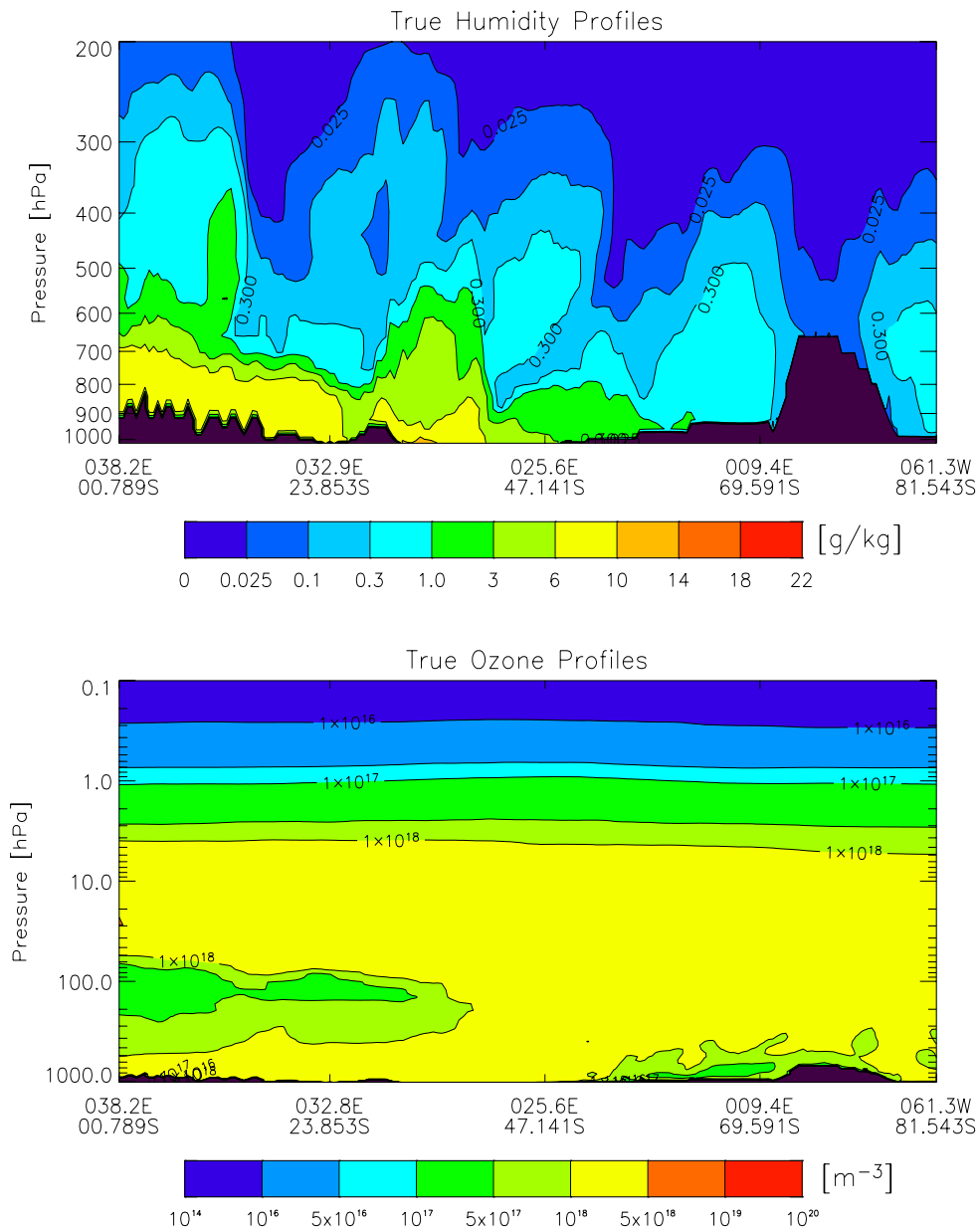


Figure 6.3: "True" specific humidity (top) and ozone (bottom) profiles for the 191 profiles, whose ground points are illustrated as the green line in Figure 6.1, obtained from a high resolution (T511L60) ECMWF analysis field from September 15, 2002, 12 UTC. Note the different pressure ranges (ordinates) of the two panels.

For the initialization of and as background data to the retrieval we used two different types of *a priori* data. On the one hand our intention was to show the performance of the retrieval algorithm under quasi realistic conditions. For this purpose we used the 24-hour ECMWF forecast field of the ECMWF analysis field introduced above. The difference between the analysis field and the 24-hour forecast field for the selected profile region denoted by the green line in Figure 6.1 is shown in Figure 6.4, top, for the temperature profiles and in Figure 6.5, top, for the humidity profiles. For ozone and SST the forecast -minus-analysis difference was not directly used, since in both cases the difference between forecast and analysis field was too small to be of direct use for testing the performance of the retrieval algorithm. The *a priori* data for ozone and SST were rather obtained by creating them consistent with the assumed *a priori* error covariance matrices (c. f. subsection 5.1.2) via the method described in subsection 5.1.4. Figure 6.4, bottom shows the differences in SST for the whole swath and Figure 6.5, bottom, shows the differences for the ozone profile slice.

Additionally, in the top panel of Figure 6.6, bias (black line), standard deviation (yellow line), empirical rms (dashed blue line), and 2 times standard deviation of bias (solid blue line) of all 22 800 profiles for temperature, humidity, and ozone are illustrated whereas in the bottom panel the same is shown for the 15 233 points of the sea surface temperature; the error data of the surface shown here contain only the points over the ocean surface.

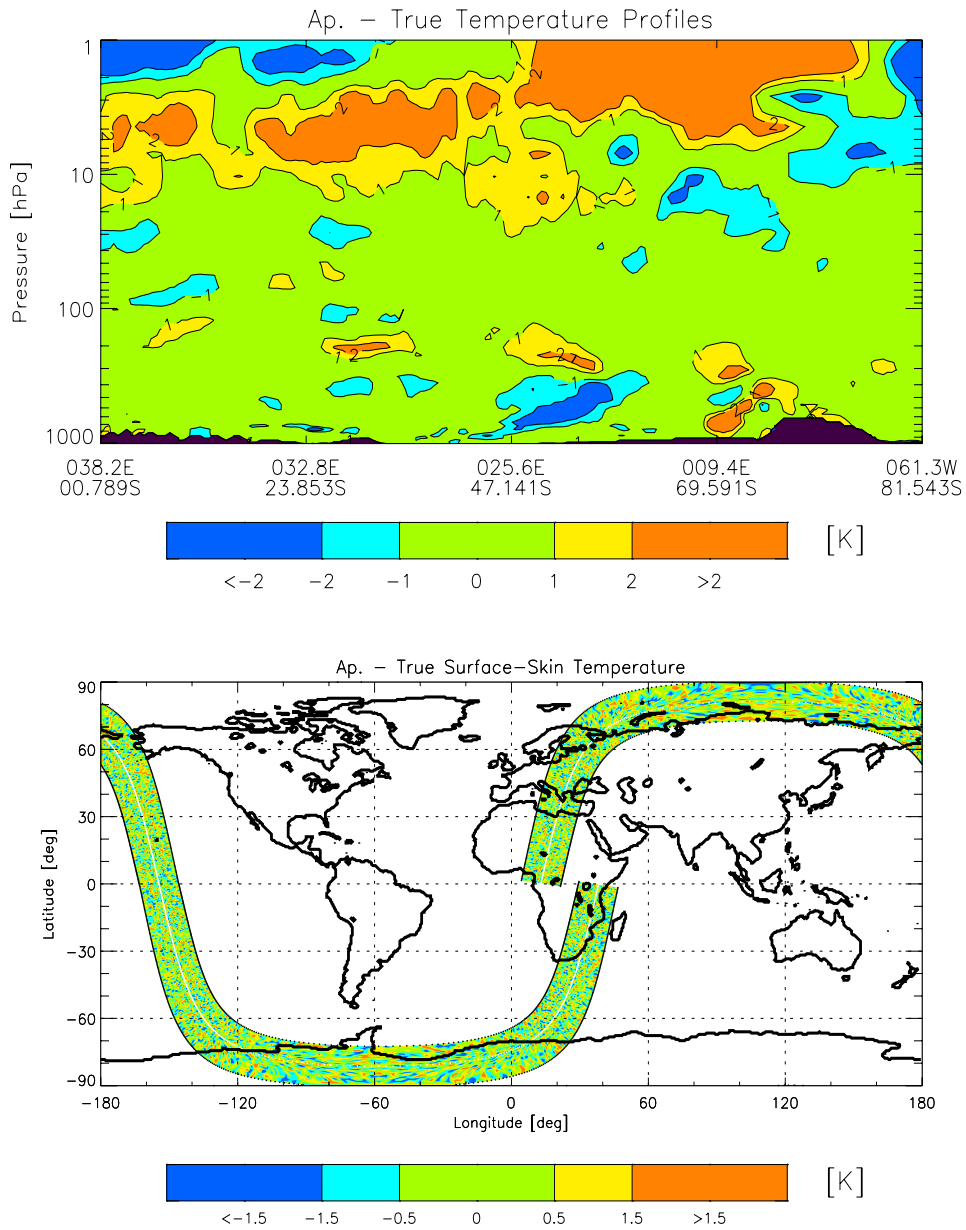


Figure 6.4: 24-hour forecast field minus analysis field for an ECMWF T511L60 analysis from September 15, 2002, 12 UTC. The profiles are illustrated for the 191 profiles whose ground points are illustrated as the green line in Figure 6.1. In the top panel the difference of the temperature profiles are shown whereas the bottom panel shows the difference in SST. The SST *a priori* data were constructed from the assumed *a priori* uncertainties of 1.5 K (c. f. subsection 5.1.2).

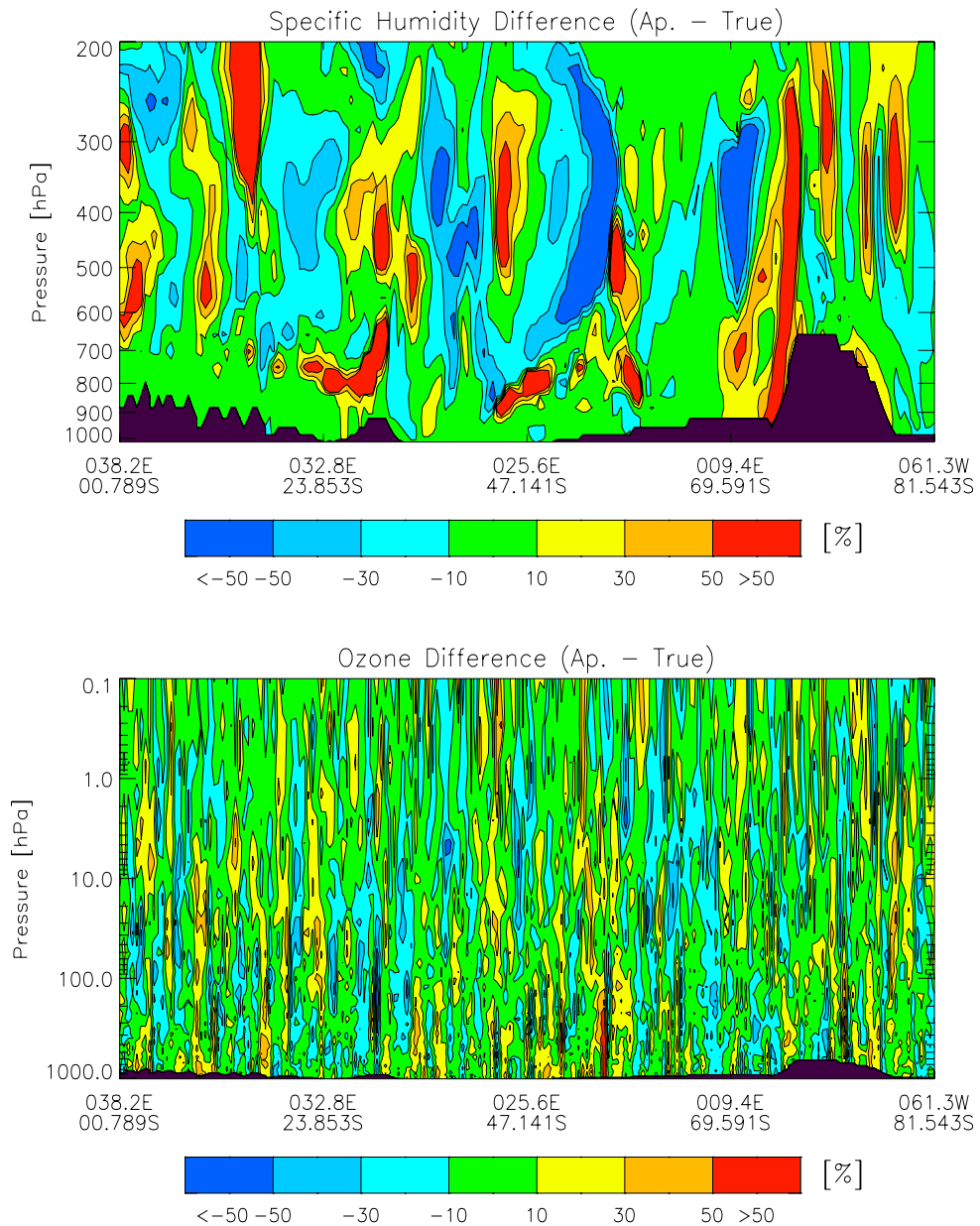


Figure 6.5: 24-hour forecast field minus analysis field for an ECMWF T511L60 analysis from September 15, 2002, 12 UTC. The profiles are illustrated for the 191 profiles whose ground points are illustrated as the green line in Figure 6.1. The top panel shows the difference of the specific humidity profiles and the bottom panel the difference of the ozone profiles. The ozone *a priori* data were constructed from the assumed *a priori* ozone error covariance matrix (c. f. subsection 5.1.2).

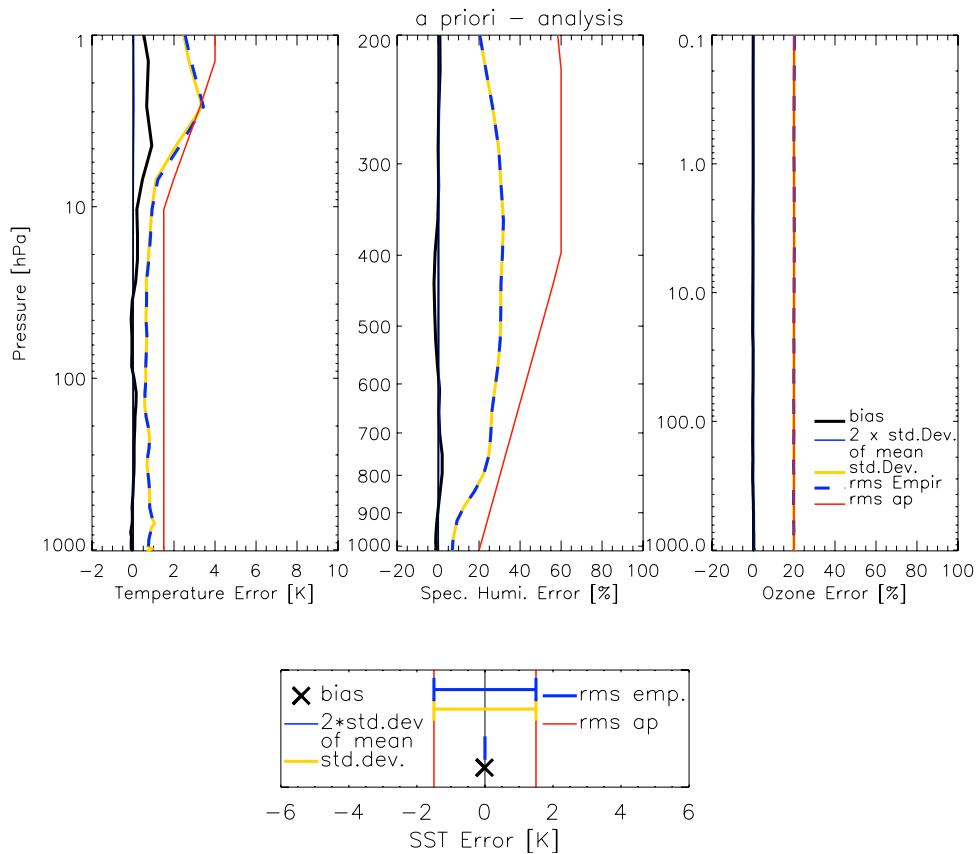


Figure 6.6: Bias (black line), 2 times standard deviation of bias (solid blue line), standard deviation (yellow line), and rms (dashed blue line) of the 24-hour forecast field minus analysis field for an ECMWF T511L60 analysis from September 15, 2002, 12 UTC, for the 22 800 temperature (top left), humidity (top middle), and ozone (top right) profiles as well as for the 15 233 SST points (bottom). The red lines denote the diagonal elements which were used to create the *a priori* error covariance matrices.

A second intention was to create a platform for a good comparison of the different channel selection methods (see section 6.2) and retrieval setups (see section 6.3) discussed in this study. For this purpose we created *a priori* data consistent with the *a priori* error covariance matrices for temperature, humidity, and ozone (c. f. section 5.1.2) by perturbing the "true" field via the method described in section 5.1.4. The results of this process are illustrated in Figure 6.7 (difference between true and *a priori* temperature profile (top) and true and *a priori* SST (bottom)) and in Figure 6.8 (difference between true and *a priori* humidity (top) and ozone (bottom) profiles). It is re-called that the *a priori* SST uncertainty was set to 1.5 K.

Figure 6.9 shows the error data of this kind of *a priori* setup. Once more the black line illustrates the bias, the yellow line the standard deviation, and the dashed blue line the rms. A specific comment has to be made on the humidity data: As can be seen in Figure 6.9, top middle, the *a priori* data is in some parts no longer consistent with the *a priori* error covariance matrix. The reason for this is that a cut-off (at most 90% perturbation was allowed) was introduced to avoid unphysical (negative) humidity values which would lead to inconsistencies in the retrieval.

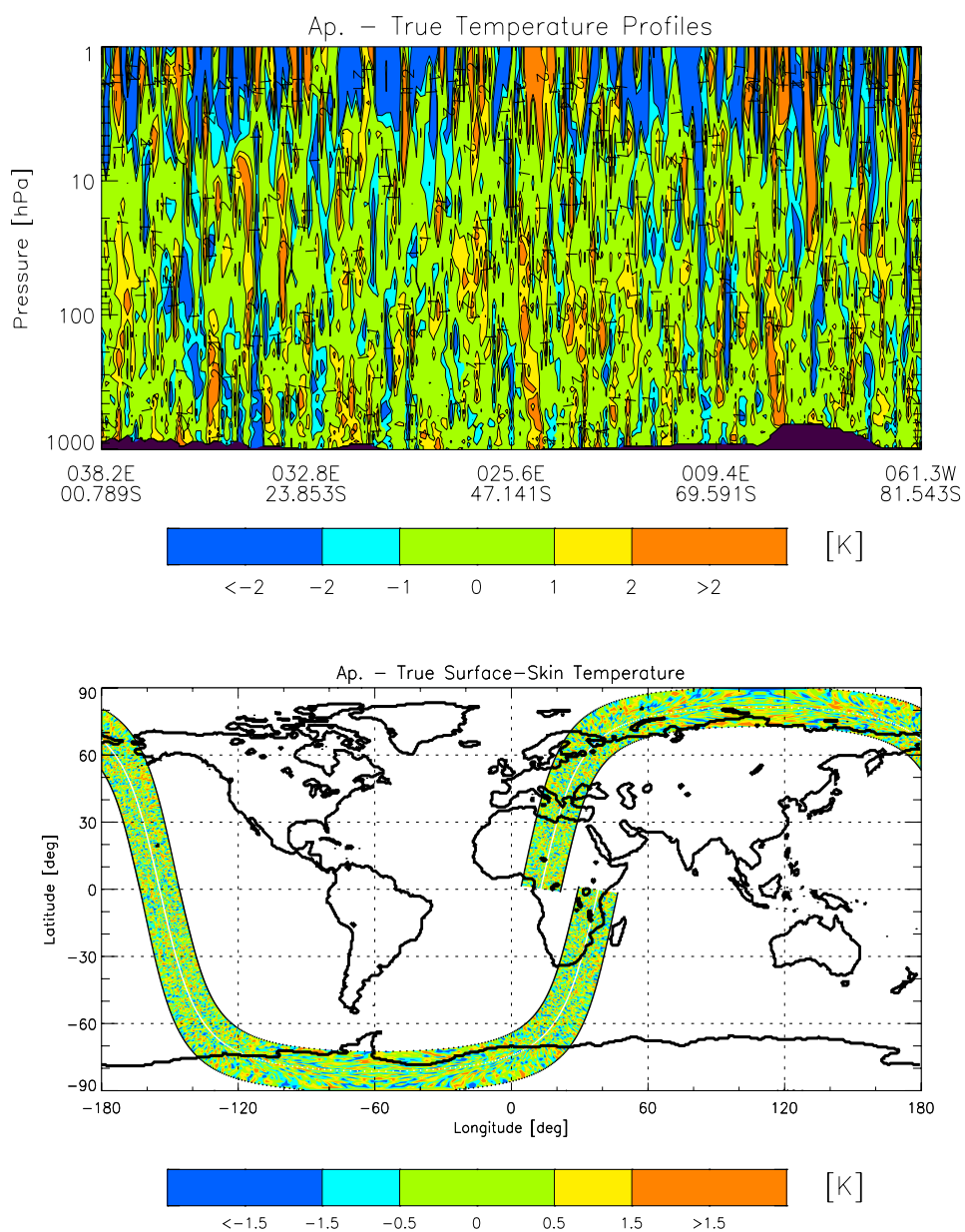


Figure 6.7: Difference between the "true" field (high resolution T511L60 ECMWF analysis field from September 15, 2002, 12 UTC) and the *a priori* field created out of the "true" field via the method described in section 5.1.4. In the top panel the difference of the temperature profiles are shown whereas the bottom panel indicates the difference in SST.

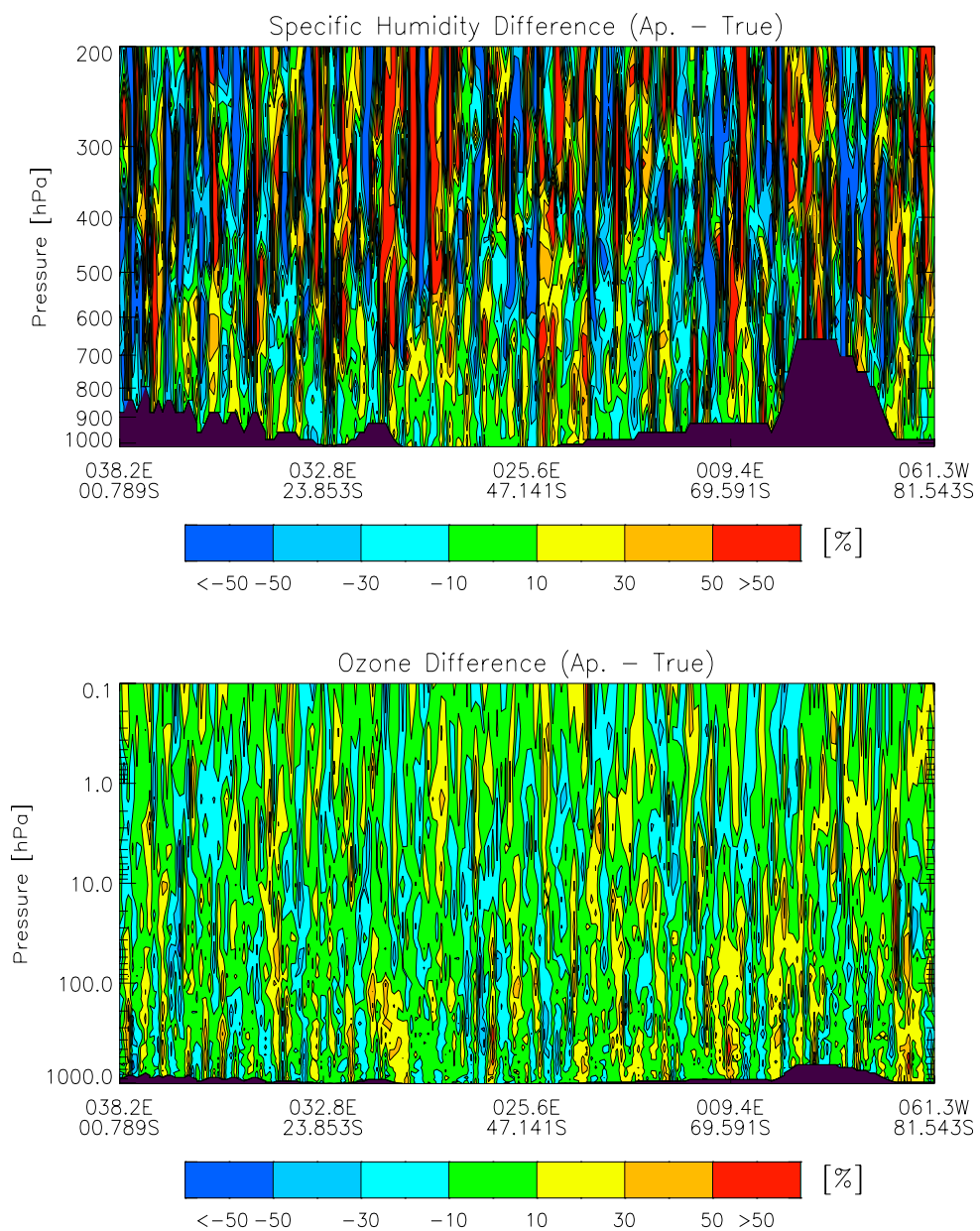


Figure 6.8: Difference between the "true" field (high resolution T511L60 ECMWF analysis field from September 15, 2002, 12 UTC) and the *a priori* field created out of the "true" field via the method described in section 5.1.4. The top panel shows the difference of the specific humidity profiles and the bottom panel the difference of the ozone profiles.

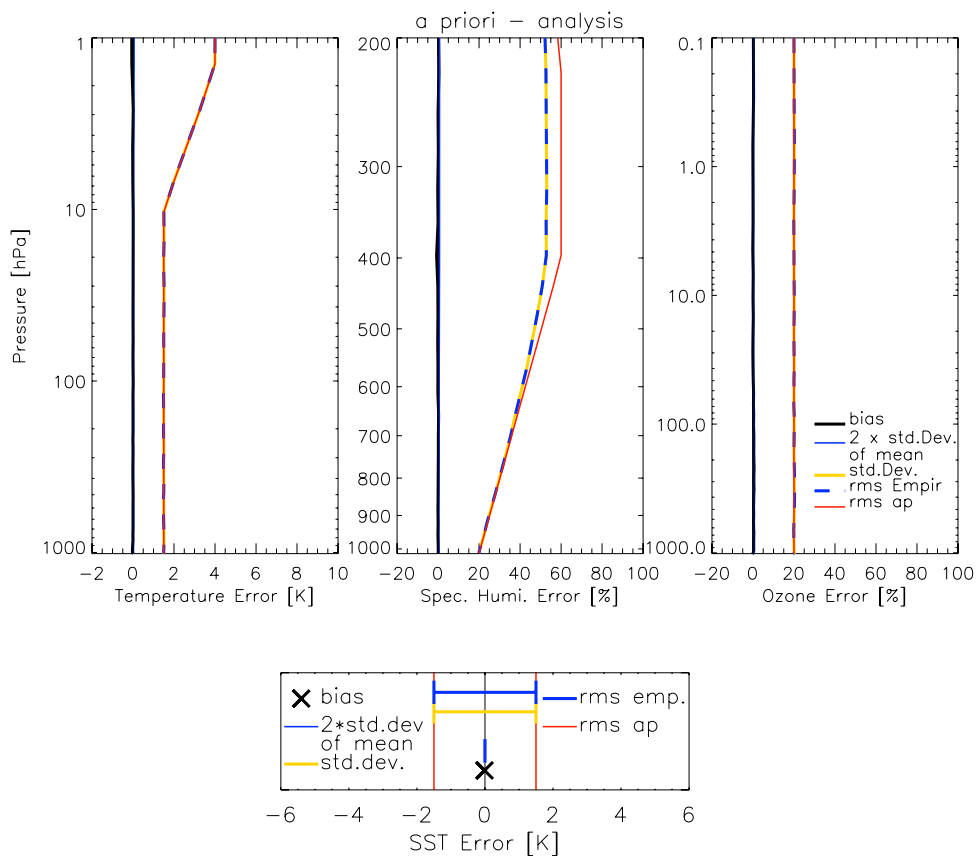


Figure 6.9: Bias (black line), 2 times standard deviation of bias (solid blue line), standard deviation (yellow line), and rms (dashed blue line) of the *a priori* data consistent with the *a priori* error covariance matrices minus analysis field for an ECMWF T511L60 analysis from September 15, 2002, 12 UTC, for the 22 800 temperature (top left), humidity (top middle), and ozone (top right) profiles as well as for the 15 233 SST points (bottom). The red lines denote the diagonal elements which were used to create the *a priori* error covariance matrices.

6.1 Performance Analysis of the Joint Algorithm

The aim of this section is to show the performance of the joint algorithm via the comparison of three different initial sets (i. e. different *a priori* data combined with different data sets used to perform the channel selection; subsection 6.1.1) and by showing the characterization functions of the retrieval for some representative profiles (subsection 6.1.2).

6.1.1 Retrieval Results for a Full Orbit

The first set of this section uses the *a priori* data illustrated in Figure 6.4 and Figure 6.5 which combines the 24-hour forecast data for temperature and humidity profiles with *a priori* data consistent with the *a priori* error covariance matrices for ozone profiles and SST. The selected channels used in this set were derived in performing the IC algorithm (c. f. section 5.2.1) for selecting ~ 300 channels on the CIRA86aQ climatology [Kirchengast *et al.* (1999)] with suitable ozone profiles obtained from U. S. standard profiles (source: http://nssdc.gsfc.nasa.gov/space/model/atmos/us_standard.html).

The second set consists of the same *a priori* data as the first set but uses the 24-hour forecast data themselves for channel selection (except in the case of ozone where the same channels as in the first set were used).

The third set uses the *a priori* data illustrated in Figure 6.7 and Figure 6.8 which consists of data consistent with the *a priori* error covariance matrices for temperature, humidity, ozone, and SST (c. f. section 5.1.2) by perturbing the "true" field via the method described in section 5.1.4.

In Figure 6.11 the results of the retrieval process for the temperature profile for these three initial sets are illustrated for the 191 profiles indicated by the green line of Figure 6.1. Comparing the results of the upper two panels with the initial state shown in Figure 6.4, top, we find improvements in the troposphere where the parts with a difference bigger than ± 2 K as well as those parts with differences between 1 and 2 K have clearly decreased. In the stratosphere we find similar improvements with the restriction that the higher we get up the smaller is the gain in information we obtain from the measurement.

A deeper view is obtained by examining the error statistic data for all 22 800 profiles shown in Figure 6.10 in detail. Comparing the left and the middle panel with the initial state given by the top left panel of Figure 6.6 we find that the bias arising in the stratospheric *a priori* data could mostly be deleted by the inclusion of information from the IASI instrument. Furthermore, a decrease in standard deviation and rms, respectively, could be gained, significantly seen in the stratosphere but also present in the tropospheric region.

A comparison of the left and the middle panel of Figure 6.10 which has the equivalent meaning of the comparison of the retrieval results for two different data sets used in the channel selection process points out that the differences only occur in the second digit. Since the usage of the climatology for the channel selection process is much more

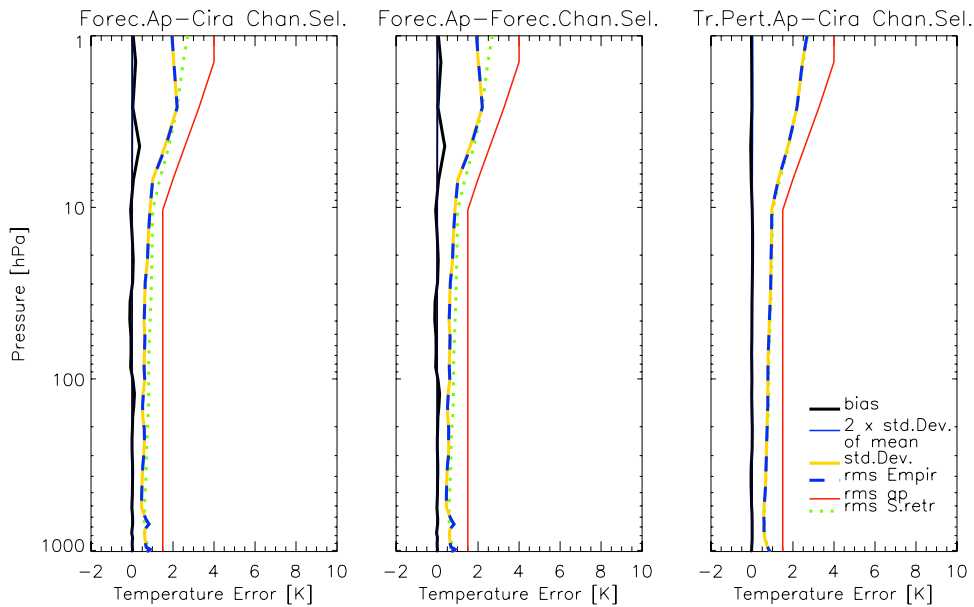


Figure 6.10: Error statistic data for temperature profiles for three different initial data sets: left panel: 24-hour forecast data for temperature and humidity profiles combined with *a priori* data consistent with the *a priori* error covariance matrices for ozone profiles and SST as first guess and the CIRA86aQ climatology [Kirchengast *et al.* (1999)] with suitable ozone profiles obtained from U. S. standard profiles used for the channel selection process; middle panel: the same first guess as in the left panel but using the forecast data themselves (except for ozone) for the channel selection process; right panel: *a priori* data consistent with the *a priori* error covariance matrices for temperature, humidity, and ozone profiles and SST as first guess and the same channel selection set as in the left panel. The legend corresponds to the legend of Figure 6.6. The additional dotted green line denotes the theoretical estimate of the rms (diagonal elements of the retrieval error covariance matrix, c. f. section 3.3) of the finally accepted best state estimate.

efficient than using the forecast data because we have to select the channels only one time (in comparison to a successive selection in the case of using the forecast data) we strongly suggest to perform the selection of the channels used in the retrieval process on a climatology rather than on forecast data.

Figure 6.11, bottom, and the right panel of Figure 6.10, respectively, show the results for a retrieval where the *a priori* data (c.f. Figure 6.7, top, and Figure 6.9, top left, respectively) perfectly fits the *a priori* error covariance matrices. We see that in this case the obtained standard deviation of the retrieval is the same as its theoretical estimate (diagonal elements of the retrieval error covariance matrix, c. f. section 3.3, of the finally accepted best state estimate; dotted green line of Figure 6.10) which is in contrast to the two other cases where the standard deviation is mostly better than the theoretical one resulting from the better first guess. This last case is the basic set for the comparison of the retrievals for temperature, humidity, ozone, and SST for the different channel selection methods as well as for comparing the results of the joint retrieval and the more specific ones.

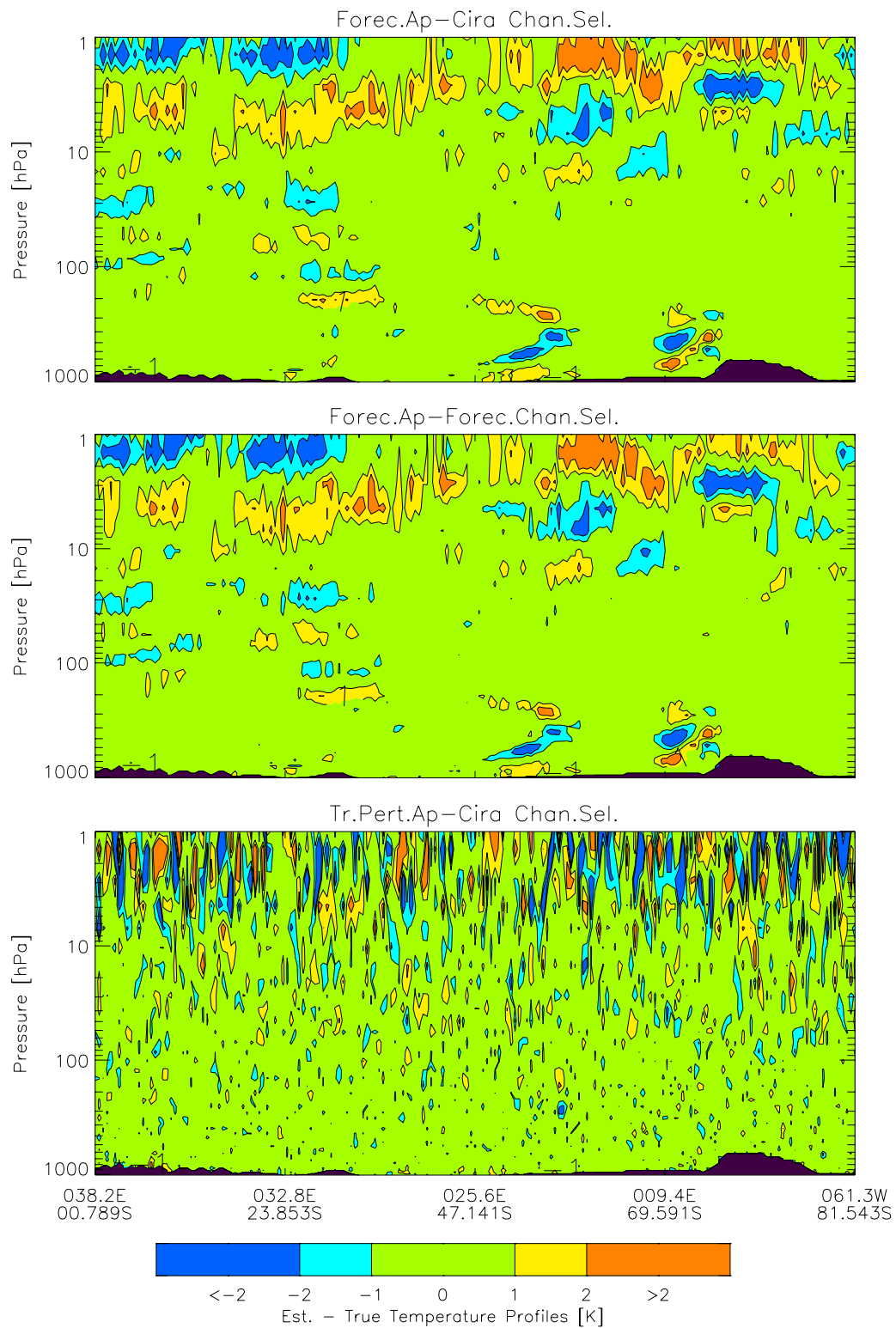


Figure 6.11: Example results of retrieved minus true temperature profiles for the 191 profiles denoted by the green dots in Figure 6.1 for three different initial data sets: The initial datasets for the topmost panel is the same as for the left panel of Figure 6.10, the two middle panels correspond to one another, and the right panel of Figure 6.10 corresponds to the bottom panel here.

Comparing the results of the retrieved humidity when using the joint algorithm (see Figure 6.12 for the error statistics and Figure 6.13 for the example results of the 191 profiles) mostly the same can be said as in the case of the estimation of temperature. We once more recognize that the resulting rms (standard deviation) for the left and the middle panel of Figure 6.12 is better than the theoretical estimate of it and once more the results for the different profile sets used in the channel selection process are quite the same.

In the case of the retrieval with an initial guess consistent with the *a priori* error covariance matrices (c. f. Figure 6.12, right panel) we observe that the theoretical estimate of the rms is slightly better than the rms obtained by the retrieval. This effect results from the fact that the perturbation of the humidity profiles, which is based on the estimation of humidity errors of the ECMWF forecast field, is quite high (up to 60 %, c. f. Figure 6.9, top middle). In this case the humidity profiles can not be retrieved exactly since our assumption of a linear, or moderately non-linear problem, respectively, is not fully satisfied. The small bias seen in the upper tropospheric region can also explained by this fact. Note, that a test run with a smaller perturbation of the first guess exhibits no differences between theoretically estimated and empirically analyzed rms as well as shows no bias occurring.

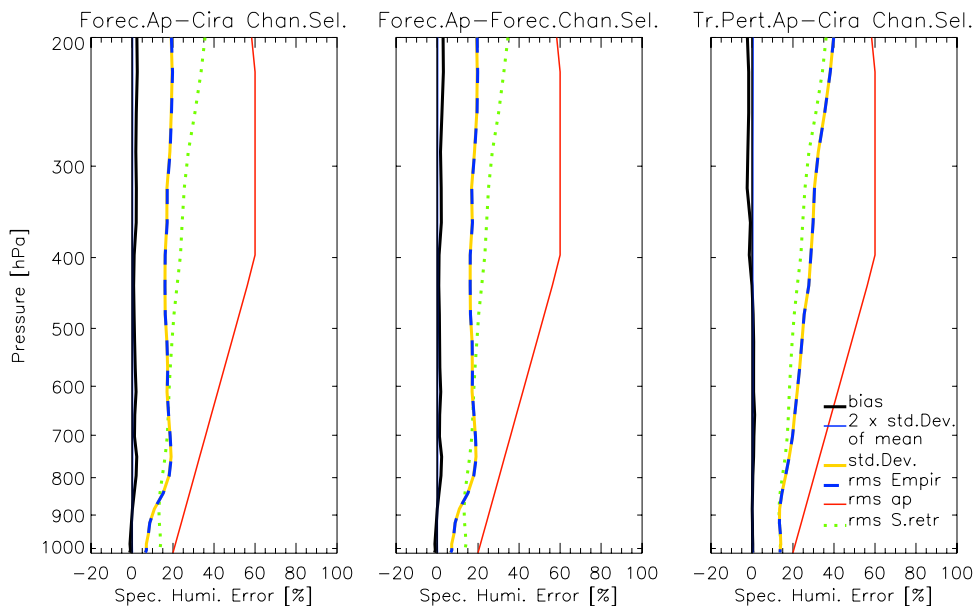


Figure 6.12: Error statistic data for humidity profiles for three different initial data sets: The initial datasets for these panels correspond to those of Figure 6.10. The legend corresponds to the legend of Figure 6.6. The additional dotted green line denotes the theoretical estimate of the rms (diagonal elements of the retrieval error covariance matrix, c. f. section 3.3) of the finally accepted best state estimate.

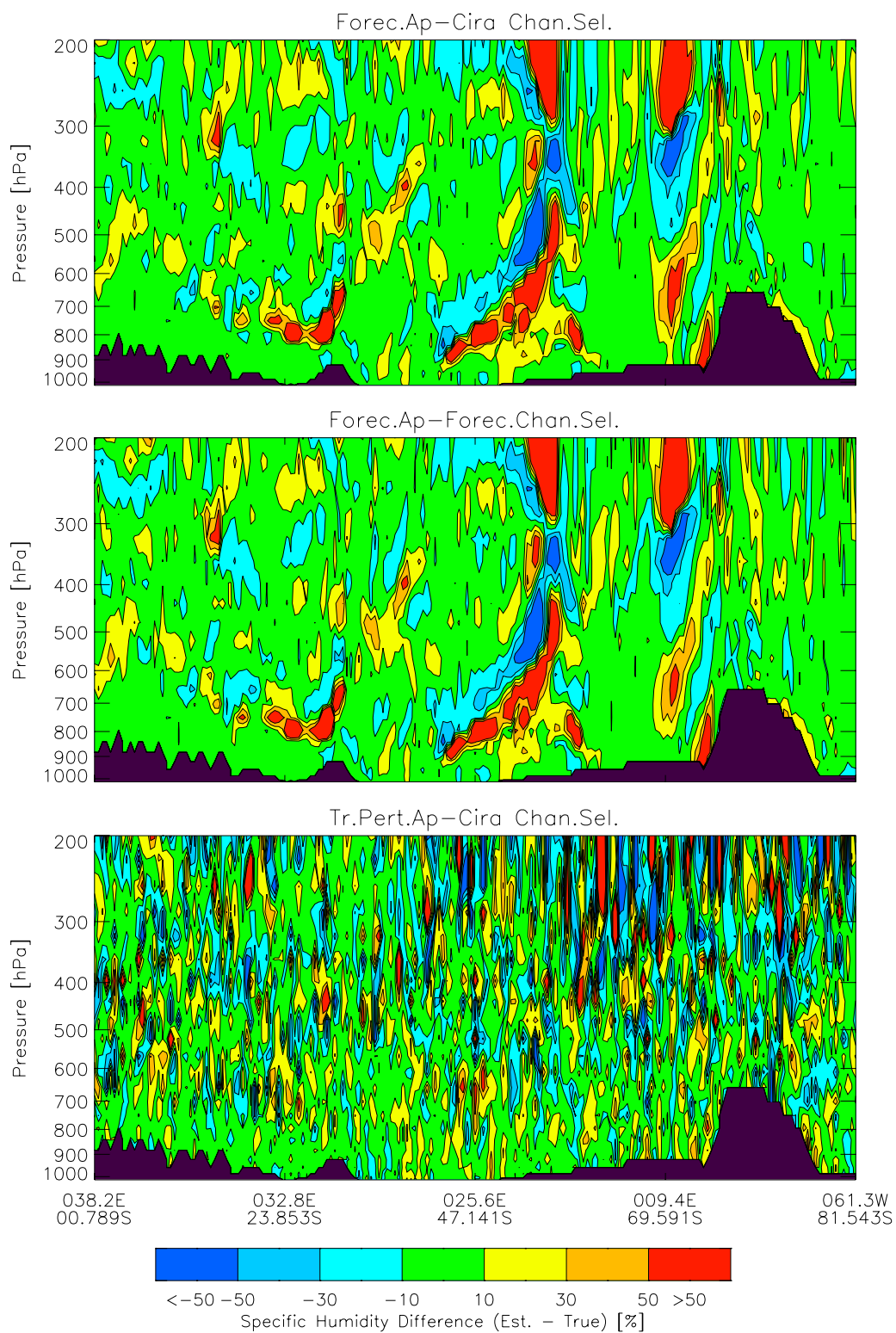


Figure 6.13: Exemplary results of retrieved minus true humidity profiles for the 191 profiles denoted by the green dots in Figure 6.1 for three different initial data sets: The initial datasets for these panels correspond to those of Figure 6.11.

In the case of the retrieved ozone profiles, when using the joint algorithm (c. f. Figure 6.14 for the error statistics and Figure 6.15 for the exemplary results of the 191 profiles*), we get the same results for all three cases. This should be evident since the initial ozone data for all three cases is the same (as mentioned above, the reason, to use an initial guess for ozone consistent with the *a priori* error covariance matrix with 20 % error in its diagonal in the case of using the 24-hour forecast data for temperature and humidity is that the 24-hour forecast for ozone has an rms of only 3 % and therefore is not really useful for showing the performance of the algorithm). What we are able to learn from this is that the ozone retrieval is rather independent from the initial guess used for temperature and humidity which is also true vice versa (c. f. subsection 6.3.3).

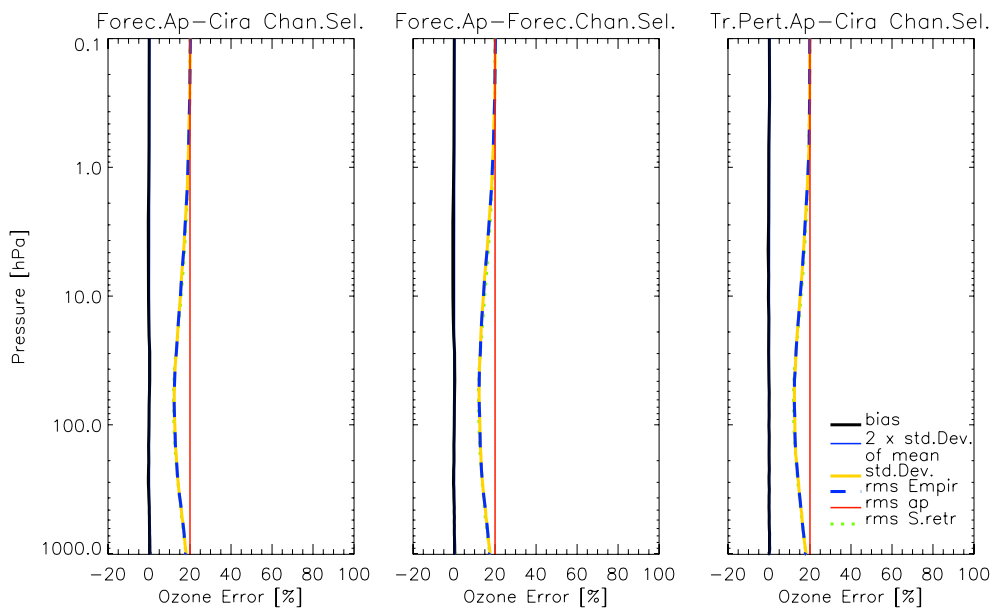


Figure 6.14: Error statistic data for ozone profiles for three different initial data sets: The initial datasets for these panels correspond to those of Figure 6.10. The legend corresponds to the legend of Figure 6.6. The additional dotted green line denotes the theoretical estimate of the rms (diagonal elements of the retrieval error covariance matrix, c. f. section 3.3) of the finally accepted best state estimate.

Figure 6.14 indicates that we get improvements of the ozone data only in regions of high concentration of ozone (“ozone layer”) due to the fact that the weighting functions of ozone exhibit important peaks only at this height (c. f. subsection 6.1.2).

*Note that for the conversion of the estimated ozone from mixing ratios to number densities we utilized the estimated states of temperature and humidity. Therefore the errors of temperature and humidity are included in the difference plots shown here. This is not true for the error analysis data of the ozone profiles since the error analysis was performed before the conversion took place.

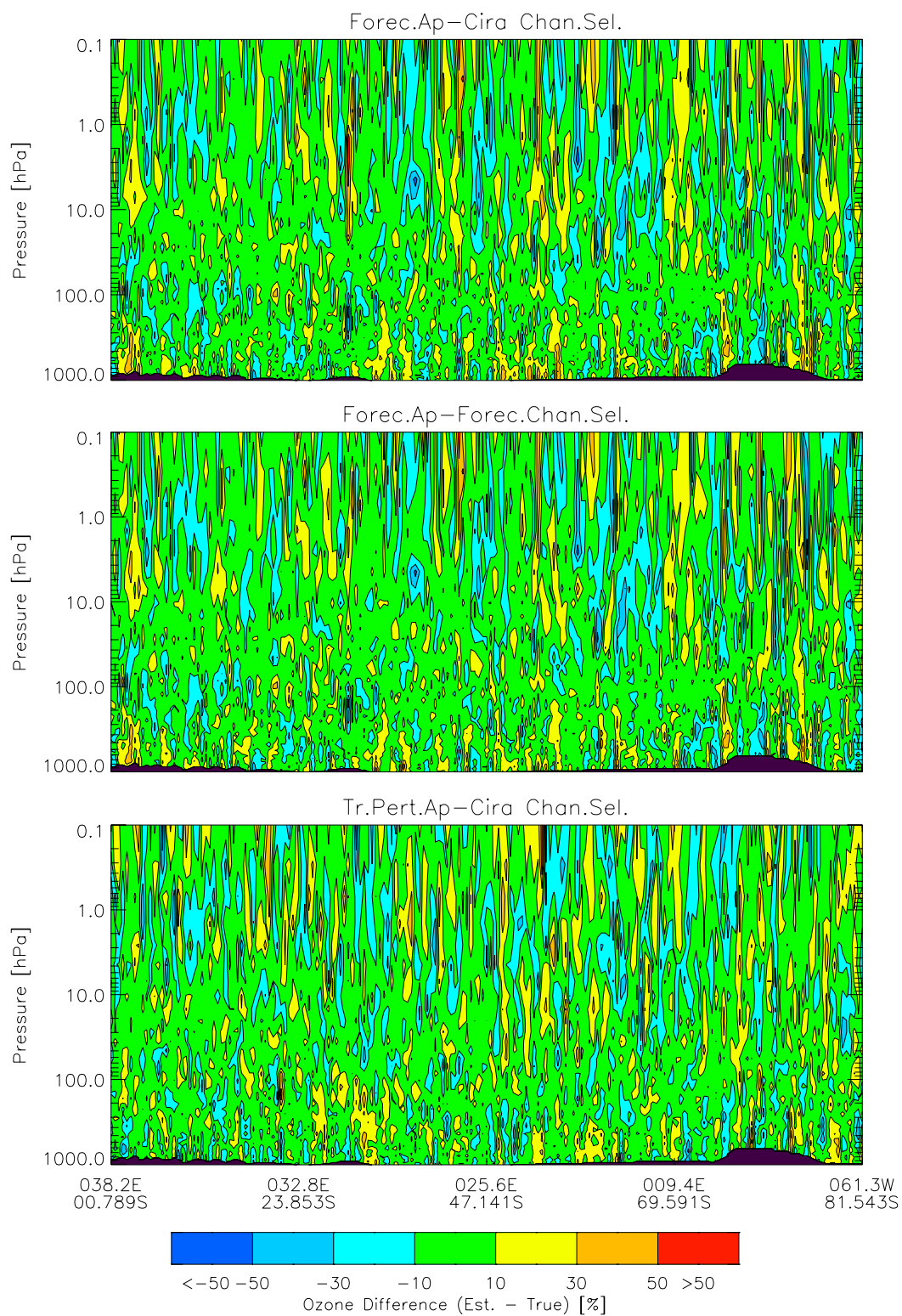


Figure 6.15: Exemplary results of retrieved minus true ozone profiles for the 191 profiles denoted by the green dots in Figure 6.1 for three different initial data sets: The initial datasets for these panels correspond to those of Figure 6.11.

For the initial guess of the surface skin temperature the same applies as for the ozone profile data. We once more detect a strong independency on the data set used for the channel selection (c. f. Figure 6.16, panel (a) and (b), and Figure 6.17, top and middle panel). Examining the differences of the SST retrieval for different initial guesses of the whole atmosphere (by comparing the panels (a) and (b) of Figure 6.16 with panel (c) of the same Figure or the top and the middle panel of Figure 6.17 with the bottom panel, respectively) we can realize slightly better results for the retrieval which uses the forecast as *a priori* data, due to the fact that the near-surface variability of the temperature profile of the 24-hour forecast is smaller compared to the initial guess consistent with the *a priori* error covariance matrices. Also in contrast to the retrieval no correlation between surface data and profile data was taken into account in the perturbation process. Despite these subtleties, any such differences of the three results are of no practical relevance.

A closer examination of Figure 6.16 shows that the retrieval exhibits better results for the rms than the theoretical estimate proposes which most distinctly can be seen in using the forecast data for temperature and humidity as first guess, but is also present in the case of using *a priori* data consistent with the *a priori* error covariance matrices for all retrieved atmospheric parameters. This can be explained by the fact that the retrieval of SST is highly dependent on the retrieval of the overlying atmosphere (c. f. subsection 6.3.1).

It has to be mentioned here that the reason for the good results all over the swath is the assumption of a clear sky all over the retrieval region. As mentioned in section 1.5, the retrieval would stop at the cloud top in the case of the presence of cloudiness over some area. However, as cloudiness can be reasonable well detected and as SST variability is small over a few days time scale, the results indicate that IASI is clearly a promising instrument for accurate SST sounding in an operational manner.

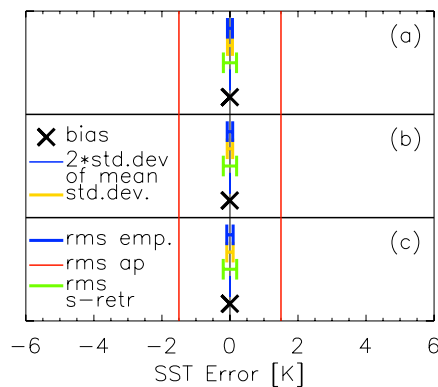


Figure 6.16: Error statistic data for SST for three different initial data sets: The initial dataset of panel (a) corresponds to the left panel of Figure 6.10, panel (b) corresponds to the middle panel of Figure 6.10, and panel (c) corresponds to the right panel of Figure 6.10.

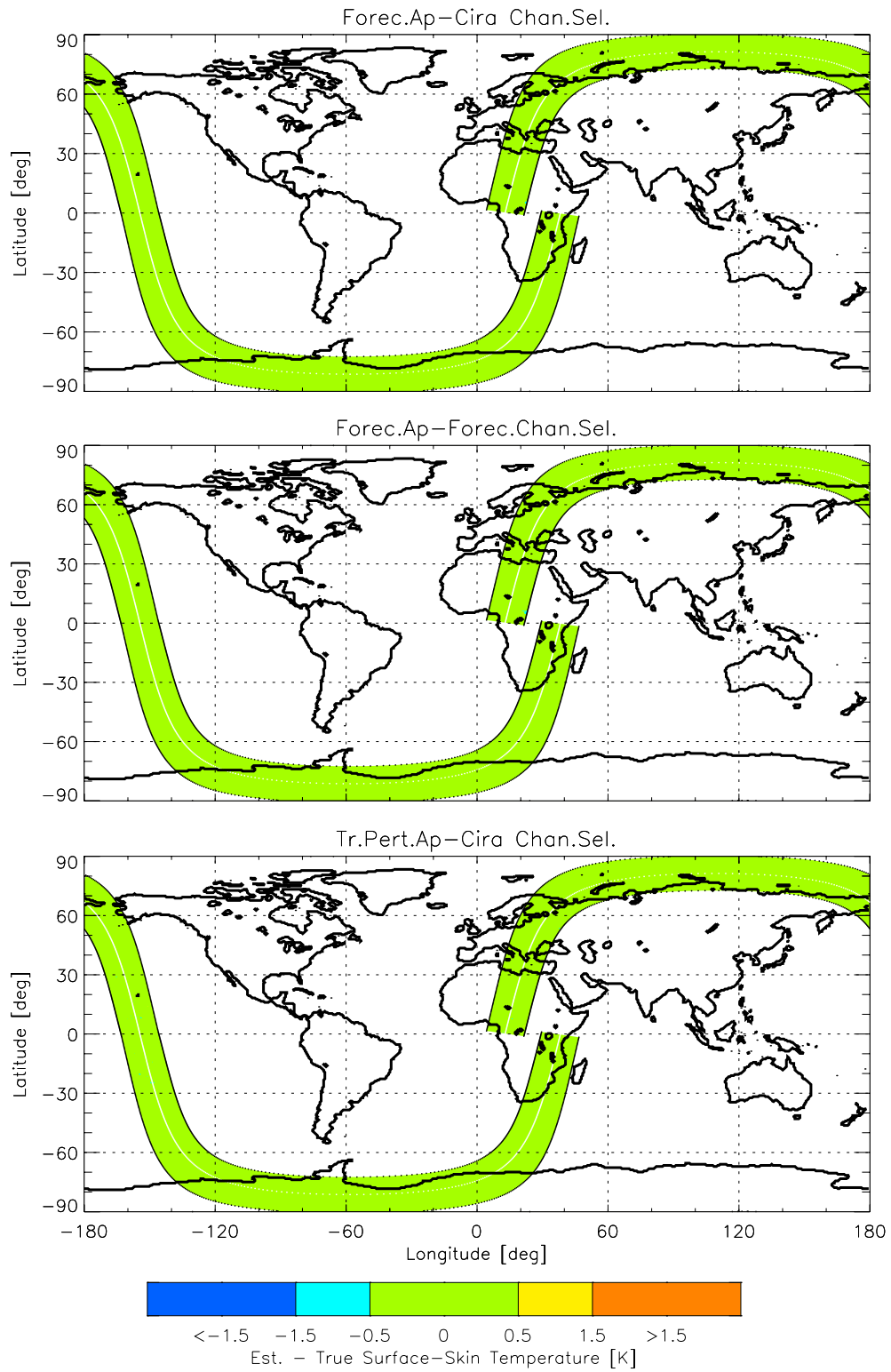


Figure 6.17: Retrieved minus true SST for three different initial data sets: The initial datasets for these panels correspond to those of Figure 6.11.

6.1.2 Profile Retrieval Characterization Results

In this subsection characterization functions of the retrieval for some representative profiles are shown. The profiles were chosen from the case of using forecast data for temperature and humidity profiles and data consistent with the *a priori* error covariance matrices for ozone and SST as first guess and using the CIRA86aQ climatology [Kirchengast *et al.* (1999)] with suitable ozone profiles obtained from U. S. standard profiles for selecting ~ 300 channels via the IC method. We will show characteristic properties of the retrieved profiles (temperature, humidity, and ozone) including correlation functions, weighting functions, resolution kernels, gain functions, and signal to noise functions.

Figure 6.18 shows the true, *a priori*, and estimated temperature (first row), humidity (second row), and ozone (last row) profiles for three different cases, a low (21.3° south, 33.0° east – first column), a mid (44.5° south, 26.2° east – second column), and a high (70.0° south, 7.9° east – third column) latitude case. These profiles are investigated in detail in the following which means that the various characterization functions mentioned above are displayed. These three profiles are illustrated by the red crosses in Figure 6.1 and are extracted from the 191 profiles of the slice illustrated in subsection 6.1.1.

Note that in the case of the ozone profile the estimated profile includes also the errors of the state of temperature and humidity since the retrieval is performed in terms of mixing ratios whereas the profiles are shown as number densities. The errors later shown in the panels (a) and (b) of Figures 6.27, 6.28, and 6.29, respectively, do not include this conversion errors since they are calculated on the mixing ratio level.

Temperature

Let us focus on the retrieved temperature profiles first. The panels (a) of Figure 6.19 and 6.20 instructively show that temperatures near the tropopause and in some stratospheric regions are most difficult to retrieve. The differences near the tropical (~ 100 hPa, c. f. Figure 6.19, panel (a)) and mid-latitude (~ 200 hPa, c. f. Figure 6.20, panel (a)) tropopause originate mainly from the limited resolution available at heights ≥ 200 hPa. In the case of the arctic profile (c. f. Figure 6.21, panel (a)) it is hard to correctly define the height of the tropopause. The salient tropospheric error peak arising at about 450 hPa in the latter case has its reason in a too optimistic assumption of the local *a priori* error (1.5 K in the whole troposphere).

The panels (b) of the Figures 6.19, 6.20, and 6.21 illustrate the estimated retrieval error of the temperature profiles. The estimated total errors (i. e. the square roots of the diagonal elements of \hat{S} , c. f. Equation 3.40) depend mainly on the shape of the weighting functions as well as on the assumed *a priori* errors. On a closer examination this total error estimate is mostly determined by the smoothing error (square roots of the diagonal elements of the smoothing error covariance matrix, c. f. Equation 3.54) which is largest in the stratosphere where the *a priori* errors are important and the resolution kernels in \mathbf{A}

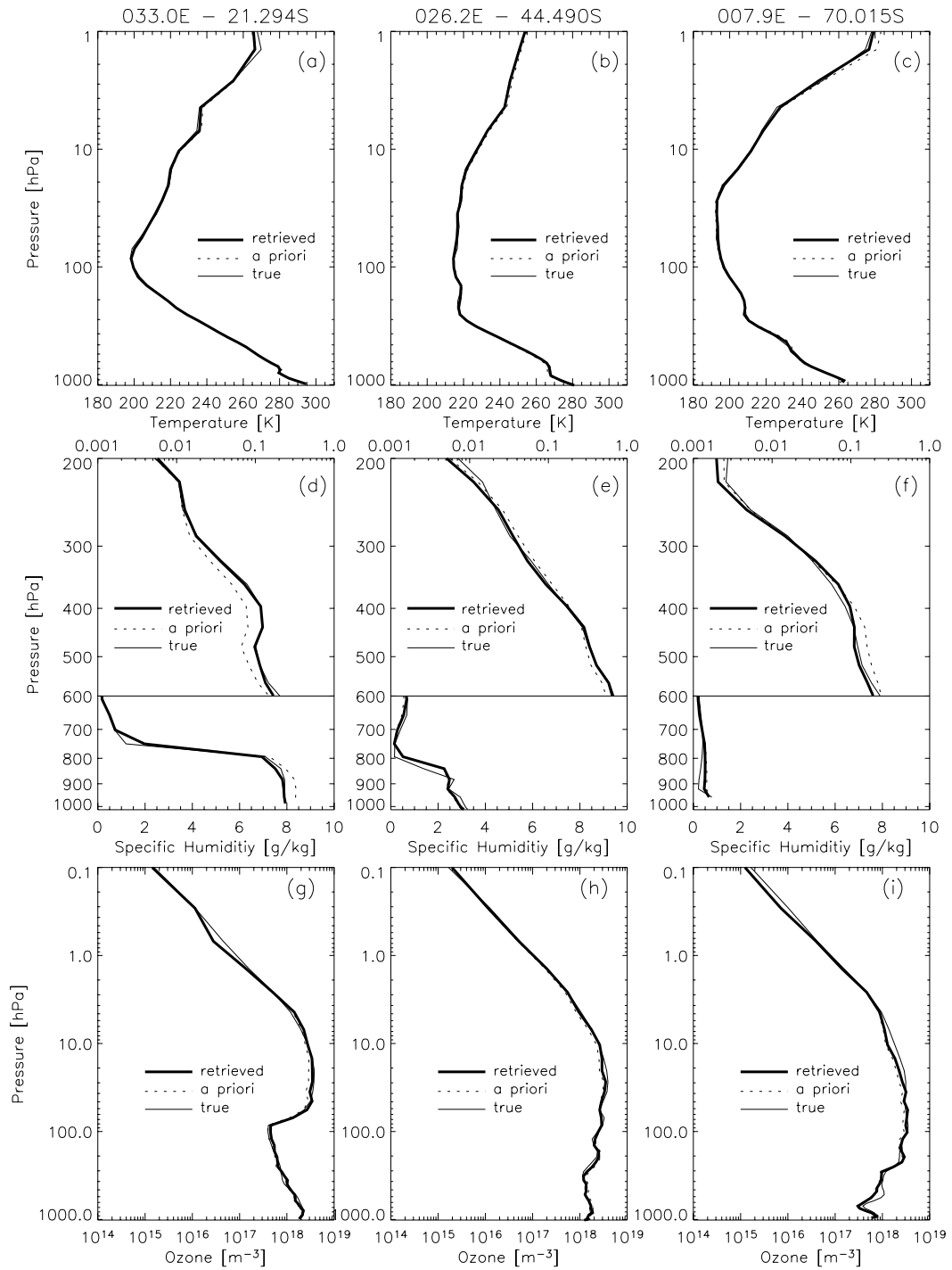


Figure 6.18: True, *a priori*, and estimated temperature (first row), humidity (second row; lower part: normal scale, upper part log-scale), and ozone (last row) profiles for three different cases, a low (first column), a mid (second column), and a high (third column) latitude case.

(discussed below) are broad. The measurement-based error (i. e. the square roots of the diagonal elements of the measurement-based error covariance matrix, c. f. Equation 3.55) depends on the shape of \mathbf{G} (also discussed below) and is comparatively small since the instrumental errors specified in \mathbf{S}_e are small.

The panels (c) of the Figures 6.19, 6.20, and 6.21 give a good indication of the influence of the *a priori* data on the retrieval by examining the "retrieval-to-*a priori*" error ratio profile (ratio of the estimated total retrieval errors to the *a priori* errors in percent). The 50% line (dotted vertical line) which is crossed by the ratio near 200 hPa implies that the *a priori* data have a major influence in the stratosphere, while the measurements improve more than a factor of 2 upon the *a priori* errors in the troposphere.

The second and the third row of Figures 6.19, 6.20, and 6.21 illustrate further characteristics of the representative temperature profiles including error correlation functions of the *a priori* (panel (d)) and measurement (panel (e)) error covariance matrices, weighting functions (panel (f)), averaging kernel functions (panel (g)), gain functions (panel (h)), and SNR functions (panel (i)). Correlation Functions (rows of \mathbf{S}_{ap} and $\hat{\mathbf{S}}$, c. f. Equation 3.40 and section 5.1.2) as well as averaging kernel functions (rows of \mathbf{A} , c. f. Equation 3.51) are shown for clarity at three selected pressure levels only (~ 400 , ~ 200 , and ~ 10 hPa), representing the troposphere, the tropopause region, and the stratosphere, respectively. Correspondingly, weighting functions (rows of \mathbf{K}), gain functions (columns of \mathbf{G} , c. f. Equation 3.48), and SNR functions (rows of $\tilde{\mathbf{K}}$, c. f. Equation 3.56) are shown for three representative channels only (1472.75, 694.25, and 649.0 cm^{-1}), which exhibit peaks at or close to the three levels chosen above. The diamond symbols indicate the retrieval levels (i. e. represent the actual values of the matrices) pointing out the usage of a non-equidistant grid.

The correlation functions (rows of the normalized covariance matrix $C_{ij} = S_{ij} / \sqrt{S_{ii}S_{jj}}$) quantify the fraction of correlation between the error at a given level i with one at any other level j . The correlation functions of the *a priori* error (panels (d)) follow the exponential drop-off structure as specified in section 5.1.2. The retrieval errors obtained in $\hat{\mathbf{S}}$ show a somehow similar but significantly sharpened correlation structure (panels (e)). This indicates that the errors in the retrieved temperature profiles (but also those of the retrieved humidity and ozone profiles, c. f. panels (e) of the Figures 6.23, 6.24, and 6.25 and of 6.27, 6.28, and 6.29, respectively) are much less correlated between neighboring levels. The sharpening is introduced into $\hat{\mathbf{S}}$ by the transformed- \mathbf{S}_e^{-1} term dominating \mathbf{S}_{ap}^{-1} in Equation 3.40[†].

[†]Weak correlation (ideally no correlation) is a favorable property, e. g., if the data are assimilated via optimal interpolation, since it simplifies the formulation of the covariance matrix.

The panels (f) of the Figures 6.19, 6.20, and 6.21 show the characteristic shapes of the weighting functions of the temperature, where each function indicates the weighting with which the temperature profile contributes to the brightness temperature (T_B) observation of a particular IASI channel. While T_B observations sensitive to the troposphere (e. g., the 1472.75 cm^{-1} channel, at least for the low- and mid-latitude case) stem from rather narrow well defined regions, the weighting functions increasingly broaden in the stratosphere, where their spread is of the order of 10 km (e. g., at 649.0 cm^{-1}). It is evident from this type of sensitivity (and based on the fact that more IASI channels peak in the troposphere than in the stratosphere) that the inversion will lead to retrievals with better resolution and accuracy in the troposphere than in the stratosphere.

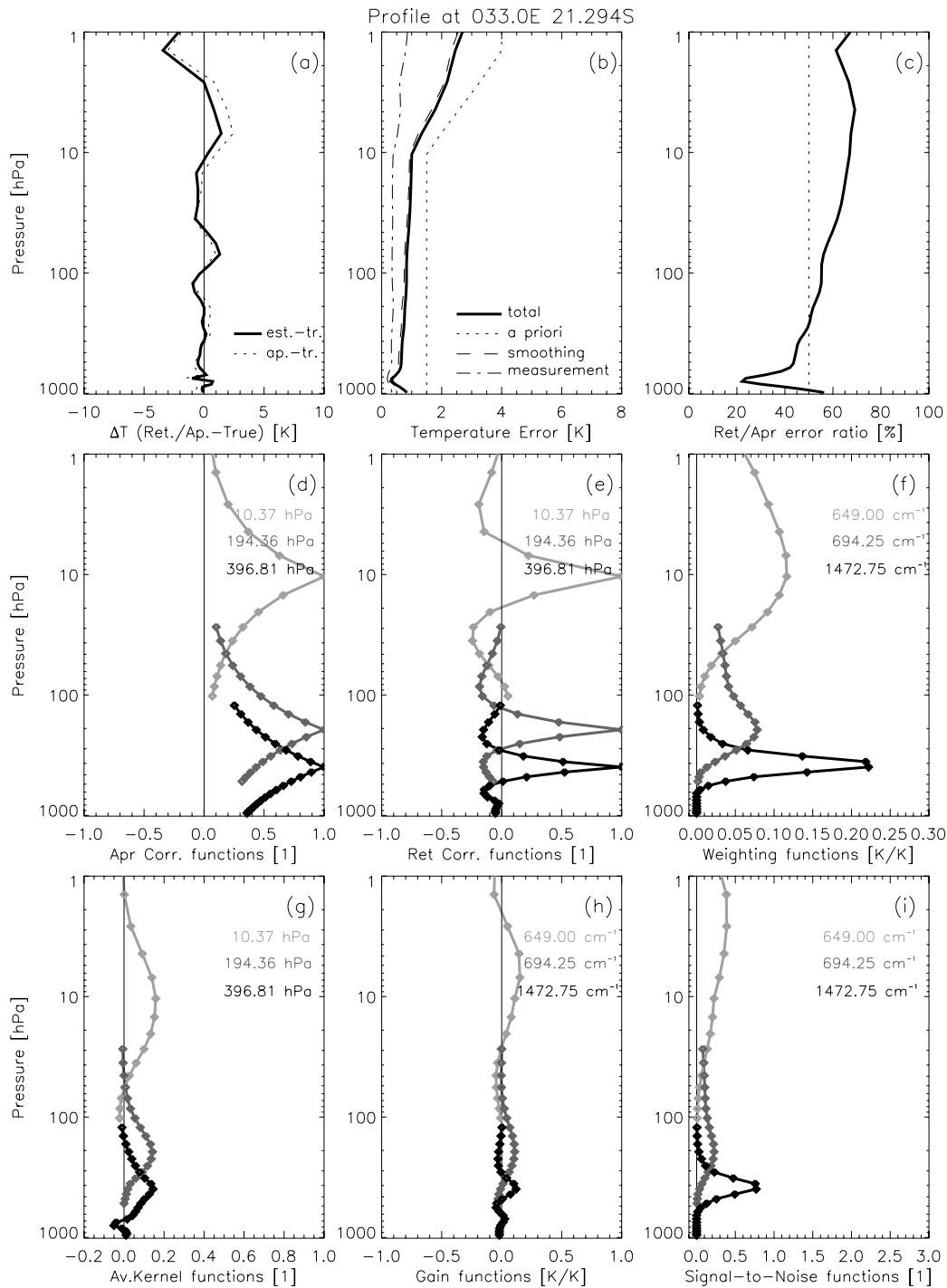


Figure 6.19: Optimal estimation results for the error analysis and various functions characterizing the retrieval performance for a low latitude temperature profile at latitude 21.3° south and longitude 33.0° east using ~ 300 channels selected by the IC method (c. f. subsection 5.2.1). For clarity the characterization functions are shown for three representative levels (~ 400 , ~ 200 , and ~ 10 hPa) and channels (1472.75, 694.25, and 649.0 cm^{-1}) only. See text for explanation and discussion of the panels.

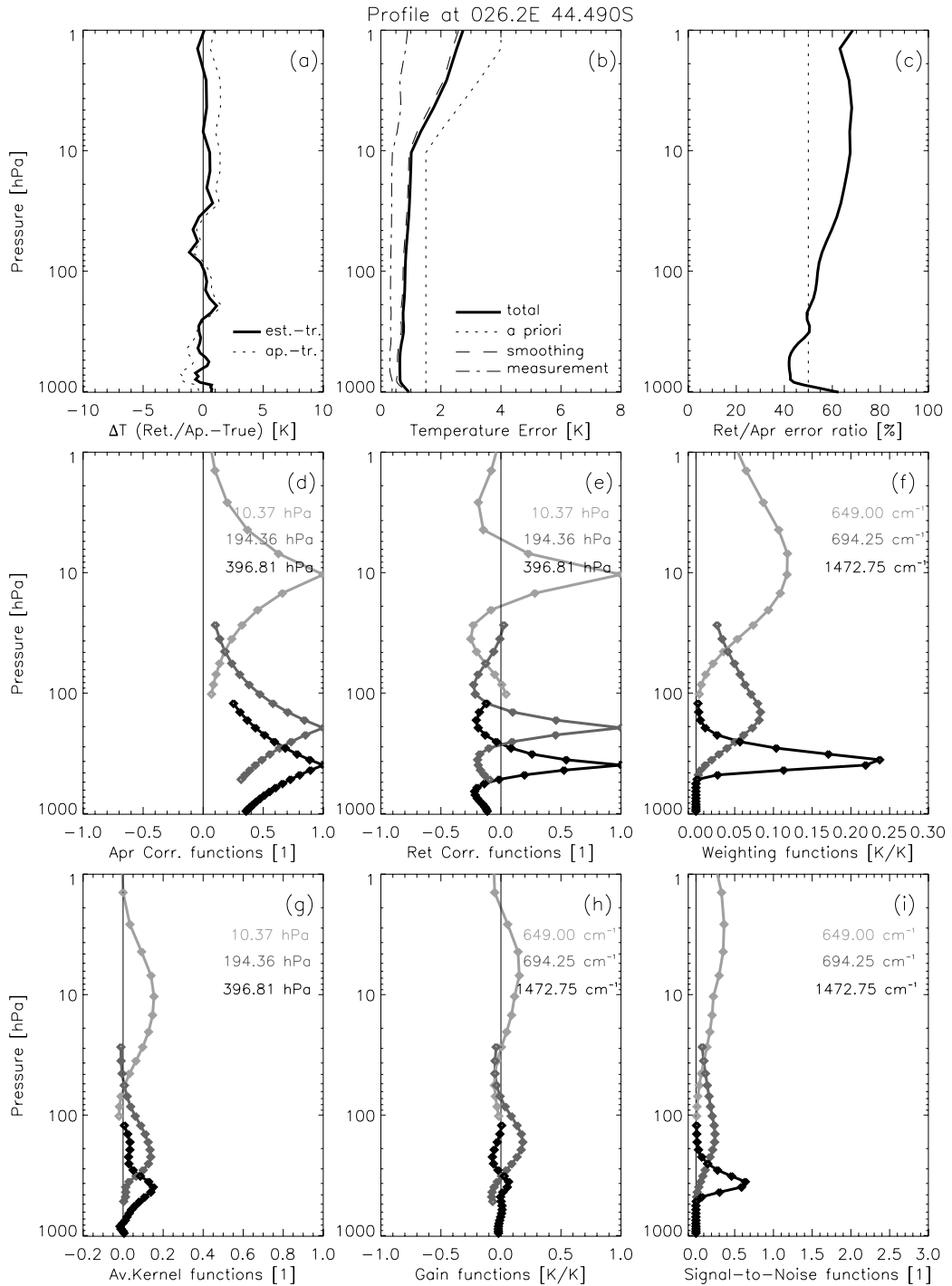


Figure 6.20: Optimal estimation results for the error analysis and various functions characterizing the retrieval performance for a mid latitude temperature profile at latitude 44.5° south and longitude 26.2° east using ~ 300 channels selected by the IC method (c. f. subsection 5.2.1). For clarity the characterization functions are shown for three representative levels (~ 400 , ~ 200 , and ~ 10 hPa) and channels (1472.75, 694.25, and 649.0 cm^{-1}) only. See text for explanation and discussion of the panels.

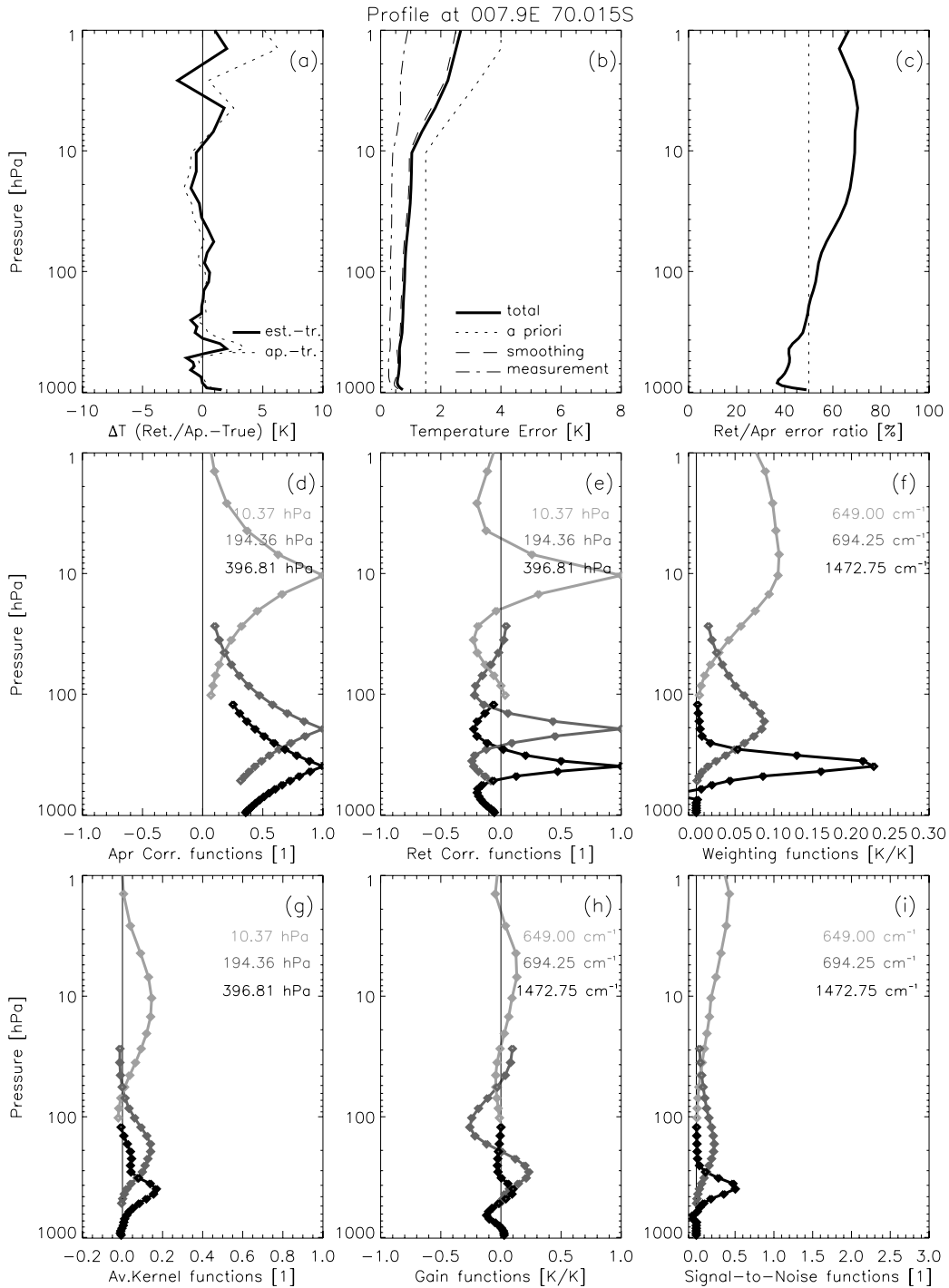


Figure 6.21: Optimal estimation results for the error analysis and various functions characterizing the retrieval performance for a high latitude temperature profile at latitude 70.0° south and longitude 7.9° east using ~ 300 channels selected by the IC method (c. f. subsection 5.2.1). For clarity the characterization functions are shown for three representative levels (~ 400 , ~ 200 , and ~ 10 hPa) and channels (1472.75, 694.25, and 649.0 cm^{-1}) only. See text for explanation and discussion of the panels.

In the panels (g) of Figures 6.19, 6.20, and 6.21, respectively, the averaging kernel functions, which measure with the spread of their main peak (FWHM) the resolution of the retrieved profile at the level of their peak (c. f. subsection 3.3.2), are displayed. The FWHM measure indicates a resolution of better than 1 km to 7 km in the troposphere decreasing to about 15 km at 10 hPa (c. f. Figure 6.22, panel (a)).

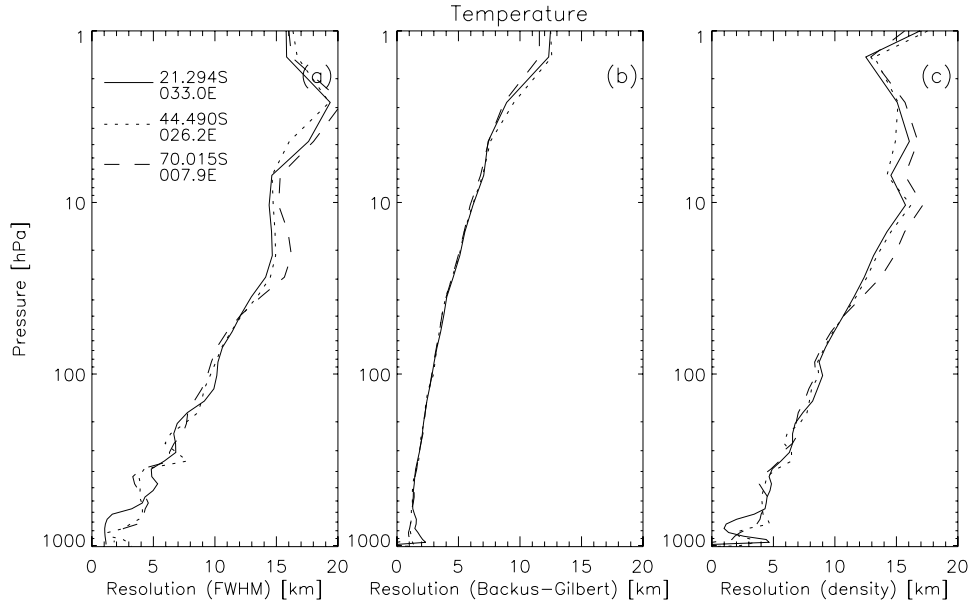


Figure 6.22: Vertical resolution of the three representative temperature profiles (a low, a mid, and a high latitude profile) for three different resolution measures. See text for explanation.

In Figure 6.22 a more detailed resolution analysis is represented. Additional to the FWHM measure two other measures are presented, the first defined by Backus and Gilbert (1970) (c. f. [Rodgers (2000)]), who define the resolution r_i at a height level i , with Δz_j as the height interval at level j , as follows:

$$r_i \equiv 12 \frac{\sum_j (z_i - z_j)^2 \frac{A_{ij}^2}{\Delta z_j}}{\left(\sum_j A_{ij}\right)^2}, \quad (6.1)$$

In the case of negative sidelobes (c. f. panels (g) of Figures 6.19, 6.20, and 6.21) we may substitute A_{ij} by $|A_{ij}|$ in the denominator, otherwise the calculated resolution would be too large [Collard (1998)]. The second measure is defined by [Purser and Huang (1993)], which relate the vertical resolution to the reciprocal of the so called *data density*, $1/\rho_i$, with the data density ρ_i as $\rho_i = A_{ii}/\Delta z_i$. Both methods have been applied to our retrieval and are shown in Figure 6.22 panel (b) and (c), respectively. We find quite similar results for the FWHM and the data density measure whereas the Backus-Gilbert measure shows a higher vertical resolution.

The reason why the results obtained by the FWHM measure is not consistent with the preliminary results of [Collard (1998)] and those reported by [Weisz (2001)] is the

assumption of smaller but more correlated *a priori* errors which result in a decreasing of the peak (lowering of the amplitudes in the averaging kernels by suppressing information from the measurement due to the assumption of a better first guess) and a broadening of the averaging kernels (due to the higher *a priori* error correlation)[‡].

The gain functions (c. f. panels (h) of Figures 6.19, 6.20, and 6.21) indicate that any specific observation contributes most to the retrieved profile near the peak of the associated weighting function. At first view it may contradict intuition, given the better retrieval performance in the troposphere, that the largest gain (especially in the case of the low latitude profile) occurs for the stratospheric channel. But on a deeper view we see that the stronger gain function of the stratospheric channel does not only mean higher sensitivity of the retrieved state of the temperature to the measured brightness temperature but also a correspondingly higher error amplification. Thus, in contrast to the weighting functions the gain functions do not directly indicate retrieval performance.

SNR functions (c. f. panels (i) of Figures 6.19, 6.20, and 6.21) resemble the shape of the weighting functions since they are just normalized versions of them (c. f. Equation 3.56). In the troposphere their magnitude is governed mainly by the small measurement errors whereas in the stratosphere they are dominated by the large *a priori* errors. The small peak value of the SNR function compared to that of the weighting function near 200 hPa is caused by the fact that in the spectral region of the "tropopause channels" (near the center of the 1600 cm^{-1} H₂O Band – $T_B < 240\text{ K}$) the measurement errors are relatively large ($\sim 0.8\text{ K}$ at 1558 cm^{-1}).

Humidity

In inspecting the humidity results for the three representative profiles (c. f. Figure 6.18 panels (d-f) for the absolute values and Figures 6.23, 6.24, and 6.25 for the retrieval characteristics) we see that the largest part of information can be gained in a region between 200 hPa and 600 hPa (c. f. panel (a) of the three Figures). Problems arise at heights lower than 600 hPa due to less information gained by the IASI instrument in this region and quite small *a priori* errors ($< 40\%$ at heights lower than 600 hPa). The reason of the big differences at heights < 700 hPa, especially in the mid latitude case (c. f. Figure 6.24, panel (d)), can be explained by the fact that the forecast does not catch well the height of the maritime boundary layer (c. f. Figure 6.18, panel (e)). Since this is a very sharp structure where quite large humidity gradients can occur the resolution of the IASI instrument is too low to resolve it. This better performance above 700 hPa can also be figured out by the panels (b) – increase of measurement and smoothing errors below 700 hPa and above ~ 300 hPa – and (c) – when averaging over all three profiles the "retrieval-to-*a priori*" error ratio has values below 50% in atmospheric regions between ~ 300 hPa and ~ 600 hPa.

[‡]Tests with higher *a priori* errors and a smaller correlation gave quite similar results as reported by [Weisz (2001)]. Additionally, all three measures deliver comparable results.

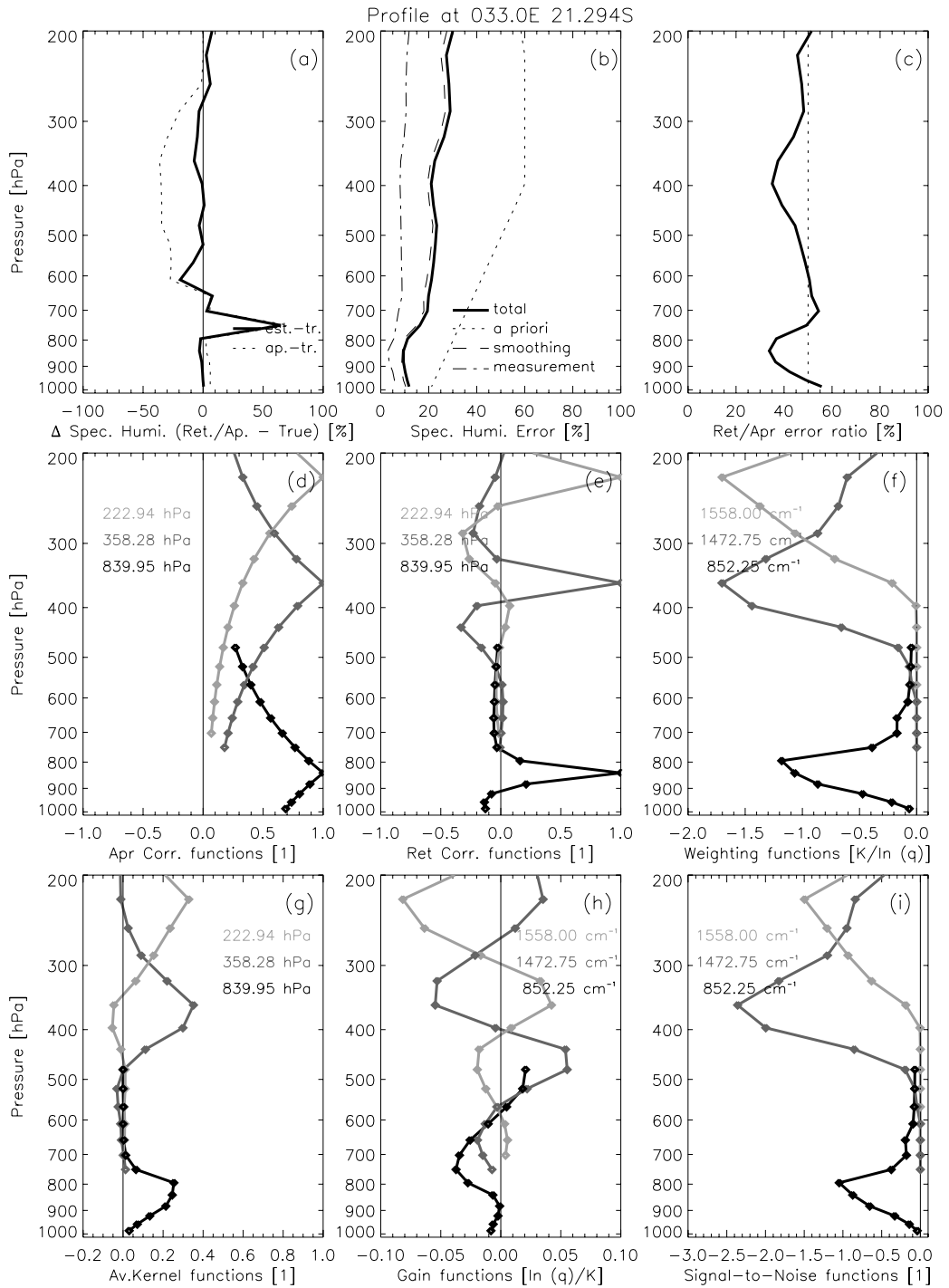


Figure 6.23: Optimal estimation results for the error analysis and various functions characterizing the retrieval performance for a low latitude humidity profile at latitude 21.3° south and longitude 33.0° east using ~ 300 channels selected by the IC method (c. f. subsection 5.2.1). For clarity the characterization functions are shown for three representative levels (~ 840 , ~ 360 , and ~ 220 hPa) and channels (852.25, 1472.75, and 1558.0 cm^{-1}) only. See text for explanation and discussion of the panels.

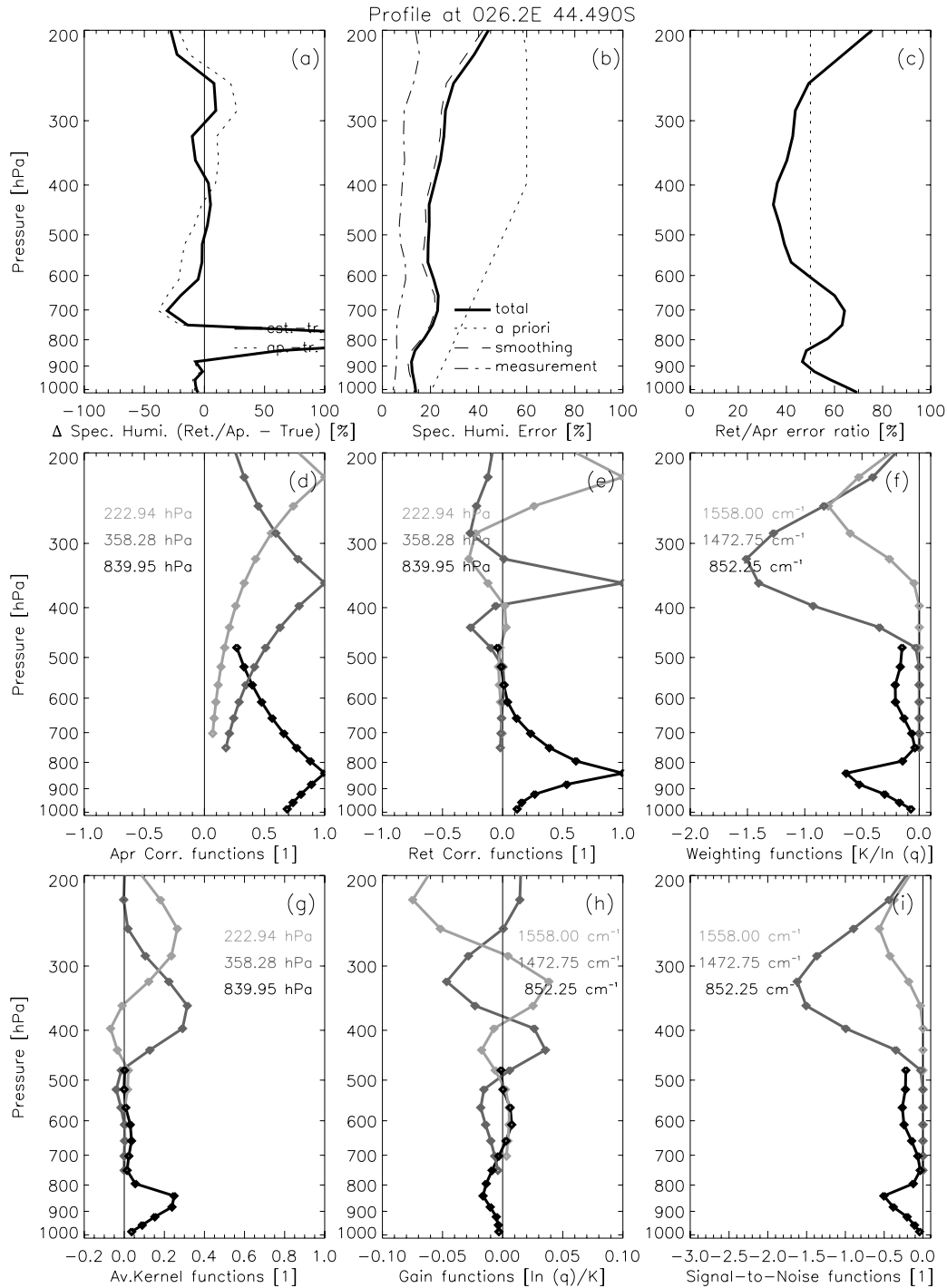


Figure 6.24: Optimal estimation results for the error analysis and various functions characterizing the retrieval performance for a mid latitude humidity profile at latitude 44.5° south and longitude 26.2° east using ~300 channels selected by the IC method (c. f. subsection 5.2.1). For clarity the characterization functions are shown for three representative levels (~840, ~360, and ~220 hPa) and channels (852.25, 1472.75, and 1558.0 cm^{-1}) only. See text for explanation and discussion of the panels.

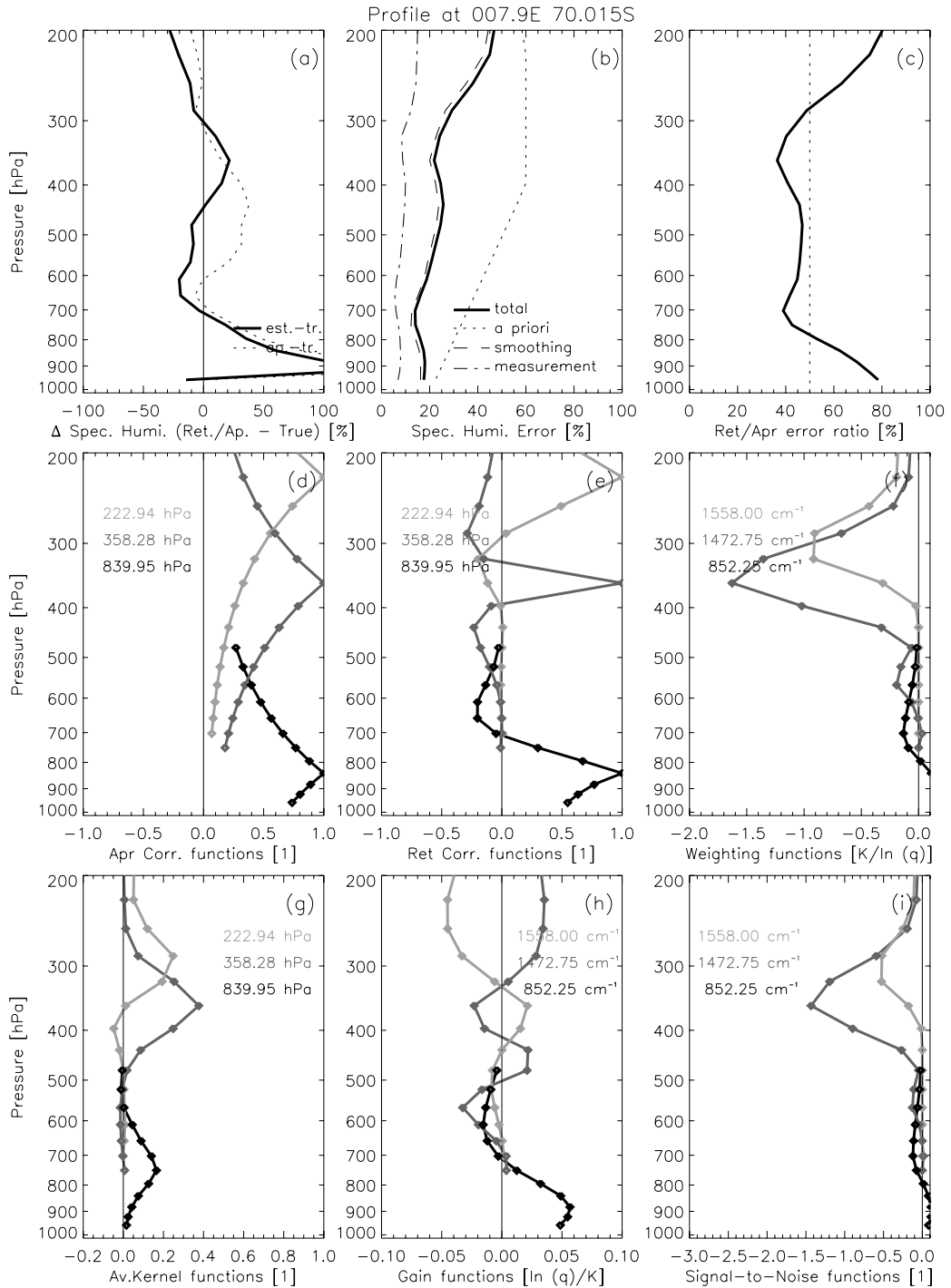


Figure 6.25: Optimal estimation results for the error analysis and various functions characterizing the retrieval performance for a high latitude humidity profile at latitude 70.0° south and longitude 7.9° east using ~300 channels selected by the IC method (c. f. subsection 5.2.1). For clarity the characterization functions are shown for three representative levels (~840, ~360, and ~220 hPa) and channels (852.25, 1472.75, and 1558.0 cm⁻¹) only. See text for explanation and discussion of the panels.

The characterization functions illustrated in the second and third row of Figures 6.23, 6.24, and 6.25 which were theoretically well explained in the temperature section earlier are shown for three selected pressure levels, too (~ 840 hPa, ~ 360 hPa, and ~ 220 hPa) where the first one should represent the lower troposphere and the two other ones the upper tropospheric region. The corresponding channels are displayed in the weighting functions, gain functions and SNR functions are 852.25 cm^{-1} , 1472.75 cm^{-1} , and 1558.0 cm^{-1} .

Like the tropospheric weighting functions for temperature (c. f. Figure 6.19, (f)) the weighting functions for humidity (c. f. Figures 6.23, 6.24, and 6.25, (f)) exhibit a rather sharp and narrow shape which will lead to a quite good vertical resolution throughout the whole tropospheric region.

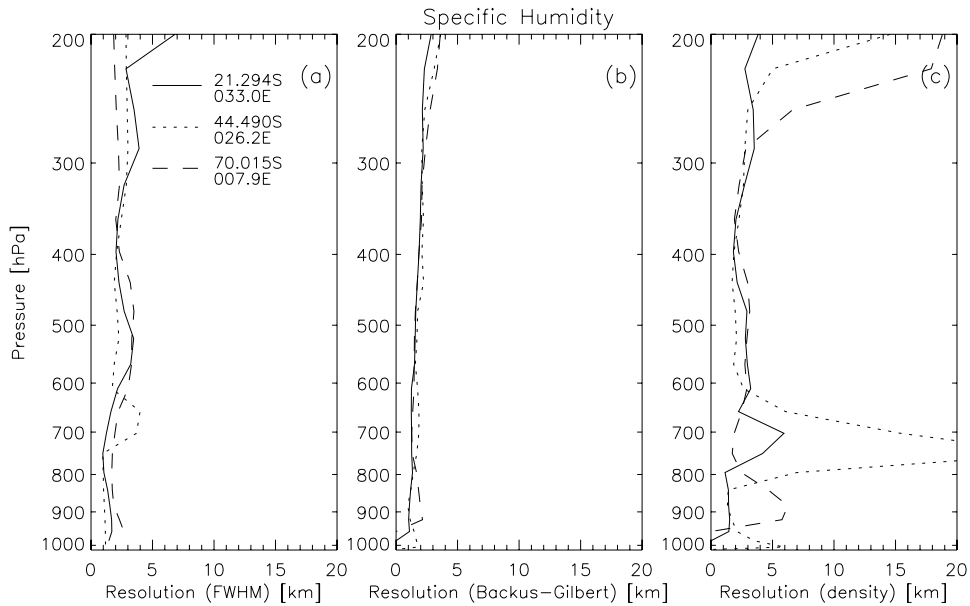


Figure 6.26: Vertical resolution of the three representative humidity profiles (a low, a mid, and a high latitude profile) for three different resolution measures. See text for explanation.

In addition to the averaging kernel functions (c. f. panels (g) of Figures 6.23, 6.24, and 6.25) we show once more – this time for the humidity – the measures for the vertical resolution defined in the temperature part (see Figure 6.26). In general all three measures exhibit a vertical resolution of about 2 km near the surface which increases to about 3 km at 200 hPa. The best indication of retrieval problems between ~ 700 hPa and ~ 900 hPa is given by the reciprocal data density measure and weakly also in the FWHM case.

Gain and SNR functions (c. f. panels (h) and (i) of Figures 6.23, 6.24, and 6.25) appear to show similar characteristics as mentioned for the tropospheric temperature case.

Ozone

Focusing on the retrieved ozone (c. f. Figures 6.18 panels (g-i) for the absolute values and Figures 6.27, 6.28, and 6.29 for the retrieval characteristics) we have to notice in all three different latitude cases that the information gained by the estimation process has a reasonable magnitude only in regions with high relative ozone amount, i. e. in the lower stratosphere. This is illustrated by the total retrieval error, which is dominated like in the temperature and humidity case by the smoothing error, as well as by the "retrieval-to-*a priori*" error ratio which has a magnitude of almost 50% only at this height and in no case is dropping under this value. Additionally the retrieval correlation functions (panels (e)) exhibit a comparatively narrowing behavior solely in the ozone layer region.

On a closer examination of the weighting functions, especially of the channel at 1039.75 cm^{-1} , we see the possibility to approximately deduce the thickness and location of the part of the atmosphere where ozone has its maximum concentration due to the fact that this channel peaks in the whole region of high ozone concentration. This results in a vertical resolution (c. f. Figure 6.30) of the retrieval for ozone delivered by the IASI instrument which is quite coarse, too. The FWHM measure results in about 20 km over the whole treated region, whereas the Backus and Gilbert measure seems once more to be too optimistic. The measure defined by the reciprocal of the data density results in a vertical resolution of about 20 km only in the region of high ozone concentration and is beyond 50 km elsewhere.

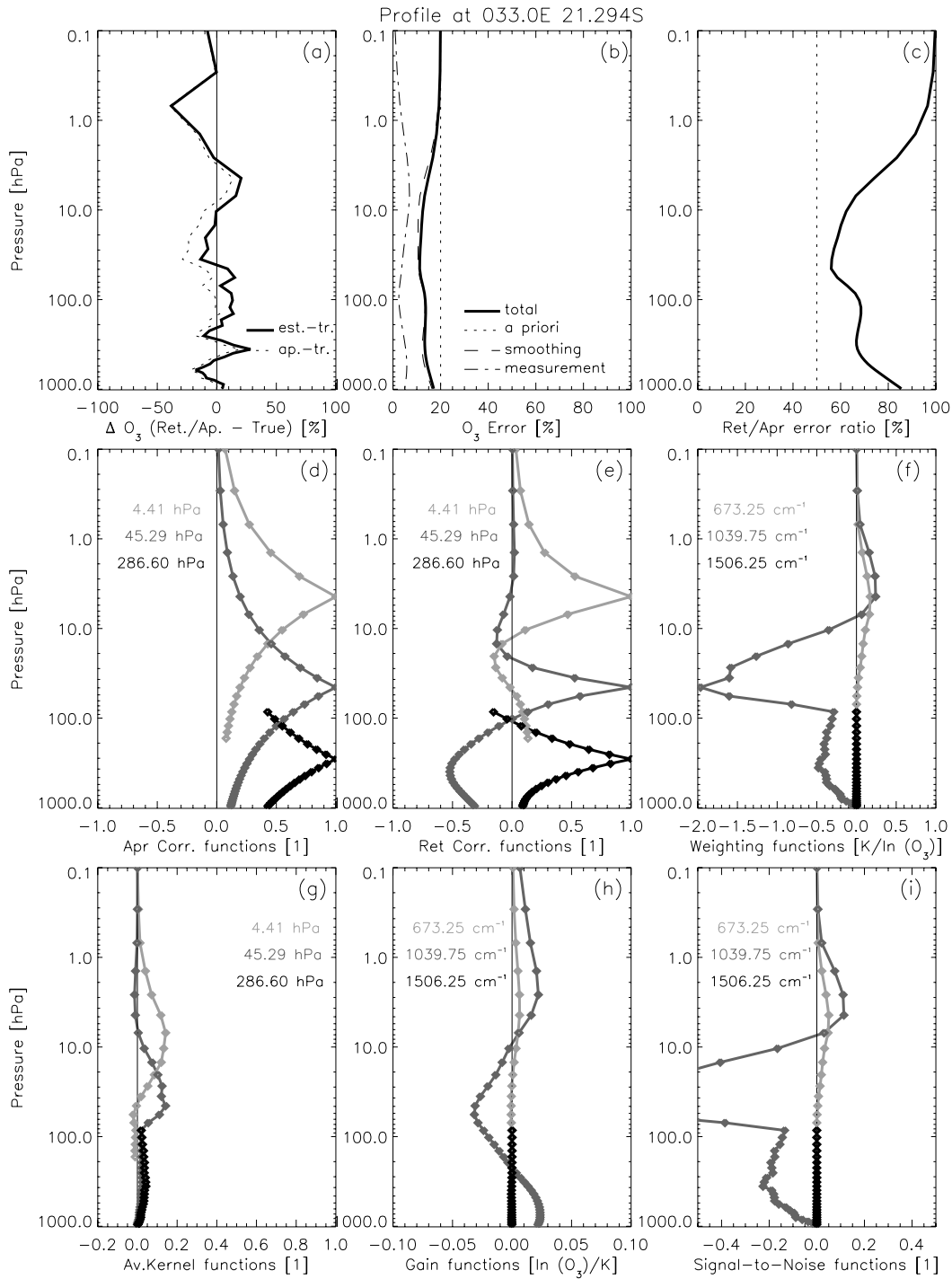


Figure 6.27: Optimal estimation results for the error analysis and various functions characterizing the retrieval performance for a low latitude ozone profile at latitude 21.3° south and longitude 33.0° east using ~ 300 channels selected by the IC method (c. f. subsection 5.2.1). For clarity the characterization functions are shown for three representative levels (~ 286 , ~ 45 , and ~ 4 hPa) and channels (1506.25, 1039.75, and 673.25 cm^{-1}) only. See text for explanation and discussion of the panels.

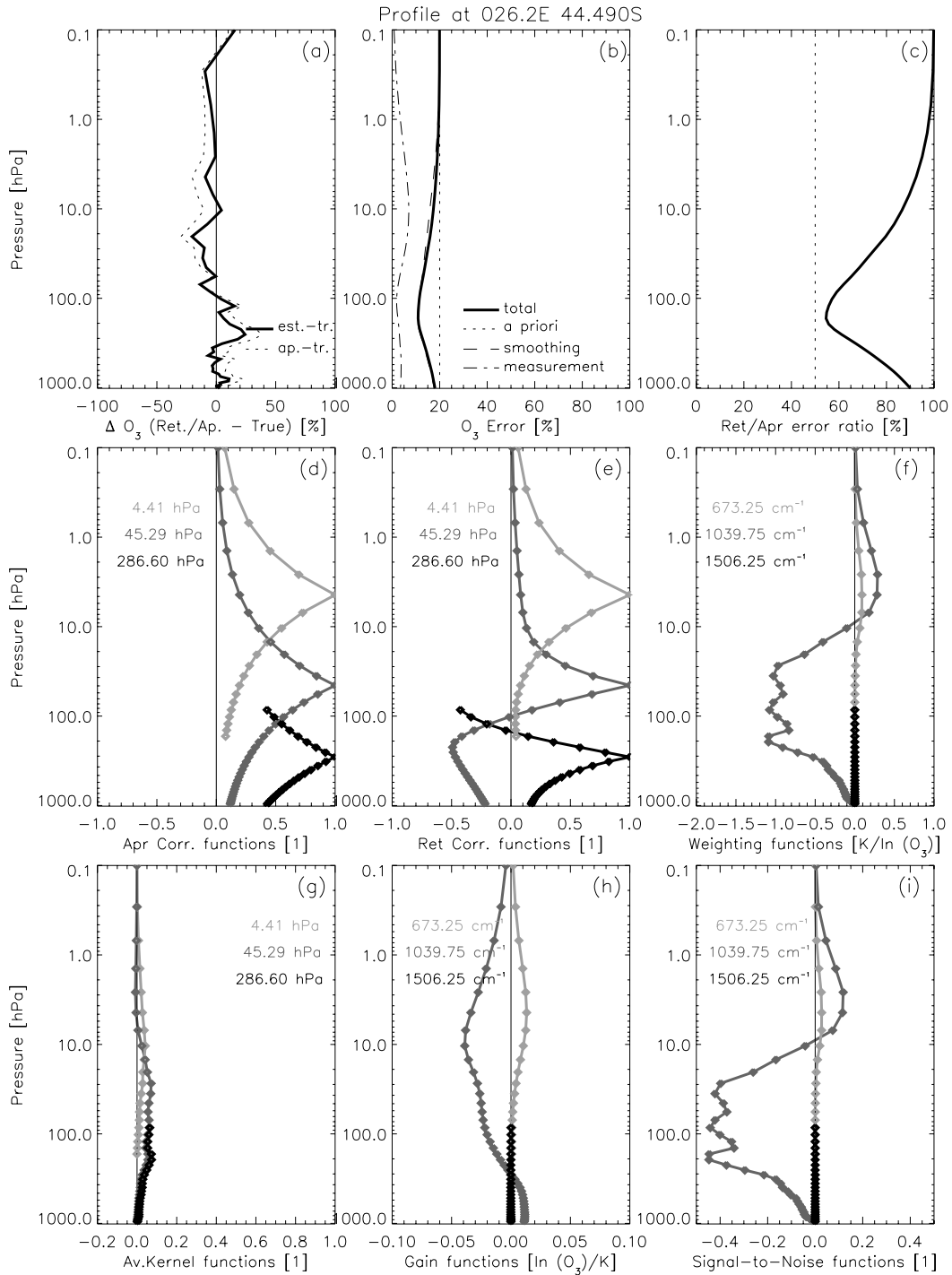


Figure 6.28: Optimal estimation results for the error analysis and various functions characterizing the retrieval performance for a mid latitude ozone profile at latitude 44.5° south and longitude 26.2° east using ~300 channels selected by the IC method (c. f. subsection 5.2.1). For clarity the characterization functions are shown for three representative levels (~286, ~45, and ~4 hPa) and channels (1506.25, 1039.75, and 673.25 cm^{-1}) only. See text for explanation and discussion of the panels.

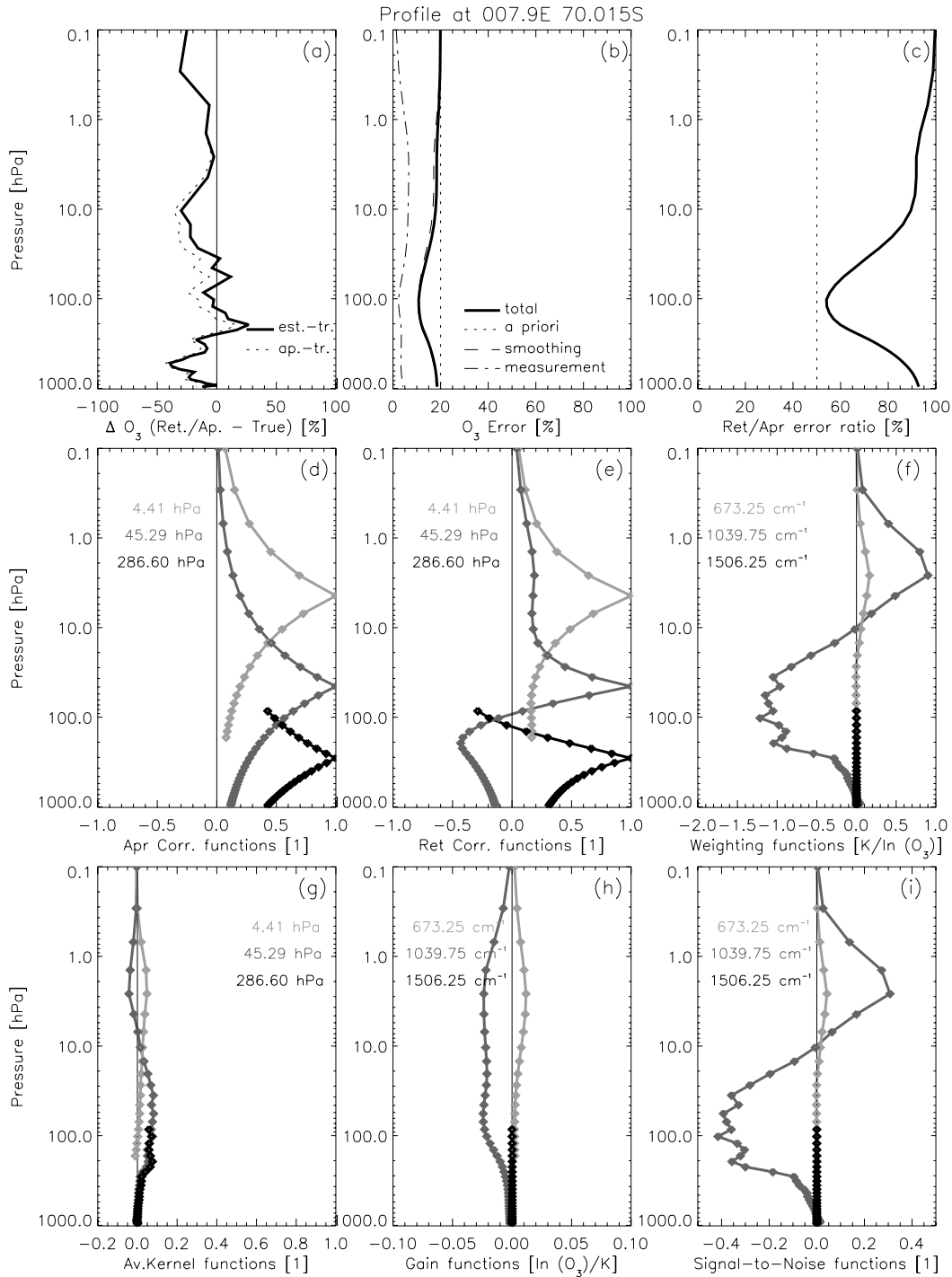


Figure 6.29: Optimal estimation results for the error analysis and various functions characterizing the retrieval performance for a high latitude ozone profile at latitude 70.0° south and longitude 7.9° east using ~300 channels selected by the IC method (c. f. subsection 5.2.1). For clarity the characterization functions are shown for three representative levels (~286, ~45, and ~4 hPa) and channels (1506.25, 1039.75, and 673.25 cm^{-1}) only. See text for explanation and discussion of the panels.

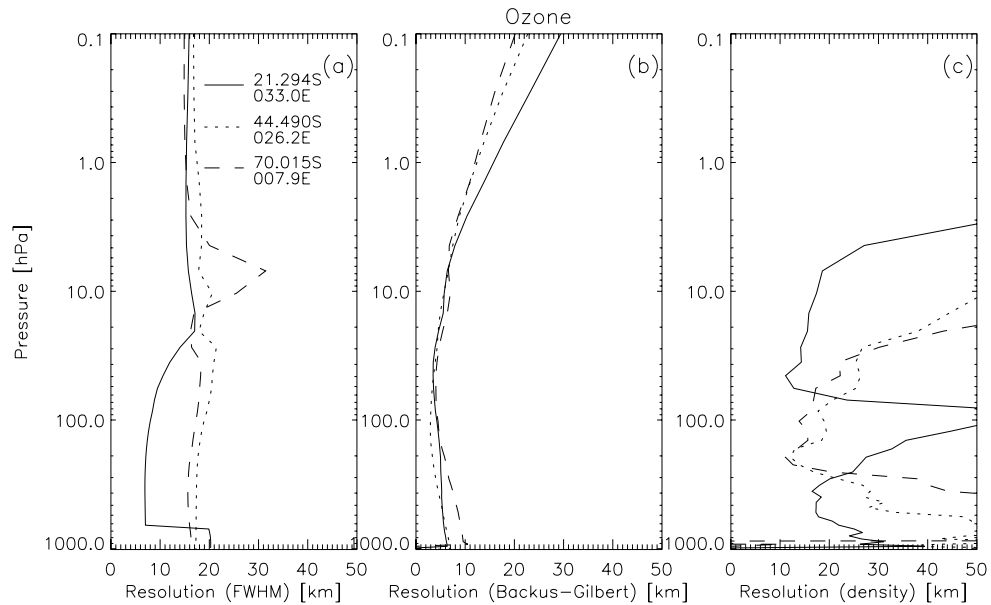


Figure 6.30: Vertical resolution of the three representative ozone profiles (a low, a mid, and a high latitude profile) for three different resolution measures. See text for explanation.

In summary it is observed that the retrieved ozone profile consist mostly of *a priori* information and has reasonable information of the sensor only in those parts of the atmosphere where the concentration of the ozone is high which leads us to the expectation to obtain at least significant improvements in the calculation of the ozone column amount. This is consistent with the expectations of the IASI Science Plan [Camy-Peyret and Eyre (1998)].

6.2 Comparison of Different Channel Selection Methods

The task of the current section is the comparison of the two different channel selection algorithms described in section 5.2 (IC theory and MS approach) for three sets of numbers of selected channels. As initial input set for all six cases we used the *a priori* data illustrated in Figure 6.7 and Figure 6.8 which consists of data consistent with the *a priori* error covariance matrices for temperature, humidity, ozone, and SST (c. f. section 5.1.2) by perturbing the "true" field via the method described in section 5.1.4. The selected channels used in this set were derived in performing the IC and MS algorithm (c. f. section 5.2.1) on the CIRA86aQ climatology [Kirchengast *et al.* (1999)] with suitable ozone profiles obtained from U. S. standard profiles. The comparison of this initial set with a more realistic input (e. g., using a 24-hour forecast field as first guess) is given in section 6.1.

The three different sets of numbers of selected channels were chosen to get approximately 3.5%, 10% and 20% of the full number of IASI channels (c. f. section 2.2) which resulted in an averaged number of selected channels per profile of 300 channels for the smallest dataset ($\sim 3.6\%$), 887 channels for the medium dataset ($\sim 10.8\%$), and 1808 channels for the largest dataset ($\sim 22.1\%$). On a closer examination this can be split up into the different atmospheric parameters the channels are selected for. Therefore the averaged numbers of selected channels per profile were 89/ 324/ 858 channels for temperature, 87/ 336/ 766 for humidity, 64/ 167/ 224 for ozone and 60/ 60/ 60 for SST, respectively. We see that the number of selected channels for the different atmospheric species do not follow the rough multiplication factors between total sets ($\times 3$ and $\times 2$ between 3.5%, 10% and 20%). The reason for this is that the IASI spectral interval has only two small bands for the surface and the ozone channels which means that the number of channels with reasonable information for these parameters is limited. Thus, we have filled up the remaining amount by temperature and humidity channels.

Numerical Efficiency		
channel set	IC	MS
300	1.00	0.98
887	3.74	4.25
1808	11.25	13.13

Table 6.1: Comparison of the numerical efficiency for the six different channel selection cases. The set with ~ 300 channels selected by IC theory acts as our reference case. We see that in the case of the small number of selected channels both retrievals (with IC and MS selected channels) have the same performance (apart from small differences which may be explained by hardware effects) whereas with an increasing number of channels the cost in computer time increases more than linearly.

Let us now start with the intercomparison of the results for the different cases. A general view yields that the performance differences are not tremendous in all four cases – temperature (c. f. Figure 6.31), humidity (c. f. Figure 6.32), and ozone (c. f. Figure 6.34) profiles as well as sea surface temperature (c. f. Figure 6.33) – although the numerical

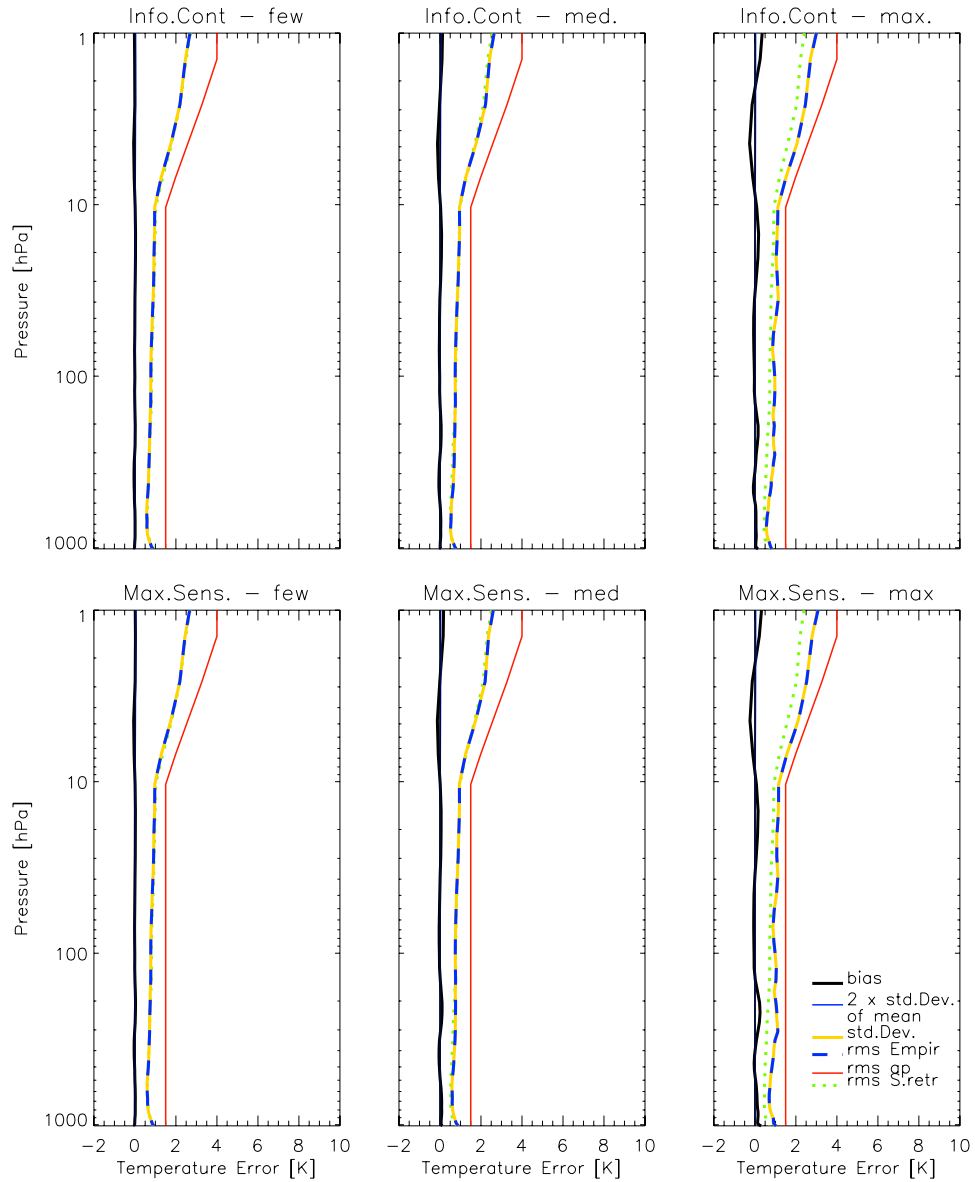


Figure 6.31: Temperature results of the joint retrieval algorithm for six different retrieval cases. Bias (black line), 2 times standard deviation of bias (solid blue line), standard deviation (yellow line), rms (dashed blue line), theoretical estimate of the rms (dotted green line), and diagonal values of the used *a priori* error covariance matrix (red line). Explanation see text.

efficiency is of course significantly better for the case of selecting about 3.5% of the channels only (c. f. Table 6.1).

On a closer examination of the temperature results (c. f. Figure 6.31) we obtain that the theoretical estimation of the rms is decreasing slightly with increasing number of selected channels. This is not the fact for the empirical rms which is virtually the same for the small and the medium set but increases significantly for the case of ~ 1800 selected channels. Furthermore, the maximum set of selected channels results in the appearance

of slight bias structures which are not present in the two other sets.

A comparison of the two different channel selection methods (IC, top three panels of Figure 6.31 and MS, bottom three panels of Figure 6.31) yields no significant difference for the cases with the small and the medium number of selected channels, only the set with 1808 selected channels shows a slightly better performance in the IC case which can be traced back to the fact that the IC theory selects fewer linearly dependent channels, in the sense explained in section 5.2.

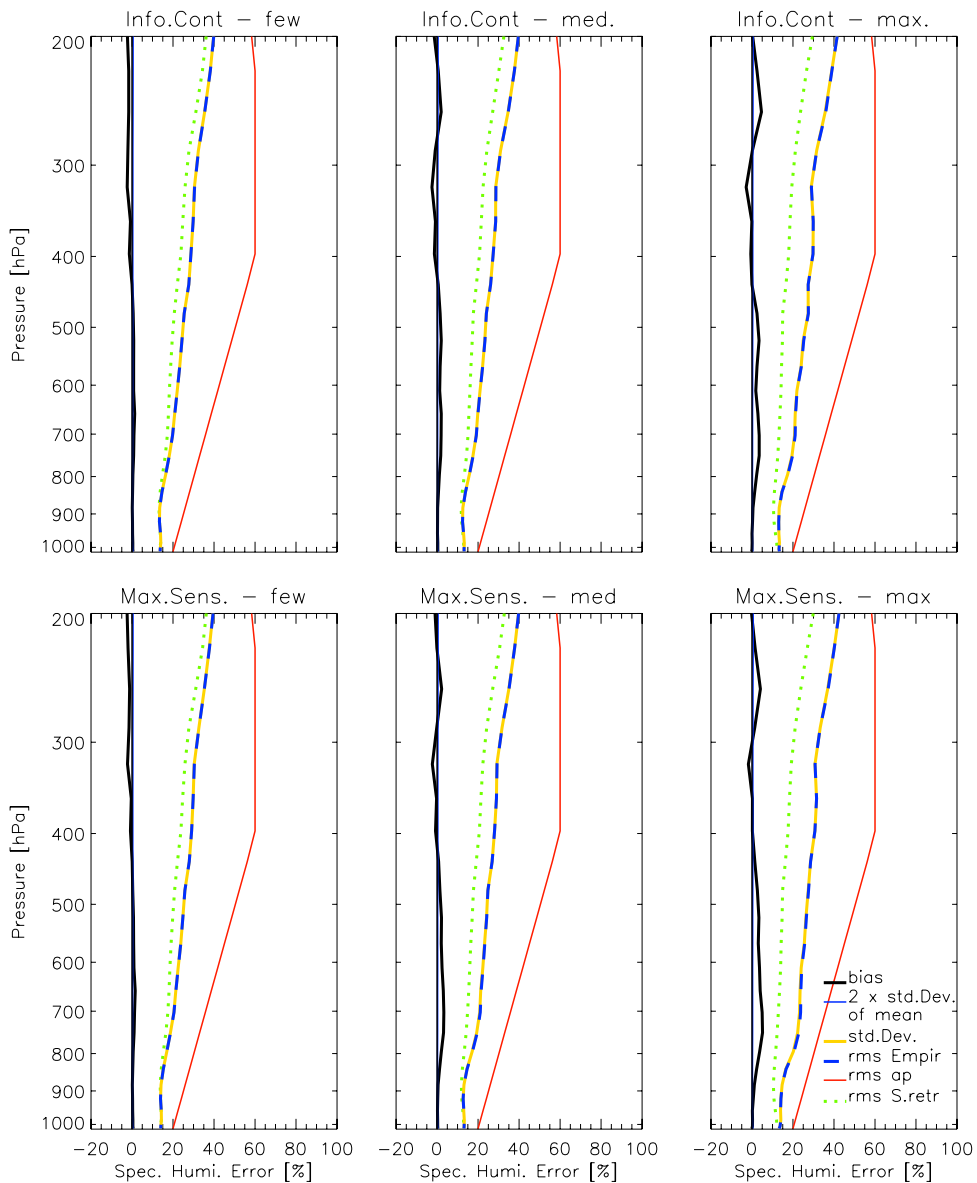


Figure 6.32: Humidity results of the joint retrieval algorithm for six different retrieval cases. Bias (black line), 2 times standard deviation of bias (solid blue line), standard deviation (yellow line), rms (dashed blue line), theoretical estimate of the rms (dotted green line), and diagonal values of the used *a priori* error covariance matrix (red line). Explanation see text.

Inspecting the humidity results more closely (c. f. Figure 6.32), we find that except for the difference between the theoretical estimate of the rms and the rms obtained by the retrieval which is present in all three panels, which does not occur in the case of retrieval results for the temperature and ozone profiles (c. f. Figures 6.31 and 6.34), and which was explained in subsection 6.1.1, the results for humidity using the joint algorithm show the same features as the temperature results do, i. e. no explicit gain in information but increasing numerical effects for increasing number of channels.

The results for the sea surface temperature show a difference between theoretical estimate and empirically analyzed rms for the case of few selected channels (c. f. Figure 6.33, panel (a) for IC and panel (d) for MS) which is decreasing with increasing number of channels with the result of almost no gap in the case of 1808 selected channels (c. f. Figure 6.33, panel (c) for IC and panel (f) for MS). This feature results from the fact that due to the increase of channels in the overlying atmosphere the theoretical estimate of the rms decreases and therefore causes a decrease of the theoretical estimate of the surface via correlation, too. The differences between the theoretical estimate and the empirically analyzed rms can thus be explained by the fact that the retrieval of SST is significantly dependent on the retrieval of the overlying atmosphere (c. f. subsection 6.3.1). Comparing IC to MS selection, the IC selection leads to slightly better performance and also an increased channel number leads to slightly improved performance in the IC case. Given the much higher computational demand for more channels and the preference for a lower channel number for temperature and humidity retrieval, a channel number increase for SST will not be warranted in practice, however.

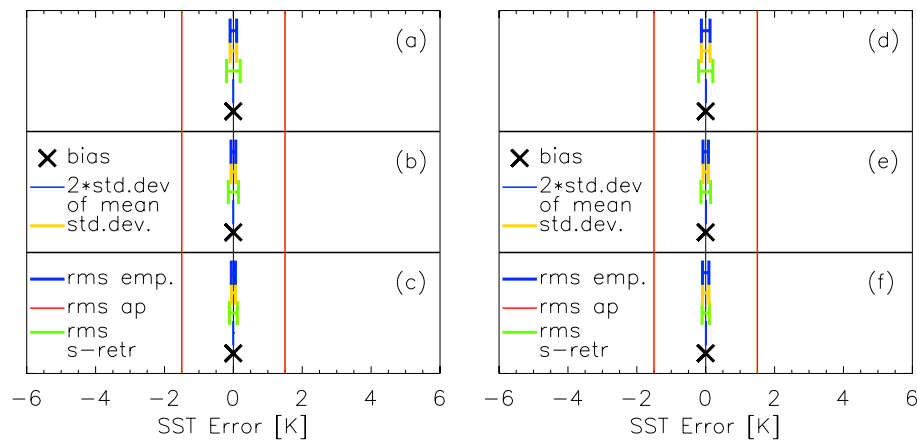


Figure 6.33: SST results of the joint retrieval algorithm for six different retrieval cases. Bias (black crosses), 2 times standard deviation of bias (thin blue line), standard deviation (yellow line), rms (thick blue line), theoretical estimate of the rms (green line), and *a priori* error (red line). Panel (a-c) show the retrieval results for IC selected channels, Panel (d-f) for MS selected channels. The topmost row shows the results for about 300, the middle row for 887, and the bottom row for 1808 selected channels, respectively.

In the case of the ozone results (c. f. Figure 6.34) we find once more that the results for the sets with a small and medium number of selected channels (left and middle panels

of the two rows) match well. In inspecting the cases for the maximum number of selected channels (rightmost panels of Figure 6.34) we find once more the gap between the theoretical estimate and the analyzed rms as well as the occurrence of an additional bias which appears in the troposphere in the case of ozone.

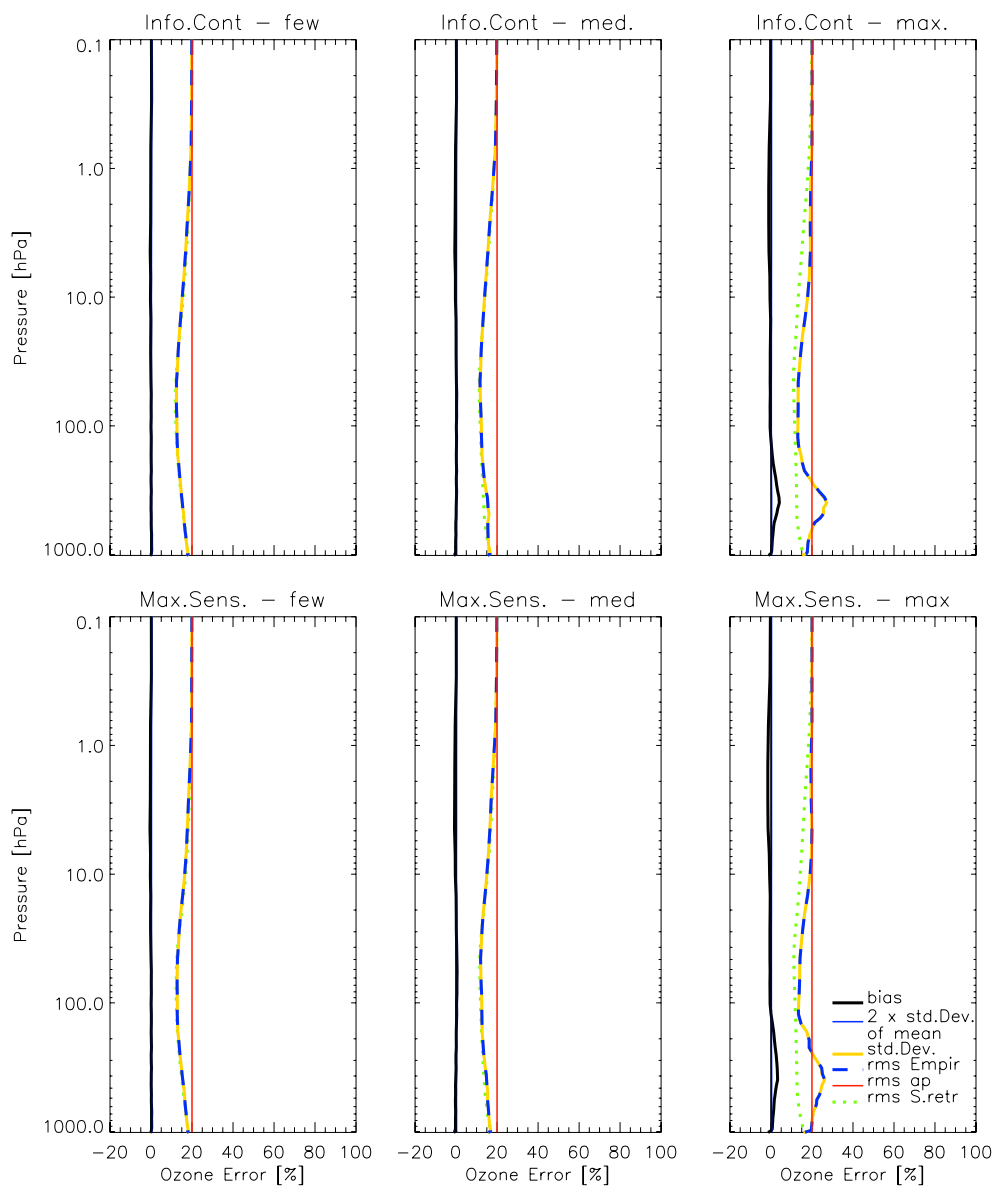


Figure 6.34: Ozone results of the joint retrieval algorithm for six different retrieval cases. Bias (black line), 2 times standard deviation of bias (solid blue line), standard deviation (yellow line), rms (dashed blue line), theoretical estimate of the rms (dotted green line), and diagonal values of the used *a priori* error covariance matrix (red line). Explanation see text.

In summary we can say that these results suggest that the simpler MS channel selection approach, in the case of using a climatology for the selection of the used channels as implicated by the results of section 6.1, has the same efficiency as the IC method and closely similar performance. Tentatively the IC results are slightly better, presumably due to the more even distribution of the selected channels (c. f. section 5.2), so the IC selection seems generally preferable.

6.3 Comparison between the Joint Algorithm and more Specific ones

In this section we exemplify the clearly improved performance of the joint retrieval algorithm developed in this study compared to more specific retrieval setups. In the first part (subsection 6.3.1) we will focus on the comparison of single parameter retrievals and the joint algorithm whereas the second part (subsection 6.3.2) points out the differences when a special region (upper troposphere) is retrieved for its own. As a last point the impact of an additional ozone retrieval in the joint algorithm is discussed in subsection 6.3.3, i. e. we try to find out whether the inclusion of the ozone retrieval in the joint algorithm helps or troubles the primary focus of joint temperature, humidity, and SST retrieval.

As initial input set for all the cases dealt with here, we once more used the *a priori* data illustrated in Figure 6.7 and Figure 6.8 which consist of data consistent with the *a priori* error covariance matrices for temperature, humidity, ozone, and SST (c. f. section 5.1.2) by perturbing the "true" field via the method described in section 5.1.4. The selected channels used in these examples were derived in performing the IC algorithm (c. f. section 5.2.1) for selecting ~ 300 channels on the CIRA86aQ climatology [Kirchengast *et al.* (1999)] with suitable ozone profiles obtained from U. S. standard profiles.

6.3.1 Single Parameter Retrievals

Let us first focus on the impact on the estimated temperature profile when using the joint algorithm and performing a temperature only retrieval (without retrieving humidity and SST), respectively. The single temperature retrieval is the only case where we deviate from our strict principle of comparing data exclusively if the same input was used. We had to decrease the magnitude of the perturbation of the humidity to 15% at the surface up to 40% at 100 hPa since the retrieval becomes very un-robust if the more realistic values which were dealt with in the other cases were used. This 15% up to 40% uncertainty was used since it roughly reflects the uncertainty expected for humidity profiles obtained in the current study if the joint temperature and humidity algorithm is used and it lies in the range of humidity uncertainty proposed by [Lerner *et al.* (2002)] for obtaining a stable temperature only retrieval. The necessity of this optimistic humidity uncertainty assumption on its own already points to the advantages of joint retrievals.

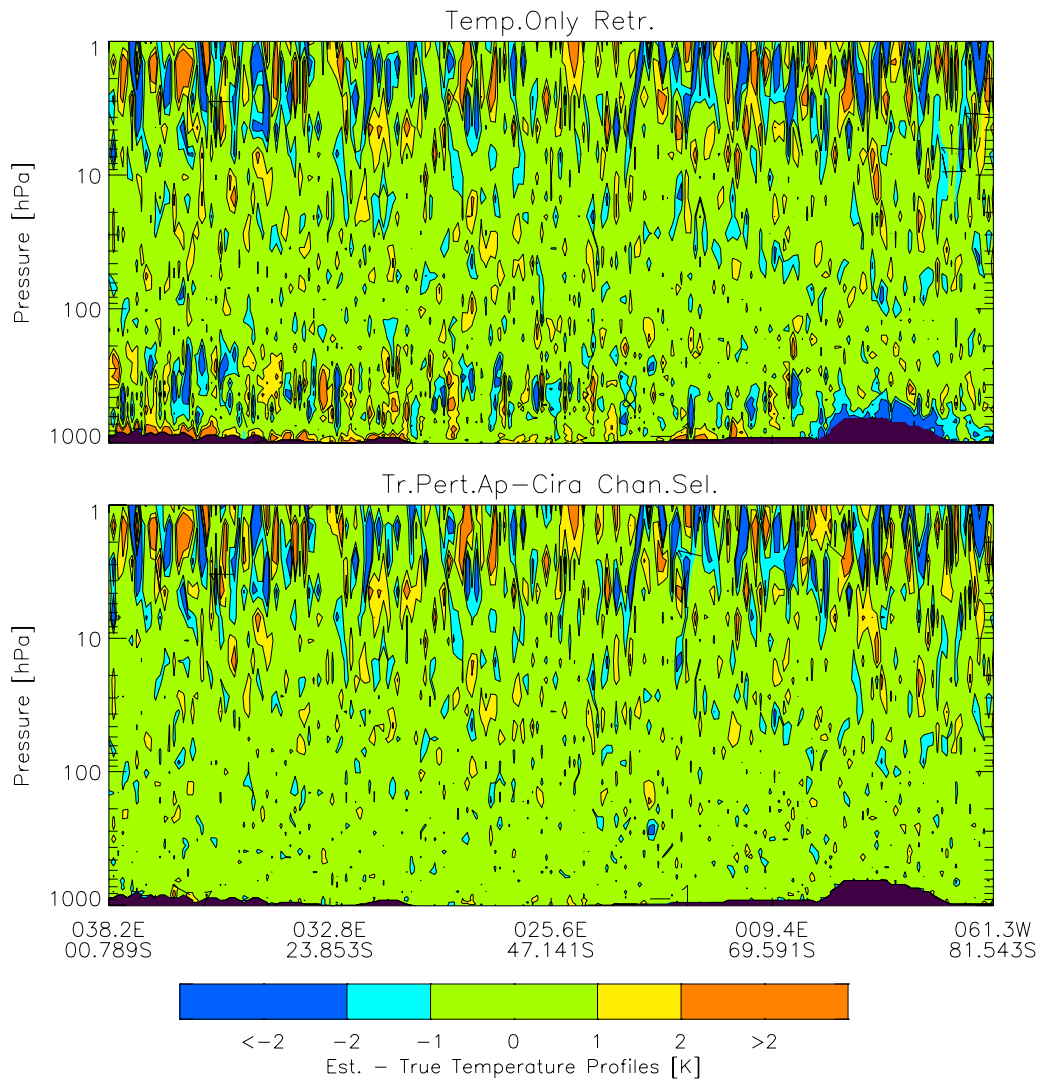


Figure 6.35: Temperature only retrieval (top) versus joint temperature humidity, ozone, and SST retrieval (bottom). Exemplary results for the 191 profiles denoted by the green dots in Figure 6.1 of retrieved minus true temperature profiles. Explanation see text.

In inspecting Figure 6.35 and Figure 6.36 we can identify two regions, which were also mentioned in an earlier study based on a temperature only retrieval (c. f. [Weisz *et al.* (2003)]), where a loss in retrieval quality is obtained by the usage of the single temperature retrieval. The first is the boundary layer where on the one hand we obtain a warm bias in the tropic and mid-latitude region originating from a warmer surface than the overlying atmosphere and on the other hand a cold bias occurring over Antarctica where the surface is actually colder than the atmosphere (c. f. Figure 6.35). These problems are resulting from the absence of an additional SST retrieval based on the inclusion of surface channels as done in the joint retrieval.

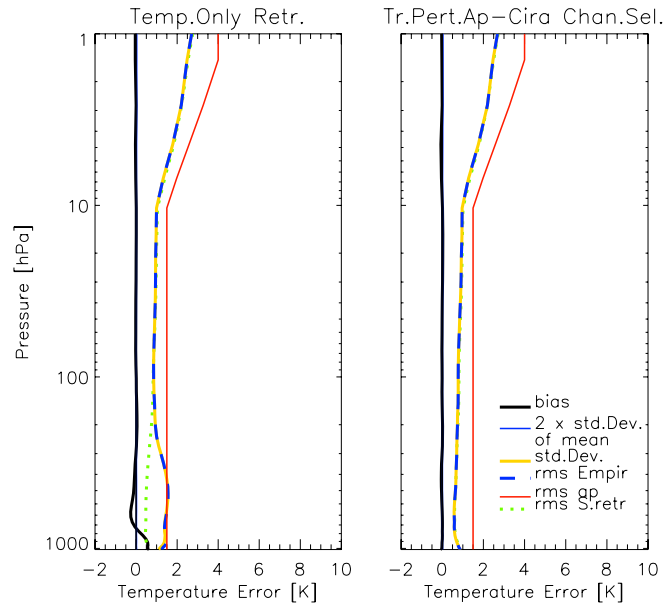


Figure 6.36: Temperature only retrieval (left) versus joint temperature humidity, ozone, and SST retrieval(right). Bias (black line), 2 times standard deviation of bias (solid blue line), standard deviation (yellow line), rms (dashed blue line), theoretical estimate of the rms (dotted green line), and diagonal values of the used *a priori* error covariance matrix (red line). Explanation see text.

The second region where the joint retrieval algorithm shows a clearly improved performance in contrast to the temperature only retrieval is the troposphere where the absence of the simultaneously retrieved humidity results in differences between the theoretical estimation of the rms (which is the same for both retrieval setups) and the empirical one of partly more than 1 K. Figure 6.36 illustrates this behavior.

In contrast to these tropospheric regions the retrieval in the stratosphere (beginning from ~ 200 -100 hPa upwards) shows no appreciable differences between the temperature only and the joint algorithm which can be traced back to the fact that even in the case of the joint retrieval humidity sensitivity is small to negligible at atmospheric regions higher than ~ 200 -100 hPa.

Comparable to the differences between the temperature only retrieval and the joint algorithm the differences between the results for the humidity profiles when performing a humidity-only retrieval and estimating the states of temperature, humidity, ozone, and SST together are quite significant (c. f. Figure 6.37 and Figure 6.38). Apart from the loss in performance due to the effects of non-linearities which take place even in the joint retrieval (c. f. section 6.1) the estimated state for the humidity-only retrieval exhibits further differences.

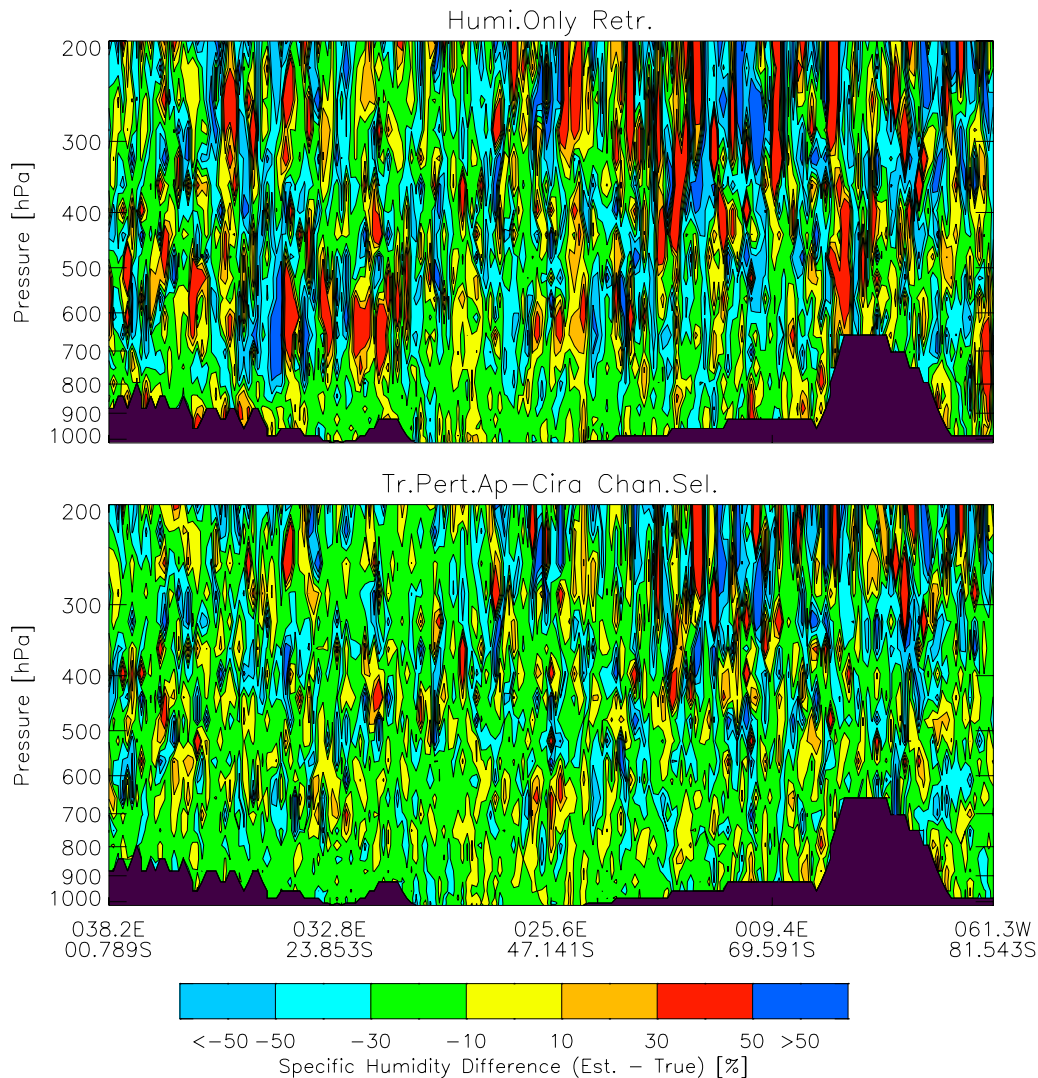


Figure 6.37: Humidity only retrieval (top) versus joint temperature humidity, ozone, and SST retrieval (bottom). Exemplary results for the 191 profiles denoted by the green dots in Figure 6.1 of retrieved minus true humidity profiles. Explanation see text.

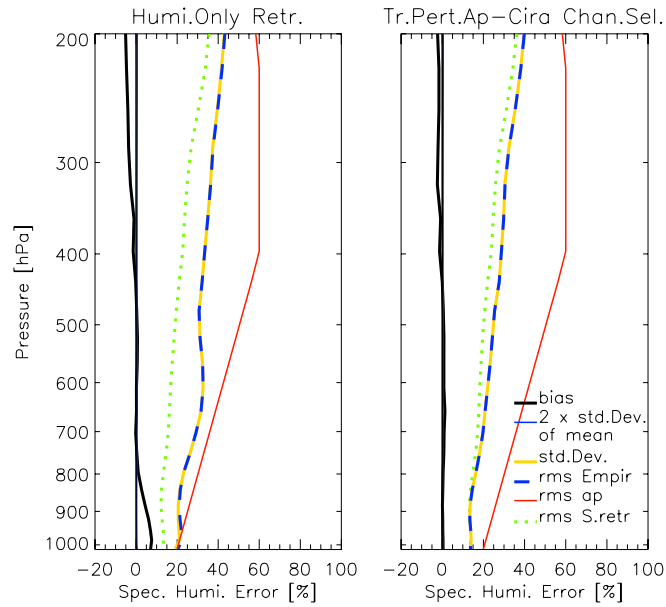


Figure 6.38: Humidity only retrieval (left) versus joint temperature humidity, ozone, and SST retrieval(right). Bias (black line), 2 times standard deviation of bias (solid blue line), standard deviation (yellow line), rms (dashed blue line), theoretical estimate of the rms (dotted green line), and diagonal values of the used *a priori* error covariance matrix (red line). Explanation see text.

We obtain a bias of up to 10% in the boundary layer (lower than ~ 800 hPa) as well as another one of up to 5% from about 350 hPa upwards. An additional effect is the increase of the standard deviation of the retrieved humidity in the whole inspected region most significantly observed in the regions below ~ 500 hPa resulting from the fact that the primary region for the peaking of the humidity weighting functions lies in the domain between ~ 500 hPa and ~ 200 hPa. Evidently the joint retrieval accounts for the temperature-humidity coupling, while the humidity-only retrieval cannot do so.

Figure 6.39 and Figure 6.40 illustrate the differences between a SST only and the joint retrieval. Comparing the error analysis data of the single SST retrieval (c. f. Figure 6.40, (a)) with the results from the joint temperature, humidity, ozone, and SST retrieval (c. f. Figure 6.40, (b)) the latter show a significantly improved performance including empirical rms data which is quite consistent with the theoretical estimate whereas the former exhibits a small bias and deviations of the results which are almost as large as the ones used as input.

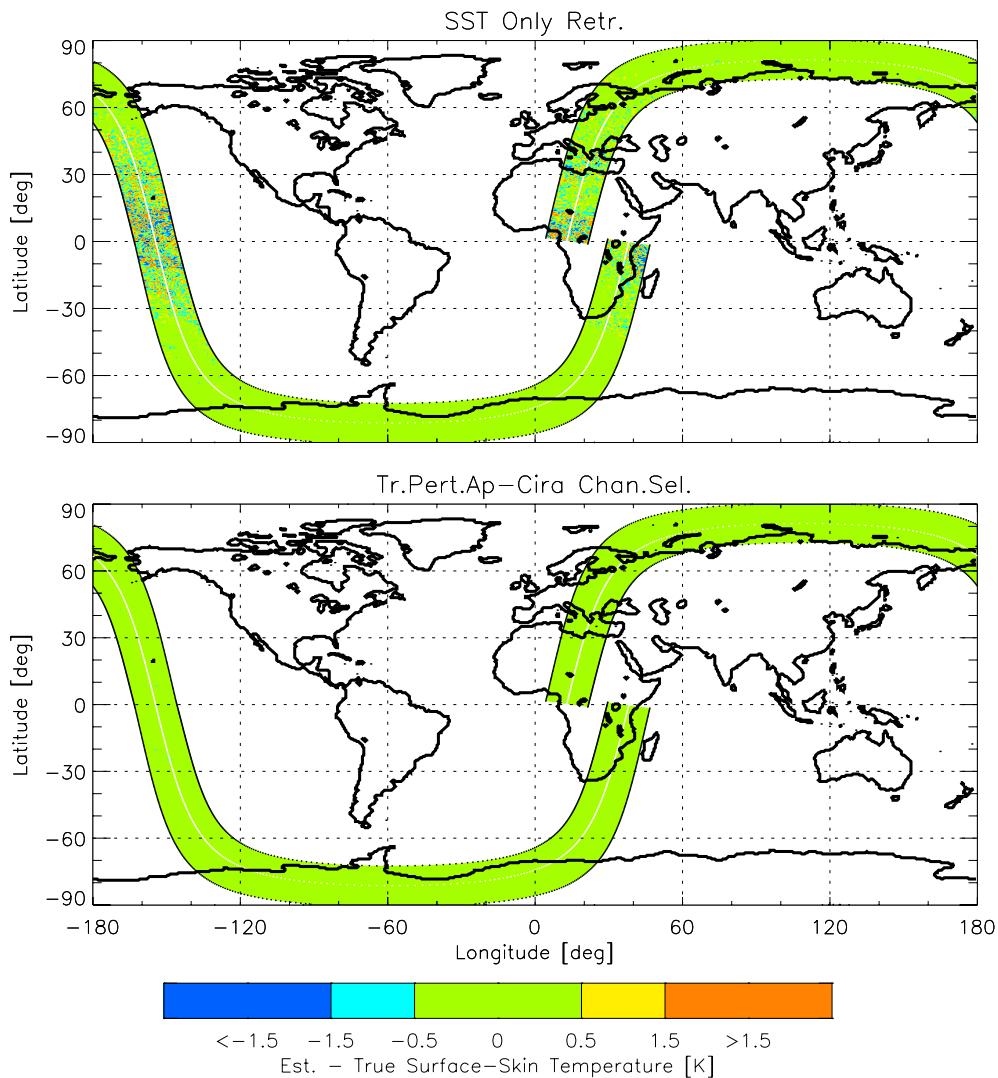


Figure 6.39: SST only retrieval (top) versus joint temperature humidity, ozone, and SST retrieval (bottom). Retrieved minus true SST for the full swath shown in Figure 6.1. Explanation see text.

A closer examination of the error analysis data of the single SST retrieval (i. e. splitting it up into low, mid, and high latitudes) as well as geographical positioning of the occurrences of the big differences in Figure 6.39, top, we find that the reason for this large errors lies in the tropics, more exact, in regions with warm sea surface temperature. Probably the main physical reason behind this is the significant water vapor continuum absorption over warm tropical oceans even in the "atmospheric window" channels (e. g., [Liou (2002)]). In these regions the retrieval is very unstable resulting in rms values which are larger than the input ones. Tests which were processed using the true temperature or humidity profiles, respectively, showed a better performance but in no way reached the quality obtained by the joint algorithm. Therefore it has to be pointed out that for a highly accurate estimate of the sea surface temperature the usage of the joint temperature, humidity, ozone, and SST retrieval algorithm is essential.

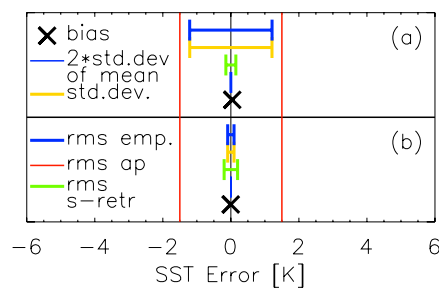


Figure 6.40: SST only retrieval (a) versus joint temperature humidity, ozone, and SST retrieval(b). Bias (black crosses), 2 times standard deviation of bias (thin blue line), standard deviation (yellow line), rms (thick blue line), theoretical estimate of the rms (green line), and *a priori* error (red line). Explanation see text.

In summary we have to point out that the joint temperature, humidity, ozone, and SST retrieval algorithm exhibits a clearly improved performance in contrast to the more specific retrieval setups. In temperature and humidity profiling significant improvements of the retrieval quality in the troposphere can be gained by the aid of one another and, additionally the temperature profile becomes more exact by including surface parameters into the retrieval algorithms. On the other hand, the surface retrieval, especially in the tropics, needs the estimation of the overlying atmosphere in order to obtain results of high quality. Hence, each constituent of the joint algorithm benefits from each other, so the joint retrieval is the obvious method of choice.

6.3.2 Upper Troposphere Humidity Retrieval

In this subsection we try to find out if it is useful to perform a retrieval for a special region, more precisely, to focus on the upper troposphere where the IASI instrument has a lot of peaking water vapor channels which could provide us the opportunity, to retrieve humidity in a numerically efficient way within a region which has a significant lack of knowledge of this specific atmospheric constituent.

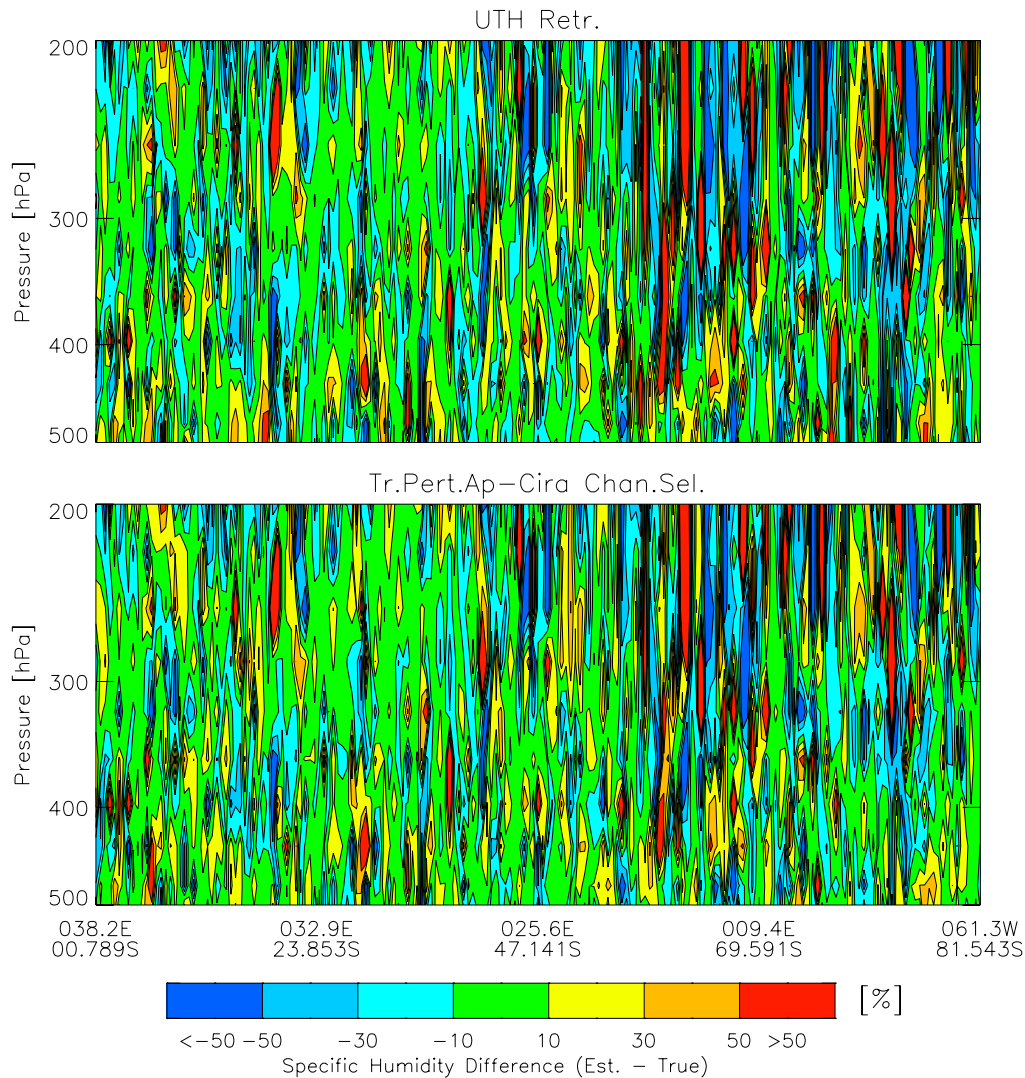


Figure 6.41: Upper troposphere humidity retrieval using the joint temperature and humidity algorithm (top) versus joint temperature humidity, ozone, and SST retrieval (bottom). Exemplary results for the 191 profiles denoted by the green dots in Figure 6.1 of retrieved minus true humidity profiles. Explanation see text.

Thus we used a joint temperature and humidity retrieval algorithm (which exhibits the same performance as the joint algorithm including an additional ozone retrieval, c. f. subsection 6.3.3) and started the estimation process restricted to the region between 200 hPa

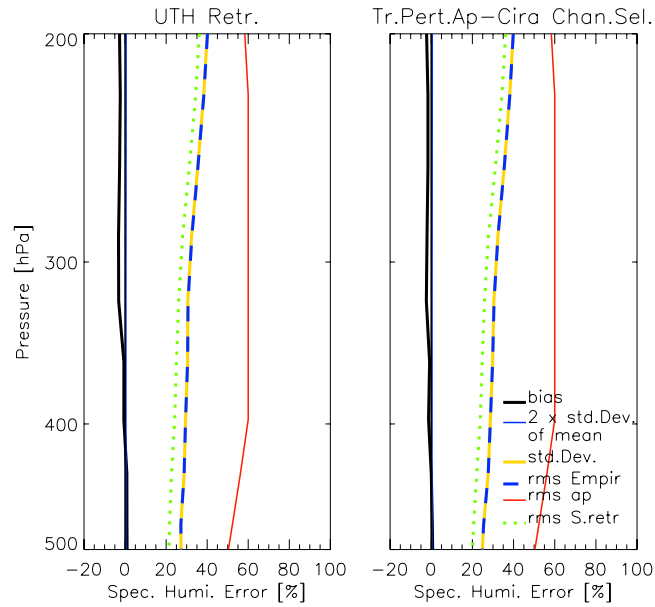


Figure 6.42: Upper troposphere humidity retrieval using the joint temperature and humidity algorithm (left) versus joint temperature humidity, ozone, and SST retrieval (right). Bias (black line), 2 times standard deviation of bias (solid blue line), standard deviation (yellow line), rms (dashed blue line), theoretical estimate of the rms (dotted green line), and diagonal values of the used *a priori* error covariance matrix (red line). Explanation see text.

and 500 hPa (including some additional levels above and below these limits to account for a needed freedom at the boundaries).

The results of this process as well as the results of the reference case (described in subsection 6.1.1) are illustrated in Figure 6.41 and Figure 6.42. We find that both methods perform quite similar apart from small lacks (about 1% higher bias gained by the upper-troposphere-humidity (UTH) retrieval between about 350 hPa and 200 hPa as well as a small increase in the rms at 500 hPa which could be deleted by including one or two more levels at the lower boundary of the retrieval region) but with the opportunity that the run restricted to the upper tropospheric region needs only $\sim 40\%$ of the CPU time of the full run. On the other hand this factor-of-2 efficiency opportunity is highly compensated by the large additional information gained by the full algorithm including the gain in knowledge of temperature and humidity in the lower parts of the troposphere as well as the temperature in the stratosphere, ozone, and SST. Also, care in avoiding any potential biases is vital for climatological exploitation of the data which is our main purpose in mind.

6.3.3 Impact of Additional Ozone Retrieval in the Joint Algorithm

The purpose of this section is to clarify the effects of an inclusion of ozone profiling into the joint algorithm on the results of the estimated temperature and humidity profiles. Thus we performed two test runs, both via using the joint temperature, humidity, and SST algorithm mentioned in subsection 6.3.2. As reference case once more the case with using the initial guesses for temperature, humidity, ozone, and SST as illustrated in Figure 6.7 and Figure 6.8 which consists of data consistent with the *a priori* error covariance matrices for temperature, humidity, ozone, and SST (c. f. section 5.1.2) by perturbing the "true" field via the method described in section 5.1.4 was used. One test run was processed with the same initial setup as the reference case whereas the second one was performed via using the true ozone profiles.

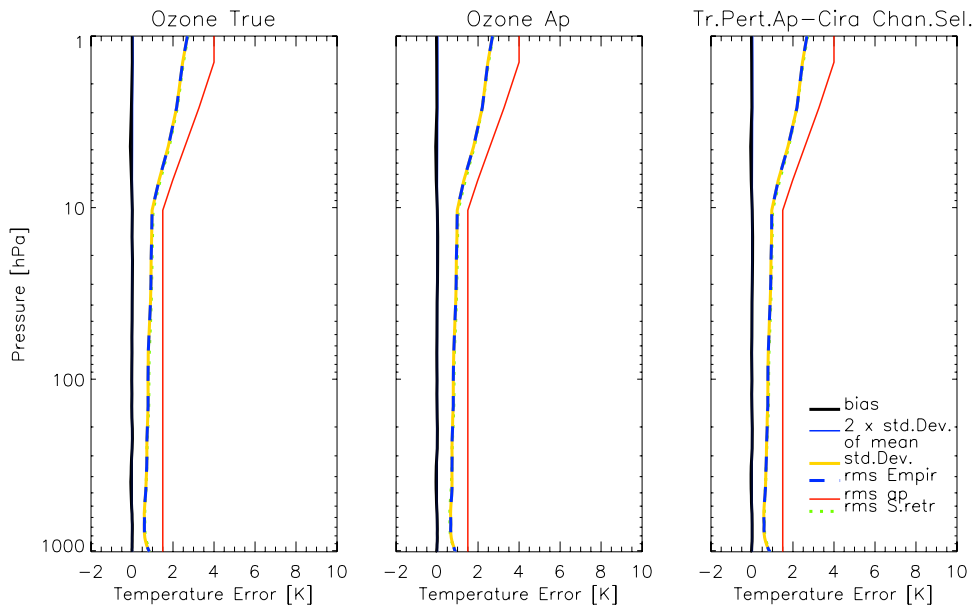


Figure 6.43: Temperature results of the study concerning the impact of the ozone data on the joint algorithm. The left hand side shows the results for a joint temperature, humidity, and SST retrieval with true ozone profiles inserted, the panel in the middle illustrates the results obtained by the same retrieval algorithm but with ozone *a priori* data consistent with the *a priori* error covariance matrix for ozone inserted, whereas the panel on the right hand side shows the results of the joint temperature, humidity, ozone, and SST retrieval.

In inspecting the results for the temperature (c. f. Figure 6.43) and humidity (c. f. Figure 6.44) profiles for the reference case (panels on the right hand side of both figures) as well as for the two test run cases (the panels on the left hand side of both figures show the results for the run where the true ozone was inserted, the middle panels illustrate the retrieved temperature and humidity for the run where the same initial dataset was used as in the reference case) no differences in the results of this three cases can be found. An additional check of the resulting numerical values also showed differences only in the second digit.

An analysis of the numerical efficiency exhibits an about 5% better performance without the ozone retrieval. Thus the decision to include or exclude simultaneous ozone retrieval will generally depend on whether the additional gain of information about the ozone content of the atmosphere or the optimization of numerical efficiency is more important. Our baseline is to include ozone as another important climatological constituent together with water vapor.

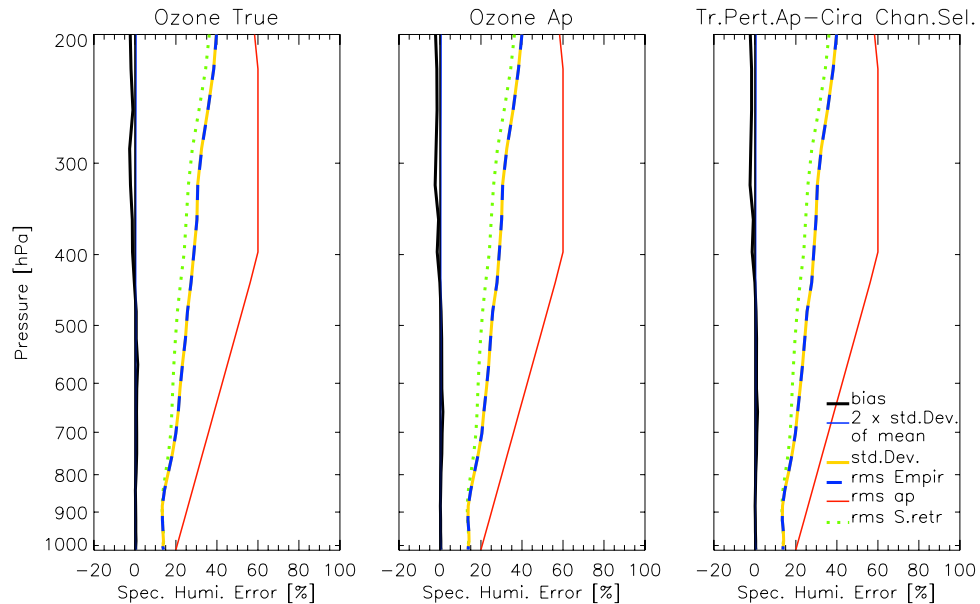


Figure 6.44: Humidity results of the study concerning the impact of the ozone data on the joint algorithm. The left hand side shows the results for a joint temperature, humidity, and SST retrieval with true ozone profiles inserted, the panel in the middle illustrates the results obtained by the same retrieval algorithm but with ozone *a priori* data consistent with the *a priori* error covariance matrix for ozone inserted, whereas the panel on the right hand side shows the results of the joint temperature, humidity, ozone, and SST retrieval.

Summary and Conclusions

In this work we first presented an introduction to the theory of radiative transfer which was followed by an overview of the METOP satellite and a comprehensive description of its instrument IASI. Thereafter an overview on forward modeling and inversion schemes as well as a detailed description of the optimal estimation retrieval methodology was provided.

These introductory chapters were followed by a description of the setup of the joint retrieval algorithm developed within the current study and of the implementation of the channel selection schemes. Finally, detailed simulation experiments were carried out to investigate the performance of the inversion scheme used.

Retrieval algorithms which are based on the physics of the atmosphere, i. e. on our ability to model the physical-functional chain between measurements on the one hand and the atmospheric parameters on the other hand, are strongly depending on the forward model. In our case the problem of the forward simulation is reducible to the problem of computing atmospheric transmittances for the evaluation of the radiances as a function of the state of the atmosphere, which are measured at the TOA. Taking into account the large number of IASI channels the forward model needs to be not only accurate but in particular fast. In the last few years several models have been developed (and are currently in the process of development) for the simulation of IASI measurements. Most of them are so called fast models, performing the transmittance calculation via a regression scheme. The transmittances are then used for the calculation of radiances (or brightness temperatures, respectively) as well as for analytic Jacobians.

The current study was based, in terms of forward modeling, on the usage of the fast radiative transfer model RTIASI [*Matricardi and Saunders (1999)*] which performs the regression on the optical depths rather than on the transmittances themselves. RTIASI was found to be suitable for the calculation of radiances and Jacobians for temperature, humidity, ozone, and SST for our purpose of a combined temperature, humidity, and ozone profile and SST retrieval and it provides satisfactory forward model error characteristics.

Since the IASI instrument has more than 8000 channels we had to implement channel reduction algorithms due to the fact that the large computational burden is neither desirable nor practical in many applications. Therefore we introduced a two-step procedure for down-selecting the channels. The first step includes the removal of channels containing

significant contributions from "foreign" atmospheric constituents (N_2O , CH_4 , SO_2 , and CO) not relevant for the retrieval of the atmospheric parameters dealt with here. The second step was the selection of the most informative channels out of the remaining sample via two approaches for the sake of computational efficiency and retrieval robustness. Both methods, the so called "maximum sensitivity" approach and the information content (IC) technique which is slightly more expensive in selecting the appropriate channels, perform similar in tropospheric and stratospheric regions, whereas the IC method exhibits slightly better results for the Surface skin temperature (SST). We found that the retrieval performance does not significantly degrade due to this channel reduction.

The solution of the inverse problem was implemented via a joint optimal estimation approach for temperature, humidity, ozone, and SST. The non-linearity of the radiative transfer problem was taken into account by using an iterative inversion algorithm employing a Taylor series expansion about a first guess (*a priori*) value. As inputs for it, RTIASI-simulated measurements superposed by reasonable noise, Jacobians for temperature, humidity, ozone, and SST, respectively, *a priori* profiles for the same atmospheric species, as well as parameters for establishing the statistical models of the uncertainties (*a priori* and measurement error covariance matrices) were used.

A reason to use the optimal estimation scheme and at the same time a major advantage of it is that it allows a rigorous analysis of errors and an overall characterization of the retrieval performance. This enables us to compare our results with the requirements claimed by the IASI Mission Rationale and Requirements [*Camy-Peyret and Eyre (1998)*]. According to them IASI measurements shall provide information on temperature profiles in the troposphere and lower stratosphere with an accuracy of 1 K and a vertical resolution of 1 km in the lower troposphere. Additionally, IASI should measure humidity profiles with an accuracy of 10% and a vertical resolution of 1-2 km. Regarding the vertical resolution we employed measures based on the averaging kernel matrix, \mathbf{A} (FWHM of \mathbf{A} , Backus-Gilbert spread, or data density, c. f. [*Rodgers (2000)*]) in this work. The Backus-Gilbert spread, which is the measure most independent of the statistical models of the uncertainties of the *a priori* data yields, in the case of temperature, for 1 K accuracy a vertical resolution of ~ 1 km to 3 km in the troposphere. In the case of humidity, the Backus-Gilbert spread exhibits the same vertical resolution for an accuracy of $\sim 15\%$ to 20% in specific humidity in the troposphere. These results are consistent with those reported by [*Collard (1998)*] (although in the case of humidity [*Collard (1998)*] focused on relative humidity and just stated an estimate for the accuracy of specific humidity) and constitute a significant improvement in accuracy and vertical resolution compared to current infrared sounders, although the formal requirements cited above are failed to be met.

In the current study various sensitivity matrices like the averaging kernel matrix (sensitivity of the retrieved profile to the true profile), the gain matrix (sensitivity of the retrieved profile to the measurements) as well as the impact of the *a priori* data on the retrieval were studied. Additionally, we investigated the retrieval error correlation functions and signal-to-noise ratios. In the following the main conclusions found by investigating these retrieval characteristics are summarized:

- In general we found that the optimal estimation algorithm used, provides profiles of temperature and humidity, which improve significantly over the *a priori* profiles throughout the retrieval domains of interest in the atmosphere. In the case of ozone, improvements were found especially in those stratospheric regions which exhibit high concentrations of this gas. The SST retrieval is found very robust and accurate with rms errors at the 0.1 K level, essentially independent of *a priori* information.
- The retrieval depends on the shape and the width of the weighting functions and therefore relies on the sensitivity of the measured radiances to the targeted atmospheric parameters and, in this context, partly also on the ability of the utilized forward model to characterize the transmissions and weighting functions at high spectral resolution. Difficulties or weaknesses in retrieving atmospheric parameters contained in the joint algorithm at levels where the sensitivity of the Jacobian matrix \mathbf{K} is insufficient are found in the case of temperature in some stratospheric regions, in the case of humidity in the lower troposphere and in the case of ozone in almost all regions except the domain of highest concentrations of ozone. The sensitivity to SST is very good, especially due to the "atmospheric window" channels.
- The theoretical estimates of the rms, i. e. the square roots of the diagonal elements of the retrieval error covariance matrix, depend in their magnitude on the weighting functions; in general they mainly reproduce the shape of the assumed *a priori* errors. In the troposphere, where the measurements dominate the *a priori* data in terms of information, we obtain, in the case of temperature, theoretical estimates of the rms which lie between 0.5 K and 1 K which are increasing to about 1 K at 10 hPa whereas at greater heights <10 hPa the retrieval error approaches the *a priori* error. In the case of humidity, we find theoretical errors of about 15% to 20% up to ~ 400 hPa, which are increasing to about 35% at 200 hPa. For ozone, the best estimate lies near 10% at a height of about 60 hPa but shows almost no difference to the assumed *a priori* error at heights lower than 400 hPa or higher than 5 hPa.
- Regarding the sensitivity of the retrieved profiles to the measurements (gain matrix, \mathbf{G}) we recognize that channels peaking in the stratosphere still contribute significantly to the information in the retrievals. In the case of ozone this is obvious since the main impact of the information about ozone in the measurement lies in the (lower) stratosphere, whereas in the case of temperature to a large extent this is due to the presence of larger *a priori* errors in that height region.
- In summary it can be stated that in the case of temperature beginning from the upper troposphere up into the stratosphere, the retrieval is increasingly influenced by the *a priori* data, whereas in the troposphere the contributions from the measurements are dominating the retrieved temperature as well as the retrieved humidity. The estimation of ozone is in general highly influenced by the *a priori* data with the largest impact of the measurements lying in the region of maximum ozone concentrations (ozone layer). Thus the tropospheric region – once more focusing on temperature and humidity – can be considered as well probed by the IASI instrument, implying

that the true state will be well reproduced by the measurements in this part of the atmosphere. Hence, *a priori* data are least important in the troposphere, especially in the case of temperature, but also in the case of humidity where initial *a priori* data sets with an average disturbance up to 60% receive quite significant gains in information. These statements are expressed well by the profiles of the retrieval-to-*a priori* error ratios and the averaging kernels as well as by the signal-to-noise ratios. At the same time these characterization profiles also reveal the strong need for *a priori* data for temperature and humidity from the tropopause region upwards.

The joint algorithm was found to highly improve the results of more specific retrieval setups tested (single parameter retrievals) and to solve many problems of these specific implementations. Compared to temperature only retrievals, biases arising in the boundary layer as well as problems in the tropospheric region due to the absence of simultaneous humidity retrievals can be corrected. Compared to humidity only retrievals, humidity biases in the upper tropospheric region (from about 350 hPa upwards) are corrected and the standard deviation is reduced. Compared to SST only retrievals, the joint algorithm corrects instabilities of the retrieved SST which occur mainly in the low and low-mid latitudes and results in a quite significant improvement – the empirical rms is lower than 0.1 K. In practice only the joint algorithm, consistently accounting for the parameter inter dependencies, should thus be employed.

A further comparison of the joint algorithm with a retrieval focused on the upper troposphere domain only, especially on the humidity in that region, showed a gain in numerical efficiency but a small decrease in the performance of the retrieval. In addition, it was found that the results for temperature, humidity, and SST are quite independent from the initial guess of the ozone data if it remains in the domain of linearity or moderate non-linearity, respectively (a few 10% uncertainty level). This is also true vice versa.

The results obtained in this study provide guidance for future advancements including a further improvement of the statistical model of the *a priori* uncertainties for temperature and humidity (e. g., the usage of the relevant ECMWF *a priori* error covariance matrices). An additional improvement could be expected from the usage of the newest version of the forward model RTIASI, which contains a new scheme for prediction of the water vapor continuum, a refinement of the vertical pressure grid, an inclusion of trace gases such as CO₂, N₂O, CO and CH₄ as profile variables, as well as the introduction of a solar term to evaluate the solar radiance reflected by a land or water surface in a non-scattering atmosphere (c. f. [Matricardi (2003)]). As a future step towards real data the complete temperature, humidity, ozone, and SST algorithm should be applied to AIRS data.

In summary this study strongly indicates that the high spectral resolution measurements of the IASI sensor indeed have high potential to significantly improve upon current operational sensors for temperature and humidity profiling and that they may get a key position for the much needed monitoring of climate changes in the thermal structure and moisture distribution of the atmosphere in the future.

Appendix A

IASI - RTIASI Data

A.1 Construction of the Simulated IASI Swath

A.1.1 Calculation of the Points on a Measurement Ray

For calculating the measurement ray points located on the surface of the earth as well as those points lying on the sounding ray (c. f. Figures in Table A.2 and Table A.3), the principles of spherical trigonometry were used:

Sine rule:

$$\frac{\sin \alpha}{\sin a'} = \frac{\sin \beta}{\sin b'} = \frac{\sin \gamma}{\sin c'}$$

Cosine rule for sides:

$$\cos c' = \cos a' \cos b' + \sin a' \sin b' \cos \gamma$$

Cosine rule for angles:

$$\cos \gamma = \sin \alpha \sin \beta \cos c' - \cos \alpha \cos \beta$$

(A.1)

with $a' = a/R_E$, $b' = b/R_E$,
and $c' = c/R_E$.

The simulation of the IASI swath was performed by first calculating the ground points of a special METOP track using a standard orbit software extracted from the Mission Analysis Planning System of the EGOPS software package [Kirchengast et al. (2002)]. The orbit is specified by the following two-line-element (tle) file:

```

METOP-1                M1                betalim = 10.0
1      1  96213USR 00213.50000000  .00000000  00000-0  00000-0  0  0010
2      1  98.7047 264.3857 0011650  90.0000 294.1230 14.21635855  0

```

The special meaning of the individual elements is described in Table A.1.

Line 0	
Meta-information describing the satellite	
Line 1	
Column	Description
01	Line Number of Element Data
03-07	Satellite Number
08	Classification (U=Unclassified)
10-11	International Designator (Last two digits of launch year)
12-14	International Designator (Launch number of the year)
15-17	International Designator (Pieces of the launch)
19-20	Epoch Year (Last two digits of the year)
21-32	Epoch (Day of the year and fractional portion of the day)
34-43	First Time Derivative of the Mean Motion
45-52	Second Time Derivative of the Mean Motion (decimal point assumed)
54-61	BSTAR Drag Term (decimal point assumed)
63	Ephemeris Type
65-68	Element Number
69	Checksum (Modulo 10) (Letters, blanks, periods, plus signs = 0; minus signs = 1)
Line 2	
Column	Description
01	Line Number of Element Data
03-07	Satellite Number
09-16	Inclination [Degrees]
18-25	Right Ascension of the Ascending Node [Degrees]
27-33	Eccentricity (decimal point assumed)
35-42	Argument of Perigee [Degrees]
44-51	Mean Anomaly [Degrees]
53-63	Mean Motion [Revolutions per day]
64-68	Revolution Number at epoch [Revolutions]
69	see Column 69 of Line 1

Table A.1: Description of the individual elements of an tle file (source: <http://celestrak.com>).

The points are computed with a time difference of 8 seconds which is approximately the time between two consecutive full swath measurement (c. f. Table 2.2). The step time

between measuring two pixels is not accounted for. The earth was assumed spherical with a mean radius $R_E = 6371$ km. A further approximation which was made is the assumption that all rays are straight lines (which is not accurately true for obliquity angles greater than about 30° off nadir in a real atmosphere). All those approximations are fully adequate in the context of the present performance analysis study, however.

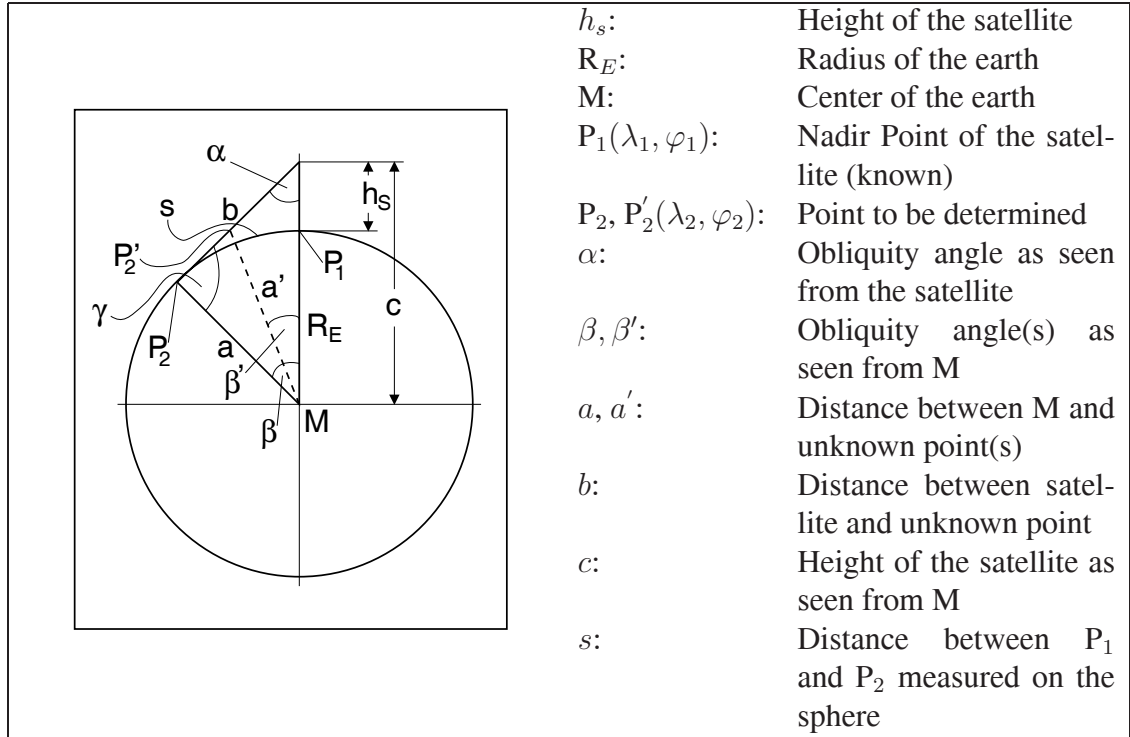


Table A.2: Geometry used for the generation of the simulated IASI swath – part 1.

The distance s between the ground track point of the satellite, $P_1(\lambda_1, \varphi_1)$ (c. f. Table A.2) and another point on the surface $P_2(\lambda_2, \varphi_2)$, defined by a special obliquity angle α is obtained via:

$$\begin{aligned} a &= R_E \\ c &= R_E + h_s \\ \sin \gamma &= \frac{c}{a} \sin \alpha \quad \implies \quad \gamma = \pi - \arcsin \left[\frac{c}{a} \sin \alpha \right], \end{aligned} \quad (\text{A.2})$$

since the sine rule (c. f. Equations A.1) delivers the angle in the first quadrant. This yields:

$$\begin{aligned} \beta &= \pi - (\alpha + \gamma) \\ s &= \beta \cdot a, \end{aligned} \quad (\text{A.3})$$

where a equals R_E .

In the case of a point located on the ray-path the same equations are true, except that:

$$a \longrightarrow a' = R_E + h_L, \quad (\text{A.4})$$

where h_L is the level height which, in case of the forward Model RTIASI is the height corresponding to one of the pre-defined pressure levels.

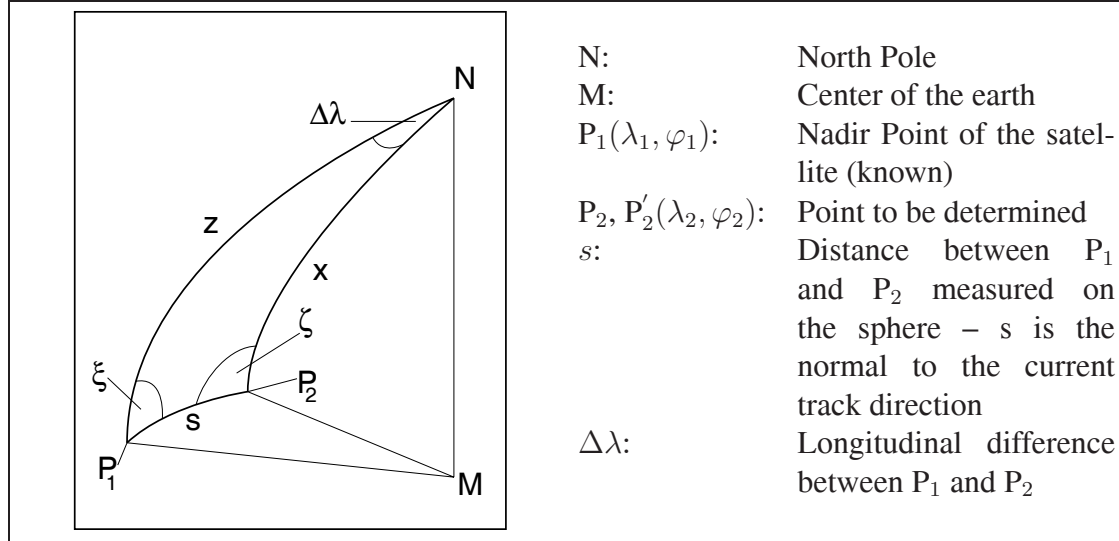


Table A.3: Geometry used for the creation of the simulated IASI swath – part 2.

Having the distance, s , between the (known) nadir point of the satellite, P_1 , and the point searched for, P_2 , we can use the cosine rule for sides (c. f. Equations A.1) to determine the geographical longitude and latitude of P_2 :

$$x = \arccos [\cos z \cos s + \sin z \sin s \cos \xi], \quad (\text{A.5})$$

where z is the polar angle between the North Pole and the point P_1 measured from the center of the earth:

$$z = \frac{\pi}{2} - \varphi_1, \quad (\text{A.6})$$

and ξ is the (known) angle normal to the (known) current track direction. The difference in longitude between P_1 and P_2 can be obtained by:

$$\Delta\lambda = \arccos \left[\frac{\cos s - \cos x \cos z}{\sin x \sin z} \right]. \quad (\text{A.7})$$

Collecting the results of Equations A.5 and A.7, and using the relation between polar angles and geographic latitudes, Equation A.6, the geographic latitude and longitude of the unknown point, P_2 , can be written as follows:

$$\begin{aligned} \varphi_2 &= \frac{\pi}{2} - x, \\ \lambda_2 &= \lambda_1 + \Delta\lambda. \end{aligned} \quad (\text{A.8})$$

A.1.2 Calculation of the Surface Height Including Orography

The surface height at any required location is obtained by a simple approximation procedure. First the point at the end of a ray for a surface height of 0 m is calculated with the procedure described in subsection A.1.1. For this point, the height according to the used field (in this work high resolution ECMWF analysis fields were used) is identified. If this height is lower than a predefined value (20 m in this study) this point is chosen to be the surface point, if not, a point according to the identified height is calculated via the procedure described in subsection A.1.1. Now the surface height of this new point according to the used field is identified and the difference between this new surface height and the surface height of the previous point is calculated. Convergence is reached, when the difference is lower than the predefined value of 20 m.

A.2 RTIASI Pressure Levels

Level Number	Pressure [hPa]	Level Number	Pressure [hPa]
1	0.10	23	253.71
2	0.29	24	286.60
3	0.69	25	321.50
4	1.42	26	358.28
5	2.61	27	396.81
6	4.41	28	436.95
7	6.95	29	478.54
8	10.37	30	521.46
9	14.81	31	565.54
10	20.40	32	610.60
11	27.26	33	656.43
12	35.51	34	702.73
13	45.29	35	749.12
14	56.73	36	795.09
15	69.97	37	839.95
16	85.18	38	882.80
17	102.50	39	922.46
18	122.04	40	957.44
19	143.84	41	985.88
20	167.95	42	1005.43
21	194.36	43	1013.25
22	222.94		

Table A.4: Pressure levels used as input grid for the fast radiative transfer Model RTIASI (see [Matricardi and Saunders (1999)]).

A.3 IASI Level 1c Noise Values

wavenumber [cm ⁻¹]	Noise Stdev. [K]	wavenumber [cm ⁻¹]	Noise Stdev. [K]
650	0.419	1750	0.170
700	0.157	1800	0.200
750	0.145	1850	0.224
800	0.145	1900	0.250
850	0.150	1950	0.240
900	0.150	2000	0.130
950	0.165	2050	0.135
1000	0.165	2100	0.141
1050	0.176	2150	0.151
1100	0.200	2200	0.172
1150	0.200	2250	0.200
1200	0.095	2300	0.239
1250	0.096	2350	0.287
1300	0.098	2400	0.351
1350	0.100	2450	0.400
1400	0.105	2500	0.700
1450	0.105	2550	0.900
1500	0.111	2600	1.100
1550	0.116	2650	1.300
1600	0.125	2700	1.600
1650	0.137	2750	1.935
1700	0.160		

Table A.5: IASI Level 1c Noise Values at every 50 cm⁻¹ (Table after [Weisz (2001)]; values from Peter Schlüssel, personal communications, 2000).

A.4 Determination of the Number of Channels in the Channel Selection Algorithms

The number of selected channel per level is determined by taking 10% of the total number of peaking channels. In addition, maximum and minimum thresholds varying according to the average number of selected channels and to the retrieval scheme, c. f. Tables A.6 and A.7, are defined (for temperature there are two sets defined according to the pressure level range of the humidity retrieval, i. e. upper set (<): Level 1-16, lower range Level 17-43). The explicit way of determining the number of channels, n , can be written as follows (c. f. [Lerner et al. (2002)]):

$$n = \min \{ \min [n_{peak}, \max (f \cdot n_{peak}), n_{min}] , n_{max} \} , \quad (\text{A.9})$$

where n_{peak} is the number of weighting functions peaking at the currently treated level, f is the fractional factor which was set 0.1 (10%) in this study, and n_{min} and n_{max} are the minimum and maximum threshold numbers defined in Tables A.6 and A.7.

Single Temperature Retrieval						
	upper region			lower region		
	min	medium	max	min	medium	max
n_{min}	1	20	70	2	25	75
n_{max}	2	25	90	3	35	90
Single Humidity Retrieval						
	upper region			lower region		
	min	medium	max	min	medium	max
n_{min}	0	0	0	2	30	80
n_{max}	0	0	0	4	50	95
Single Ozone Retrieval						
	upper region			lower region		
	min	medium	max	min	medium	max
n_{min}	5	30	30	5	30	30
n_{max}	6	50	50	6	50	50
Single SST Retrieval						
	upper region			lower region		
	min	medium	max	min	medium	max
n_{min}	0	0	0	60	60	60
n_{max}	0	0	0	80	80	80

Table A.6: Minimum and maximum threshold numbers for the determination of selected channels (part 1).

Joint Temperature, Humidity, and SST Retrieval						
Temperature						
	upper region			lower region		
	min	medium	max	min	medium	max
n_{min}	1	5	20	2	10	25
n_{max}	2	7	25	3	17	40
Humidity						
	upper region			lower region		
	min	medium	max	min	medium	max
n_{min}	0	0	0	2	10	30
n_{max}	0	0	0	4	25	50
SST						
	upper region			lower region		
	min	medium	max	min	medium	max
n_{min}	0	0	0	60	60	60
n_{max}	0	0	0	80	80	80
Joint Temperature, Humidity, Ozone, SST						
Temperature						
	upper region			lower region		
	min	medium	max	min	medium	max
n_{min}	1	5	10	2	9	13
n_{max}	2	9	13	3	13	23
Humidity						
	upper region			lower region		
	min	medium	max	min	medium	max
n_{min}	0	0	0	2	10	17
n_{max}	0	0	0	4	18	35
Ozone						
	upper region			lower region		
	min	medium	max	min	medium	max
n_{min}	5	20	30	5	20	30
n_{max}	6	30	50	6	30	50
SST						
	upper region			lower region		
	min	medium	max	min	medium	max
n_{min}	0	0	0	60	60	60
n_{max}	0	0	0	80	80	80

Table A.7: Minimum and maximum threshold numbers for the determination of selected channels (part 2).

Appendix B

Basic Physics and Statistics

B.1 Basic Radiation Laws

All bodies above absolute zero temperature emit radiation. A body absorbing all incoming radiation is known as a blackbody. To observe blackbody spectra Max Planck (1858 – 1947) postulated that the radiation of frequency ν_f (to distinguish it from the wavenumber, ν) assumes energy amounts only in discrete quanta described by:

$$E = h\nu_f, \quad (\text{B.1})$$

where E is the energy and h is the Planck constant. Hence, individual nuclei, atoms, molecules, etc., absorb or emit radiation in discrete pieces, i. e. photons, carrying energy of multiples of $h\nu$.

Planck's Law describes the spectral intensity $B_{\nu_f}(T)$, emitted by the blackbody for a given temperature at a special frequency, ν_f :

$$B_{\nu_f}(T) = \frac{2h\nu_f^3}{c^2(e^{h\nu_f/kT} - 1)}. \quad (\text{B.2})$$

If one replaces the frequency, ν_f , by the wavelength, λ , the Planck function takes the form:

$$B_{\lambda}(T) = \frac{2hc^2}{\lambda^5(e^{hc/\lambda kT} - 1)}. \quad (\text{B.3})$$

Of course the Planck function can also be expressed in terms of the wavenumber, ν , (with: $\lambda\nu = 1$; $\lambda d\nu + \nu d\lambda = 0$):

$$B_{\nu}(T) = \frac{2hc^2\nu^3}{(e^{h\nu/kT} - 1)}. \quad (\text{B.4})$$

Integrating over all wavenumbers gives the total flux F , emitted by a blackbody which is described by the *Stefan-Boltzmann Law*:

$$F = \pi B(T) = \pi \int_0^{\infty} B_{\nu}(T) d\nu = \sigma T^4, \quad (\text{B.5})$$

where σ is the Stefan-Boltzmann constant:

$$\sigma = \frac{2 \pi k^4}{15 h^3 c^2}. \quad (\text{B.6})$$

For a radiance, I_ν , emitted by an arbitrary object there exists an associated temperature referred to as *brightness temperature*, T_B , at which a blackbody would emit the same radiation. Hence, we can write:

$$T_B \equiv B_\nu^{-1}(I_\nu) = \frac{hc\nu}{k \ln(1 + \frac{2hc^2\nu^3}{I_\nu})}. \quad (\text{B.7})$$

For any temperature T , the Planck function has a single maximum at a certain wavelength which follows from the so called *Wien's displacement Law*:

$$\lambda_{max} = \frac{b}{T}, \quad (\text{B.8})$$

where b is given in section B.5.

Most solids and liquids behave like blackbodies and therefore can be described by Equations B.2 to B.7. This is not true for gases. Their emission is less than for an equivalent blackbody. *Kirchhoff's law* applies for the so called gray bodies, postulating that:

$$\alpha_\nu = \epsilon_\nu, \quad (\text{B.9})$$

where α_ν is the absorptance and ϵ_ν the emittance of a body. They are defined by:

$$\begin{aligned} \alpha_\nu &= \frac{\text{absorbed radiation at } \nu}{\text{incident radiation at } \nu}, \\ \epsilon_\nu &= \frac{\text{emitted radiation at } \nu}{B_\nu(T)}. \end{aligned} \quad (\text{B.10})$$

Note that Kirchhoff's law is valid only under the assumption of thermodynamic equilibrium which is approximately true for atmospheric regions below 80 km.

Incident radiation can be modified not only by absorption but as well by reflection and scattering and of course it can just be transmitted through the medium. Thus we define the reflectance, ρ_ν , and the transmittance, T_ν , as:

$$\begin{aligned} \rho_\nu &= \frac{\text{reflected radiation at } \nu}{\text{incident radiation at } \nu}, \\ T_\nu &= \frac{\text{transmitted radiation at } \nu}{\text{incident radiation at } \nu}. \end{aligned} \quad (\text{B.11})$$

Since energy is conserved, we have $\alpha_\nu + \rho_\nu + T_\nu = 1$. Further more detailed descriptions of basic radiation laws can be found, for example, in [*Hanel et al. (1992)*, *Salby (1996)*].

B.2 Conversion of Physical Parameters

This section gives a summary on the conversion of the units of the physical parameters used in this study, i. e. only the conversion from mass to volume mixing ratios and to number densities (used to illustrate ozone). Similar explanations can be found in e. g., [Reuter *et al.* (1997)].

Let us start with the conversion from mass to volume mixing ratio. The mixing ratio by mass, m_m , of an atmospheric parameter given in [kg/kg] (e. g., ozone or water vapor mass mixing ratio as provided in this unit by ECMWF) is defined as the mass of this atmospheric parameter, m_p , divided by the total mass of the atmosphere without the mass of the atmospheric parameter, m_t in a given volume:

$$m_m = \frac{m_p}{m_t} = \left[\frac{\text{kg}}{\text{kg}} \right]. \quad (\text{B.12})$$

The mixing ratio by volume, m_V , is defined as the number of molecules (atoms, etc.) of the special parameter, N_p , divided by the total number of particles of the atmosphere without the number of the special treated parameter, N_t , in a given volume:

$$m_V = \frac{N_p}{N_t} = [1, \text{ppmv}, \text{ppbv}, \text{pptv}, \text{etc.}]. \quad (\text{B.13})$$

With:

$$N = \nu N_A \quad \text{with:} \quad \nu = \frac{m}{M}, \quad (\text{B.14})$$

where ν [mol], is the molar abundance, N_A [1] is the Avogadro constant, m is the mass [kg], and M [kg/mol] is the molar mass. This can be transformed into:

$$m_V = \frac{N_p}{N_t} = \frac{\nu_p}{\nu_t} = \frac{\frac{m_p}{M_p}}{\frac{m_t}{M_t}} = \frac{m_p}{m_t} \frac{M_t}{M_p}. \quad (\text{B.15})$$

Hence, to convert an atmospheric constituent from mass mixing ratio to volume mixing ratio we have to multiply the mass mixing ratio by the reciprocal ratio of its molar masses, M_t/M_p , which is sufficient for humidity since we have the molar mass of dry air (see section B.5).

In the case of ozone we have to note that the subscript t denotes the total mass (or number of particles) of the whole atmosphere without the mass of the atmospheric parameter. This means that:

$$\nu_t = \nu_a - \nu_p = \frac{m_a}{M_a} - \frac{m_p}{M_p}, \quad (\text{B.16})$$

where the subscript a means air. Since $\frac{m_p}{M_p} \ll \frac{m_a}{M_a}$ we can, however, neglect the second term in Equation B.16 which yields:

$$m_V \approx \frac{N_p}{N_a} = \frac{m_p}{m_a} \frac{M_a}{M_p}. \quad (\text{B.17})$$

Let us now turn to the conversion of mass mixing ratios to number densities. We start by defining a virtual temperature T_v by:

$$T_v = \left(1 + \frac{R_w - R_d}{R_d} q \right) T, \quad (\text{B.18})$$

where R_w is the specific gas constant of wet air, R_d is the specific gas constant of dry air, T is the temperature, and q is the specific humidity in [kg/kg] defined as the ratio of the mass of water vapor in a moist air parcel to the total mass of the moist air parcel:

$$q \equiv \frac{m_w}{m_d + m_w} = \frac{\rho_w}{\rho}, \quad (\text{B.19})$$

where ρ_w is the mass density of water vapor in a given volume, and ρ is the mass density of moist air. Now we get the mass density of the atmosphere for a given pressure p and virtual temperature T_v via using a special form of the ideal gas law ($p = R \rho T$):

$$\rho = \frac{p}{R_d T_v}. \quad (\text{B.20})$$

With this the conversion of a given mass mixing ratio (e. g., ozone) in [kg/kg] to number density, is given by:

$$n_p = \frac{\rho m_{m,p}}{m_p}, \quad [\text{m}^{-3}], \quad (\text{B.21})$$

where n_p in [m^{-3}] denotes the number density of the atmospheric parameter, $m_{m,p}$ its mass mixing ratio, and m_p its mass in [kg]. In the case of ozone, m_p is the molecular mass of ozone, m_{O_3} , given by:

$$m_{O_3} = 3 m_O m_u, \quad (\text{B.22})$$

where m_O is the atomic mass of oxygen in m_u 's, and m_u is the atomic mass unit given in section B.5.

B.3 Basic Statistical Properties

In this section a brief summary of the statistic properties (bias, standard deviations, variances, covariances, and rms) used in this study is given (c. f. [Steiner and Kirchengast (2004)]).

Let us define difference profiles $\Delta \mathbf{x}$ ($\Delta \mathbf{x} = (\Delta x_1, \dots, \Delta x_i, \dots, \Delta x_N)^T$, with i denoting the height levels, N the dimension of the state vectors, and T the matrix transpose) between the retrieved, \mathbf{x}_{retr} , and the *a priori*, \mathbf{x}_{ap} , profiles, respectively, and the true profile, \mathbf{x}_{true} , in the form:

$$\Delta \mathbf{x} = (\mathbf{x}_{retr,ap} - \mathbf{x}_{true}). \quad (\text{B.23})$$

The calculation of the mean of the difference profiles leads to the bias profile, \mathbf{b} :

$$\mathbf{b} = \left[\frac{1}{n} \sum_{k=1}^n \Delta \mathbf{x}_k \right], \quad (\text{B.24})$$

with n as the number of events in the ensemble. As a next step, the bias is subtracted from each profile, giving the bias-free profiles, $\Delta \mathbf{x}_{biasfree}$:

$$\Delta \mathbf{x}_{biasfree} = \Delta \mathbf{x} - \mathbf{b}. \quad (\text{B.25})$$

With these bias-free profiles we compute the empirical error covariance matrix, \mathbf{S}_{empir} :

$$\mathbf{S}_{empir} = \left[\frac{1}{n-1} \sum_{k=1}^n (\Delta \mathbf{x}_{k,biasfree}) (\Delta \mathbf{x}_{k,biasfree})^T \right], \quad (\text{B.26})$$

with its diagonal elements, S_{ii} , representing the variances at height level i and with its non-diagonal elements, S_{ij} , representing the covariances between height levels i and j . The square root of the diagonal of the error covariance matrix gives the standard deviation profile, \mathbf{s} :

$$\mathbf{s} \quad \text{with:} \quad s_i = \sqrt{S_{ii}}. \quad (\text{B.27})$$

The root mean square error profile, \mathbf{rms} then reads:

$$\mathbf{rms} \quad \text{with:} \quad rms_i = \sqrt{b_i^2 + s_i^2}. \quad (\text{B.28})$$

B.4 Atmospheric Constituents

Constituent	Mixing Ratio	Vertical Distribution	Controlling Process
N ₂	0.78708	Homogeneous	Vertical mixing
O ₂	0.2095	Homogeneous	Vertical mixing
H ₂ O	≤ 0.030	Decreases sharply in troposphere; increases in stratosphere; highly variable.	Evaporation, condensation, transport; production by CH ₄ via oxidation.
Ar	0.0093	Homogeneous	Vertical mixing
CO ₂	~ 370 ppmv	Homogeneous	Vertical mixing; produced by surface and anthropogenic processes.
O ₃	~ 10 ppmv	Increases sharply in the stratosphere; highly variable.	Photochemical production in the stratosphere; destruction at surface; transport
CH ₄	~ 11760 ppbv	Homogeneous in the troposphere; decreases in the middle atmosphere.	Production by surface processes; oxidation produces H ₂ O
N ₂ O	~ 320 ppbv	Homogeneous in the troposphere; decreases in the middle atmosphere.	Production by surface and anthropogenic processes; dissociation in the middle atmosphere; produces NO; transport
CO	~ 70 ppbv	Decreases in the troposphere; increases in the stratosphere.	Production anthropogenically and by oxidation of CH ₄ ; transport
NO	~ 0.1 ppbv	Increases vertically.	Production by dissociation of N ₂ O, catalytic destruction of O ₃
CFCl ₃ (CFC-11)	~ 270 pptv	Homogeneous in the troposphere; decreases in the stratosphere.	Industrial production; mixing in the troposphere; photo-dissociation in the stratosphere.
CF ₂ Cl ₂ (CFC-12)	~ 530 pptv	see CFC-11.	see CFC-11.

Table B.1: Table after [Liou (1992)] – updated; from [Weisz (2001)]. The volume mixing ratios are representative for the troposphere and the stratosphere. The mixing ratio of ozone represents the stratospheric value. The radiatively active gases are H₂O, CO₂, O₃, CH₄, N₂O and CFCs.

B.5 Physical Constants

Constant		value	uncertainty	unit
c	speed of light in vacuum	299 792 458	exact	m s^{-1}
h	Planck constant	$6.626\,0693 \times 10^{-34}$	$0.000\,0011 \times 10^{-34}$	J s
		$4.135\,667\,43 \times 10^{-15}$	$0.000\,000\,35 \times 10^{-15}$	eV s
k	Boltzmann constant	$1.380\,6505 \times 10^{-23}$	$0.000\,0024 \times 10^{-23}$	J K^{-1}
		$8.617\,343 \times 10^{-5}$	$0.000\,015 \times 10^{-5}$	eV K^{-1}
σ	Stefan-Boltzmann constant	$5.670\,400 \times 10^{-8}$	$0.000\,040 \times 10^{-8}$	$\text{W m}^{-2} \text{K}^{-4}$
m_u	atomic mass unit	$1.660\,538\,86 \times 10^{-27}$	$0.000\,000\,28 \times 10^{-27}$	kg
G	Newtonian constant of gravitation	6.6742×10^{-11}	0.0010×10^{-11}	$\text{m}^3 \text{kg}^{-1} \text{s}^{-2}$
N_A	Avogadro constant	$6.022\,1415 \times 10^{23}$	$0.000\,0010 \times 10^{23}$	mol^{-1}
n_0	Loschmidt constant at 273.15 K and 1013.25 hPa	$2.686\,7773 \times 10^{25}$	$0.000\,0047 \times 10^{25}$	m^{-3}
R^*	molar gas constant	8.314 472	0.000 015	$\text{J mol}^{-1} \text{K}^{-1}$
b	Wien's displacement law constant	$2.897\,7685 \times 10^{-3}$	$0.000\,0051 \times 10^{-3}$	m K
e	elementary charge	$1.602\,176\,53 \times 10^{-19}$	$0.000\,000\,14 \times 10^{-19}$	C

Table B.2: Physical Constants according to CODATA 2002. Source: The NIST reference on constants, units, and uncertainties available at: <http://physics.nist.gov/cuu/>.

B.6 Parameters of Earth and Atmosphere

Parameter		value	unit
The Earth-Sun System			
AU	astronomical unit (mean distance earth-sun)	$1.495\,978\,70 \times 10^{11}$ 499.004 782	m s
	solar constant	1370	W m^{-2}
	mean radius of the sun	6.96×10^8	m
The Earth			
V_E	volume of the earth	1.070×10^{21}	m^3
M_E	mass of the earth	5.9736×10^{24}	kg
ρ_E	mean density of the earth	5.515×10^3	kg m^{-3}
ω_E	mean rotation rate	7.292115×10^{-5}	rad s^{-1}
g_m	mean acceleration of gravity	9.80665	m s^{-2}
g_p	polar acceleration of gravity	9.832186	m s^{-2}
g_e	equatorial acceleration of gravity	9.780326	m s^{-2}
	gravitational parameter (GM_E)	3.9869×10^{14}	$\text{m}^3 \text{s}^{-2}$
R_m	mean radius of the earth	6371.0	km
R_e	equatorial radius of the earth	6378.137	km
R_p	polar radius of the earth	6356.752	km
f	flattening: $f = (R_e - R_p)/R_e$	1/298.257222	
d_j	Julian day	86400	s
d_s	mean sidereal day	86164.09054	s
y_j	Julian year	365.25	d_j
	sidereal year	365.25636	d_j
	tropical year	365.2421897	d_j
	anomalous year (apse to apse)	365.25964	d_j
	obliquity of ecliptic	23.4393	$^\circ$
p_0	standard surface pressure	1013.25	hPa
T_0	standard temperature	273.15	hPa
Dry Air			
m_d	molar mass of dry air	28.964	kg kmol^{-1}
R_d	specific gas constant of dry air	287.06	$\text{J kg}^{-1} \text{K}^{-1}$
ρ_d	density of dry air at p_0 and T_0	1.2922	kg m^{-3}
Water Vapor			
m_w	molar mass of water	18.016	kg kmol^{-1}
R_w	specific gas constant of water vapor	461.50	$\text{J kg}^{-1} \text{K}^{-1}$
ρ_w	density of liquid water at p_0 and T_0	1000	kg m^{-3}
ρ_i	density of ice at p_0 and T_0	917	kg m^{-3}

Table B.3: Parameters of earth and atmosphere. Sources: [Ahrens (1995), Andrews (2000), Raith (1997)].

Appendix C

Abbreviations

C.1 List of Acronyms

Acronym	Description
A/D	Analogue/Digital
AD	adjoint
AIRS	Advanced Infrared Sounder
AMSU	Advanced Microwave Sounding Unit
AO	Announcement of Opportunity
ASCAT	Advanced Scatterometer
ASI	Agenzia Spaziale Italiana
ATOVS	Advanced TOVS
AVHRR	Advanced Very High Resolution Radiometer
CC	Corner Cube
CIRA	COSPAR International Reference Atmosphere
COSPAR	Committee on Space Research
CNES	Centre National d'Etudes Spatial
CPU	Central Processing Unit
ECMWF	European Centre for Medium-Range Weather Forecasts
EGOPS	End-to-end GNSS Occultation Performance Simulator
ENVISAT	Environmental Satellite
EPS	EUMETSAT Polar System
ERS	European Remote Sensing (Satellite)
ESA	European Space Agency
EUMETSAT	European Organisation for the Exploitation of Meteorological Satellites

continued on next page

<i>continued from previous page</i>	
Acronym	Description
FOV	Field of View
FT	Fourier Transform
FTC	Fast Transmittance Coefficient
FWHH	Full Width at Half Height
FWHM	Full Width at Half Maximum
GENLN2	General line-by-line atmospheric transmittance and radiance model
GNSS	Global Navigation Satellite System
GOME	Global Ozone Monitoring Experiment
GPS	Global Positioning System
GRAS	GNSS Receiver Atmospheric Sounder
HWHP	Half Width at Half Power
HIRS	High Resolution Infrared Radiation Sounder
HIRTRAN	High Resolution Transmittance Model
IASI	Infrared Atmospheric Sounding Interferometer
IC	Information Content
IFOV	Instantaneous Field of View
IJSP	Initial Joint Polar System
IR	Infrared
ISRF	Instrument Spectral Response Function
ISSWG	IASI Sounding Science Working Group
LEO	Low Earth Orbit
LW	Long wave
METOP	Meteorological Operational (Satellite)
MHS	Microwave Humidity Sounder
MS	Maximum Sensitivity
MSU	Microwave Sounding Unit
NASA	National Aeronautics and Space Administration
NE Δ T	Noise Equivalent Temperature Difference
NESDIS	National Environmental Satellite, Data and Information Service
NOAA	National Oceanographic and Atmospheric Administration
NWP	Numerical Weather Prediction
OPD	Optical Path Difference
pdf	probability density function
RMS	Root Mean Square
RS	Remote Sensing
RT	Radiative Transfer
RTIASI	Radiative Transfer Model for IASI
<i>continued on next page</i>	

<i>continued from previous page</i>	
Acronym	Description
SAT	Surface Air Temperature (2 m Temperature)
SI	Systèm International (dUnités)
SNR	Signal-to-noise Ratio
SPOT	Système Pour l'observation de la Terre (satellite)
SST	Surface Skin Temperature; Sea Surface Temperature
SVD	Singular Value Decomposition
SW	Short wave
TIGR	TOVS Initial Guess Retrieval
TIROS	Television and Infrared Observation Satellite
TL	Tangent Linear
TLE	Two Line Element (File)
TOA	Top of the Atmosphere
TOVS	TIROS Operational Vertical Sounder
UTC	Coordinated Universal Time
UV	Ultraviolet
VHRR	Very High Resolution Radiometer
VIS	Visible
WMO	World Meteorological Organization
WWW	World Weather Watch
ZPD	Zero Path Difference

Table C.1: The Table contains the relevant acronyms used in the current work.

C.2 List of Units

Unit	Description
°C	degrees Celsius
C	Coulomb
cm	centimeter
deg	Degree
°	Degree
eV	electron Volt
g	gram
GHz	Giga Hertz
hPa	hecto Pascal
J	Joule
K	Kelvin

continued on next page

<i>continued from previous page</i>	
Unit	Description
kg	kilogram
km	kilometer
kmol	kilomol
m	meter
Mbits	megabits
mol	mol
mrad	milliradian
ms	milliseconds
mW	milli Watt
Pa	Pascal
ppbv	parts per billion by volume
ppmv	parts per million by volume
pptv	parts per trillion by volume
rad	radian
s	second
sr	steradian
W	Watt
%	percent
μm	micrometer

Table C.2: The Table contains the explanation of several units used in the current work.

References

- [Ahrens (1995)] Ahrens, T. J. (Ed.), *Global Earth Physics – A Handbook of Physical Constants*, American Geophysical Union, Washington, DC, 1995.
- [Aires *et al.* (2002)] Aires, F., W. B. Rossow, N. A. Scott, and A. Chédin, Remote sensing from the infrared atmospheric sounding interferometer instrument 2. simultaneous retrieval of temperature, water vapor and ozone atmospheric profiles, *Journal of Geophysical Research*, 107(D22), 4620, doi:10.1029/2001JD001,591, 2002.
- [Andrews (2000)] Andrews, D. G., *Atmospheric Physics*, Cambridge University Press, Cambridge, 2000.
- [Bell (1972)] Bell, R. J., *Introductory Fourier Transform Spectroscopy*, Academic Press, New York, 1972.
- [Born and Wolf (1999)] Born, M., and E. Wolf, *Principles of Optics*, Cambridge Univ. Press, Cambridge, 1999, (7th expand. ed.).
- [Camy-Peyret and Eyre (1998)] Camy-Peyret, C., and J. Eyre, The IASI Science Plan, *ISSWG report*, 1998.
- [Cayla (1996)] Cayla, F., Simulation of IASI spectra, *CNES document*, pp. IA–TN–0000–5627–CNE, 1996.
- [Chandrasekhar (1950)] Chandrasekhar, S., *Radiative Transfer*, Oxford University Press. (Reprinted and slightly revised by Dover Publications, Inc., New York, in 1960.), Oxford, 1950.
- [Chapman (1930)] Chapman, S., A theory of upper atmospheric ozone, *Mem. R. Meteorol. Soc.*, 3, 103–125, 1930.
- [Collard (1998)] Collard, A. D., Notes on IASI Performance, *U. K. MO Forecasting Research Technical Report No. 256*, 1998.
- [Crutzen (1970)] Crutzen, P., The influence of nitrogen oxides on atmospheric ozone content, *Q. J. R. Meteorol. Soc.*, 96, 320–325, 1970.

- [Emery et al. (2001)] Emery, W. J., S. Castro, G. A. Wick, P. Schluessel, and C. Donlon, Estimating Sea Surface Temperature from Infrared Satellite and In Situ Temperature Data, *Bulletin of the American Meteorological Society*, 82, 2773–2785, 2001.
- [Eyre (1991)] Eyre, J., A Fast Radiative Transfer Model for Satellite Sounding Systems, *ECMWF Technical Memorandum*, 176, 1991.
- [Eyre and Woolf (1988)] Eyre, J., and H. M. Woolf, Transmittance of atmospheric gases in the microwave region: a fast model, *Applied Optics*, 27, 3244 – 3249, 1988.
- [Fleming and McMillin (1977)] Fleming, H. E., and L. M. McMillin, Atmospheric transmittance of an absorbing gas. 2. a computationally fast and accurate transmittance model for slant paths at different zenith angles, *Applied Optics*, 16, 1366 – 1370, 1977.
- [Friedman (1969)] Friedman, D., Infrared characteristics of ocean water (1.5-15 μm), *Applied Optics*, 8, 2073 – 2078, 1969.
- [Gelb (1974)] Gelb, A. (Ed.), *Applied Optimal Estimation*, MIT Press, Cambridge, MA, 1974.
- [Goody (1964)] Goody, R. M., *Atmospheric Radiation*, Clarendon Press, Oxford, 1964.
- [Goody and Yung (1989)] Goody, R. M., and Y. L. Yung, *Atmospheric Radiation Theoretical Basis*, Clarendon Press (second edition), Oxford, 1989.
- [Hale and Querry (1973)] Hale, G. M., and M. R. Querry, Optical constants of water in the 200 nm to 200 μm wavelength region, *Applied Optics*, 12, 555 – 563, 1973.
- [Hanel et al. (1992)] Hanel, R. A., B. J. Conrath, D. E. Jennings, and R. E. Samuelson, *Exploration of the Solar System by infrared remote sensing*, Cambridge University Press, Cambridge, 1992.
- [Hannon et al. (1996)] Hannon, S., L. Strow, and W. W. McMillan, Atmospheric Infrared Fast Transmittance Models: A Comparison of Two Approaches, in *Proceedings of SPIE Conference 2830, Optical Spectroscopic Techniques and Instrumentation for Atmospheric and Space Research II*, Denver, 1996.
- [Hastie et al. (2001)] Hastie, T., R. Tibshirani, and J. Friedman, *The Elements of Statistical Learning: Data Mining, Inference, and Prediction*, Springer Verlag, New York, 2001.
- [Kirchengast et al. (1999)] Kirchengast, G., J. Hafner, and W. Poetzi, The CIRA86aQ_UoG model: An extension of the CIRA-86 monthly tables including humidity tables and a Fortran95 global moist air climatology model, *Tech. Rep. for ESA/ESTAC No. 8/1999*, IGAM, University of Graz, Austria, 1999.

- [Kirchengast et al. (2002)] Kirchengast, G., J. Fritzer, and J. Ramsauer, End-to-end GNSS Occultation Performance Simulator Version 4 (EGOPS 4) Software User Manual (Overview and Reference Manual), *Tech. Rep. for ESA/ESTAC No. 3/2002*, Inst. for Geophys., Astrophys., and Meteorol. (IGAM), Univ. of Graz, Austria, 2002.
- [Kourganoff (1952)] Kourganoff, V., *Basic Methods in Transfer Problems*, Oxford University Press. (Reprinted by Dover Publications, Inc., New York, in 1963.), Oxford, 1952.
- [Lerner et al. (2002)] Lerner, J. A., E. Weisz, and G. Kirchengast, Temperature and humidity retrieval from simulated Infrared Atmospheric Sounding Interferometer (IASI) measurements, *Journal of Geophysical Research*, 107, 10.1029/2001JD900,254, 2002.
- [Liou (1992)] Liou, K. N., *Radiation and Cloud Processes in the Atmosphere*, Oxford University Press, Oxford, 1992.
- [Liou (2002)] Liou, K. N., *An Introduction to Atmospheric Radiation*, Oxford University Press, Oxford, 2002.
- [Liu et al. (2000)] Liu, X., T. S. Zaccheo, and J.-L. Moncet, Comparison of Different Non-Linear Inversion Methods for Retrieval of Atmospheric Profiles, in *Proceedings of the 10th Conference of Satellite Meteorology*, pp. 293–295, Long Beach, California, 2000.
- [Masuda et al. (1988)] Masuda, K., T. Takashima, and T. Takayama, Emissivity of pure sea waters for the model sea surface in the infrared window regions, *Remote Sensing of Environment*, 24, 313 – 329, 1988.
- [Matricardi (1999)] Matricardi, M., RTIASI-1 User's Guide, *Tech. rep.*, ECMWF, Research Department, U. K., 1999.
- [Matricardi (2003)] Matricardi, M., RTIASI-4, a new version of the ECMWF fast radiative transfer model for infrared atmospheric sounding interferometer, *ECMWF Technical Memorandum*, 425, 63pp, 2003.
- [Matricardi and Saunders (1999)] Matricardi, M., and R. Saunders, A Fast Radiative Transfer Model for Simulation of Infrared Atmospheric Sounding Interferometer Radiances, *J. Appl. Optics*, 38, 5679–5691, 1999.
- [Maybeck (1982)] Maybeck, P. S., *Stochastic Models, Estimation, and Control*, vol. II, Academic Press, New York, 1982.
- [Maybeck (1994)] Maybeck, P. S., *Stochastic Models, Estimation, and Control*, vol. I, Navtech Book & Software Store, Arlington, VA, 1994.

- [McMillin and Fleming (1976)] McMillin, L. M., and H. E. Fleming, Atmospheric transmittance of an absorbing gas: A computationally fast and accurate transmittance model for absorbing gases with constant mixing ratios in inhomogeneous atmospheres, *Applied Optics*, 15, 358 – 363, 1976.
- [McMillin et al. (1979)] McMillin, L. M., H. E. Fleming, and M. L. Hill, Atmospheric transmittances of an absorbing gas. 3, *Applied Optics*, 18, 1600 – 1606, 1979.
- [Menke (1984)] Menke, W., *Geophysical Data Analysis: Discrete Inverse Theory*, Academic Press, New York, 1984.
- [Messiah (1990)] Messiah, A., *Quantenmechanik 2*, Walter de Gruyter, Berlin, 1990.
- [Messiah (1991)] Messiah, A., *Quantenmechanik 1*, Walter de Gruyter, Berlin, 1991.
- [Press et al. (1992)] Press, W. H., B. P. Flannery, S. A. Teukolsky, and W. T. Vetterling, *Numerical Recipes in FORTRAN: The Art of Scientific Computing*, Cambridge University Press, Cambridge, 1992.
- [Purser and Huang (1993)] Purser, R. J., and H.-L. Huang, Estimating Effective Data Density in a Satellite Retrieval or an Objective Analysis, *J. Appl. Met.*, 32, 1092–1107, 1993.
- [Raith (1997)] Raith, W. (Ed.), *Bergmann-Schaefer – Erde und Planeten*, Walter de Gruyter, Berlin, 1997.
- [Rayer (1995)] Rayer, P. J., Fast transmittance model for satellite sounding, *Applied Optics*, 34, 7387 – 7394, 1995.
- [Reuter et al. (1997)] Reuter, H., M. Hantel, and R. Steinacker, *Meteorologie*, pp. 131 – 310, vol. 7 of [Raith (1997)], 1997.
- [Rieder and Kirchengast (1999)] Rieder, M., and G. Kirchengast, Physical-statistical retrieval of water vapor profiles using SSM/T-2 sounder data, *Geophys. Res. Lett.*, 26, 1397–1400, 1999.
- [Rodgers (1996)] Rodgers, C. D., Information Content and Optimization of High Spectral Resolution Measurements, in *Proceedings of SPIE Conference 2830, Optical Spectroscopic Techniques and Instrumentation for Atmospheric and Space Research II*, pp. 136 – 147, Denver, 1996.
- [Rodgers (2000)] Rodgers, C. D., *Inverse Methods for Atmospheric Sounding: Theory and Practice*, World Scientific, Singapore, 2000.
- [Rothman et al. (1996)] Rothman, L. S., et al., HAWKS96, The HIRTRAN Atmospheric Workstation, in *Proceedings of the fourth Conference of Atmospheric Spectroscopy Applications*, Reims, 1996.

- [Salby (1996)] Salby, M. L., *Fundamentals of Atmospheric Physics*, Academic Press, San Diego, 1996.
- [Schmetz *et al.* (1995)] Schmetz, J., W. P. Menzel, C. Velden, X. Wu, L. van de Berg, S. Nieman, C. Hayden, K. Holmlund, and C. Geijo, Monthly mean large scale analysis of upper troposphere humidity and wind field divergence derived from three geostationary satellites, *Bull. Amer. Meteor. Soc.*, 76, 1578 – 1584, 1995.
- [Seinfeld and Pandis (1998)] Seinfeld, J., and S. Pandis, *Atmospheric Chemistry and Physics*, Wiley-Interscience, 1998.
- [Shannon and Weaver (1976)] Shannon, C. E., and W. Weaver, *Mathematische Grundlagen der Informationstheorie*, Oldenbourg, München, 1976, first published: 1949.
- [Sherlock (2000)] Sherlock, V. J., Impact of RTIASI Fast Radiative Transfer Model Error in IASI Retrieval Accuracy, *Forecasting Research Technical Report No. 319*, 2000.
- [Spencer and Braswell (1997)] Spencer, R. W., and W. D. Braswell, How dry is the tropical free troposphere? implications for global warming theory, *Bull. Amer. Meteor. Soc.*, 78, 1097 – 1106, 1997.
- [Steiner and Kirchengast (2004)] Steiner, A. K., and G. Kirchengast, Ensemble-Based Analysis of Errors in Atmospheric Profiles Retrieved from GNSS, Occultation Data, in *Occultations for Probing Atmosphere and Climate*, edited by G. Kirchengast, U. Foelsche, and A. K. Steiner, pp. 149 – 160, Springer, Berlin, 2004.
- [Susskind *et al.* (1983)] Susskind, J., J. Rosenfeld, and D. Reuter, An accurate radiative transfer model for use in the direct physical inversion of HIRS2 and MSU temperature sounding data, *J. Geophys. Res.*, 88, 8550 – 8568, 1983.
- [Thépaut and Moll (1990)] Thépaut, J.-N., and P. Moll, Variational Inversion of Simulated TOVS Radiances using the Adjoint Technique, *Q.J.R.Met.Soc.*, 116, 1425 – 1448, 1990.
- [Thomas and Stamnes (1999)] Thomas, G. E., and K. Stamnes, *Radiative Transfer in the Atmosphere and Ocean*, Cambridge University Press, Cambridge, 1999.
- [Weisz (2001)] Weisz, E., Temperature Profiling by the Infrared Atmospheric Sounding Interferometer (IASI): Advanced Retrieval Algorithm and Performance Analysis (ph. d. thesis), *Tech. Rep. Wissenschaftl. Ber. No. 11*, Institute for Geophysics Astrophysics, and Meteorology, Institute of Physics, University of Graz, Austria, 2001.
- [Weisz *et al.* (2003)] Weisz, E., G. Kirchengast, and J. A. Lerner, An efficient channel selection method for Infrared Atmospheric Sounding Interferometer data and characteristics of retrieved temperature profiles, *Tech. Rep. Wissenschaftl. Ber. No. 15*, IGAM, University of Graz, Austria, 2003.

- [Weisz *et al.* (2004)] Weisz, E., G. Kirchengast, and M. Schwärz, An efficient channel selection method for Infrared Atmospheric Sounding Interferometer data and characteristics of retrieved temperature profiles, 2004, (manuscript in preparation).
- [Zuev (1974)] Zuev, V. E., *Propagation of Visible and Infrared Radiation in the Atmosphere*, John Wiley & Sons, New York, 1974.